ION-BOMBARDMENT-INDUCED STRUCTURAL TRANSFORMATIONS IN OXIDES

ION-BOMBARDMENT-INDUCED STRUCTURAL TRANSFORMATIONS IN OXIDES

by

Hussein Mostafa Naguib, B. Eng.

A Thesis

Submitted to the School of Graduate Studies

in Partial Fulfilment of the Requirements

for the Degree

Doctor of Philosophy

McMaster University

October 1971

DOCTOR OF PHILOSOPHY (1971)
(Metallurgy and Materials Science)

McMASTER UNIVERSITY
Hamilton, Ontario

TITLE: Ion-bombardment-induced structural transformations in oxides

AUTHOR: Hussein Mostafa Naguib, B. Eng. (Cairo University, Egypt)

SUPERVISOR: Professor R. Kelly

NUMBER OF PAGES: xv, 240

SCOPE AND CONTENTS

In this dissertation, transmission electron microscopy, reflection electron diffraction, gas-release, and electrical-conductivity measurements have been used to study bombardment-induced structural transformations in oxides, and their implications to other non-metallic substances. Results are presented for bombardment-induced crystallization of amorphous thin films of ZrO_2; bombardment-induced amorphization of crystalline pellets of TeO_2, MoO_3, V_2O_5 and Bi_2O_3; and high-dose formation of lower oxides with MoO_3 and V_2O_5. Using the results of this experimental study along with information concerning 30 other solids, a thermal-spike model and a bond-type criterion are shown to be successful in predicting the behaviour of these materials under ion impact.

To my wife

NAGWA

and to

HATEM and RANIA

ACKNOWLEDGMENTS

The author sincerely appreciates the patient interest and encouragement of his supervisor Professor R. Kelly, throughout the course of this work, and also for his many valuable criticisms and suggestions during the preparation of this thesis.

The author also wishes to thank Professor J. D. Embury for the time he gave in discussing the electron microscopy and diffraction. Thanks are extended to the many members of the Department of Metallurgy and Materials Science who contributed helpful comments and advice.

Thanks are due to Miss. V. Komczynski for her skill and patience in typing the manuscript, and to Messrs. T. Tandi and D. Hodgson for their technical assistance.

Finally, the author gratefully acknowledges the following groups for their financial support: Cairo University (Egypt) in the form of study leave, the Department of Metallurgy and Materials Science (McMaster University) in the form of graduate fellowships, and the National Research Council (Canada) in the form of research grants to Professor R. Kelly.

ERRATUM

Page	Line	
3	8	replace "impinge" with "grow"
14	13	replace "models" with "studies"
16	9	Note that m = 1/3 is also applicable to the present work due to the overlapping of the ranges of validity [22].
137	15	add "much" before "greater"
180	4	add "a" before "completely"

TABLE OF CONTENTS

LIST OF ILLUSTRATIONS

LIST OF TABLES

CHAPTER 1

INTRODUCTION

Over the past decade, the bombardment of solids by heavy ions has been an active field of research. It has been carried out for a variety of reasons:

(1) Ion-bombardment studies have been undertaken with a view to increasing the knowledge of atomic collision processes. For example, the study of atomic ejection from the surface of a crystal under ion bombardment has provided a wealth of information on such phenomena as sputtering, secondary-electron emission, and focused collision sequences; at the same time the various experimental results have confirmed a variety of theoretical predictions [Cf. Refs. 1-4].

(2) The implantation of inert-gas ions followed by thermal heating of the bombarded solids has been undertaken with a view to studying diffusion processes and thereby providing indirect information on the damage induced by the bombardment (Cf. Ch. 3 in this dissertation).

(3) The use of heavy ions as damaging particles has become important as a means of simulating the effects of neutron [5] and fission-fragment damage [6] in reactor materials. The small elastic scattering cross section of the neutrons ($\sim 10^{-24}$ cm^2) results in a relatively low density of damage and a failure to recognize many fundamental processes. Fission fragments, on the other hand, are not the simplest type of particle either to obtain or to interpret, not only because of the resulting high levels of radio-activity which make subsequent studies difficult and time-consuming, but also

because the energies involved lead to both ionization and collision effects, the geometry of the damage regions is complicated, and the range of accessible doses is not great. The use of heavy ions is therefore providing a simple and cheap method of bombardment. Moreover, in a matter of hours with energetic heavy ions, one can produce the radiation damage conditions which prevail after many years in a reactor.

(4) More recently, ion implantation has become important as a means of changing the electrical and chemical properties of the bombarded materials. Of particular interest is the doping of semiconductors in order to produce changes in the conductivity of the material in a highly controlled manner. In order to assess the industrial potential of this technique, the fundamental material aspects of ion implantation are extensively studied such as the penetration profiles, the type of site on which the implanted atoms are located, the electrical activity, and the effects of damage on the material with particular reference to how this can be minimized. An extensive review of work in the field of ion implantation of semiconductors, particularly Si and Ge, up to early 1970 has been given by Mayer et al. [4].

(5) In addition, ion bombardment has been used in many applications of a more minor nature. Thus, according to Carter and Colligon [1], it is now used to clean surfaces, to carry out micromachining, and to produce thin films (especially for microcircuits). It is also the basic process responsible for the action of modern high-speed oil-free pumping devices.

In this dissertation, heavy-ion bombardment has been used to study bombardment-induced structural transformations in oxides, and, the

implications of these changes to other solids. The impact of high doses of heavy ions on a solid has as its usual result one of two things. Either the solid remains crystalline, with or without a phase change, or else the solid becomes disordered (amorphized). Much less usual are examples where an amorphous material is made to crystallize due to ion impact. It will be shown in this context, that when thin films of amorphous ZrO_2 are bombarded with Kr^+-ions, small crystalline regions (<1000 Å) appear and gradually impinge until complete crystallinity is achieved.

Using the results of ion-impact crystallization of amorphous ZrO_2, along with the results concerning the behaviour of 20 other solids, a thermal-spike model is presented to predict the behaviour of these materials under ion impact. In particular, those solids for which the ratio T_c/T_m, i.e. (crystallization temperature)/(melting temperature), is small are predicted to undergo self-annealing following ion impact, while large values of T_c/T_m are predicted to mean that the solid retains extensive disordering (amorphization) following ion impact.

With this proposed thermal spike model a number of predictions have been made concerning the stability of some substances which have apparently not yet been studied by ion bombardment. Among these, TeO_2, MoO_3, V_2O_5, and Bi_2O_3 are considered to be particularly significant tests of the model, since any disordering would occur in spite of the low value of T_c, thence in spite of the effects of ambient temperature and of beam heating. Using gas-release measurements and reflection electron diffraction, it has been possible to show that these oxides behave as

predicted, i.e. amorphize at low doses ($< 1 \times 10^{14}$ ions/cm^2). Other models for predicting the stability of materials on irradiation have been discussed. A bond-type criterion, based on estimating the amount of ionic character, was found particularly effective in predicting the behaviour of 38 substances on irradiation.

Finally, it has been shown that structural transformations induced by high doses of heavy ions may be accompanied by a marked electrical conductivity increase in some oxides such as MoO_3 and V_2O_5. This is attributed to preferential sputtering of oxygen atoms from the oxides, which leads to the formation of lower, highly conductive, oxides. This result, which has never been noted before, is regarded as having particularly important practical implications. For example, it implies severe limitations on the use of certain oxides in radiation environments, or in preparing thin films by sputtering oxide cathodes; at the same time, however, it indicates a possible means of fabricating new solid-state devices.

Because of the interdisciplinary nature of this investigation, a general background review of some topics in the ion bombardment of solids, followed by a description of the basic ideas concerning the diffusion of inert gases in ion-bombarded solids and its applications to studying radiation damage, are included in the next two chapters.

CHAPTER 2

ION BOMBARDMENT OF SOLIDS

2.1 Introduction

This chapter is intended to provide a general background review of certain aspects of the subject of ion bombardment which are basic to understanding the theoretical models and experimental problems involved in the present dissertation. Since there are a number of thorough reviews (Ref. [1-4] and [7-13]), which have presented detailed treatments of the existing theories, there will be no attempt to give a complete derivation of the material presented. Included are discussions of the displacement process, the penetration of ions, the spatial distribution of damage, and spike phenomena.

2.2 The displacement process

2.2.1 The displacement threshold

A very simple but effective method of estimating the energy which would be required to move an atom from its site and to force it into the surrounding lattice to form a Frenkel defect has been described by Seitz [14]. The energy of sublimation, E_c, of a typical atom or ion in a solid is in the region of 5 or 6 eV, so that the energy required to move an atom from an internal site, as opposed to a surface site, might be expected to be about twice as large (since twice as many bonds are involved). Atoms on neighbouring sites, however, will oppose this

removal and so the energy required to carry the process through will be at least 4 E_c. On the basis of this kind of intuitive reasoning, it follows that some 25 eV of energy will have to be transferred in a collision if the struck atom is to be displaced permanently from its normal lattice position to an interstitial site. In the most simple treatments of radiation damage this displacement energy (E_d), as it is normally called, is given a value of exactly 25 eV.

If we consider a real crystal lattice, however, it is obvious that E_d depends upon the direction in which the struck atom moves, and it may also vary from site to site in the crystal lattice if the sites are not all equivalent. Moreover, if a lattice atom receives an energy E_2 from a bombarding particle, then we should in reality define a probability $P(E_2)$ that the atom is displaced. This probability will rise from zero at some lower energy to unity above some higher value. The exact variation of P with E_2 is unknown, and we will generally assume in calculations that the value of the displacement energy is fixed at 25 eV.

2.2.2 The differential cross section for collision

A moving particle colliding with a stationary atom is deflected from its course by an amount which depends on its energy and on its closest distance of approach. The deflection is greater for smaller energies and for closer approaches. The probability that a given amount of energy will be transferred from the particle to the atom is best expressed in terms of an area through which the particle trajectory must

pass if the energy transfer is to occur (Fig. 2.1). This area is called the differential cross section for energy transfer. Specifically, if the particle has energy E_1 and if it transfers an energy between E_2 and $(E_2 + dE_2)$ to the lattice atom, the differential cross section is written as:

$$\frac{d\sigma(E_1,E_2)}{dE_2}\ dE_2 \tag{2.1}$$

For screened coulomb interaction between an ion and an atom or between two atoms, Lindhard et al. [15] derived the following general form of the differential cross section:

$$d\sigma(E_1,E_2) = \pi a^2\ \frac{dt}{2t^{3/2}}\ f(t^{1/2}) \tag{2.2}$$

where $t = \dfrac{\varepsilon E_2}{\hat{E}_2}$

$\hat{E}_2 = \gamma E_1$

E_1 = incident energy

E_2 = transferred energy, $0 \le E_2 \le \hat{E}_2$

$\gamma = \dfrac{4M_1M_2}{(M_1+M_2)^2}$

M_1 = mass of the incident (scattered) particle

M_2 = mass of the target (recoiling) particle

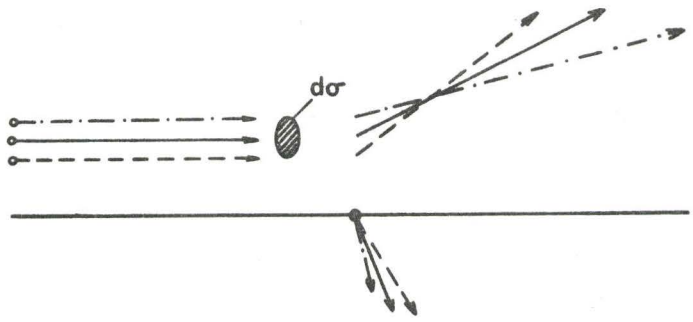

Fig. 2.1 Definition of the differential cross section. Note that dσ can also be represented as an annulus.

$$\varepsilon = \left(\frac{M_2 E_1}{M_1+M_2}\right)\left(\frac{Z_1 Z_2 e^2}{a}\right)^{-1}$$

Z_1 = atomic number of incident particle

Z_2 = atomic number of target particle

a = Thomas-Fermi screening radius

$= 0.8853\ a_o\ (Z_1^{2/3} + Z_2^{2/3})^{-1/2}$ (2.2a)

a_o = the first Bohr radius of the hydrogen atom = 0.529 Å

$f(t^{1/2})$ is a function that depends on the assumed form of the screening function

Lindhard et al. [16] have calculated the function $f(t^{1/2})$ for the collision of neutral Thomas-Fermi atoms. They also showed that in the case of the power-law approximation to the Thomas-Fermi atom, i.e. where the potential is in the form $V(r)\ \alpha r^{-1/m}$, this function can be expressed as:

$$f(t^{1/2}) \approx \lambda_m t^{(\frac{1}{2}-m)}, \qquad (2.3)$$

where the constants m and λ_m will have the values of $1 \lesssim m \lesssim 1/3$ and $0.3 \lesssim \lambda_m \lesssim 1.5$ in the important regions of screened coulomb interactions. Then from (2.2), (2.2a) and (2.3), they obtained the differential cross section in the form:

$$d\sigma(E_1,E_2) = CE_1^{-m} E_2^{-1-m} dE_2 \tag{2.4}$$

with

$$C = \frac{\pi}{2} \lambda_m a^2 \left(\frac{M_1}{M_2}\right)^m \left(\frac{2Z_1Z_2e^2}{a}\right)^{2m} \tag{2.4a}$$

where e is the unit of electrical charge.

In fact, having defined $d\sigma(E_1,E_2)$, the differential cross section for collision, the whole displacement process can be easily described since many important quantities are defined in terms of $d\sigma(E_1,E_2)$. For example, the total cross section, σ_d, for a collision with the energy transfer E_2 lying anywhere between E_d and $\hat{E}_2$, is:

$$\sigma_d = \int_{E_d}^{\hat{E}_2} \frac{d\sigma(E_1,E_2)}{dE_2} dE_2 \tag{2.5}$$

Using (2.4) and (2.5) one can define the average energy transfer in collision, $\langle E_2 \rangle$, as:

$$\langle E_2 \rangle = \frac{1}{\sigma_d} \int_{E_d}^{\hat{E}_2} E_2 \frac{d\sigma(E_1,E_2)}{dE_2} dE_2 \tag{2.6}$$

Eq. (2.5) permits the definition of a mean free path, ℓ_p, for collision, i.e. the average distance covered by the incident particle before it makes a collision, as:

$$\ell_p = \frac{1}{N\sigma_d} \quad , \tag{2.7}$$

where N is the number of target atoms per unit volume. Finally, one can formulate the mean specific energy loss, (dE/dx), and nuclear stopping cross section (S_n) as:

$$S_n = -\frac{1}{N}\left(\frac{dE}{dx}\right) = \int_{E_d}^{\hat{E}_2} E_2 \frac{d\sigma(E_1,E_2)}{dE_2}\, dE_2 \qquad (2.8)$$

In addition, three other important quantities, describable in terms of $d\sigma(E_1,E_2)$, will appear elsewhere in this chapter, namely, the electronic stopping cross section, nuclear collision energy, and defect density.

2.2.3 The number of displaced atoms

The simplest model of calculating the number of displaced atoms in a cascade, $\nu(E_1)$, was proposed by Kinchin and Pease [7]. Their treatment was based on the following assumptions:

(a) random slowing down

(b) elastic two-body collision

(c) hard-sphere scattering

(d) an atom recoiling with energy E_2 is displaced when $E_2 > E_d$

(e) no energy is lost if $E_2 > E_d$, while all the energy is lost if $E_2 < E_d$

(f) an atom of energy E_1 makes a replacement collision if $E_1 - E_2 < E_d$

Assumptions (b) and (c) lead to a probability of energy transfer between E_2 and $E_2 + dE_2$ given by $P(E_1, E_2) = 1/E_1$. By integrating the number of displacements produced at a given energy multiplied by the

probability of this energy, for both primary and knock-on atoms, Kinchin and Pease obtained

$$\nu(E_1) = \frac{E_1}{2E_d} \qquad (2.9)$$

Alternative models [Cf. 1 & 3] have been used to modify Eq. (2.9) by improving the above assumptions. The weakest point of these models is assumption (c) of hard-sphere scattering. However, it has frequently been shown that the number of displaced atoms is not strongly dependent on the form of the interaction potential. For example, using the power-law approximation to the Thomas-Fermi cross section (Eq. 2.4), and neglecting the loss of defects by replacement collisions, Sigmund [17 & 18] used the Kinchin and Pease model to obtain:

$$\nu(E_1) = \frac{6}{\pi^2} \frac{E_1}{U} \ln \left(1 + \frac{U}{E_d}\right) \qquad (2.10)$$

where U is the binding energy lost by an atom when leaving a lattice site. Taking $E_d = 4E_b$, where E_b is the bond energy, and substituting $U = E_d$, Eq. (2.10) reduces to:

$$\nu(E_1) = 0.42\ E_1/E_d \qquad (2.10a)$$

This equation is essentially the same as Eq. (2.9) despite rather different underlying assumptions.

As a matter of fact, Eq.(2.10a)contains the assumption that each displaced atom has had to break its four nearest-neighbour bonds (as in Si and Ge). However, Sigmund [17] points out that if all the atoms within a localized region became displaced, then only two bonds on the average would have to be disrupted per atom. This would increase $\nu(E_1)$ by about a factor of 2.

The essential feature of the different theories on defect production by heavy ions is that they calculate an upper limit for $\nu(E_1)$. At least six factors may play a role in complicating such calculations:

(1) A considerable amount of vacancy-interstitial recombination is expected to occur at the end of the cascade, without any thermal activation being required. Such athermal rearrangement occurs whenever two defects are formed close enough for coalescence to occur. At present, there are no good estimates of the extent of such recombination in ion-bombarded materials. However, in computer simulation of the collision cascade induced by 10 keV-Fe, for instance, Beeler [19] found that almost half of the point defects were lost in athermal annihilations.

(2) Another complication is due to the migration of displaced atoms either to each other or to defects in the crystal (e.g. grain boundaries, dislocations, etc.). This will make $\nu(E_1)$ depend on the natural defect structures, on the accumulated radiation damage, and on the dose rate.

(3) Another difficulty is due to the anisotropy of the threshold displacement energy, E_d, mentioned in sec. (2.2.1). Using a mean value for E_d rather than the anisotropic one will increase the approximation in evaluating $\nu(E_1)$ particularly with single-crystal targets. The magnitude of this effect is difficult to estimate though is believed to be as much as a factor of three. (Ref. [11], p. 101)

(4) A fully representative description of damage production should include recognition of all types of energy-loss process involved in the slowing down of the bombarding ions in the target. These losses fall into two major groups:

(a) Nuclear stopping, $(dE/dx)_n$, due to the screened coulomb collisions between the moving ion and the target atoms. This is written as:

$$\left(\frac{dE}{dx}\right)_n = -N\, S_n \tag{2.11}$$

where S_n is the nuclear stopping cross section (Eq. 2.8). Using a power-law differential cross section as given by Eq. (2.4), we obtain:

$$\left(\frac{dE}{dx}\right)_n = \frac{-NC}{1-m}\, \gamma^{1-m}\, E_1^{1-2m} \quad (\text{for } m \neq 1) \tag{2.12}$$

$$\text{or} \quad = \frac{-NC}{E_1}\, \ell n\, \frac{\gamma E_1}{E_d} \quad (\text{for } m = 1) \tag{2.12a}$$

(b) Electronic stopping, $\left(\frac{dE}{dx}\right)_e$, due to the interaction between the electrons associated with the moving ion and the various electrons (both bound and free) of the target atoms. This can be expressed in a similar form to $(dE/dx)_n$:

$$\left(\frac{dE}{dx}\right)_e = -NS_e\,, \tag{2.13}$$

where S_e is the electronic stopping cross section, best described in terms of range parameters as will be discussed in sec. (2.3.2).

In general, $(dE/dx)_n$ is dominant for low energies (low E_1), when $\nu(E_1) = E_1/2E_d$ is a good approximation. However, at high energies $\nu(E_1) << E_1/2E_d$ and electronic losses should be introduced by replacing E_1 with the nuclear collision energy, E_n, defined as:

$$E_n = \int_0^{E_1} \frac{S_n}{S_e+S_n}\, dE_1 \tag{2.14}$$

Thus, E_n is the portion of E_1 that goes into nuclear stopping and $\nu(E_1)$ becomes:

$$\nu(E_1) = \frac{E_n}{2E_d} \quad . \tag{2.15}$$

(5) Usually in calculating the number of displaced atoms $\nu(E_1)$, the possibility of channeling of the incident ions is neglected. This can influence $\nu(E_1)$ by:

(a) reducing its value, for whilst an ion is channelled it is less likely to make displacement collisions,

(b) making $\nu(E_1)$ become dose dependent since channelled trajectories will be less likely in a damaged lattice.

There have been a number of studies made on this effect [Cf. Ref. 3] and although the effect of channelling is clearly established and given roughly by these models, exact analysis must await the availability of more realistic interatomic potentials. However, as shown by Thompson [3], channelling might be introduced in a rather crude way by raising the whole expression to the power (1-2C), where C is a number much less than 1, and we then have:

$$\nu(E_1) = \left(\frac{E_n}{2E_d}\right)^{1-2C} \qquad \text{for } E_n >> E_d \tag{2.16}$$

(6) It has been shown theoretically, experimentally, and by computer simulation of the displacement cascade (see summary in Ref. [3]) that below a certain critical energy E_f^{cpd} much of the energy in the cascade is focused into the closest packed directions (denoted by superscript cpd).The effect of focusing is to prevent further multiplication of

the cascade, for once the momentum is focused, collisions are either head-on leading at most to replacement, or else they are glancing and not energetic enough to create displacements. In the simple treatment of calculating the number of displaced atoms one should therefore use either $2E_d$ or E_f^{cpd} as the limit of cascade multiplication, whichever is greater. Thus if $E_f^{cpd} > 2E_d$ then;

$$\nu(E_1) = \frac{E_1}{E_f^{cpd}} \tag{2.17}$$

otherwise the original equation (Eq. 2.9) will hold. In general, one expects little effect on $\nu(E_1)$ amongst the light or medium-weight elements but in heavy elements a reduction of 50% is possible.

Combining the last three effects (known as dynamic effects), namely electronic losses, channelling, and focusing, we then have the following expression for $\nu(E_1)$, the number of displaced atoms in a cascade [3]:

$$\nu(E_1) = \left(\frac{E_n}{E_f^{cdp}}\right)^{1-2C} \quad \text{for} \quad E_f^{cpd} > 2E_d \tag{2.18}$$

$$\nu(E_1) = \left(\frac{E_n}{2E_d}\right)^{1-2C} \quad \text{for} \quad E_f^{cpd} < 2E_d \tag{2.18a}$$

2.2.4 Density of defects in cascades

The average concentration of defects (Frenkel pairs) in a cascade can be generally obtained from the following equation [3]:

$$C_d \simeq t\beta \int_{E_d}^{\hat{E}_2} \nu(E_2) \frac{d\sigma}{dE_2} dE_2 \tag{2.19}$$

or

$$C_d = \frac{t\beta S_n}{2E_d} \tag{2.19a}$$

where β is the flux of bombarding particles, in cm^{-2} sec^{-1} and t is the duration of the bombardment, in secs. Thus, we can calculate C_d by calculating the damage function $\nu(E_2)$ as described in the previous section and the nuclear stopping cross section S_n from Eq. (2.8) combined with the appropriate differential cross section. For example, for energetic heavy ions in the energy region of interest in this work, Eq. (2.19a) can be formulated as:

$$C_d = \frac{t\beta}{2E_d} \frac{C}{1-m} \gamma^{1-m} E_1^{1-2m} \qquad (2.20)$$

For m = 1/2, which is applicable to most of the present work, this reduces to

$$C_d = t\beta\, C\gamma^{1/2} / E_d \qquad (2.21)$$

Eq. (2.21) shows that, in the case of heavy ions (i.e. where m = 1/2), C_d is independent of bombarding energy, which implies a constant linear density of displaced atoms along the ion's track.

Sigmund et al. [20] have presented another approach for calculating C_d, thus,

$$C_d = \frac{\nu(E_1)}{V(E_1)} \qquad (2.22)$$

with

$$V(E_1) = \delta^{2/3} \frac{4\pi}{3} R^3(E_1) \qquad (2.22a)$$

= the volume of the cascade

$R(E_1)$ is the effective radius of the damage volume as a function of incident energy, which is defined as

$$R^2(E_1) = \langle \Delta r^2 \rangle_D = \langle \Delta x^2 \rangle_D + 2\langle y^2 \rangle_D \ , \qquad (2.23)$$

the x-direction being parallel to the initial velocity and the y-direction perpendicular to it. Averages are taken over the damage distribution (Cf. sec. (2.4)), and $\Delta x = x - \langle x \rangle$. $\langle \Delta x^2 \rangle_D$ and $\langle y^2 \rangle_D$ are [21,22] the widths of the distribution of damage due to many events with identical initial conditions. δ is a parameter introduced by the authors to take into account the reduction in cascade volume for a single event. Values of δ have been given as a function of the mass ratio M_2/M_1 for various values of m. The use of $\delta^{2/3}$ in Eq. (2.22a) is only correct as long as there is no formation of subcascades, i.e. $M_1 \gtrsim M_2$.

2.3 The penetration depth of ions

In studies dealing with understanding ion bombardment phenomena such as radiation damage, sputtering, and doping by ion implantation, it is often important to have information about the penetration depth of fast moving atoms. Extensive studies providing such information have been performed in the last decade, either experimentally, or by computer simulation, or theoretically by the development of unified range-energy relations by Lindhard and his colleagues. An extensive review of these studies up to 1966 has been given by Carter and Colligon [Ref. 1, Ch. 5], while a survey of most of the recent work was given by Nelson [Ref. 2, Chs. 3 & 4] and Mayer et al. [Ref. 4, Ch. 2].

In the absence of depth distribution measurements, the most generally accepted way of obtaining range data, at present, is by means of the theoretical treatment of Lindhard et al. [15,16,23] (referred to subsequently as LSS). As such measurements were outside the scope

of this dissertation, the LSS treatment has been used to supply range parameters for the materials used, whenever it was needed. In this section some of the general concepts involved in range calculations will be given, along with the theoretical framework of the LSS treatment. The validity of this treatment will also be discussed.

2.3.1 General concepts

As we have indicated previously in sec. (2.2.3), a heavy charged particle travelling through matter loses energy by Coulomb interactions both with the target nuclei (i.e. nuclear stopping, $(dE/dx)_n$), and with bound or free electrons (i.e. electronic stopping, $(dE/dx)_e$). Nuclear excitation and radiation losses can be neglected because of their small cross sections. The total stopping power, $(dE/dx)_t$ is, therefore, usually expressed as the sum of the nuclear and electronic stopping, i.e.

$$\left(\frac{dE}{dx}\right)_t = \left(\frac{dE}{dx}\right)_n + \left(\frac{dE}{dx}\right)_e \qquad (2.24)$$

It can be generally stated that nuclear stopping dominates at low energies (e.g. 40 keV Xe in Al) while electronic stopping dominates at large energies (e.g. Xe of several MeV in Al). The transition from one region of stopping to the other occurs smoothly and depends in addition on the mass and atomic number of the colliding particles.

Since the incoming ion interacts with a large number of the target atoms before it comes to rest, and the energy transfer in each collision will be different, the range and stopping power are statistical concepts. In order to define the range of a charged particle, the following concepts are frequently used (Fig. 2.2):

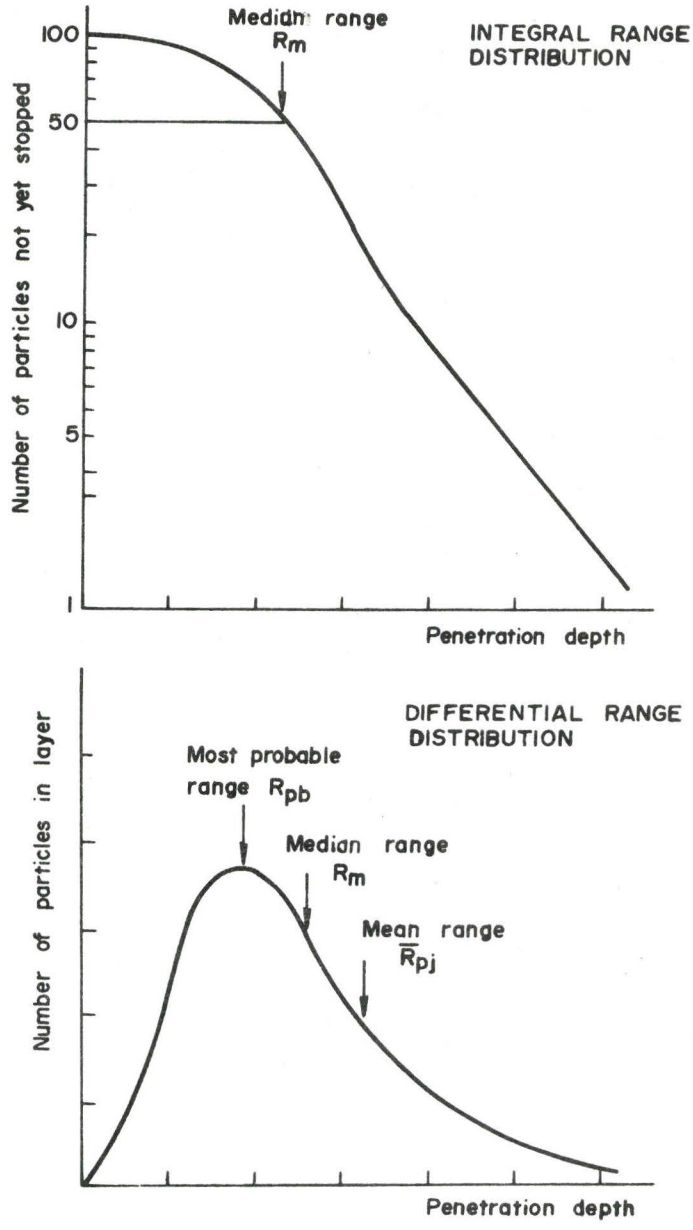

Fig. 2.2 a) Shows a typical residual or integral range distribution on a semi-log plot; b) shows the corresponding differential distribution. The positions of the most probable, median, and mean ranges are indicated.

*The total (true) range, R, is the sum of the path lengths between successive collisions for a single event.

*The average total range, $\bar{R}$, is the arithmetic average of all total ranges.

*The projected mean range, $\bar{R}_{pj}$, is the average penetration depth as projected along the incident direction of ions.

*The most probable range, R_{pb}, is the most probable depth of penetration normal to the surface (the peak, if any, in the differential range distribution).

*The median range, R_m, is the projected depth of penetration by which 50% of the ions have been brought to rest.

*The maximum range, R_{max}, is the upper limit for ion penetration as observed for the vanishingly small fraction of ions which suffer no nuclear collision events.

Another important quantity is the projected range straggling, $\langle \Delta x^2 \rangle$, or mean square fluctuation in range, while for some purposes the skewness, etc., of the range distribution must be considered in terms of higher moments of the range such as $\langle \Delta x^3 \rangle$ and $\langle \Delta x^4 \rangle$.

Most experiments are performed by measuring the number of ions which penetrate to depths exceeding a certain depth and the experiments directly give the so called "integral range distribution" (Fig. 2.2a). From these results it is of course easy to calculate the number of ions stopped in a certain depth interval and thus to derive the "differential range distribution" (Fig. 2.2(b)).

2.3.2 The theoretical background of the LSS treatment

As we have mentioned in the introduction to this section, the LSS group was able to develop a "unified theory" for atomic stopping. Thus, a universal range-energy relation has been obtained in terms of two dimensionless parameters ρ and ε, quantities which might be called the reduced range and reduced energy. In the same way a dimensionless specific energy loss $d\varepsilon/d\rho$ is used. The parameters ρ and ε are defined through the following formulae where $\bar{R}$ is the average total range and E_1 is the incident energy

$$\rho = \bar{R}NM_2\, 4\pi a^2 \frac{M_1}{(M_1+M_2)^2} \tag{2.25}$$

$$\varepsilon = \frac{E_1 a M_2}{Z_1 Z_2 e^2 (M_1+M_2)} \tag{2.26}$$

where the notations are as given with Eq. (2.2a) or immediately following. By deriving a differential cross section in the form given by Eq. (2.2), LSS then obtained a universal relationship for the nuclear stopping in the form:

$$\left(\frac{d\varepsilon}{d\rho}\right)_n = \int_0^{\varepsilon} \frac{1}{2t^{3/2}} f(t^{1/2})\, \frac{dt}{\varepsilon} \tag{2.27}$$

where, again, all the notations are as defined in Eq. (2.2a). The resulting universal relationship between $\left(\frac{-d\varepsilon}{d\rho}\right)_n$ and $\varepsilon^{1/2}$ is shown by the solid line in Fig. (2.3) ($\varepsilon^{1/2}$ is proportional to ion velocity).

To obtain the stopping contribution due to electronic collisions, LSS have derived a velocity-proportional electronic stopping power,

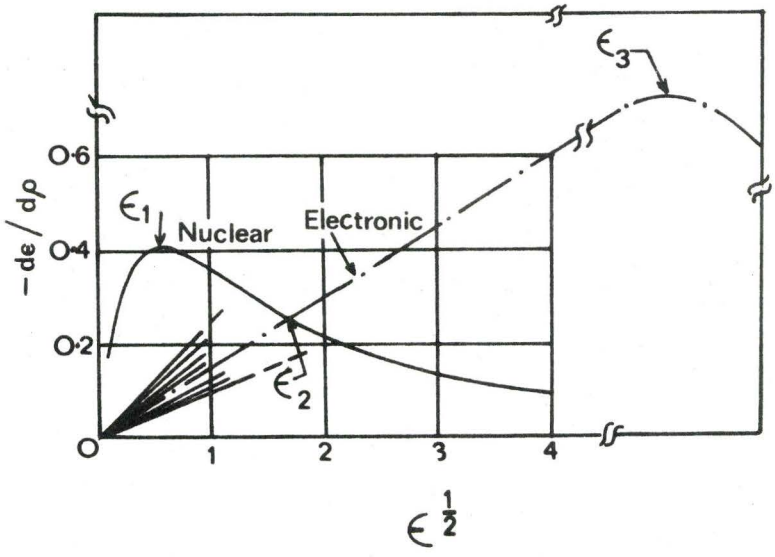

Fig. 2.3 Theoretical nuclear and electronic stopping-power curves as based on the LSS treatment.

$(d\epsilon/d\rho)_e$, given by:

$$\left(\frac{d\epsilon}{d\rho}\right)_e = -k\epsilon^{1/2} \tag{2.28}$$

with

$$k = \frac{\xi_e(0.0793)Z_1^{1/2}Z_2^{1/2}(M_1+M_2)^{3/2}}{(Z_1^{2/3}+Z_2^{2/3})^{3/4}M_1^{3/2}M_2^{1/2}}$$

where ξ_e is a constant of the order of $Z_1^{1/6}$. The electronic stopping calculations therefore do not produce a universal $(d\epsilon/d\rho)_e$ curve, but rather a set of curves each characterized by a particular value of k, as shown in Fig. (2.3). For most combinations of projectile and target, the appropriate values of k fall between 0.1-0.25, while in the present work k = 0.15 is a good approximation.

It is seen in Fig. 2.3 that nuclear stopping is the more important process at low energies, that it reaches a maximum value around $\varepsilon = 0.35$ (i.e. ε_1 in Fig. 2.3) and that it then falls off. Electronic stopping, on the other hand, increases linearly with velocity over a very wide range, and hence becomes the dominant process for energies greater than $\varepsilon = 3$ (i.e. for $\varepsilon > \varepsilon_2$). At much higher energies, $(-d\varepsilon/d\rho)_e$ also passes through a maximum and subsequently falls off as ε^{-1}. This high-energy region is what is known as "the Bethe formula region", where the ion velocity exceeds that of the orbital electrons, but it is far beyond the energy range of interst in most ion-bombardment studies.

To obtain a range-energy relationship from these $(d\varepsilon/d\rho)$ curves in Fig. (2.3), LSS treat the forms of energy loss as being independent; hence, the overall rate of energy loss, $(d\varepsilon/d\rho)_{total}$, is obtained by adding the appropriate $(d\varepsilon/d\rho)_e$ value for electronic stopping to the universal value $(d\varepsilon/d\rho)_n$ for nuclear stopping. This can then be integrated from the bombarding energy down to zero to give the range as a function of energy, thus

$$\rho(\varepsilon,k) = -\int_0^{\varepsilon} \frac{d\varepsilon}{(d\varepsilon/d\rho)_n + (d\varepsilon/d\rho)_e} \qquad (2.29)$$

This $\rho(\varepsilon,k)$ is accordingly neither universal nor has a simple form. Eq. (2.29) has been extensively tabulated [e.g. 24] for a Thomas-Fermi differential scattering cross section.

2.3.3 Comments on the validity of the LSS theory

Before we leave this section it seems justified to make some comments on the validity of the theoretical treatment of LSS for range calculations:

1. LSS assumed that the arrangement of atoms in the target is random. Because the role of the crystal structure is ignored, their results apply strictly only to amorphous substances and are otherwise lower limits. For amorphous substances aggreement with experiments should generally be good (probably ~30% [e.g. 25,26])

2. The range of an ion calculated from Eq. (2.29) is the average total range $\bar{R}$, as defined in sec. (2.3.1). In most experiments, however, it is the projection $\bar{R}_{pj}$ of this average total path length on the direction of incidence that is of interest. The relation between $\bar{R}$ and $\bar{R}_{pj}$ has been discussed by LSS and by Schiøtt [27]. They express the correction term in the empirical form

$$\frac{\bar{R}}{\bar{R}_{pj}} = \frac{\bar{\rho}}{\bar{\rho}_{pj}} = 1 + \frac{bM_2}{M_1} \qquad (2.30)$$

where b is slowly varying function of E_1 and $\bar{R}$. In the energy region where nuclear stopping dominates and for $M_1 > M_2$, $b \simeq 1/3$ is a fair approximation. Increased electronic stopping at higher energies leads to a smaller value for b.

Schiøtt [27] discusses the procedure to be followed in obtaining a more quantitative correction. Values of the ratio $\bar{R}/\bar{R}_{pj}$ combined with values of $\bar{R}$ as calculated from the LSS theory provide projected ranges $\bar{R}_{pj}$ for a large variety of projectiles and bombardment energies.

3. A further complication arises when the bombarded material consists of two (or more) different atomic species. If the atomic numbers of the atoms involved are not widely separated, in which case the stopping cross sections have approximately the same energy exponent, then a simple range formula is readily calculated using Eq. (2.29). For example, for the two components A and B of the compound A_xB_y:

$$R = \frac{R_A R_B M_{A_xB_y}}{xM_A R_B + yM_B R_A} \quad \mu g/cm^2, \tag{2.31}$$

where R_A and R_B are the ranges in A and B respectively in $\mu g/cm^2$ (it is important here to distinguish between normal length units and $\mu g/cm^2$) and M_A, M_B, and $M_{A_xB_y}$ are the molecular weights of A, B, and A_xB_y respectively.

However, range formulas are not easily obtained when the atomic numbers are considerably different and special calculations are needed for each compound [e.g. 27]. It is noted, however, that ranges for such materials derived using an equation of the type of Eq. (2.31) are in fair agreement with existing experimental values even for such extreme cases as UO_2 and WO_3 [25,28].

4. The LSS treatment assumed, as a first approximation, that the range distribution is Gaussian. In fact, experiments show that the range distribution may be very asymmetric, the degree of asymmetry being associated with the relative importance of nuclear collision processes. Sanders [29], and more recently Winterbon et al. [22], have generalized the LSS treatment to include higher-order moments of the range distribution, within the approximation of an inverse power potential. From these moments, they showed that it is possible to construct a

distribution function of the projected range for comparison with experiments.

5. The use of Thomas-Fermi statistical concepts in the LSS treatment leads to an electronic stopping power that increases monotonically with increasing Z_1 (projectile) for a given value of Z_2 (target) and ion velocity. However, experimental studies [See e.g., Ref. 4, p.27] have shown that electronic stopping has a marked periodic dependence on the atomic number of the incident ion. It has been shown [4] that the effect of this "Z_1-oscillation" on the range distribution is usually less than 10% for various ions bombarded into Si, and hence can often be neglected. In heavier substrates, such as Ge, the magnitude of this correction should be even smaller. However, for channelled ions, the effect of Z_1-oscillations is far from negligible.

2.4 Spatial damage distribution in a cascade

Theoretical analysis of the spatial distribution of structural damage in a cascade has been of interest for many years. However, the most accurate estimate of such a distribution known at present is that introduced only four years ago by Sigmund and Sanders [21], and, recently extended by Winterbon, Sigmund, and Sanders [22] (referred to subsequently as WSS).

The basic physical assumptions entering the WSS treatment are those formulated by LSS as described in the previous section. For example, they assumed binary collisions between incident ions and target atoms, neglected the binding energy of the target atoms, and did not

include a displacement threshold energy, which means, in effect, they calculated the spatial distribution of <u>energy</u> and not of displaced atoms. An integro-differential equation determining this energy distribution was derived using a power–law approximation to the Thomas-Fermi potential (Eq. 2.4) and neglecting the electronic stopping component. Exact solutions of the equation were difficult to obtain; it was, however, found possible to calculate exact expressions for averages over the distribution functions. The result is that there is one single length unit proportional to E^{2m} characterizing both the range and damage distributions. Results were, for the most part, expressed as moments over the damage and range distributions as a function of the ratio M_2/M_1. Part of these results is shown in Fig. (2.4) where first and second order moments over the damage and range distributions are given as functions of M_2/M_1. Also, a comparison between range moments with the corresponding damage moments is shown in Fig. (2.5). In these figures: $\langle x \rangle_R$ is the mean projected ion range (i.e. $\bar{R}_{pj}$ in Section 2.3.1), $\langle x \rangle_D$ is the mean projected damage depth, $\langle x \rangle$ is either $\langle x \rangle_R$ or $\langle x \rangle_D$, $\langle \Delta x^2 \rangle$ is $(x-\langle x \rangle)^2$, and $\bar{R}$ is the mean total ion range as approximated by

$$\bar{R} = \int_0^{E_1} \frac{dE_1}{NS_n} \qquad (2.32)$$

The theoretical analysis of WSS has, finally, arrived at the following conclusions:

(1) The damage distribution roughly agrees with the distribution of ions for $M_1 \leq M_2$, while the range distribution is much sharper (and

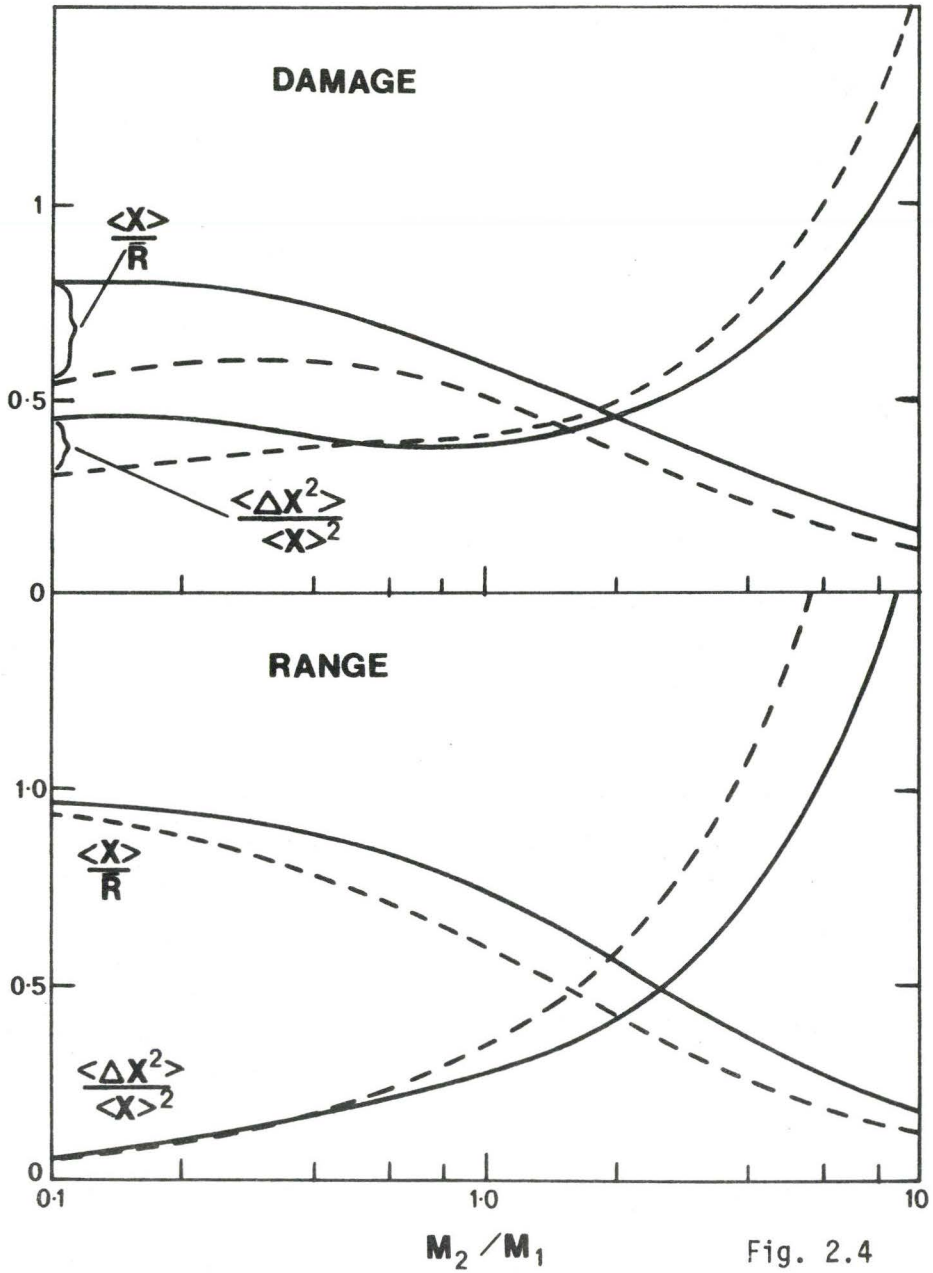

Fig. 2.4

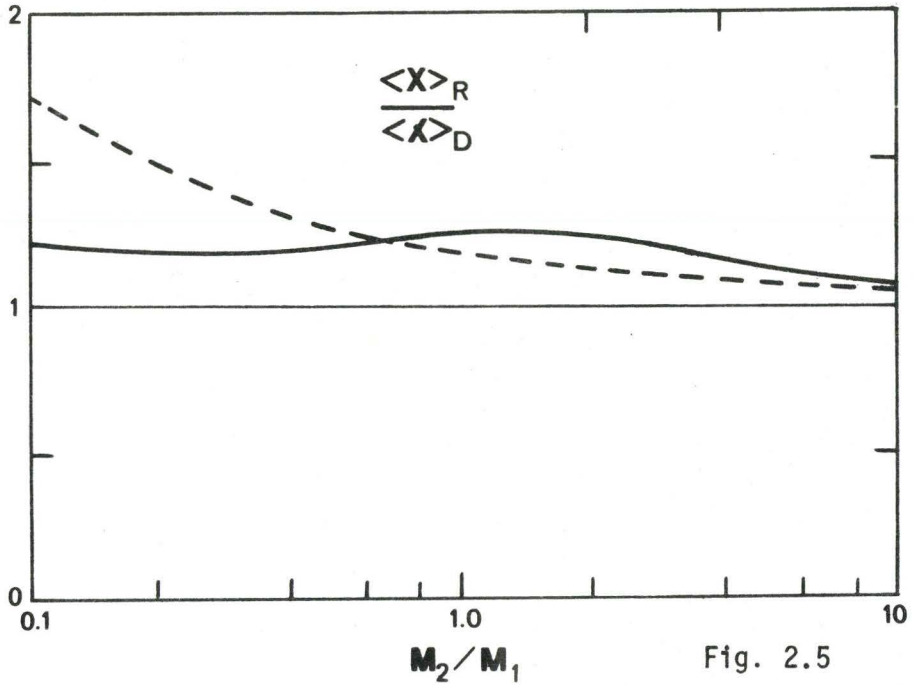

Fig. 2.5

Fig. 2.5 Ratio of average projected range to damage depth vs. M_2/M_1. Dashed line, m = 1/3; solid line, m = 1/2 (WSS [22]).

Fig. 2.4 First and second order averages over damage and depth distribution vs. M_2/M_1. Dashed line, m = 1/3; solid line, m = 1/2 (WSS [22]).

deeper) than the damage distribution for $M_1 >> M_2$.

(2) The damage distribution turned out to be approximately Gaussian for $M_1 \lesssim M_2$, while for $M_1 >> M_2$ it is roughly equal to the variation with depth of nuclear stopping.

(3) For all cases of power-law scattering, the mean damage depth $\langle x \rangle_D$ is consistently smaller than the mean projected ion range $\langle x \rangle_R$ (i.e. $\bar{R}_{pj}$), which means that the projectile comes to rest beyond the centre of the cascade.

(4) The damage distribution, for most cases, is slightly cigar-shaped, with the transverse extent of the defects typically 60% of that along the x-direction.

(5) The results have shown that hard-sphere scattering (which had been extensively used in early work on damage distribution) is too poor an approximation to allow quantitative conclusions, and sometimes even produces results that differ qualitatively from those obtained with the (more accurate) power-law cross section .

(6) In principle, both range and damage profiles, whether with Gaussian or non-Gaussian shapes, can be constructed from the moments $\langle \Delta x^n \rangle$ by the use of Edgeworth's expansion. However, this expansion is fairly bad for $M_1 > M_2$.

Finally, it is useful to point out briefly some of the reservations which have to be kept in mind when experimental results, if any, are compared with the WSS treatment:

(1) In these calculations the inelastic scattering was neglected, but evidence exists that displacements may occur in ionic insulators

owing to electrostatic forces which result from the ionization of atoms by electronic stopping processes. It may, thus, be invalid to use the WSS approach in analyzing results obtained for these materials.

(2) Experiments can be used for quantitative comparisons only when done at sufficiently low doses to prevent saturation effects. With single crystals, the ion beam must not be aligned with a channelling direction, while even with polycrystals channelling must be demonstrably minimal.

(3) Indirect experimental techniques based on the change of physical properties may be used only if one can distinguish properties affected by ion bombardment damage alone from those affected by implanted ions.

(4) Results obtained by electron microscopy of large defects [e.g. 30] are not necessarily comparable with the WSS damage distribution theory for, at least, two reasons:

(a) not all deposited energy leads to visible damage

(b) image-size distributions of damage clusters are not comparable to the quantities discussed by the WSS theory, since they concern properties of single collision cascades while the theory gives the mean damage distribution for many ions with the same initial conditions. In fact, an image-size distribution will always be a lower limit to the WSS distribution.

In view of the above reservations, there are as yet very few experimental results on damage distributions which can be used for quantitative comparison with the WSS theory [e.g. 31-33]. In general,

agreement is found as good as can be expected considering the approximations in the theory.

2.5 Spike phenomena

The various "spike" concepts were introduced to radiation damage theory to account for the sudden deposition of energy by rapidly moving particles (or lattice atoms) both along their tracks as well as towards the ends of the tracks. They represent localized regions in which the material is highly agitated in a manner similar to a localized melting, and during the time of this disturbance some activated processes may occur, such as the annealing of radiation-induced point defects, or a localized rearrangement (phase change) of the lattice.

The types of spike which might be relevant to the present context (i.e. bombardment with low or intermediate-energy heavy ions) are thermal, displacement, and plasticity spikes. Thus, in this section, the classical thermal-spike treatment will be briefly outlined along with a discussion of the recent sputtering experiments which provide strong evidence supporting the existence of these spikes. This will be followed by a short description of displacement and plasticity spikes.

2.5.1 Thermal spikes

When the displaced atoms degrade their energies below roughly 25 eV no further displacements will occur and this energy must be dissipated by lattice vibration and heating. This type of energy dissipation forms what is known as a thermal spike. A very useful way to regard this effect is in terms of a sudden delivery of heat to a restricted

volume of the lattice (spherical or point source). The temperature distribution due to a spike will be, accordingly, given by [8]:

$$T(r,t) = \frac{Q}{8(\pi\kappa t)^{3/2}} \exp\left(\frac{-r^2}{4\kappa t}\right), \qquad (2.33)$$

where Q is the source strength related to the incident energy E, κ is thermal diffusivity, r is the radius, and t is the time.

To avoid the mathematical difficulty of a singularity at zero time, it is usual to consider only what happens after a starting time $t_o = r_o^2/4\kappa$, where r_o is the mean atomic radius obtained from the equation:

$$\frac{4\pi r_o^3}{3} = \frac{1}{N}, \qquad (2.34)$$

where N is the number of atoms per unit volume. (One could, alternatively, use an even larger value of t_o in order to exclude events involving very high and perhaps meaningless temperatures).

An estimate of the temperature in a spike, T_s, can be made [34] by assuming the transferred energy (E_2) to be shared amongst atoms in the volume $\frac{4}{3}\pi r_s^3$, so that every atom within the spike has the average energy

$$E_s = \frac{E_2}{\frac{4}{3}\pi r_s^3 N} + \frac{3}{2} kT_o \qquad (2.35)$$

where T_o is the ambient temperature of the lattice and k is Boltzmann's constant. The spike temperature thus follows as

$$T_s = \frac{E_s}{\frac{3}{2}k}, \qquad (2.36)$$

the main problem being to deduce r_s as a function of time.

With $r_s \simeq 100$ Å and $E_2 = 40$ keV, E_s is about 0.21 eV and the temperature is about 1600°K.

Concerning the mechanism by which heat leaks out of the spike into the rest of the crystal, it may be assumed that energy is transmitted in two-body collisions of three types: ion-ion, electron-electron, and ion-electron. The first two are between particles of equal mass, so that the transfer is very efficient and up to 100% of the energy can be exchanged in a single collision. An ion-electron collision, however, is very inefficient due to the widely different masses, the maximum energy transfer being only $4m_o/M_2$. The mean time between collisions for electrons with velocity v_e and spacing d (similar to the interatomic spacing) will be $d/v_e = 5 \times 10^{-16}$ sec for 1 eV, whereas for ion-ion collisions $d/v_i = 10^{-13}$ sec at 1 eV. The electron spike must, therefore, go to completion by dissipating its energy long before ion-ion collisions take effect. It is concluded that the loss of ion energy in temperature spikes is only due to ion-ion collisions, and that the loss of energy to the electron system may be ignored.

If the thermal spike intersects a free surface and is sufficiently hot for a long enough time, atoms will be released from the surface by a process of evaporation. Such atoms will form a characteristic energy spectrum and measurements on atoms sputtered from surfaces should provide some indication of this behaviour. Using Maxwell-Boltzmann statistics to describe the energy distribution within the spike, Thompson and Nelson [34] arrived at the following expression for the total thermally sputtered yield:

$$S_t(T_s) = \frac{3^{5/2}\pi^{3/2}\sigma\tau_s N^3 r_s^8 E_b^5}{M_2^{1/2}\gamma E_1 (E_s)^{7/2}} \exp\left(\frac{-3E_b}{2E_s}\right) \qquad (2.37)$$

where E_1 is the incident energy, E_b is the surface binding energy, τ_s is the time duration of the thermal spike, and σ is the hard-sphere collision cross section of Bohr

$$\frac{2\pi a_B^2 E_R Z_1 Z_2 (M_1+M_2)}{eE_1 (Z_1^{2/3}+Z_2^{2/3})^{1/2} M_2} \qquad (2.38)$$

where E_R is the Rydberg energy (13.6 eV) and e is 2.718.

Using a time of flight technique, Thompson and Nelson [34] found that a small fraction of atoms ejected from a Au crystal, subjected to bombardment with 43 keV Xe^+ ions at 500°C, fell within a spectrum having a peak near 0.15 eV. The magnitude and behaviour of this peak was consistent with the theoretical energy spectrum of evaporation from spikes having an average temperature of about 1477°C and lasting about 10^{-11} sec.

More recently, Thompson [35] has compared the energy spectra of atoms sputtered from Au crystals after 40 keV-Ar^+ and 40 keV-Xe^+ ion bombardments which give respectively 20 keV and 40 keV maximum recoil energy. If ejections were due solely to random cascades, focused collision sequences (simple and assisted), or channelling one would expect the low recoil energy to give the most intense contribution to the spectrum at low energies. In fact, the reverse is observed and the peak moves to lower energy, which is consistent with the high energy recoil producing the hottest spike and hence the most evaporation.

Eq. (2.37) suggests an exponential increase in the thermal sputtering ratio S_t as a function of target temperature (contained in E_s). Confirmation of this feature came from an experiment in which the sputtering rate was observed as a function of temperature [36]. Near room temperature, it was expected, for theoretical and experimental reasons, that focused collision sequences and random cascades would be the dominant mechanisms of sputtering. But as T_o rose, there should come a point where T_s was great enough for evaporation to overtake the collisions and the sputtering rate should then rise rapidly with temperature. In fact, results were obtained for a variety of polycrystalline metal targets, which all exhibited this behaviour.

The above sputtering experiments have been taken as direct experimental evidence for the existence of thermal spikes. In addition, computer simulation of radiation damage [3,11] shows the existence of this type of spike, and the results were in a good quantitative agreement with the spike picture presented here.

Thermal spikes, by their nature, may play an important role in bombardment-induced phase transformations in solids, but that will be left for discussion in later chapters.

2.5.2 Displacement spikes

As the primary energy degrades to the order of several hundred electron volts, the distance between successive collisions decreases to the order of the interatomic distance. At this stage the primary starts to act collectively with several lattice atoms almost simultaneously and the displacement events are no longer widely separated. Consequently,

the primary expends its energy over a rather small atomic volume creating violent, localized damage, in which the displaced atoms move away from the centre of the region, and because their energies are low, come to rest at small distances from this centre. A denuded vacancy-rich zone is thus created at the extended centre, with a region containing an excess of interstitial atoms around the periphery of this volume. This picture of the situation near the end of a displacement cascade was theoretically introduced, in a number of classical papers, by Brinkman [37,38]. The theory also indicates that the atoms in the region just enclosing the interstitials will be heated to a high temperature, producing a thermal spike similar to that described in the previous section. During this time the atoms are free to flow back into the denuded zone, since the lattice does not retain its strength at temperatures well above the melting point. Thus the atoms between the centre and the interstitial shell can be considered as unstrained material free to respond to the pressure exerted by the interstitials. If the time of the collapse of the denuded zone is longer than the duration of the thermal spike, the vacancy rich zone and interstitials will persist; but if the reverse is true the multiple vacancy zone will flow outside and fill it, thus annihilating the interstitials with resultant formation of what is called by Brinkman a "displacement spike".

It should be noted, however, that in this model, focusing, crowdion, and channelling events have been neglected, whereas these will certainly occur even when generated from displacement-spike regions. Indeed Seeger [39,40] suggests that a different type of displacement

spike may be formed. It has the usual vacancy-rich core, but the interstitials are created remote from this core via focusing, crowdion, and channelling events. Thus the conditions for collapse of the vacancy-rich core are absent and the resulting structure is one of stable "depleted zones" and interstitial rich regions.

Further discussion on displacement spikes will be given in connection with bombardment-induced phase changes, in Ch. 4.

2.5.3 Plasticity spikes

The atoms in the heated zone of a thermal spike should exert a pressure on the surrounding medium, and the resultant stresses might cause plastic flow within the spike region. Estimates of these pressures have been given by Seitz and Koehler [8] and Dienes and Vineyard [9]. A spike is considered which has a spherical symmetry and the irradiated crystal is assumed to be elastically isotropic. Then, from classical elasticity theory for an isotropic medium, the radial pressure exerted by the spike region of radius r_s at a distance r from the center is given by:

$$P_r = 4\mu\left(\frac{\Delta V}{3V}\right)\left(\frac{r_s}{r}\right)^3 \qquad (2.39)$$

where μ is the shear modulus and $\Delta V/3V$ is the fractional change in the linear dimensions of the heated sphere. It is, therefore, possible to calculate values of the radial compressive stress P_r for thermal spikes of varying intensity, and to estimate the probability that plastic flow will occur. Taking $(\Delta V/3V) < 0.01$ for most solids at the melting point and 4μ close to 10^{12} dynes/cm^2, Seitz and Koehler [8] estimate P_r to

be $\sim 10^{10}$ dynes/cm^2, i.e. 10^4 atmospheres, at the boundary of the molten zone, which is well above typical yield stress.

2.5.4 Comments

Before we leave this section it seems important to make some comments on the terminology used, since, as pointed out by Chadderton [11], there is a very great deal of confusion and difference over the terminology in spike theory. Some authors (e.g. Ref. [8,9]) put thermal, displacement, and plasticity spikes into a general class which they call temperature spikes. There is much to be said for this approach since there are generally displacements in thermal spikes, heat generation in displacement spikes, and pressure or plastic flow in both thermal and displacement spikes. However, in the present account and in whatever follows, the following approach will be taken:

1. Thermal spikes, as described in sec. (2.5.1), will be considered as a sudden delivery of heat to a localized region in the lattice, without regard to displacements.

2. Displacement spikes will be considered to mean the particular situation described by Brinkman, as outlined in sec. (2.5.2). Any other similar effect will either be given the very general name of displacement cascade, or if there is some feature which particularly characterizes it, then it will be named accordingly. In particular, we will not use "displacement spike" to refer to "displacement cascade".

3. Any discussion of pressure effects, will be given in connection with the particular type of spike of interest. Thus, the concept of a plasticity spike will not be used at all.

CHAPTER 3

DIFFUSION OF INERT-GAS ATOMS IN SOLIDS AND GAS-RELEASE PHENOMENA

3.1 Introduction

To use inert-gas motion as a solid-state probe for studying bombardment-induced structural changes, as will be described in Ch. 7, it is necessary to first examine the basic elements of the diffusion of inert-gases in ion-bombarded solids. The format for the present chapter is: a) to give the general phenomenological equations for diffusion of inert gases in ion-bombarded solids; b) to describe briefly the different geometries and types of diffusion of major interest in ion-bombardment studies; c) to discuss gas-release phenomena in terms of a system of annealing stages; and finally, d) to note the possibility of gas release by vaporization of the target.

The first two sections are largely drawn from the theoretical treatment given by Kelly and Matzke [41], while Refs. [42 & 43] could be used as general references to this chapter.

3.2 The diffusion equations

The diffusion equations usually used for impurity and self-diffusion studies are of two types:

a) the equation for normal or true diffusion:

$$\frac{\partial C_1}{\partial t} = \frac{D}{\lambda^2} \frac{\partial^2 C_1}{\partial x^2} , \qquad (3.1)$$

where C_1 is the concentration in fractional units of the diffusing species in the absence of trapping, λ is the mean atomic spacing, and x is the diffusion distance in units of λ.

b) the equation for single-jump diffusion, i.e. the equation for a release process with either one or a very small number of rate-controlling jumps:

$$\frac{\partial C_1}{\partial t} = -k\, C_1 \tag{3.2}$$

where k is a proportionality constant, which will often be similar to what is called "the diffusion rate constant". The latter can be defined as the rate of jumping along a given line or as twice the rate of jumping to a particular lattice site. k may be assumed related to ΔH, the activation enthalpy of the process, through the usual equation

$$k = k_o \exp\left(\frac{-\Delta H}{RT}\right) \tag{3.3}$$

As the motion of inert-gas atoms in solids is usually accompanied by weak trapping (e.g. transient gas-gas or gas-damage interactions), or strong trapping (e.g. bubble formation), it is often necessary to consider modified diffusion equations. In fact, Eq. (3.1) may be extended to include trapping terms, thus to be expressed as:

$$\frac{\partial C_2}{\partial t} = \frac{D}{\lambda^2} \frac{\partial^2 C_2}{\partial x^2} - \frac{\partial m}{\partial t} \tag{3.4}$$

with

$$\frac{\partial m}{\partial t} = \frac{DC_2}{\lambda^2 L^2} - bm$$

where C_2 is the concentration (in fractional units) of mobile gas in the presence of trapping, m is the concentration (in fractional units) of trapped gas, L is the diffusion trapping length (in units of λ), b is what is called "the detrapping rate constant", which is similar to, but not identical with, k in Eq. (3.2). It is worth emphasizing that L is not the same as the spacing of the trapping centers, as follows from the relation $L^2 = \lambda^2/6f$, where f is the atomic fraction of point traps.

3.3 Diffusion geometries in ion-bombardment studies

Solutions for the diffusion equations described in the previous section are available assuming different diffusion geometries (profiles) beneath the surface of the bombarded solid. The main types of diffusion geometry of interest in ion-bombardment work are shown in Fig. 3.3. In addition, solutions for single-jump diffusion with either a discrete ΔH or a uniform spectrum of ΔH's are also available. In all cases, the surfaces are assumed permeable (i.e. $C^{diff.} = 0$ at $x = 0$) and the diffusion parameters are assumed uniform (diffusion with non-uniform parameters has been recently discussed by Kelly and Nghi [44] and will not be considered in the present context).

The solutions for certain geometries and types of diffusion could be summarized as follows:

a. Plane Source

The plane source solution of Eq. (3.1) is given as [3]:

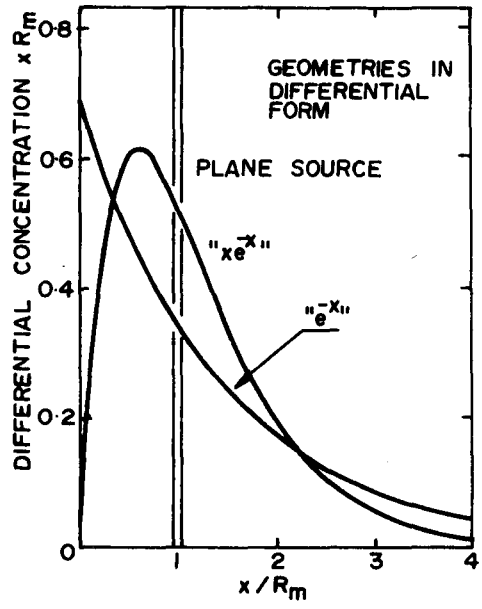

(a)

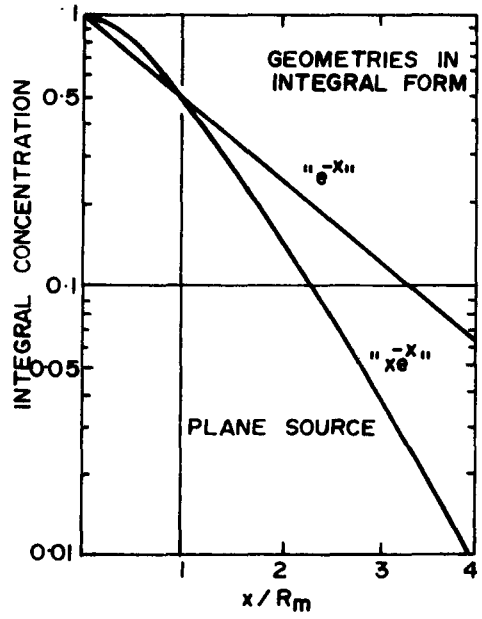

(b)

Fig. 3.1(a) and 1(b). The diffusion geometries of major interest in ion-bombardment studies

$$C^{diff} = \frac{1}{\sqrt{4\pi Dt}} \{ \exp\left(\frac{-(p-x/\lambda)^2}{4Dt}\right) - \exp\left(\frac{-(p+x/\lambda)^2}{4Dt}\right) \} \quad (3.5)$$

x and p = 0, 1, 2, 3,...

where C^{diff} is, as usual, in fractional units; p is the position of the source beneath the surface, in units of λ; and x is the distance from the surface, in units of λ. This geometry is <u>not</u> applicable for the studies used in this dissertation; rather, it is suitable mainly either for targets bombarded at very low energies (< 1 keV), as it avoids assuming diffusing species to be initially present between x = 0 and x = 1; or for light targets bombarded at very high energies (> 300 keV), where the diffusing materials tend to be absent between x = 0 and x ≃ $R_{pb}/2$.

b. <u>The "e^{-x}" distribution</u>

This can be expressed as:

$$C^{diff} = \left(\frac{\ell n 2}{R_m}\right) \exp\left(\frac{-x\ell n 2}{R_m}\right) = \left(\frac{1}{\bar{R}_{pj}}\right) \exp\left(\frac{-x}{\bar{R}_{pj}}\right) \quad (3.6)$$

where R_m is the median and $\bar{R}_{pj}$ the mean projected range. The corresponding solution to Eq. (3.1) follows by multiplying (3.5) by (3.6) and integrating appropriately.

This distribution is again not of interest to the present context since it generally assumes deep penetration of the diffusing species. It is, therefore, most suitable when channelling plays an important role, thence for materials which do not highly distort during bombardment.

c. The "xe^{-x}" distribution

This distribution, which might be described as "peaked with an exponential tail", Fig. (3.1a) , can be written as:

$$C^{diff} = \left(\frac{x}{R_{pb}^2}\right) \exp\left(\frac{-x}{R_{pb}}\right) \qquad (3.7)$$

while the solution to Eq. (3.1) follows by multiplying (3.5) and (3.7) and integrating appropriately.

The ideal mean projected range for this geometry is given by:

$$\bar{R}_{pj} = 2\, R_{pb} \qquad (3.8)$$

The shape of Eq. (3.7) is nearly indistinguishable from a function of the type $(Ax^{1/2})$ $(\exp(-Bx^{3/2}))$ which has been suggested in work on distributions in Ta_2O_5 [45] and WO_3 [46]. It is therefore the most suitable geometry for the gas-release studies undertaken in Ch. 7, as the work in this chapter involves bombardment of crystalline oxides where (as with Ta_2O_5 or WO_3) drastic distortion in the crystal lattice is induced by bombardment.

d. Concept of single-jump diffusion

The normal diffusion solutions, such as those described in a, b, and c, do not appear to be valid in connection with the type of gas release known as damage diffusion or stage I as will be described below in sec. (3.4). Such gas release is believed rather to be compatible with single rate-controlling jumps which are governed either by one or

more discrete ΔH's or by a spectrum of ΔH's.* As shown in Fig. (3.2) discrete ΔH's are recognized by narrow maxima which do not exist when there is a ΔH spectrum.

C_1^{int} for single-jump diffusion with a single discrete ΔH is given simply by:

$$C_1^{int} = \exp(-kt) \tag{3.9}$$

The existence of one-step motion means that no assumption about the

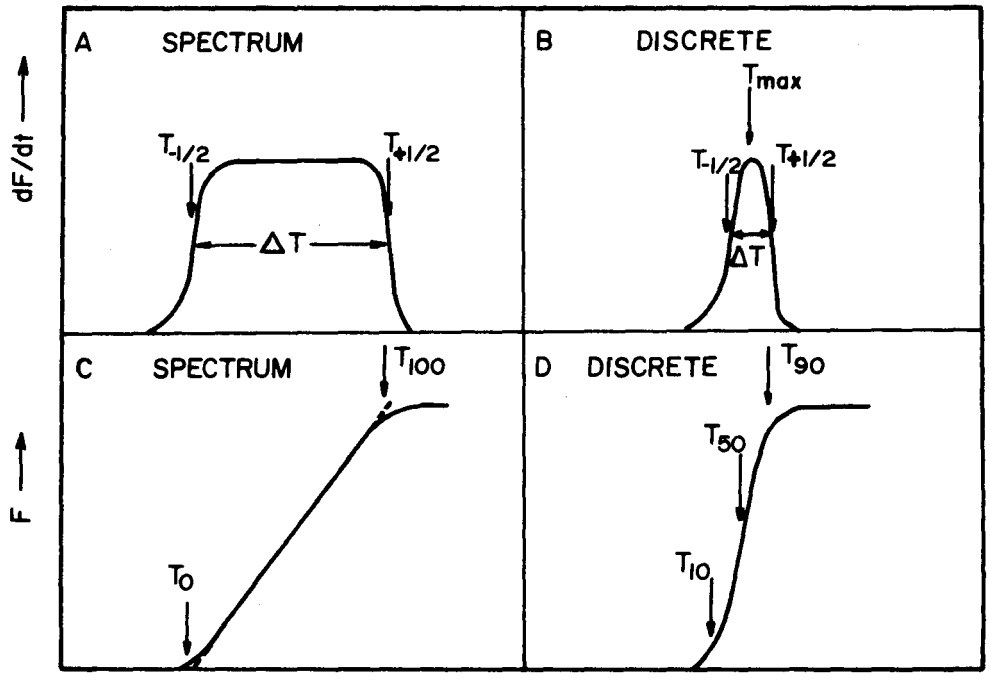

Fig. 3.2 Schematic examples of dF/dt vs T and F vs T, where F is fractional gas-release, t is time, T is temperature. a) dF/dt vs T for a uniform spectrum of ΔH's; b) dF/dt vs T for a discrete ΔH; c) F vs T for a uniform spectrum of ΔH's; d) F vs T for a discrete ΔH.

*Examples of diffusion or diffusion-like processes governed by single rate-controlling jumps are nucleation, evaporation, detrapping, and motion near surfaces. Discrete ΔH's appear in the work of Kornelsen on tungsten [53], while ΔH spectra appear in the work of Kelly on various oxides [47].

geometry is necessary. Kelly [47] has shown that C_1^{int} for single-jump diffusion with a uniform spectrum of ΔH's can be given approximately by:

$$C_1^{int} \approx 1 - \frac{RT}{\Delta H_2 - \Delta H_1} \ell n\, \theta k_o t + \frac{\Delta H_1}{\Delta H_2 - \Delta H_1} \qquad (3.10)$$

where ΔH_1 and ΔH_2 are the limits of the ΔH spectrum and θ is a numerical constant with the value of 1.781.

3.4 System of stages in gas-release studies

Extensive studies on gas release following labeling by ion-bombardment techniques on a variety of substances has led to the establishment of a system of stages for inert-gas motion. This system is in some aspects analogous to that used in work on the recovery of physical changes introduced by irradiation, cold working, and quenching, though there is not a one-to-one correspondence. It is based on broad, qualitative similarities in the recovery behaviour being found which suggest that the various specimens show common recovery processes. Using isochronal annealing programs, the processes can be separated, at least in principle. Alternatively, linear temperature increases combined with flow-through detection can be used (equivalent to differentiating the isochronal recovery curves). This gives annealing peaks each of which implies a separate recovery process. The peaks occur at different temperatures, or different temperature regions, and in ideal cases can be represented as shown in Fig. (3.3). The designation of the stages (and substages), their definitions, and the basic mechanisms for gas release, together with some typical systems studies, are summarized in Table (3.1).

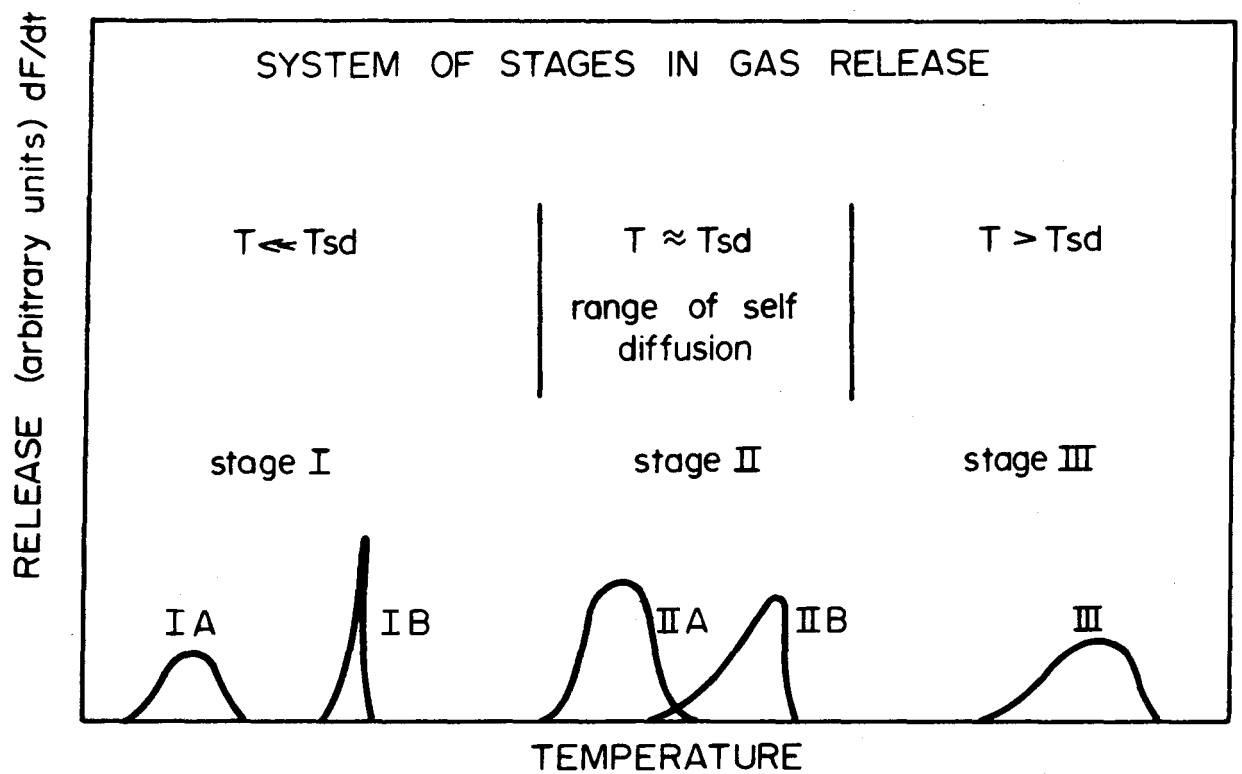

Fig. 3.3 Systematic representation of the system of stages in gas release studies for the case of a linear temperature increase (dF/dt vs T). T_{sd} refers to the temperature of self-diffusion (After Matzke [135])

Table 3.1 Summary of gas-release stages

Stage	Substage	Temperature range	Mechanism	Materials showing stage
I	A	$T \ll T_{sd}$	diffusion of gas atoms which are fortuitously located in high-mobility sites	KCl, KBr[48]; UC[49,50]; Al_2O_3[51]; Fe_2O_3 [42]; SiO_2, TiO_2, Nb_2O_5 [47]; W[52-54]
	B	$T < T_{sd}$	gas being swept out during the annealing of radiation-induced structural changes, e.g. amorphousness	Al_2O_3, TiO_2, U_3O_8, MgO[74]; Fe_2O_3, [50,55-57]; SiO_2 [58]; Ge, Si, GaAs [59]; Ta_2O_5, Nb_2O_5 [60]
II	A	$T \approx T_{sd}$	normal homogeneous volume diffusion of the bombarded gas atoms	LiF[61];KCl, KBr, KI[62,63]; NaCl[64]; CaF_2, BaF_2[65]; UO_2[66]; ThO_2[67]; UC[68]; CaO, NiO, MgO[65]; SiO_2[58]; Al_2O_3, Fe_2O_3, Cr_2O_3, TiO_2, U_3O_8[55]; Ta_2O_5, Nb_2O_5[60]; SnO_2[69]; Ag[70,71]; Ge, Si, GaAs[59]
	B	$T \geq T_{sd}$	Normal diffusion with weak trapping or temporary trapping due to gas-gas or gas-damage interactions	Same substances as for stage (IIA) but at higher doses
III		$T \gg T_{sd}$	normal diffusion with strong trapping of gas in pre-existing defects or bubbles	Al_2O_3[50,55,65,74]; Pt[72]; Au[71,73]

In the following subsections, the possible mechanisms for these stages will be briefly discussed. However, we shall stress those stages which are particularly relevant to the gas-release studies given in Ch. 7, namely stages IB and IIA.

It was found most convenient, even if apparently illogical, to start our discussion with stage IIA, not only because it is related to normal volume diffusion, which all readers are familiar with, but also because it is the best understood among the stages, and once it has been detected the other stages can be identified more easily.

3.4.1 Stage IIA

This stage is assumed to represent normal homogeneous volume diffusion, and occurs often at temperatures compatible with self diffusion. It consists simply of successive jumps, in uncorrelated directions, of the diffusing atom in the regular (undamaged) lattice of the host crystal. The motion may be from one lattice position to a neighbouring position or else amongst interstitial positions. It is, therefore, subject to the usual diffusion equation (Eq. 3.1). The forms taken by differential concentration solutions for different geometries have already been discussed in Section 3.3. These solutions can be converted to integral form as follows:

$$C_1^{int} = \int_x^{\infty} C_1^{diff}\, dx,$$

while the highly useful fractional release forms can be constructed as

$$F = 1 - C_1^{int}\big|_{x=0}$$

Thus, the fractional gas release due to an "xe^{-x}" distribution showing stage IIA is

$$F = 1 - \frac{2Z}{\sqrt{\pi}} - (1-2Z^2)\exp(Z^2)\mathrm{erfc}(Z) \qquad (3.11)$$

where $Z^2 \equiv Dt/R_{pb}^2$ and $D = D_o \exp(-\Delta H/RT)$.

For treating experimental data of the form F vs T (fractional gas release vs temperature), it is often convenient that F be made explicit in $\Delta H/T$. This has been first done by Kelly and Brown [71]. They assumed an idealized value for the pre-exponential factor D_o and derived expressions for $\Delta H/T$ as a function only of F. This method was extended [41,65] to more general relations of the form

$$\frac{\Delta H}{T} = A - 4.6 \log_{10}\left(\frac{R_m^2\, 0.3}{t_{min} D_o}\right) \qquad (3.12)$$

where t_{min} is the annealing time at a given temperature, in mins, and A is a constant, depending on the geometry and the value of F. The different values of A are given in Table (3.2). (Other approaches to

Table 3.2

Values of A in Eq. (3.12)*

Distribution	F=0.1	F=0.5	F=0.9
plane source	78.8	75.2	68.5
xe^{-x}	80.9	75.2	67.9
e^{-x}	83.3	75.0	67.2
single-jump diffusion with discrete ΔH**	81.3	77.5	75.1

*From Ref. [41]

**Take $R_m = 1$ in this case.

evaluate release curves of the type F vs T for stage IIA are discussed by Matzke [63]).

Experimental data will also be given in this work in the form of dF/dt vs T (i.e. the rate of gas release vs temperature). In such cases, the basic expression for $\Delta H/T$ has been given as [41]:

$$\frac{\Delta H}{T_{max}} \approx A' + 4.6 \log_{10} \left(\frac{T_{max} D_o}{R_m^2 \beta_{min} 0.3} \right) \qquad (3.13)$$

where T_{max} is the peak's maximum temperature, β_{min} is the rate of heating in C^0/sec (assumed linear), and A' is a constant depending on the geometry and type of diffusion; see Table (3.3).

Table 3.3

Values of A' in Eq. (3.13)*

Distribution	A'
plane source	69.5
xe^{-x}	68.3
e^{-x}	67.5
single-jump diffusion with discrete ΔH**	69.5

*From Ref. [41]

**Take $R_m = 1$ in this case.

In analyzing gas-release curves, it is important to examine the results in terms of what is called a "peak width formula", which has the form $\Delta T/T_{max}$. For experiments conducted with <u>step heating</u>, the width of the gas-release "peak" is most conveniently defined as the

difference between the temperatures for 90% and 10% release, i.e. T_{90}-T_{10}, and can be estimated by rearranging the $\Delta H/T$ formulae (Eq. 3.12). Under conditions of linearly increasing temperature, a possible definition of peak width is the full width at half height, i.e. $\Delta T_{1/2}$, (Fig. 3.2). Approximate expressions for $\Delta T_{1/2}$ or similar quantities are considered in Ref. [42], while more rigorous forms are given in Ref. [75], where the general expression is deduced as:

$$\frac{\Delta T_{1/2}}{T_{max}} = A''-B'' \log_{10} \left(\frac{T_{max}^2 D_o}{R_m^2 \beta_{min}\, 0.3}\right) \qquad (3.14)$$

Values for the constants A" and B" are given in table (3.4) for different distributions.

Table (3.4)

Values of A" and B" in Eq. (3.14)*

Distribution	A"	B"
plane source	0.0935	0.0063
xe^{-x}	0.1380	0.0092
e^{-x}	0.1750	0.0117
single-jump motion with discrete ΔH**	0.0673	0.0044

*From Ref. [75]

**Take R_m = 1 in this case.

Stage IIA has been observed with many materials in ion bombardment work (Cf. Table (3.1) and certain empirical rules have been obtained. These rules concern the onset of gas release, the activation enthalpy,

and the relation to self diffusion.

Fig. (3.4) shows that stage IIA gas release starts between 0.4 and 0.5 T_m (T_m = melting temperature) for a surprisingly great variety of materials, including ionic crystals and metals of many lattice structures. Plotted are the temperatures for 10% release during a 5 min. annealing following bombardment with 40 keV ions. The effective distance per minute is thus about 10 atom layers, which seems to be a reasonable definition of "onset" of release [43].

A second relation can be obtained involving the "self diffusion temperature", i.e. the temperature at which gas release would occur if governed by self diffusion parameters. It has been shown that [51], for a wide variety of systems, all of which involve low or moderately low doses, release components occur having similar temperatures to those of volume self-diffusion. The following correlation was found [42]:

$$T_{IIA} = (0.86 \pm 0.10)\, T_{sd} \qquad (3.15)$$

The ΔH's deduced from the gas release curves for the materials of Fig. (3.4)are shown in Fig.(3.5). Evidently, the ΔH's increase linearly with the melting point, as required by the form of Eq. (3.12) or (3.13).

3.4.2 Stage IIB

At higher gas concentrations and hence higher damage concentrations, an interaction of gas atoms with damage or with other gas atoms leads to a decreased mobility, and, thus to a new substage, stage IIB.

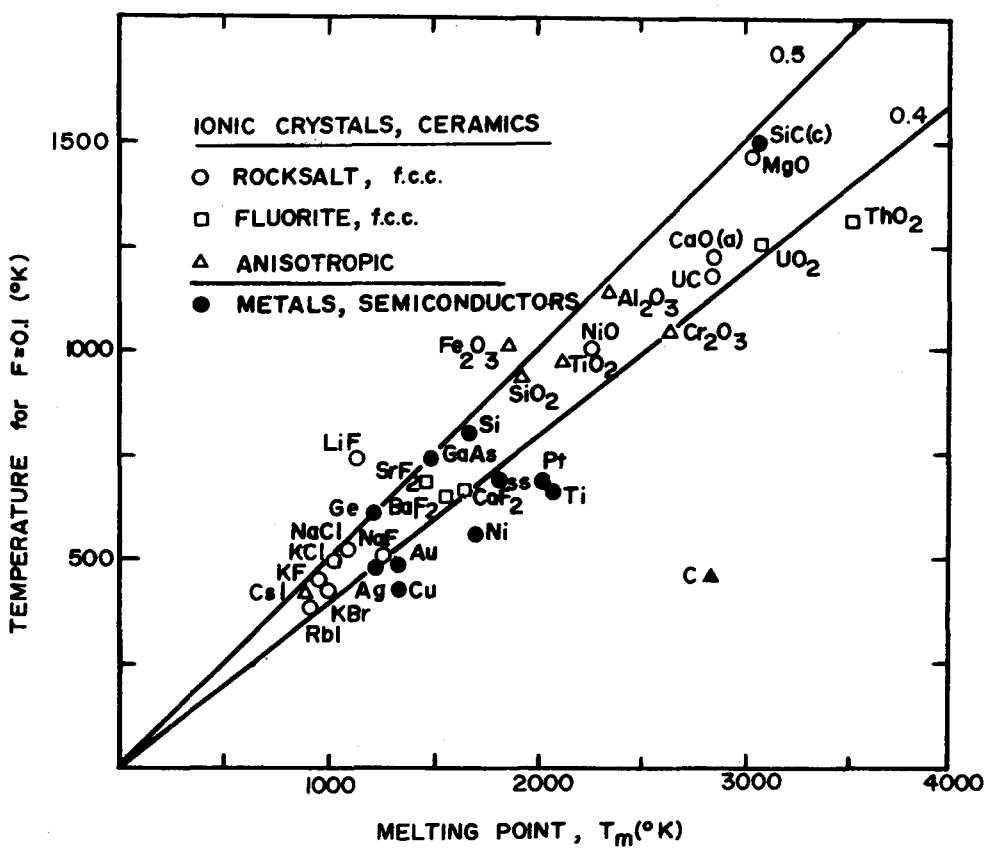

Fig. 3.4 Dependence of the onset of gas release (F = 0.1 at 40 keV energy with F = fractional release, corresponding to a diffusion of about 10 atom layers/min) on the melting point, T_m. (After Matzke [135])

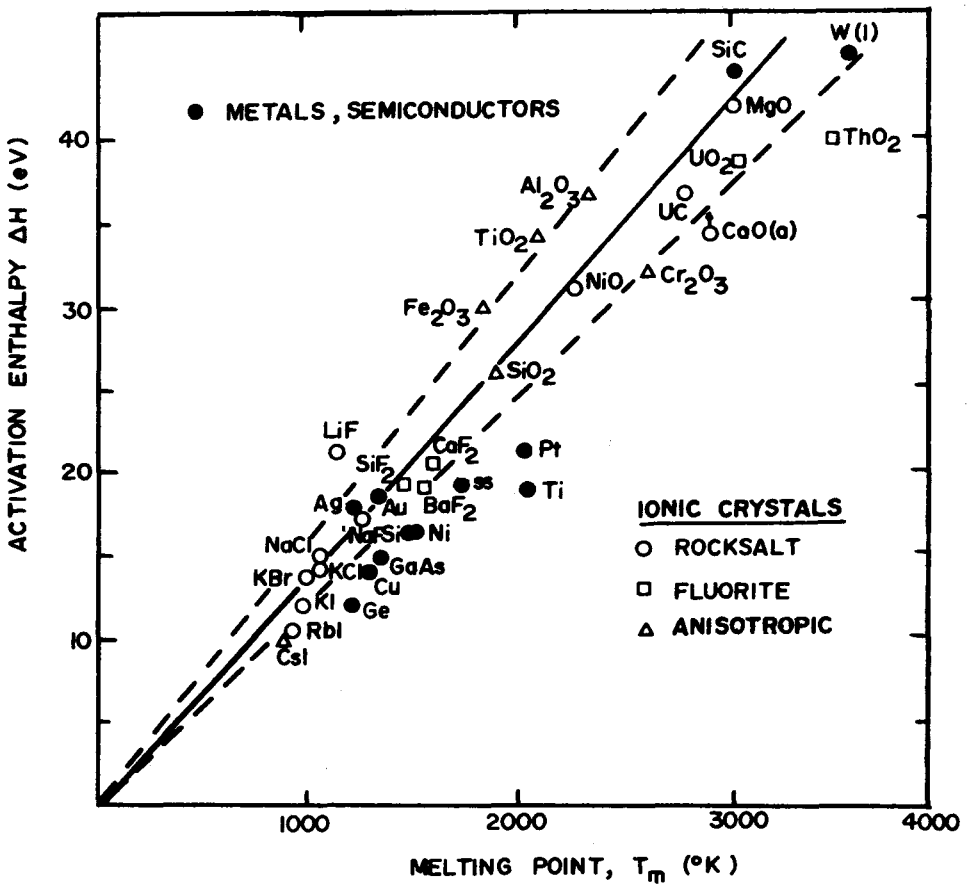

Fig. 3.5 Dependence of the activation enthalpy, ΔH, of stage IIA release on the melting point, T_m. (After Matzke [135])

This stage occurs within the temperature range of self-diffusion of the matrix atoms as well, and was therefore not distinguished in early work. It appears as either a shifting of the stage IIA gas-release curve toward higher temperatures [62,63], or as a satellite peak beside that for stage IIA [53,62].

The mechanism of stage IIB is fairly well accepted as normal diffusion with weak or temporary trapping, i.e. where there is a correlation with self diffusion plus a contribution from transient gas-gas or gas-damage interactions. Since there are many types of defects, e.g. vacancy clusters of different size, dislocation lines or loops with different cores and strain fields, stacking faults etc., one cannot necessarily expect the same trapping behaviour and the same trapping energies for different irradiation conditions. This lack of specificity on the trapping centers creates a problem in formulating a unique analysis for the diffusion of inert gas in stage IIB, and a complete analysis has not therefore been made yet. Stated briefly, the problem is one of solving Eq. (3.4) under conditions when D, L, and b are all functions of x and/or C.*

3.4.3 Stage IA

Stage IA, which is most prominent at low bombardment energies and low doses, is most simply described as any gas-release process occuring well below the temperatures of both volume self-diffusion (Stage IIA) and the annealing of bombardment-induced disorder (Stage IB).

---

*The analysis given in Ref. [44] is probably a step towards a complete understanding of stage IIB.

It can be explained in terms of gas which is fortuitously located in high mobility (e.g. interstitial) sites [42,43,53] and would be expected to be described by Eq. (3.4) but without the detrapping form:

$$\frac{\partial C_2}{\partial t} = \frac{D}{\lambda^2} \cdot \frac{\partial^2 C_2}{\partial x^2} - \frac{DC_2}{\lambda^2 L^2} \qquad (3.16)$$

Provided Eq. (3.16) is applicable, the quantity F_{IA}, the total fraction of gas exhibiting stage IA release, is given by [42]:

$$F_{IA} = (2L/R_{pb} + 1)(L/R_{pb} + 1)^{-2} \approx 2R_{pb}/L \qquad (3.17)$$

where R_{pb} is, as usual, the most probable range of the gas. An xe^{-x} type distribution is here assumed, but this is not an important point, since all distributions give similar relations.

3.4.4 Stage IB

Stage IB also occurs below the temperatures of volume self-diffusion and is most prominent at high doses independently of the bombardment energy. Various techniques, e.g. reflection electron diffraction [74], replica electron microscopy [61], measurements of ranges [28], measurements of solubility [76], Rutherford backscattering combined with channelling [77], etc. were employed to show that stage IB gas release coincides with the recrystallization or the annealing of radiation induced phase changes either involving amorphousness [28,75,78,79] or polycrystallinity [75,77]. The mechanism of stage IB was, therefore, attributed to the sweeping action of either the crystalline-amorphous

interface or the crystal-polycrystal interface. This type of behaviour, which implies that the diffusant is bound to the appropriate interface, is a common though not a universal phenomenon. It has been inferred to occur with Kr, Xe, Zn, Cd, I and Hg implanted into Si [75,77-79], though was explicitly demonstrated not to occur with Si containing Rb, Cs, P, As, Sb, Bi, Be and Te [78,80,81]; so also with Ge, some diffusants move during crystallization (Kr, Xe, Hg [75,77,82]) while others do not (In, Tl, Sb, Bi [82]).

Stage IB data could, if desired, be interpreted in terms of an activation enthalpy. It is generally found [51] that the full width at half maximum of the peak corresponding to stage IB has a value which, to a first approximation, can be compared with the predicted value for release governed by single-jump kinetics with a discrete ΔH; release governed by diffusion kinetics would have given half widths a factor of two to three greater. It was concluded [51] therefore that the activation enthalpy ΔH_{IB} could be obtained by using the $\Delta H/T$ formula for single-jump motion with a discrete ΔH (Tables (3.2), (3.3) and (3.4)).

In subsequent work [75] it was noted, however, that stage IB can also be described in terms of "sequential motion", i.e. a series of R jumps all in the same direction such as would be expected for spontaneous crystal growth. It was shown that such motion could be described by the relation

$$\frac{\Delta H}{T_{max}} = 68.1 + 4.6 \log_{10} \frac{T_{max} D_o}{R^2 \beta_{min} 0.3} \quad \text{(all R)}$$

$$\frac{\Delta T_{1/2}}{T_{max}} << 0.06 \qquad R >> 1 \tag{3.18}$$

where the notations are as given before. Accordingly, the single jump is a special case of sequential motion when R = 1. The authors then proposed that the similarity of $\Delta T_{1/2}$ for stage IB to what is expected for single-jump motion is misleading. They point out that the beginning of the gas release for this stage has to be described by sequential motion with R = 1 and the completion by sequential motion with R = αR_m, where α is a number such that αR_m is the thickness of the disordered layer in units of λ, the mean atomic spacing. In this case the temperature width should be roughly:

$$\frac{\Delta T}{T_{max}} \simeq 0.066 \log_{10} \alpha R_m \qquad (3.19)$$

For αR_m = 22 mean atomic spacings, this becomes

$$\frac{\Delta T}{T_{max}} \approx 0.089 \qquad (3.20)$$

which is found to be in good agreement with what is observed for gas release associated with disorder annealing for about 6 substances given in [75].

The values obtained for the activation enthalpies, ΔH_{IB}, are believed, by analogy with the work of Turnbull and Cohen [83] on the growth of a crystal into an undercooled liquid, to be similar to those for self-diffusion in the disordered phase;unfortunately, however, there is virtually nothing with which to compare the results and verify this contention.

3.4.5 Stage III

Stage III describes any gas release occuring well above the temperatures of volume self-diffusion. It has been attributed to strong trapping of gas in pre-existing defects (e.g. voids) or in gas-filled bubbles. Such rare gas which has precipitated into bubbles constitutes the least mobile form it can take, with release being brought about by the mobility (or possible resolution) of the bubbles. The diffusion theory of stage III is, therefore, similar to that for stage IIA (normal volume-diffusion), including the same F and $\Delta H/T$ expressions though with a suitable D_{bubble} substituted for D [e.g. 42]. For example, if (as is usual) the bubble moves by surface diffusion we have

$$D_{bubble} = \left(\frac{3}{2\pi a^4}\right) D_{surface} ,$$

when a is the bubble radius in units of the mean atomic spacing.

3.5 Vaporization

An unambiguous interpretation of diffusion data is possible only if one knows whether or not gas is being released by vaporization of the target. For this purpose a "minimum vaporization temperature" can be defined as the temperature at which the amount of vaporization in the time scale of the experiment (usually taken as 5 min) is comparable to the median range, R_m. For experiments conducted either with step heating or isothermally, the number of atom layers vaporizing was shown

in [65] to be given by:

$$A \leq \frac{2.96 \times 10^8 \, t_{min} \, P_{mm} \, M_{vapor}^{1/2}}{M_{solid}^{1/2} \, T^{1/2} \, \rho^{2/3}} \qquad (3.21)$$

where t_{min} is the heating time, in mins., P_{mm} is the vapor pressure, in torr, ρ is the density of the solid, and M is the molecular weight. For experiments in which the temperature increases linearly with time, i.e. $T = \beta_{min} \, t_{min}$, the number of atom layers vaporized can be shown [62] to be equal to:

$$A \leq \frac{2.96 \times 10^8 \, P_{mm} \, M_{vapor}^{1/2} \, RT^{3/2}}{M_{solid}^{1/2} \, \rho^{2/3} \, \beta_{min} \, \Delta H_{vapor}} \left(1 - \frac{3RT}{2\Delta H} + ..\right) \qquad (3.22)$$

The inequality in Eqs. (3.21) and (3.22), which arises from the uncertain value of the "efficiency of condensation", is applicable only if P_{mm} is an equilibrium value; the expression is exact if P_{mm} is based on weight-loss data. The minimum vaporization temperature follows by trial and error substitution of vapor pressures into Eq. (3.21) or (3.22).

CHAPTER 4

RADIATION-INDUCED STRUCTURAL TRANSFORMATIONS IN SOLIDS

(Discussion of previous work)

4.1 Introduction

Studies of radiation-induced structural transformations in solids constitute the earliest work in the field of radiation effects, and incidently, were initiated by European investigators. As early as 1893, sufficient mineralogical data had been collected for Broegger [84] to generalize and define metamict materials as originally crystalline materials which have in the course of time assumed the properties of amorphous substances. More studies revealed that all metamict specimens contained uranium or thorium either as a constituent or as an important impurity ($> 0.1\%$). In addition, Joly [85] was able to establish that the pleochroic halos in mica, fluorspar, etc. were of radioactive origin. These observations led Hamberg [86] in 1914 to the conclusion that the metamict state results from bombardment, over geological periods, with alpha particles from natural radioactive elements. This has been confirmed in the middle 1930's, after extensive studies on a wide variety of minerals [87]. (A summary of present-day information on the metamict state has been given by Pabst [88]). It is also of interest that the first laboratory-scale radiation-damage experiment was performed in 1922,

when Mügge [89] attempted to disorder minerals by exposure to the radiation of uranium. Unfortunately, presumably because of the small exposures, these experiments were unsuccessful.

Prior to the construction of the first reactors (~ 1940), it had been realized [90] that the intensive bombardment suffered by structural materials in such reactors would lead to deleterious changes in their physical properties. A tremendous number of investigations on radiation effects, including radiation induced phase transformations, soon followed on many solids at both a fundamental and a theoretical level, and using all types of incident radiation. A survey of work in this field up to 1964 has been given by Penkovskii [91] for metals and alloys, and by Kircher and Bowman [92] for a variety of materials and components. In addition, the recent interest in ion implantation (see Ch. 1), particularly as a technique for doping semiconductors, has resulted in a large number of investigations [4] in the field of radiation effects, particularly bombardment-induced lattice disorder due to heavy ions.

In view of the large literature, this chapter is <u>not</u> intended to present a survey of the available information on radiation-induced structural changes in solids. Instead, with a view to keeping within the main interest of this dissertation, examples will be given on bombardment-induced transformations in non-metallic substances, particularly oxides, along with a discussion of the available models explaining these phenomena. These transformations may be classified into three categories: (1) Radiation-induced amorphization of crystalline

solids; (2) radiation-induced changes in the crystal form; (3) radiation-induced crystallization of amorphous material. There are other types of transformations such as order-disorder, martensitic, precipitation of second phase, etc., but these are most common for metals and alloys and are, therefore, beyond the scope of this dissertation.*

4.2 Bombardment-induced amorphization of crystalline solids

This by far is the most general form of transformation induced by high-dose heavy-particle irradiation of non-metallic solids. In fact, to the best of the author's knowledge, the conversion to an amorphous phase has been reported only twice for metallic substances ($Pd_{80}Si_{20}$ [94] and U_6Fe [95]).

There are a large number of experimental techniques which have been used to study the disordering resulting from particle impact. The most direct information is probably that gained from two sources. Firstly, there is the work using different types of diffraction, e.g. x-ray diffraction [e.g. 96-98], small angle x-ray scattering [99,100], low-energy electron diffraction (LEED) [e.g. 101], electron diffraction [e.g. 74,102,103], and, transmission electron microscopy [e.g. 104-108]. Secondly, there are channelling techniques [e.g. 77,109]. The considerable changes in the various properties of solids connected with their disordering made it possible, however, for a number of other methods, somewhat less direct in nature, to be used particularly in ion-bombardment disordering studies. These include, for example, optical

*An extensive review of work on metals and alloys up to 1966 has been given by Damask [93].

effects [100,110-112], solubility measurements [76,113], replica electron microscopy [61,114], or gas-release measurements (examples are given in table 3.1).

The above experimental techniques provided a strong evidence of disordering (amorphization) in a number of non-metallic substances. Among these are: α-quartz [e.g. 58,96,98,115], α-Al_2O_3 [e.g. 74,75,97], TiO_2 (rutile) [74,115], α-Fe_2O_3 [55,75], U_3O_8 [74,97], C (diamond) [113, 116], $ZrSiO_4$ (zircon) [e.g. 97,113], Ge [e.g. 59,99,100,104], Si [e.g. 59, 105,106,110-112], and GaAs [e.g. 59,108]. Examples are given in table 4.1, while many others (such as GaP, Nb_2O_5, SiC, and WO_3) could have been added. These results have provided a general picture for the disordering process, even though many of the details have not yet been resolved. The main features can be briefly described as follows:

1. The disordering process begins at a certain threshold dose, D_0, its value depending on the bombarded material [e.g. 113], the mass and energy of the bombarding ions, [e.g. 51] and the bombarding temperature [117,118]. Below this dose the accumulation of displaced atoms and vacancies may result in a distortion in the lattice, often in the form of lattice expansion [e.g. 98], but without a major breakdown of the original structure.

2. As the solid becomes saturated with displacements at the threshold dose, D_0, a relatively rapid conversion (usually sigmoidal with dose [113,119,120]) to a disordered state sets in. At still higher doses ($> D_0$) the bombarded crystal contains heavily disordered spherical zones surrounded by crystalline regions containing other

Table 4.1

Examples of substances which readily amorphize under ion impact

Substance	Ion dose in μAmin/cm^2 to cause disorder-induced gas release such that F_{IB} = 0.25	Ion dose in μAmin/cm^2 to cause amorphous electron-diffraction pattern
Al_2O_3	0.5 [113]	<50 [135]
diamond	1.5 [113]	...
Fe_2O_3	5 [75]	>50 [135]
GaAs	>0.1, < 50 [59]	2 [108]
Ge	≈0.5 [75,59]	0.3 [120]
Si	≈0.5 [75]	0.3 [120]
SiO_2	>2 x 10^{-4}, < 0.1 [58]	0.1 [58]
Ta_2O_5	<2 [60]	<10 [60]
TiO_2	5 [75]	<50 [135]
U_3O_8	<2 x 10^{-4} [74]	<2 x 10^{-4} [135]
$ZrSiO_4$	0.2 [113]	...

*Note that 1 μAmin is equivalent to 3.74 x 10^{14} singly charged ions and that F_{IB} stands for fractional gas release due to stage IB (Cf. sec. 3). The bombardments were in most cases carried out with 5-40 keV Kr or Xe.

defects [98,104]. Finally, the proportion of disorder reaches saturation which indicates that at these (high) doses the individual disordered zones have overlapped sufficiently to produce a completely disordered layer [e.g. 74,104,105,108].

3. There is agreement that the disordered layer formed at high doses does not possess long range order [e.g. 77,104-108] and, therefore, it has been usually defined as an amorphous layer. The question is still open, however, about the exact structure of this layer in comparison with the structure of natural amorphousness.* However, at least for Si, recent studies [112,121] showed that there is a correlation between the characteristic of amorphous sputtered films and heavily bombarded layers.

4. The thickness of the amorphous layer is determined by the range of the bombarding ions. Consequently light ions produced thicker amorphous layers than heavy ions [120]. However, the dose required to form an amorphous layer by light ions is much greater than for heavy ions [119,120]. This is in part because of the increased contribution of electronic processes relative to nuclear stopping for light ions.

5. Recent channelling measurements show that a significant reduction in lattice disorder occurs whenever the incident ions are channelled [111,119,120]. As a result, the dose required for the formation of an amorphous layer is much larger (~5 times in the case of 1 MeV Xe^{+}-Si) for an aligned beam as compared to a random bombardment [122].

---

*More details on natural amorphousness will be given in sec. (5.2).

6. The amount of disorder is also markedly decreased by increasing the target temperature during bombardment [106,119]. Consequently, higher doses are required [106] to form the amorphous layers at elevated temperatures.

7. For most substances, the amorphous layer induced by bombardment crystallizes at similar temperatures as those for natural amorphousness [75]. However, the isolated disordered regions characteristic of intermediate doses anneal at markedly lower temperatures than those of layers [120].

8. The recrystallization of an amorphous layer usually occurs in an epitaxial manner wherever the amorphous phase has formed over the parent single crystal [e.g. 74]. Where the amorphous material does not lie over single crystal, however, recrystallization is polycrystalline [105,108].

9. The annealing of disordered layers, at least for Si and Ge [120],was demonstrated to begin mainly at the disorder-crystal interface. It could also begin, however, from any remnant crystalline regions still present as discussed in [75] and [96].

4.3 Bombardment-induced change in the crystal form

A number of neutron and fission-fragment induced structural transformations from one crystal form to another have been reported in the literature. Most of these transformations, however, were investigated in metals and alloys, and only to a lesser extent have minerals and ceramic materials been studied.

A quite spectacular example of this behaviour is found in the compound ZrO_2, which has been found upon irradiation to transform from the room-temperature monoclinic to the cubic high-temperature phase which is not stable below 1900°C. Klein [122] first observed the transformation during a study of CaO stabilized ZrO_2. Afterwards, this phenomenon was extensively studied both by Wittels et al. at Oak Ridge [123-127], and also by Adam and Cox at Harwell [128]. In both cases, bulk specimens were subjected to neutrons or fission fragments and x-ray diffraction was used to observe the transformation. The Oak Ridge group concluded that fission fragments were necessary to produce a phase transformation in ZrO_2, the impurity content in itself being relatively unimportant and neutron bombardment being quite ineffective; the Harwell group, on the other hand, emphasized the role of the impurities and the state of the oxide in stabilizing the transformation in the regions affected by the passage of the energetic particles (neutrons or fission fragments). They noted that there is no practical way of irradiating ultra-high pure ZrO_2 with fission fragments without contaminating it with uranium recoils.

Similar structural changes have been observed in fast-neutron irradiated $BaTiO_3$, $PbTiO_3$, $KNbO_3$ and $PbZrO_3$ [e.g. 115,124,129]. These ceramics are normally polymorphic. $BaTiO_3$ has a tetragonal structure at room temperature, but transforms to a cubic modification at 120°C. $PbTiO_3$ also transforms from a tetragonal to cubic form but at 490°C. $KNbO_3$ is orthorhombic at room temperature, tetragonal at 228°C, and cubic at 435°C. $PbZrO_3$ transforms from an orthorhombic to a cubic

form at 230°C. These transformations result in anisotropic lattice expansion: for instance, the $BaTiO_3$ lattice expands along the a-axis and contracts along the c-axis as it attains the cubic structure [124, 129]. Similar transformations have been found to be induced by fast-neutron irradiations; however, while the normal thermal transformations are reversible, the fast neutron induced changes are not reversible. For example, on annealing a heavily irradiated $BaTiO_3$ specimen [124] at 1000°C much of the expansion induced by irradiation was recovered; but, whereas the c-axis completely recovered, the a-axis recovered the same amount such that the crystal remained cubic even after the high-temperature anneal.

Neutron-induced transitions were also claimed for a number of natural crystals such as zircon ($ZrSiO_4$), chrysoberyl ($BeO.Al_2O_3$), garnet ($Fe_3Al_2(SiO_4)_3$), and topaz ($(AlF)_2 SiO_4$). These were reviewed by Kircher and Bowman [Ref. [92], table 6.13, p. 384). It is not clear, however, if these examples are correctly interpreted as changes in crystal form, for they may involve instead a partial disordering which stopped short of amorphization due to the ineffectiveness of neutrons in producing saturation damage.

4.4 Bombardment-induced crystallization of amorphous materials

Much less usual are examples where an amorphous material is made to crystallize on irradiation. The only experimental results of which the author is aware of crystallization due to particle impact are those concerning SiO_2 and Ge.

Perhaps the first report of such a phenomenon was that by Weissmann and Nakajima [130] on fused silica. Previous studies showed that [131] upon fast neutron irradiation (~ 1.5 x 10^{20} nvt) fused silica and quartz approach a "common" state with a limiting density of 2.26 gm/cm^3. In order to reach this limiting value, the density of quartz decreases by about 14.7% whereas that of fused silica increases by about 3%. It was also shown that [96] for heavily irradiated quartz (~ 1.5 x 10^{20} nvt) a certain degree of crystallinity was still retained. Weissman and Nakajima [130] suggested that, if upon fast neutron irradiation both quartz and fused silica were to approach a common state, a long range order must be introduced into fused silica. To this end, irradiated fused silica specimens were studied by the transmission electron diffraction method and a very weak spotty powder pattern arising from small crystallites was observed for specimens exposed to radiation doses exceeding 8.6 x 10^{19} nvt. Specimens irradiated at lower doses did not yield any crystalline patterns detectable by the electron diffraction technique. The extent of crystallinity was roughly estimated to be 20%, on a volume basis.

Almost at the same time as the work of Weissmann and Nakajima, Parsons and Balluffi [132] irradiated amorphous thin films of Ge (prepared by evaporation) with fast neutrons or monoenergetic Xe ions in the energy range 20-160 KeV and examined the effects of this irradiation in an electron microscope. It was observed that small discrete crystallized regions (ranging up to several hundered $\mathring{A}$ in size) were produced throughout the amorphous matrix by the irradiation. The fast neutron

irradiation resulted in a linear increase in the number of crystallized regions for doses from 0 to 5.1 x 10^{16} n/cm^2 and a most probable crystallized region size of 190 Å. The monoenergetic Xe^+ ion bombardment resulted in a most probable crystallized region size very closely equal to the calculated ion range for incident energies from 40 to 90 KeV.* In addition, below 20 KeV no crystallization was observed, whilst above 100 KeV the most probable size decreased,and above 140 KeV again no crystallization was observed. These latter results were interpreted as confirming a displacement spike model for the crystallization. Thus the low energy cut off (20 KeV) suggests a critical spike size to be necessary before the crystallization phenomenon can operate, in agreement with Brinkman's idea of spike formation (Section 2.5.2). This low cut-off energy, however, could be merely due to failure in resolving the crystalline regions because of their small size (< 100 Å). The high-energy cut off has been explained as a result of the loss of energy in electron excitation, for which there are no displacement collisions and, therefore, few spikes would be expected to form. Further, since the target thickness was only 700 ± 100 A, Xe ions of energy ≥ 100 KeV would be expected to traverse the target completely and this, coupled with the inelastic processes,would tend to reduce the spike size.

---

*Perhaps it would have been more accurate if the size distribution had been compared with the damage mean depth $\langle x \rangle_D$ or damage mean straggling $\langle \Delta x \rangle_D$ rather than the range of the ions. However, estimates of these quantities have only become available recently through the theoretical treatment of WSS described in sec. (2.4). In addition, as we have mentioned before, image-size distributions of damage clusters are not comparable to the quantities discussed by either ion or damage theory, since they concern properties of single collision cascades while the theories give the mean ion or damage distributions for many ions with the same initial conditions. Extensions of the WSS theory so that single cascades can be described are only in part available [133].

Recently, Cox [134] has confirmed the fast-neutron induced crystallization of amorphous Ge, previously reported by Parsons and Balluffi. He also investigated the temperature dependence of the process. Thus nuclei were found to appear during irradiation at temperatures 150-200°C below the temperatures at which they appear thermally. The phenomenon is strongly temperature dependent and a 25°C difference in irradiation temperature makes a significant difference in the degree of crystallization. In addition, Cox has investigated the possibility of bombardment-induced crystallization of amorphous films of Ta_2O_5, Al_2O_3 and Si. No crystallization was observed in Al_2O_3 and Si specimens after reactor irradiation to ~2 x 10^{18} $nvt_{>1\ MeV}$ with irradiation temperatures up to 200°C. However, crystallization was apparently observed in amorphous Ta_2O_5 after fast neutron exposures in the 10^{16}-10^{17} nvt range. We note, however, that the irradiation temperature was 600°C, which is only 50-100°C below the temperature at which similar effects could be obtained thermally. The irradiation temperature is thus far too high for the effect of irradiation to be predominant in the crystallization process.

It is concluded, therefore, that the only examples known of bombardment induced crystallization in amorphous materials are those of Ge [132,134] and fused silica [130]. Moreover, in both cases only partial crystallinity was achieved.

4.5 Substances showing good radiation stability

The examples in which particle impact had a minor effect on the structure of the material include at least nine oxides, together with a variety of carbonates [115] and halides [135]. Thus ThO_2, UO_2, and PbO showed at high doses no change at all in their diffraction patterns. CaO and NiO underwent at high doses a disordering of an unestablished type characterized by a diffuse diffraction spot pattern [135] and also (in the case of NiO) by an enhanced chemical solubility [76]. MgO showed at high doses a partial conversion to a polycrystalline state [74]. Cr_2O_3 was stable to moderately high doses, and for higher doses became only partly amorphous. SnO_2, at least according to preliminary results, has failed to reveal at high doses a gas-release component in the vicinity of $\approx 280^0C$ which might be attributable to the amorphous-crystalline transition [69]. UO_2 has been shown to remain crystalline to at least 2×10^{21} fission/cm^2 [97] or 9.4×10^{16}, 40 KeV, Xe ions/cm^2 [74,136]. See Table 4.2.

4.6 Previous models for radiation-induced structural transformations

A variety of examples has been given in the preceding section of how some non-metallic solids respond structurally to high doses of heavy particles, the changes (or lack thereof) being of three kinds: crystalline → crystalline, crystalline → amorphous, and amorphous → crystalline. In this section we will discuss the various models proposed to explain these different types of structural evolution.

Table 4.2

Examples of substances which show good radiation stability*

Substance	Evidence based on disorder-induced gas release	Evidence based on reflection electron diffraction
CaO	F_{IB} = 0.25 at 270 μAmin/cm^2 [135]	Diffuse spot pattern at 270 μAmin/cm^2 [135]
Cr_2O_3	F_{IB} = 0.25 at 20-25 μAmin/cm^2[75]	Partial amorphization at 50 μAmin/cm^2 [135]
MgO	F_{IB} = 0.25 at 40-60 μAmin/cm^2[75]	Partial polycrystallinity at 50 μAmin/cm^2 [74]
NiO	F_{IB} = 0.25 at 40-60 μAmin/cm^2[75]	Diffuse spot pattern at 270 μAmin/cm^2 [135]
SnO_2	F_{IB} = 0 at 25 μAmin/cm^2 [69]	...
ThO_2	F_{IB} = 0 at 25 μAmin/cm^2 [65,74]	No change at 50 μAmin/cm^2 [135]
UO_2	as with ThO_2 [74,136]	as with ThO_2 [74,136]

*Note that 1 μAmin is equivalent to 3.74×10^{14} singly charged ions and that F_{IB} stands for fractional gas release due to stage IB (Cf. sec. 3).

The bombardments were in most cases carried out with 5-40 keV Kr or Xe.

4.6.1 Anisotropy model

A number of investigators [e.g. 74,97,135] have proposed, on the basis of work on a broad selection of materials, that anisotropic substances tend to disorder due to particle impact whereas cubic ones tend to remain crystalline. This was attributed to the anisotropy of crystal binding forces in anisotropic materials. Thus, bombardment ruptures molecular bonds and leads to displacement of atoms from normal lattice positions to preferred positions in the disrupted lattice. The stress associated with displaced atoms is accommodated by strain of the lattice, the strain being greater in directions of weakest crystal binding. The final result is, thus, claimed to be an anisotropic expansion leading either to a more isotropic crystal (Cf. examples in sec. 4.3 on titanates, niobates, and some minerals) or to complete distortion of the lattice, i.e. amorphization [e.g. 74].* Although the generalization of this model is fairly good, there are still significant exceptions. Thus there are cubic materials such as diamond, Ge, Si, and GaAs which are readily disordered, as well as anisotropic materials such as Cr_2O_3 and SnO_2 which are relatively stable. Matzke noted that MgO is cubic yet subject to disordering; the disordering occurs only at rather high doses (40-60 Amin/cm^2), however, so we would not regard MgO as a further exception. Moreover, the anisotropy model is not sufficient to explain the difference in behaviour between structurally similar anisotropic materials such as Al_2O_3 and ZrO_2. Thus the former is rendered amorphous

*These authors used the word "cubic" as equivalent to "isotropic". We would disagree with this use, as discussed in Section 7.6.3 .

on irradiation, while the latter transforms to a cubic rather than amorphous form. Finally, it is self evident that the model cannot explain the possibility of ion-impact crystallization of amorphous materials.

Further comments on anisotropy will be made in Section 7.6.3 .

4.6.2 Displacement model

Bombardment-induced structural changes can, in principle, also be attributed to displacement effects, especially in view of the fact that the number of atoms displaced per impact is comparable to the number of atoms transferred to disordered regions. Examples are found in recent work [113] on the disordering of Al_2O_3, diamond, and zircon, where it was shown that the number of atoms entering the disordered phase per impact of 10 KeV-Kr, was roughly 150 (Al_2O_3), 110 (diamond) and 300 (zircon) and thus similar to the number of displacements per impact (~200). Likewise, with Ge and Si one finds about 3000 atoms disordered per incident 40 KeV ion as compared with about 1500 atoms being displaced [120].

A major difficulty enters, however. It will be noted that the displacement process is being supposed to play two rather different roles. With the various crystalline substances listed in table (4.2) it is assumed to lead to a final product which is crystalline; but with the substances listed in table (4.1) it apparently leads to amorphization. There is certainly good precedent for these two roles, with Piercy [137] and Parsons and Balluffi [132], for example, emphasizing that displacement

cascades are regions of high effective diffusion coefficient, thence ones in which ordering might occur. Mazey et al. [106] and Berman et al. [97], on the other hand, have emphasized that displacement cascades are also regions of extreme disorder or of pronounced lattice strains, thence ones in which amorphization might occur. What is not clear is how to explain the dominance of one or the other of these different roles in individual cases and we would suggest that this is a major defect in a displacement model.

4.6.3 Thermal-spike model

Structural changes are also frequently attributed to the thermal effects of particle impact. In effect, the ideas of Parsons [104] and Cox [134] are of interest.

Parsons [104] studied the conversion of crystalline Ge to amorphous Ge by 100 KeV O^- ion bombardment at 30 K^0 or room temperature. In an attempt to explain the mechanism of the disordering and the temperature dependence of the size of the damaged regions, Parsons has proposed a model based on the concept of the thermal spike. Thus he used this concept to calculate the radius of a spherical volume heated to above the equilibrium melting temperature, T_m, to be 130 $\mathring{A}$ for the average energy Ge primary knock-on hit by a 100 KeV O ion when the specimen is at ambient temperature. As this liquid volume cools below T_m by lattice conduction in the material surrounding it, crystallization begins at its periphery and progresses toward the centre of the supercooling liquid. The region is rapidly undercooled and when the temperature of

the advancing crystallizing interface reaches the glass transition temperature (~ 300°C for Ge), crystallization ceases and the remainder of the volume remains in an amorphous state with diameter less than 130 Å. Since specimens irradiated at cryogenic temperature will cool more rapidly, the volume of the amorphous region will be larger. Although Parson's model successfully interpreted the amorphization of crystalline Ge, it is too qualitative to account for the behaviour of other materials on irradiation. It is clear, however, that if it could be formulated more quantitatively it might turn out to be widely applicable.

Cox [134] also used the concept of the thermal spike along with the classical theory of nucleation [see e.g. 142,143] to develop a model for neutron-induced crystallization of amorphous Ge. This model includes the irradiation time, irradiation temperature, and the assumption of a cylindrical thermal spike. Three activation energies are defined for the crystallization process, an activation energy W for the matrix material, W' for the cascade regions, and E' for the cascade regions during the brief time of the thermal spike. Using parameters appropriate for a thermal spike from a 1.2×10^4 eV Ge primary, the ratio of nuclei produced by thermal spikes (governed by E') to nuclei produced by preferential nucleation in the cascade regions (governed by W') was calculated for typical activation energies and ambient temperatures. The results of the Ge neutron-irradiation experiments carried out by this author were explained in terms of the temperature and activation-energy dependence of this ratio. It was concluded, therefore, that whether thermal spike or preferential nucleation accounts for radiation

enhancement of crystallization depends on the required activation energies and the irradiation temperature.

Cox's model was found consistent with his results on neutron-induced crystallization of amorphous Ge. In addition, the present writer (HMN) would point out that the model can be readily modified to include parameters for heavy ions rather than fast neutrons (for instance the total cross section of the collision $d\sigma$ will be different), or for investigating the effect of a pressure spike. However, the model requires information on various activation energies which are usually unavailable, and even Cox was not able to use the same model to analyze his results on the crystallization of Ta_2O_5. (We recall here that the Ta_2O_5 results may have been spurious due to thermal heating, see page 72). Moreover, it is not obvious if this model could be generalized to account for the other types of structural transformations.

4.6.4 Other models

Recent studies on neutron-induced phase transformations in solids have provided still other models for the transformations.

Hauser and Schenk [115] have investigated the influence of neutron irradiation for a special class of materials. These materials have thermal phase transformations which Buerger [138] has called "displacive" or "reconstructive" for first or second coordination, respectively. For the materials examined $BaTiO_3$ shows a radiation-induced phase transformation in the form tetragonal → cubic, whereas with brookite and quartz an amorphous phase occurs. The other materials ($CaTiO_3$, PbO,

$CaCO_3$, and $SrCO_3$) exhibit no radiation-induced transformation. It is, therefore, concluded that compounds showing thermal displacive transformations are more likely to suffer a radiation-induced transformation than compounds showing reconstructive transformations. The superficial and qualitative nature of the approach in this work, however, does not permit unique interpretations of the mechanism involved in the transformation. Moreover, there is not a clear distinction between the different types of transformation proposed by Buerger. In fact, Buerger points out how many transformations are "mixed" and how it is difficult to place them under any one category.

More recently, Schenk et al. [129,139-141] studied radiation-induced phase transformations in $BaTiO_3$, $PbZrO_3$, and $PbTiO_3$. The first two materials are found to undergo a transformation tetragonal → cubic as discussed in sec. (4.3), whereas the third showed a change in the lattice parameters without apparent change in crystal form. The results were explained on the basis of a thermodynamic model, where it has been shown that the phase transformation can be expected only if defect accumulation causes a shifting of the phase transition temperature towards the temperature of measurement. In the case of $BaTiO_3$ and $PbZrO_3$, the defect-induced change of enthalpy is $\delta H < 0$. However, according to this model the only transformations to be considered are those where the transformation is endothermic, reversible, and diffusionless. It is also assumed that the concentration of defects will be maintained substantially unchanged during the transformation process, i.e., as stated by the authors [144], recombination, dissociation, creation, and annealing

of defects do not take place! It is obvious, therefore, that the model is oversimplified. Moreover, as pointed out by the author [141], the main problem of the thermodynamic model is the lack of directly measured data for the defect concentration which is basic for the treatment. In addition, it would be difficult to apply the model for ion-bombardment studies, since it implies measuring thermodynamic quantities for the irradiated substances by techniques such as calorimetry or DTA, which require changes in bulk materials rather than in surface layers. Further investigations are necessary, therefore, for a possible generalization of statements concerning the influence of defects on different modifications of substances.

4.7 Concluding remarks

Although a large amount of information is now available on the phenomenon of structural transformations induced by irradiation, none of the existing models is sufficient to explain the results, or to predict the stability of materials on bombardment. In effect, whatever mechanism is operative would be hoped to account for three types of structural changes: crystalline → crystalline, crystalline → amorphous, and amorphous → crystalline, and, moreover, to do so for all known examples (not just the few chosen by each author).

Reviewing the models, it was apparent that those based on the properties of thermal spikes [as e.g. 104,134] are the least objectionable. Also, experiments which involve irradiation of metastable amorphous materials would be the most desirable, due to the limited number of studies concerning the crystallization of amorphous substances by

bombardment. It was thus decided to investigate the possibility of crystallizing amorphous ZrO_2 thin films by heavy-ion bombardment and to relate the results obtained by transmission electron microscopy to the properties of thermal spikes.

ZrO_2 is a good insulator and because of its low thermal conductivity and low thermal diffusivity would be expected to be a likely specimen for a thermal-spike model. In addition, the difficulty in forming amorphous ZrO_2, which will be discussed in the next chapter, is perhaps related to the ease of the amorphous-crystalline transition and thus implies a high probability of inducing the phase transition by bombardment. It seems logical, however, to first examine the crystallization of amorphous ZrO_2 by thermal heating (Ch. 5) and only then attempt to induce the crystallization by ion impact (Ch. 6).

CHAPTER 5

PREPARATION AND THERMAL CRYSTALLIZATION OF AMORPHOUS ZrO_2*

5.1 Introduction

Before studying bombardment-induced crystallization of amorphous ZrO_2, it is necessary to begin with investigating its crystallization behaviour during thermal heating. Only then can one differentiate between radiation effects and thermal effects.

As an introduction to this chapter, a general outline of the properties of amorphous solids will be considered. Following this will be a description of a method for preparing amorphous thin films of ZrO_2 by ion-beam sputtering. The structure of the as-prepared films, and their crystallization during thermal heating will finally be discussed.

5.2 Amorphous Solids

5.2.1 Definition

The word "amorphous" ordinarily means "without form"; however, in the present context "amorphous" is taken to be synonymous with "non-crystalline". Accordingly, amorphous solids are best identified as those materials characterized by two negative properties: no long-range order like in crystalline solids, and no short-time fluidity like in normal liquids.

---

*For the most part, this chapter is based on a paper by the author and Dr. R. Kelly [144].

In recent years, many techniques have been developed for the preparation of amorphous thin films. These include rapid quenching from the liquid state, deposition from solutions, condensation of vapor species, ion-beam sputtering, and reactive sputtering.* It has been suggested sometimes, however, that one should distinguish between those amorphous solids prepared by cooling a melt, called "real glasses", and those prepared by other techniques [e.g. Ref.[146],Ch. 14 & 15]. This argument was probably based on a classical definition of glass, given by the ASTM, as "an inorganic product of fusion which has cooled to a rigid condition without crystallizing". Recent studies [147], however, showed that amorphous substances prepared from the melt or by any other technique have the same physical properties, and, therefore, the description of a solid as amorphous or glassy must be taken as equivalent.

Possible criteria for a thin film to be best described as amorphous were proposed by Mader [148,149] to be as follows:

(a) The diffraction pattern should show broad halos that cannot be easily and uniquely assigned to the diffraction lines of a crystalline structure. It has been shown that an upper limit for the size of coherently ordered particles in such a structure can be estimated and that this limit is of order of 10 Å. Thus local order, whatever its crystallographic nature may be, does not reach beyond the next-nearest neighbor distance.

(b) High-resolution electron micrographs should not show any crystal grain structure. In a very fine grained film dark field

---

*These techniques and others are described in detail in Ref. [145].

techniques usually reveal the size of coherently diffracting crystallites down to a resolution limit of 15-20 Å.

(c) In addition to these structural features, the films designated amorphous should also differ in their annealing behaviour from very fine grained crystalline films. When fine grained crystalline films are heat treated, one observes a continuous grain growth over a wide range in temperature. Amorphous films, however, undergo a precipitous annealing stage in a very narrow temperature region, after which they show a clearly crystalline diffraction pattern.

5.2.2 Atomic arrangement in amorphous solids

Our knowledge of the internal structure of amorphous solids is derived from X-ray, neutron, and electron diffraction studies, just as in the case of crystalline solids. It is well known (Cf. Ref. [150]) that as the particle size of disoriented crystals is made smaller and smaller, the diffraction lines broaden into diffuse halos. From a Fourier analysis of such a diffraction pattern it is possible to determine the average distribution of neighboring atoms. The results usually include one intense broad peak at about the same distance as the first nearest neighbors in the unit cell of the crystalline phase, and perhaps one or two additional broader and less intense peaks corresponding to average distances near the second or third nearest neighbor values.

Extensive investigations of the structures of amorphous alloys and oxides, and comparison with the structures of liquids, have not yet been made. Most data are confined to the structure of amorphous

elements, where the diffraction studies showed that they are of two types. In the first type, the atomic distributions in the amorphous and the liquid phase are fairly similar, and these materials have therefore been referred to as having "liquid-like structure". Examples are amorphous Bi, Ga, Fe and Cr [151] and perhaps alloys or other elements. In the second type, the differences between the atomic distributions of the amorphous and liquid were such that the amorphous materials have been said to have a "lattice-like structure". Examples are Si and Ge [152]. Accordingly, it would be erroneous to equate generally "amorphous" with "liquid-like" as is sometimes suggested [153].

5.2.3 Crystallization of amorphous solids

Most investigations dealing with the crystallization of amorphous solids showed that the crystallization is typical of nucleation and growth controlled reactions. The formal theory of "crystallization from the melt" (Cf. e.g. [142,143]) is, therefore, usually used to describe the kinetics of the crystallization of amorphous solids. In spite of the similarity between the two processes one must make the following distinctions.

a. Crystallization from the melt, at the melting point, is a reversible process, i.e., takes place in thermal equilibrium. In contrast, the transition amorphous to polycrystalline is irreversible indicating that the amorphous state is metastable.

b. In terms of Fig. (5.1), which describes the rate of the transformation as a function of temperature, solidification occurs at the high temperature side of the maximum (labeled B), whereas crystallization

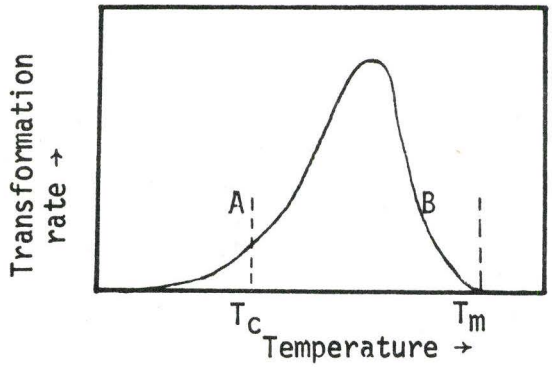

Fig. 5.1 Temperature dependence of the transformation rate of a nucleation and growth transformation.

occurs when amorphous solids are heated into the region of appreciable crystallization rate at the low temperature side of the maximum (labeled A).

As pointed out by Mader [148], the crystallization of an amorphous solid is also similar to recrystallization and grain growth processes, in that both involve a transformation rate that increases with temperature. The main difference lies in the structure of the untransformed material and in the driving force of the transformation. The crystallization of an amorphous solid does not draw on a driving force created by cold work, as does recrystallization proper, but on the free energy differences between the amorphous and crystalline states.

5.3 Preparation of amorphous ZrO_2

5.3.1 General

ZrO_2 is known to exist in an amorphous form and in three crystalline modifications: cubic, tetragonal, and monoclinic. Most techniques by which ZrO_2 is formed, for example anodic oxidation [154] or thermal

oxidation [155,156], lead to one of its crystalline modifications. ZrO_2 formed by chemical decomposition is sometimes described as amorphous [157-159] and at other times as crystalline [160,161]. Thin films of ZrO_2 prepared by evaporating the metal in vacuum ($\approx 10^{-4}$ torr) [162] have a calculated grain size of 60 Å, and give rise to wide diffuse rings in electron diffraction, which become progressively sharper on annealing.* In view of the discussion given in sec. (5.2.1), these results suggest a microcrystalline rather than amorphous structure for the evaporated ZrO_2 films.

It was found necessary, therefore, to develop another technique, for preparing thin films of amorphous ZrO_2, especially in view of the following requirements: a) the films must be sufficiently thin for transmission electron microscopy; b) they must agree with the characteristic features of an amorphous solid, as outlined in sec. (5.2.1); c) they must be homogeneous and sufficiently clean to be free of any impurities which could interfere with diffraction patterns; d) they must be easily prepared with the available equipment, since radiation damage studies need large numbers of specimens in order that reasonable data can be obtained.

These requirements were reasonably well met using the sputtering technique described in the next subsection. This technique has been widely used in recent years for preparing almost any kind of thin film (elements, alloys, compounds...), not only for electronic applications but for all areas where films may be needed. The general nature of the sputtering process is extensively reviewed by Carter and Colligon (Ref. [1] Ch. 7), while the reader who is interested in additional

---

*The size was calculated from the width of the amorphous halos.

information on the broader subject of sputtered films is referred to the review article by Maissel (Ref. [145], Ch.4) where more references are given.

5.3.2 Preparation of amorphous ZrO_2 by sputtering technique

The zirconium used as starting material was in the form of 0.1 mm foil of nominal 99.8% purity. A 50 mm. diameter piece was chemically polished using a solution containing 45 ml. nitric acid, 8-10 ml. hydrofluoric acid, and 45 ml. water [163]. The pieces were dipped in 20-30 ml. of this solution for about 5-10 secs then rapidly removed and rinsed in running water. This technique provided a very clean and smooth surface. The clean pieces were then anodized at 200 volts in 3% ammonium pentaborate using a Pt cathode, which led to the formation of a ZrO_2 layer about 5400 $\mathring{A}$ thick [164], and which, because it was thin, could be bombarded without charge build up.

The anodized Zr was now sputtered with Kr or O_2 ions using a simple ion accelerator (to be described in sec. 6.2), the target arrangement of which is shown in Figure (5.2). The collector was a 2 mm. thick aluminium disc, which was polished, cleaned, and then covered with small pieces of KCl which were prepared by cleavage from boules purchased from Korth (Kiel, Germany). These KCl crystals served as substrates for the sputtered ZrO_2. Most experiments were carried out using 6 keV ions, currents of 40-60 μA, and sputtering times of 75 min. The area subjected to the beam was changed every 5 min. by rotating the target support in order to avoid complete perforation of

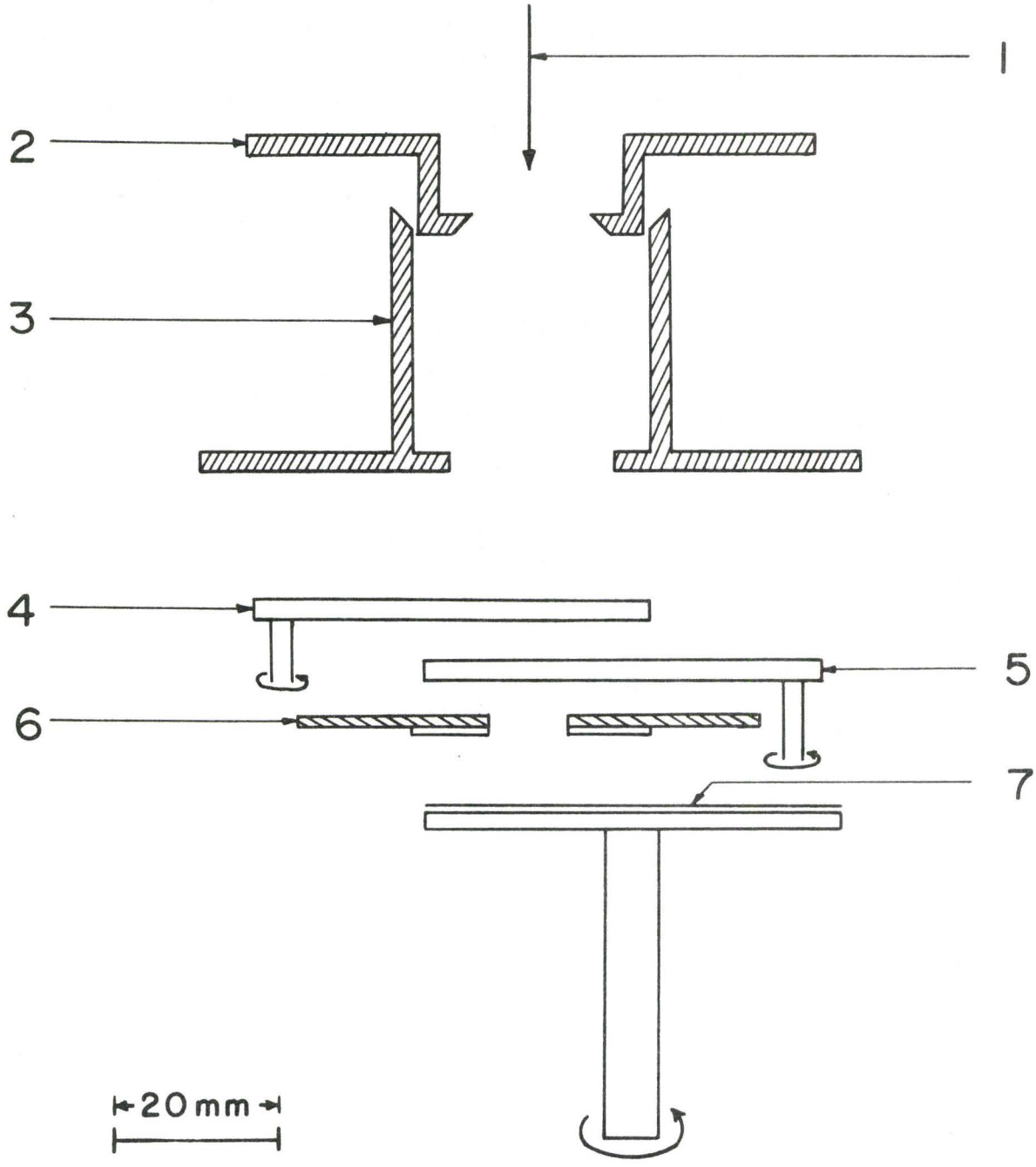

Fig. 5.2 Target arrangement used for sputtering anodized Zr: 1, ion beam; 2, 14 mm defining iris; 3, centering piece, serving also as electron suppressor; 4, shutter; 5, fluorescent screen; 6, Al disc with pieces of KCl glued on; 7, Zr anodized at 200 volts.

the anodic oxide, thence sputtering of pure Zr. All bombardments were performed with extensive use of liquid-nitrogen trapping in order to freeze out any organic impurities present in the system during operation. The vacuum in the accelerator target chamber was about 10^{-6} torr during bombardment and the experiments were carried out at room temperatures.

The ZrO_2 films collected on KCl were wet stripped from their substrate, and mounted directly on specimen grids for electron microscopic examination and further treatment as will be described below.

The zirconia films prepared by this method were 1200 ± 200 Å thick. This value was obtained by collecting part of the sputtered film in each experiment on the surface of cleaned, polished pieces of Zr instead of the KCl crystals, and comparing the interference color formed with a ZrO_2 color gauge.

Electron microscopy and electron diffraction examination before and after each crystallization process were made mainly with a Siemens Elmiskop I operated at 100 KeV, and occasionally with a Philips EM 300 .

5.4 Results

5.4.1 The structure of the as-prepared films

As seen from Fig. (5.3), sputtered films of ZrO_2 show structureless microscopic images, whether in bright or dark field, and give rise to amorphous patterns (halos) in electron diffraction. The apparent particle size in the amorphous film was estimated from the half widths of the halos in the diffraction pattern using the equation [165]:

$$b = \lambda/L \qquad (5.1)$$

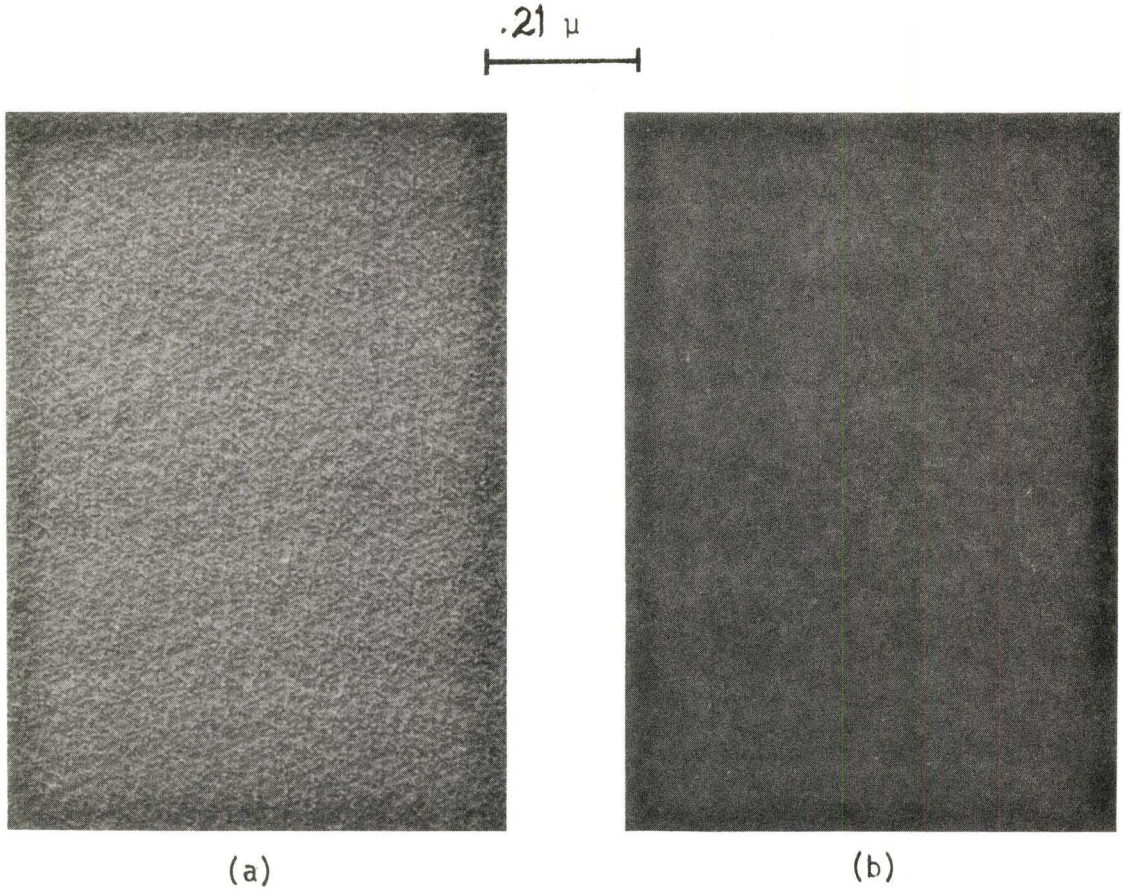

Fig. 5.3 Amorphous ZrO_2 film prepared by sputtering anodized Zr with 6-KeV Kr. a) In bright field, b) in high-resolution dark field, c) corresponding diffraction pattern.

where b is the line width (in radians) at half maximum intensity attributable to crystallite size effects, λ is the electron wavelength, and L is the mean crystal size normal to the beam. The intensities of a number of amorphous patterns were measured, using model MK IIIC double-beam microdensitometer (Joyce, Loebl & Co. Ltd., England) and the average particle size was found to be ≥ 10 Å. Here the inequality would correspond to the case where the halos resulted from more than one interatomic spacing.

The amorphous halos seen in Fig. (5.3c) might be, however, due to the overlapping of several diffraction rings, each of which is broadened only slightly due to the small crystal size [166,167]. This suggested that if dispersion of the diffraction patterns were possible, these halos might be separated into their corresponding rings. Dispersion of diffraction patterns can be accomplished by changing the camera constant (λL) either by examining the same pattern at different electron beam energies, or by changing the camera length using the diffraction lens of the Philips EM-300 at different excitations, and focusing the pattern by the diffraction lens control. Using both techniques a series of diffraction patterns was obtained, for the same area of sputtered film at different dispersion conditions. The intensities of these patterns were then determined with the microdensitometer and the results are shown in Fig. (5.4). As can be seen from this figure, even the maximum dispersion obtained, as in case (d), did not change the shape of the peak in the intensity chart. These results suggest that the sputtered films could be safely described as <u>amorphous</u>, as far as points

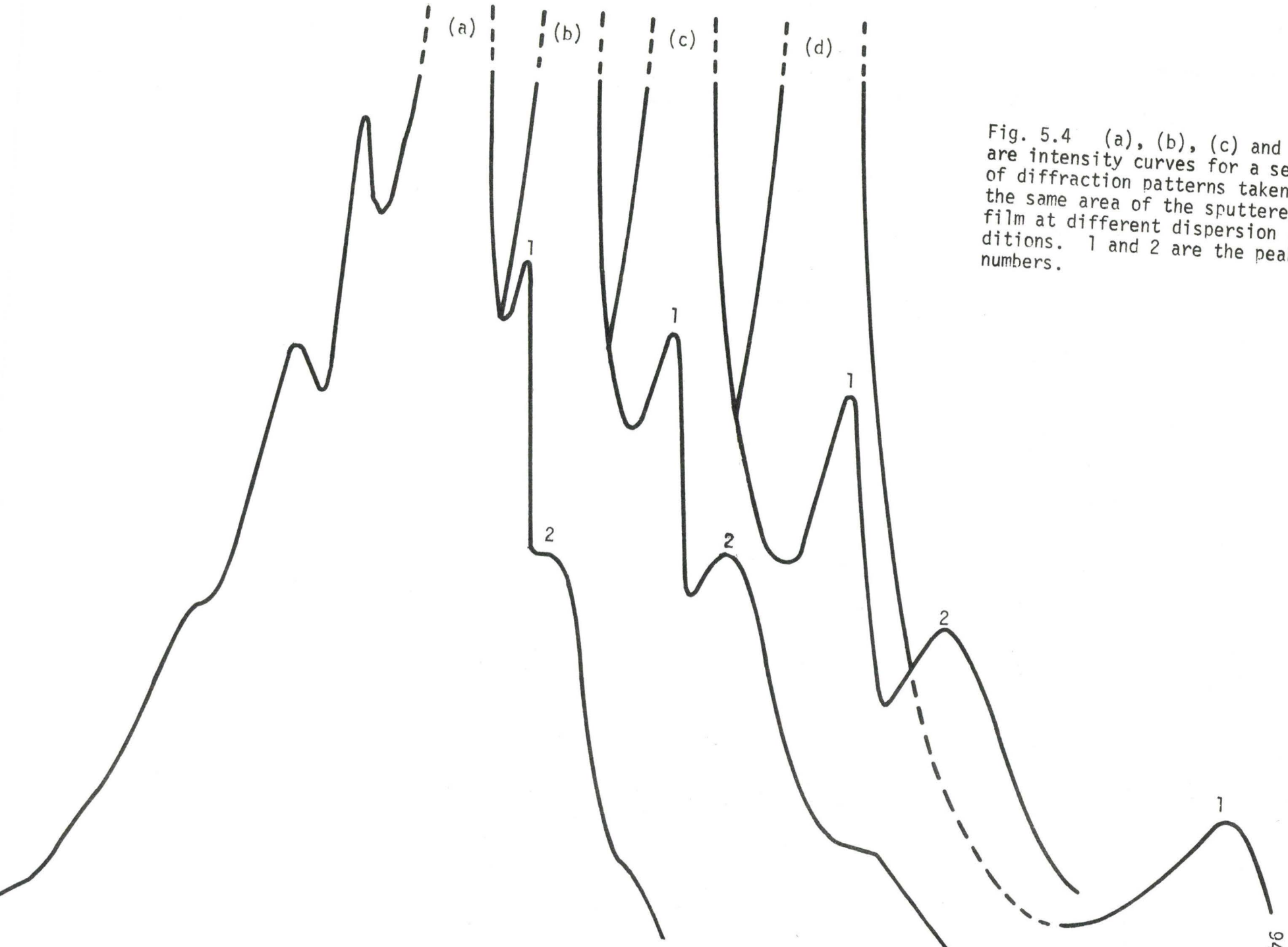

Fig. 5.4 (a), (b), (c) and (d) are intensity curves for a series of diffraction patterns taken for the same area of the sputtered film at different dispersion conditions. 1 and 2 are the peak numbers.

(a) and (b) in sec. (5.2.1) are concerned. (Point (c) will be considered in what follows.)

5.4.2 Thermal crystallization of amorphous ZrO_2 thin films

In this section the crystallization of amorphous ZrO_2 thin films during ordinary macroscopic heating will be investigated. The heating was carried out using either the microscope electron beam (pulse heating), or a small resistance furnace. Although there were no detectable differences between the crystallization behaviour using these methods, the former technique provided rapid results about the crystallization products; moreover, it enabled one to observe the creation and subsequent growth of the crystals during the transformation processes. Therefore it was found quite useful to use pulse heating after any crystallization process, either thermal or induced by ion bombardment, as will be described in Chapter 6. Nevertheless, it is worth pointing out that pulse and furnace heatings differ in that the first involves a hydrocarbon reducing atmosphere, the latter an oxidizing one. Apparently, therefore, the crystallization behaviour of amorphous ZrO_2 does not vary for the particular heating atmospheres. (A dependence of crystallization of ZrO_2 on the oxygen content of the heating atmosphere was demonstrated by Livage [159]).

Palladium electron microscope grids were used to support the sputtered ZrO_2 films during the thermal heating studies.

A. Crystallization by Pulse Heating

Crystallization by pulse heating was carried out by reducing the electron beam currents of the microscope to a minimum, then removing the condenser II movable aperture and letting the electron beam pass through a condenser I fixed aperture having a diameter of 760 μ. A very slight increase in the current accompanied by simultaneously observing the specimen provided a useful chance to follow the amorphous-crystalline transition, i.e. crystal nucleus formation and the subsequent grain growth. In fact, the increase in the current resulted in the formation of well-separated small crystalline regions having initial diameters of 300-500 Å. With continuing increase in the beam current, the crystalline regions grew to relatively large sizes with no apparent change in the intervening matrix. Fig. (5.5a) shows an electron micrograph of this stage, while 5.5(b) to (d) are series of diffraction patterns starting from completely amorphous areas at the edge of (a) and ending at a completely crystalline area. As seen in this figure the sharp diffraction pattern from the crystals appears superimposed on the diffuse diffraction halos of the matrix, which remained unchanged as crystallization proceeds. This nucleation and growth is the expected mode of crystallization of an amorphous solid with a continuous random type of structure [167] and with an abrupt (rather than spread out) annealing interval. The ZrO_2 films thus conform also to point (c) of Sec. (5.2.1).

As shown in Fig. (5.6), a further increase in the electron beam current through the same area resulted in the growth of relatively large

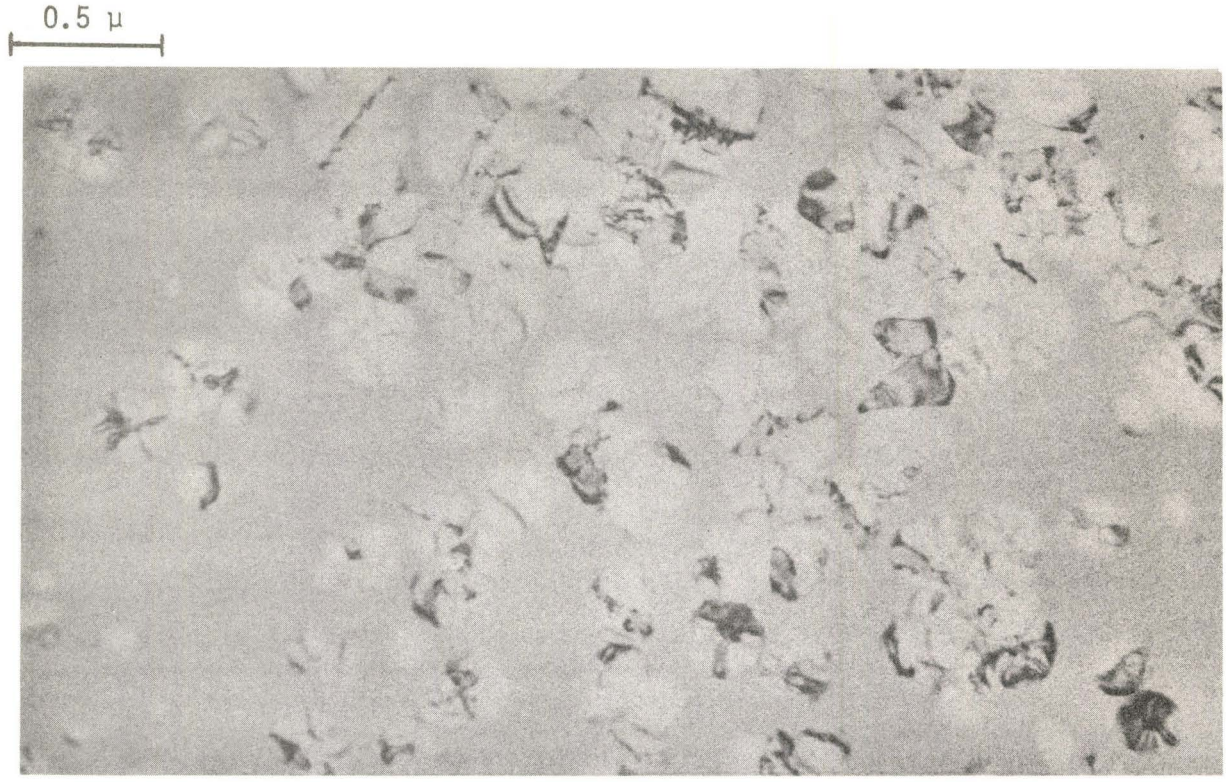

(a)

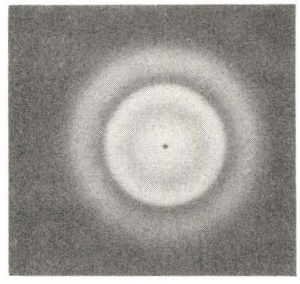

(b)

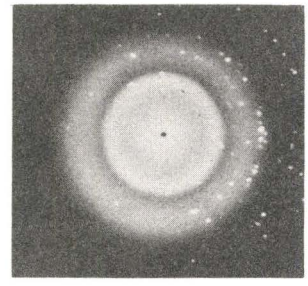

(c)

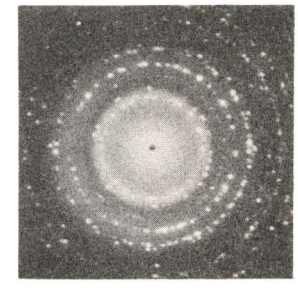

(d)

Fig. 5.5 a) Partially crystallized ZrO_2 produced by gently pulse-heating an amorphous film in the microscope. Note the presence of bending contours, which may be attributed to the volume change during the amorphous-crystalline transition. b) to d) Series of diffraction patterns starting from completely amorphous area at the edge of (a) and ending at completely crystalline area.

crystals (≈7000 Å) containing numerous bending contours. These contours are probably due to the volume change in the amorphous-crystalline transition. The diffraction pattern given in the inset of Fig. (5.6) shows that the crystallization product consisted mainly of an apparently cubic form of ZrO_2, though perhaps with small amounts of the monoclinic form also present.* Thus, as shown in table (5.1), most of the d values calculated from this pattern correspond to what was expected for cubic ZrO_2, except for a few weak lines, which are possibly among a group characteristic of monoclinic ZrO_2.**

A large increase in the electron current through areas near the grid finally caused a more extensive transformation to monoclinic ZrO_2. As seen in Fig. (5.7), the monoclinic crystals are small, being best identified by the twinning which often accompanies this form of ZrO_2 [168].

B. Crystallization by furnace heating

A tube furnace was used to provide more information on the crystallization of amorphous ZrO_2. Specimens held in Pd grids were heated isochronally in air with hold times ranging from 5 minutes to 6 hours and with microscopic examinations made after each heating. For a 5 min. time scale, no change was observed, either in the microstructure or in the diffraction pattern, until 520 ± 10°C. At this

---

*The cubic and tetragonal variants of ZrO_2 are sufficiently similar in their diffraction patterns that they are difficult to distinguish. It is for this reason that we refer to an "apparently" cubic phase.

**This possibility has been discussed in appendix (A), sec. (A.2).

0.5 μ

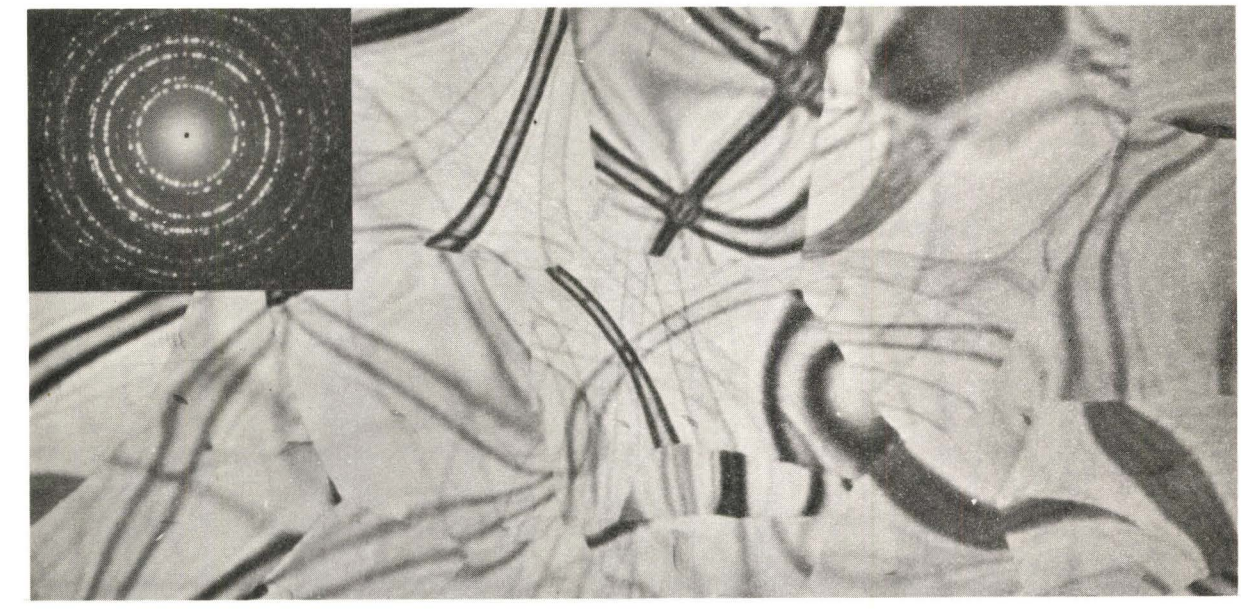

Fig. 5.6 Fully crystallized ZrO_2, mainly in an apparently cubic form, produced by somewhat more strongly pulse-heating an amorphous film. The bending contours are even more prominent than in Fig. 5.5. The corresponding diffraction pattern is shown in the inset.

0.5 μ

Fig. 5.7 ZrO_2, mainly in the monoclinic form, produced by strongly pulse-heating an area similar to that shown in Fig. 5.6. Note the characteristic twinning. The inset shows the corresponding diffraction pattern.

Table 5.1

Electron diffraction data for cubic ZrO_2

ZrO_2 (cubic) ASTM 7-337 hkl	dÅ	d values, in Å, as calculated from Fig. 5.6*
111	2.92	2.90
200	2.53	2.46
Unidentified		2.05
220	1.80	1.79
311	1.53	1.53
222	1.464	1.48
Unidentified		1.36
400	1.267	1.26
Unidentified		1.19
331	1.164	1.20
420	1.133	1.11

*See appendix (A)

temperature well separated crystalline areas with diameters of 300 - 500 Å or greater appeared without any apparent change in the amorphous matrix. Crystallization behaviour for 1/2, 1 and 6 hour heatings was similar except that, as seen in Fig. (5.8), the temperatures were lowered. In addition, similar temperatures were obtained for a given time scale, for specimens prepared by either Kr or O_2 sputtering, i.e. for specimens which may have had slightly different stoichiometries.

Alternatively, the crystallization could be investigated by carrying out a series of isothermal heatings. A typical result is shown in Fig. (5.9) for isothermal heating at 450 ± 5°C, where the curve has a sigmoidal shape suggestive of transformation kinetics typical of nucleation and growth. As seen in Fig. (5.10c) the final product of the crystallization is similar to Fig. (5.6a) including the presence of prominent extinction contours; in addition, the diffraction pattern was similar to that shown in Fig. (5.6b). Again one concludes that amorphous ZrO_2 crystallizes mainly to a nominally cubic form but with a certain amount of monoclinic phase also present.

Prolonged heating or strong pulse heating of specimens previously crystallized in the furnace resulted, as would be expected, in a transformation to a dominantly monoclinic structure, a result similar to that obtained for samples heated wholly within the microscope as in Fig. (5.7).

We would recall again that the similarity of the results for pulse heating and for furnace heating is not wholly trivial. It shows that the crystallization behaviour of amorphous ZrO_2 is not dependent

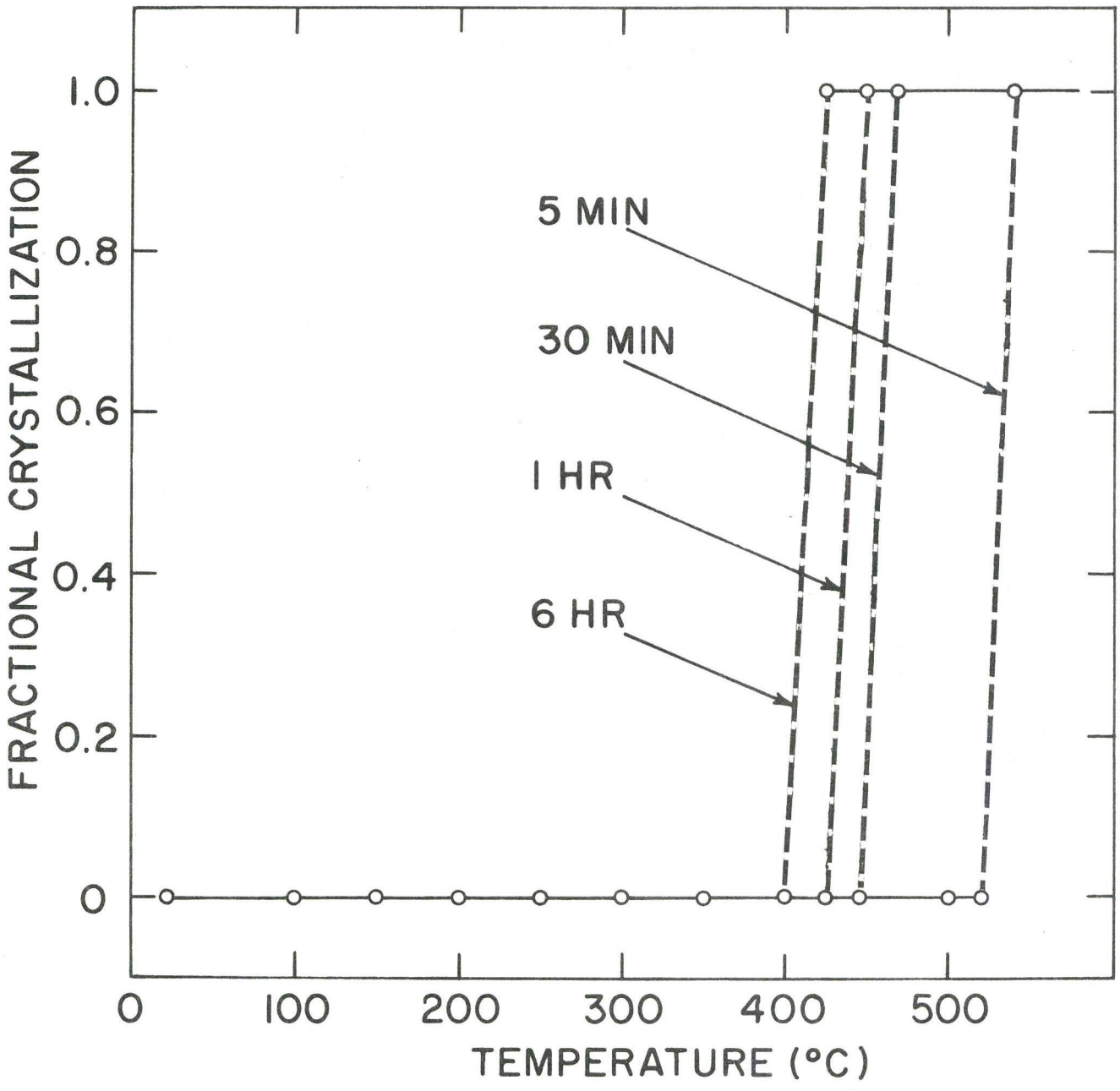

Fig. 5.8 Fractional crystallization vs. temperature for macroscopic isochronal heating of amorphous ZrO_2.

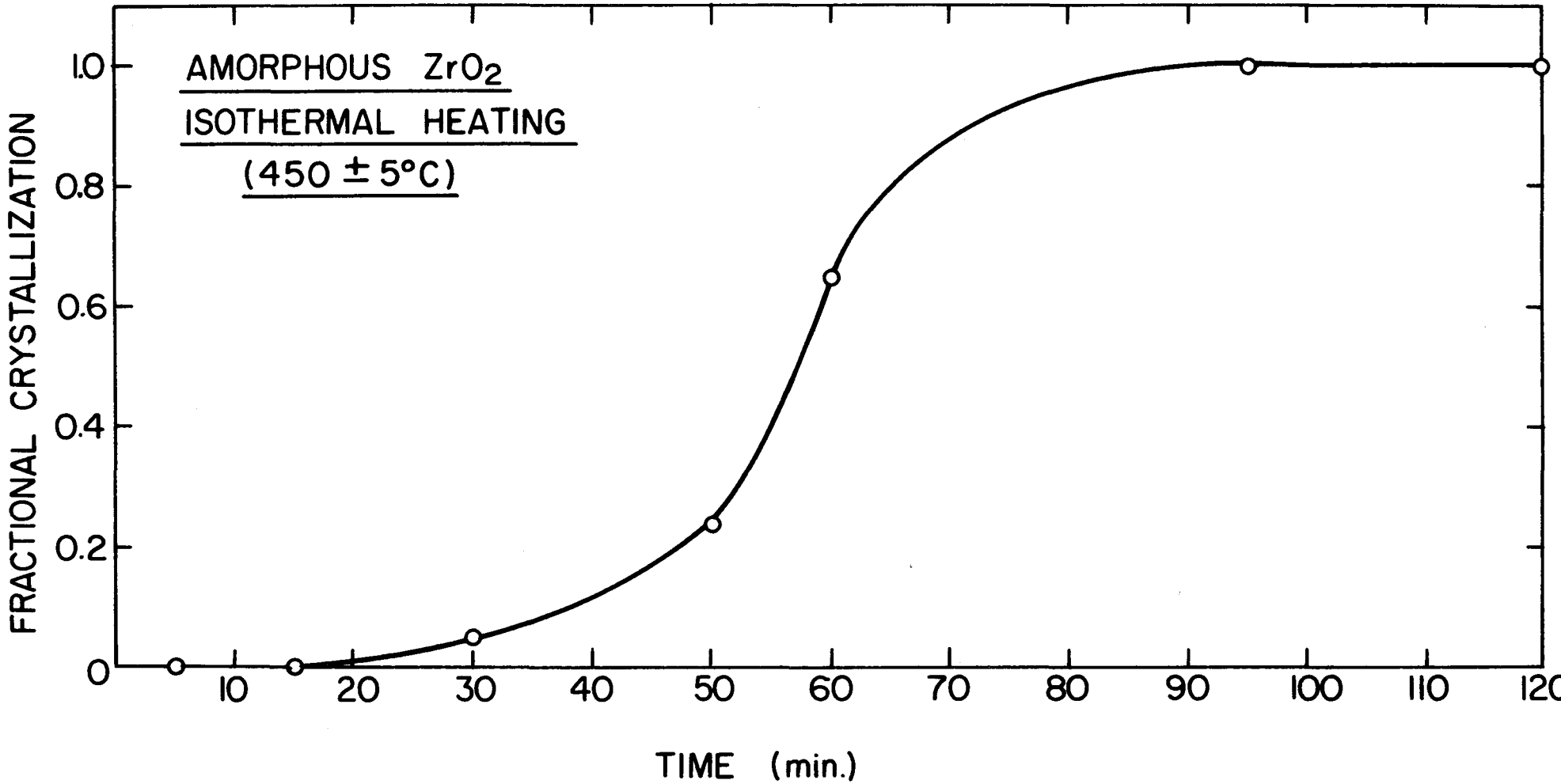

Fig. 5.9 Fractional crystallization vs. time for macroscopic isothermal heating of amorphous ZrO_2 at 450 ± 5°C.

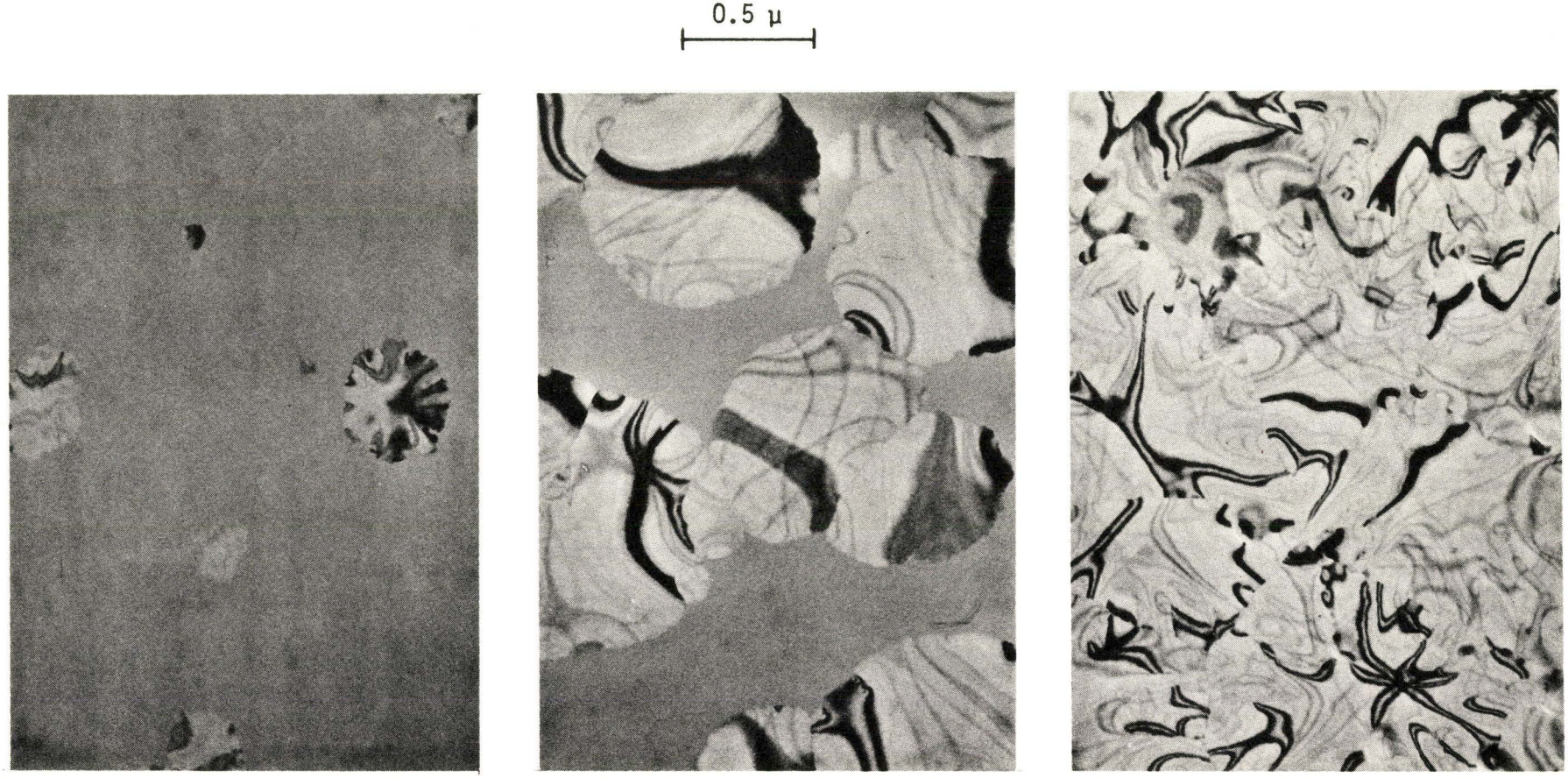

Fig. 5.10 Progressive isothermal crystallization of amorphous ZrO_2 at 450°C held for (a) 30 min, (b) 45 min, and (c) 120 min.

on the heating atmosphere, thence on possible difference in stoichiometry.

5.5 Discussion

5.5.1 Structure of amorphous ZrO_2

The present results show that the thin films of ZrO_2 prepared by ion-beam sputtering of anodized Zr could be safely described as amorphous. Thus, a) they show a structureless image in both bright and dark field; b) they give rise to broad halos, which are not due to overlapping of diffraction patterns; (c) they have particularly abrupt annealing intervals until which the diffraction patterns were unchanged. These are the same points, originally proposed by Mader [148,149], as listed in sec. (5.2.1).

A number of theories and semi-empirical rules have been proposed connecting the glass-forming ability of a substance and some feature of its structure, e.g. the geometrical arrangement of the constituent atoms, the size of the atoms, the nature of the interatomic bonds, or the strength of the bonds.* According to most of these theories the structural features of ZrO_2 are unfavourable for creating a random network such as is supposed to characterize amorphous materials. This line of argument should be treated with caution, however, since it also predicts amorphous Al_2O_3 and TiO_2, for instance, to be unstable; on the contrary, Al_2O_3 is almost invariably amorphous when formed at temperatures below 500°C [74,170], while amorphous TiO_2 has been formed by anodic oxidation [171], by vacuum evaporation of TiO_2 [172], and by ion

*These theories have been summarized and discussed by Rawson (Ref.[169], Ch. 2).

bombardment [e.g. 74]. As far as ZrO_2 is concerned, we note that an amorphous form has been prepared by chemical decomposition as well as ion-beam sputtering as described here.

The structure of chemically deposited amorphous ZrO_2 has been recently investigated by Livage et al. [159], using X-ray and neutron diffraction techniques. This study suggests that the atoms were not distributed at random in amorphous ZrO_2, but that certain distances existed between the atoms characteristic of short range order. Moreover, these distances corresponded to certain distances found mainly in the (111) plane of tetragonal ZrO_2. This suggested a two dimensional ("lattice-like", Section 5.2.2) model for the structure of amorphous ZrO_2: a thin plate consisting of Zr atoms between two oxygen layers, as shown in Fig. (5.11).

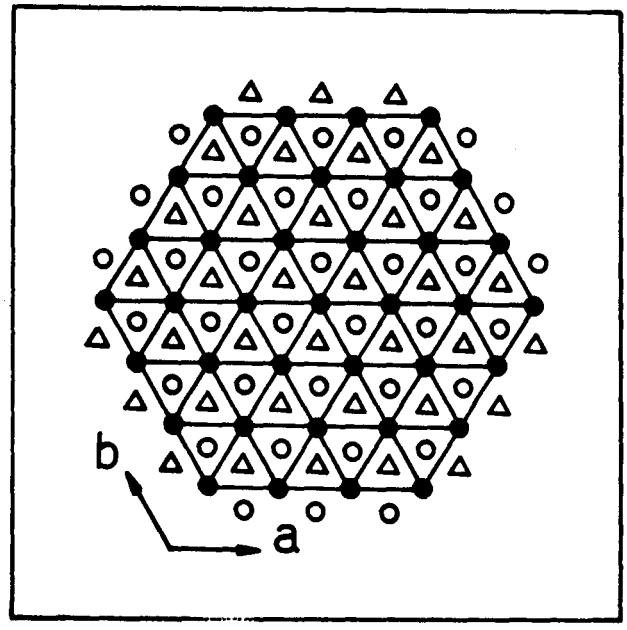

Fig. 5.11 Suggested model for amorphous ZrO_2, ● Zr atoms; O O_2 atoms situated above the Zr plane; △ O_2 atoms situated under the Zr plane [ref. 159].

The sizes of these plates have been estimated as involving diameters varying from 20 Å to 60 Å and a constant thickness of 4 Å.

Livage's model cannot be taken, however, as a universal one for all amorphous ZrO_2, i.e. as applicable regardless of the method of preparation and the experimental technique used for determining the structure. Thus, as will be discussed in the next section, amorphous ZrO_2 films prepared by different methods show different behaviour during crystallization, which could suggest different structures. Also, small particles are known [165] to yield much sharper lines in electron diffraction patterns than X-ray patterns because the electron wavelengths are shorter than the X-ray wavelengths. In fact, Mazdiyasni et al. [160] have found that ZrO_2 prepared by chemical decomposition was amorphous to X-ray, but electron diffraction patterns showed eight strong lines of cubic ZrO_2. Livage's materials may thus have been distinctly "less amorphous" than that prepared here.

Kakinoki et al. [173] investigated evaporated carbon films by electron diffraction, and found that two kinds of bond distance existed in the films, corresponding to diamond and graphite respectively. They therefore reached the conclusion that the amorphous carbon films are built up from two kinds of regions consisting of graphite-like and diamond-like configurations. Shiojiri [172] made the same argument to explain the structure of amorphous films of TiO_2 formed by vacuum evaporation, namely by assuming anatase-like and rutile-like regions to be present in the film. It then follows that the crystallization of the amorphous films involves merely a rearrangement of pre-existing regions and this explains the occurrence of both anatase and rutile in the

crystallization products.

Our observations with amorphous ZrO_2 show that the crystallization products are of two types, for the most part apparently cubic, but also monoclinic, and one could again assume the appropriate microscopic domains to be present. They would be in part cubic-like and in part monoclinic-like. We would like to point out, moreover, that there are at least two alternatives to presupposing cubic-like and monoclinic-like domains in amorphous ZrO_2. One is that only cubic-like regions are present, in accordance with Livage's model described before, and any monoclinic ZrO_2 in the crystallization products represents the beginning of the cubic-monoclinic transition. The other is that nominally cubic ZrO_2 forms independently of the structure of amorphous ZrO_2. Thus, as will be discussed in the following section, cubic ZrO_2 might form because it is kinetically or thermodynamically favoured. These two alternatives can also be applied in the case of TiO_2, i.e. that only anatase-like regions are present and any rutile formed represents the beginning of the anatase-rutile transition, or else that the crystalline structure obtained is completely independent of the structure of amorphous TiO_2. The final decision must obviously await for a detailed investigation on the structure of amorphous oxides using diffraction techniques. This subject is a study by itself and it is clearly outside the scope of this dissertation.

In general, we conclude simply that the structure of amorphous ZrO_2 is not eludicated particularly well by any of the previous work. This includes the once-popular structural arguments (like those of Zachariasen [174]), Livage's [159] thin-plate model, and Kakinoki's

model of crystal-like domains [173]. We, therefore, refrain from coming out in favor of any one point of view.

5.5.2 Thermal crystallization of amorphous ZrO_2

The present results have shown that the thermal crystallization of amorphous ZrO_2 is typical of nucleation and growth-controlled reactions; thus it involves the appearance first of small crystallized regions at temperatures ranging from 400 to 520°C, depending on the heating time, and then of larger crystals at higher temperatures. The initial crystallization products were for the most part apparently cubic, though monoclinic crystals appeared subsequently. A large increase in crystal size is involved in the crystallization, for the amorphous films had an apparent particle size of ≥ 10 Å as compared with 300 - 500 Å for the first formed cubic crystals.

The activation enthalpy, ΔH_c, governing the crystallization can be estimated by assuming [75] that the crystallization is described by:

$$\left(\frac{D_c^0 t}{\lambda}\right) \exp\left(\frac{-\Delta H_c}{RT}\right) \approx 200 \times 10^{-8} \text{ cm}. \qquad (5.2)$$

Here $D^0{}_c$ is the pre-exponential part of the diffusion coefficient for crystallization*, λ is the mean atomic spacing, and 200×10^{-8} cm is the approximate distance scale of the crystallization (i.e. one-half the size of the first-formed crystals). Four points for an Arrhenius diagram (Fig. (5.12)) are obtained from Fig. (5.8) while a fifth point follows from Eq. (5.2) by taking $\frac{1}{T} = 0$ and $D^0{}_c \approx 3 \times 10^{-1\pm1}$ cm^2/sec [65]. The result is 54 ± 3 Kcal/mole. Livage et al. [159] presented results of

*For further details about D_c^0, see page 141.

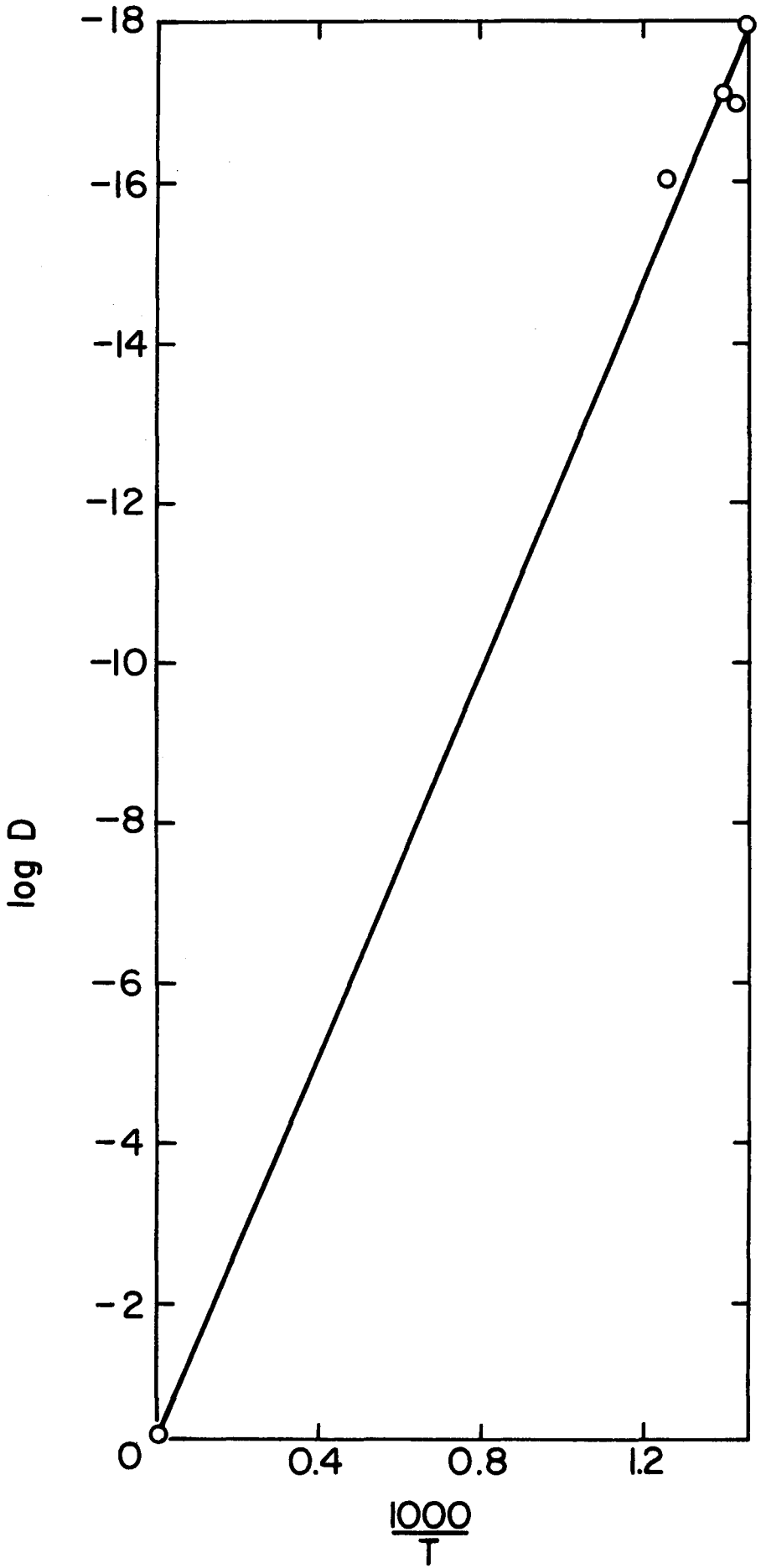

Fig. 5.12 Arrhenius diagram, 1/T vs. log D, for determining the activation enthalpy ΔH_c governing the crystallization of amorphous ZrO_2

isothermal annealing of amorphous ZrO_2, but did not analyze their data. In Appendix (C) the present author has applied standard rate kinetics to their data and gotten an activation energy of 50 ± 20 Kcal/mole. Such a value is, in spite of the large scattering due to the small scale of Livage's curve, in fair agreement with the result obtained using Eq. (5.2).

As far as the structure of the crystallization products is concerned, there is general agreement with other work. Thus the amorphous films prepared chemically [e.g. 157,159] crystallized first to a cubic form, but with increasing temperature, increasing amounts of monoclinic ZrO_2 appeared. ZrO_2 formed from evaporated zirconium films [162,175] or by decomposition of an alkoxide [160] was also at first cubic but readily evolved into the monoclinic form at temperatures varying between 400 and 600°C.

There is also some basis for understanding <u>why</u> the particular crystallization products were observed. Polezhaev [176] has suggested that the stable form of ZrO_2 is cubic for the smallest crystal sizes, tetragonal for somewhat larger crystallites, and, finally monoclinic for crystallites greater than 100 - 300 Å in extent. In effect, the observation here of crystallization products which are apparently cubic or tetragonal, can in principle be understood as being a consequence of the small <u>initial</u> dimensions (300 - 500 Å). We would point out, however, that Polezhaev's model is not fully self consistent, for it fails to explain why the cubic state persisted as the crystallites grew to have dimensions of nearly one micron. Possibly this inconsistency can be

attributed, following El-Shanshoury et al. [162], as due to the fact that in ZrO_2 powder the surface energy is important in understanding the transformation process, whereas in thin evaporated (or sputtered) films the grain boundary energy should be considered.

In the author's opinion, however, the thermodynamic argument is not general enough. Thus if it was true that tetragonal ZrO_2 was stable at small particle sizes, thence that it was the main crystallization product of amorphous ZrO_2, then one would expect similar arguments to hold with anatase and γ-alumina. On the contrary, anatase at least can be obtained as macroscopic crystals.

A safer line of argument is probably a kinetic one, such that the crystal state of ZrO_2, as well as that of related substances such as TiO_2 and Al_2O_3, is correlated with the rate of formation. According to this assumption any process causing a rapid rate of formation would result in the appearance of an amorphous oxide, like that obtained in our work by sputtering, for in such cases the molecules have insufficient time to arrange themselves into the proper lattice structure. Under circumstances of less rapid formation, the molecules have more opportunity to arrange themselves and this favours, in the case of ZrO_2, the formation of the cubic structure with its simplified atomic arrangement. Finally because this configuration has a higher free energy than the monoclinic form, it tends to transform to this stable, but somewhat more complex structure once the proper kinetic conditions occur. As a matter of interest, the argument that amorphous and other untypical configurations are kinetically favoured at high rates of formation finds a

parallel in recent work [177-178] on reactively sputtered oxide films. These studies indicate that sputtering results in greater quenching rates than those obtained by splat quenching techniques (~ 10^5-10^7°C/sec). Moreover, the kinetic approach has been quantitatively presented by Serjeant and Roy [179], where a dimensionless expression is derived (named "the glass number") for the prediction of glass formation at any prescribed cooling rate. Unfortunately, however, the model implies knowledge of the viscosity of the melt, which is not known for most high-melting temperature oxides, including ZrO_2.

Agreement with previous work is less evident as far as the temperature for the beginning of crystallization, T_c, is concerned, for that observed here (520 ± 10°C in 5 min) is substantially higher than that found in earlier work [e.g. 157,159,162] (300-450°C). We have no definite explanation at present for this discrepancy, though we would point out that similar disagreement can be found with other oxides.* Thus as seen in Table 5.2, the values of T_c for amorphous oxides formed by chemical decomposition are consistently lower than those for amorphous oxides of other origins.

5.5.3 Comparison with other materials

Finally, a comparison between ZrO_2 and other materials having amorphous forms is perhaps in order. Such a comparison can be based on the ratio of the crystallization temperature to the temperature for atomic-scale cation self-diffusion. As shown by Jech and Kelly [75] this ratio lies between 0.68 and 0.87 for Al_2O_3, Cr_2O_3, α-Fe_2O_3,

---

* See ch.(7), sec.(7.61) for further examples of varying Tc values.

Table 5.2

Crystallization temperatures (T_c) for amorphous oxides

Oxide	T_c for chemically formed amorphousness* (^{0}C)	T_c for natural amorphousness** (^{0}C)	T_c for bombardment-induced amorphousness*** (^{0}C)
Al_2O_3	265 (2 min)	650-700 (60 min) ~670 (30 min)	600-700 (5 min) 730 (1 min)
Cr_2O_3	410 (2 min)	---	445 (1 min)
Fe_2O_3	335 (2 min)	---	535 (1 min)
TiO_2	305 (2 min) 300 (? min)	450-500 (60 min)	480 (1 min)
ZrO_2	405-450 (2 min) 300-400 (? min) 430 (2 min)	520-540 (5 min)	---

*References: [171] for second TiO_2 entry; [157,158,181] for ZrO_2; [182] for remaining entries.

**References: [170,183] for Al_2O_3; [184] for TiO_2; here for ZrO_2.

***References: [74] for first Al_2O_3 entry;[75] for remaining entries.

TiO_2 (rutile), NiO, Ge and Si. $T_{self\text{-}diffusion}$ for $Zr\text{-}ZrO_2$ can be calculated by substituting ΔH = 92,500 cal/mole and D_o = 0.035 cm^2/sec [180] into the following relation (Eq. (3.12) p.50), valid for 50% completion of a single jump-process:

$$\frac{\Delta H}{T} = 77.5 + 4.6 \log_{10} \left(\frac{t_{min} D_o}{0.3}\right) \qquad (5.3)$$

Here ΔH is in cal/mole, t_{min} is in min, and D_o is in cm^2/sec. The result for t_{min} = 5 min is 1210°K, from which we conclude that

$$\frac{T_{crystallization}}{T_{self\text{-}diffusion}} = 0.66$$

Amorphous ZrO_2 of the type obtained here is thus fully analogous, as far as its crystallization temperature is concerned, to the materials studied previously by Jech and Kelly [75].

CHAPTER 6

ION-IMPACT CRYSTALLIZATION OF AMORPHOUS ZrO_2 AND ITS IMPLICATION TO OTHER MATERIALS*

6.1 Introduction

Having discussed the crystallization of amorphous ZrO_2 by thermal heating, it was our next object to produce a similar effect by heavy-ion bombardment, as was suggested at the end of Ch. 4. Thus, it will be shown in the present chapter that bombardment of amorphous ZrO_2 with 2-35 KeV Kr leads to the appearance of crystallinity. It will also be confirmed out that crystallization occured both for low currents (1 $\mu A/cm^2$) and for high currents (> 10 $\mu A/cm^2$), and in addition occured both for free oxide films and for oxide still attached to the KCl substrate. In effect, the crystallization appeared to be due to causes other than ion-beam heating.

After first considering a number of possible mechanisms that could explain the ion-impact crystallization of amorphous ZrO_2, we will set up a model, which was in part anticipated by Parsons [104] (Cf. Sec. 4.6.3), based on the properties of thermal spikes. This model will be shown to account satisfactorily not only for the behaviour of amorphous ZrO_2 alone, but also for that of most oxides and non-metallic substances that undergo structural transformation on irradiation.

---

*This chapter is largely based on two publications by the author and Dr. R. Kelly [144,185].

6.2 The ion-bombardment techniques

All ion-bombardment experiments for the radiation damage studies and all the sputtering experiments for preparing the specimens, as described in sec. (5.3), were carried out with the ion accelerator system shown in Fig. (6.1). Brief description of the ion accelerator will be presented in this section whereas more details have been given elsewhere [118].

The ion accelerator was designed to produce heavy gas ions, such as O_2^+, Kr^+, Xe^+ and Ne^+ at energies up to 40 KeV and at currents varying from 1-100 μA. It has no mass separation though it permits suppression of secondary electrons. The lack of mass separation is to some extent compensated by the exclusive use of heavy ions, since impurities would all be of low mass, and would create less damage than one predicts from their abundance. Had light ions such as He been used, the damage due to impurities could have dominated and rendered the experiments meaningless [186]. A radio frequency type of ion source is used for the production of the gas ions. The radio frequency excitation voltage, which is applied externally to the source, originated with an 80 watt, 80 megacycle rf oscillator. The rf field within the coil of the oscillator causes electrons to move from wall to wall with the result that the gas in the ion source is partially ionized [187]. In addition, a magnetic coil provides an axial magnetic field of 600 gauss at the extraction canal. The magnetic field is used firstly to intensify the discharge, by converting linear electron paths into helical paths so that the electrons are used more efficiently; secondly, it pulls the plasma towards the

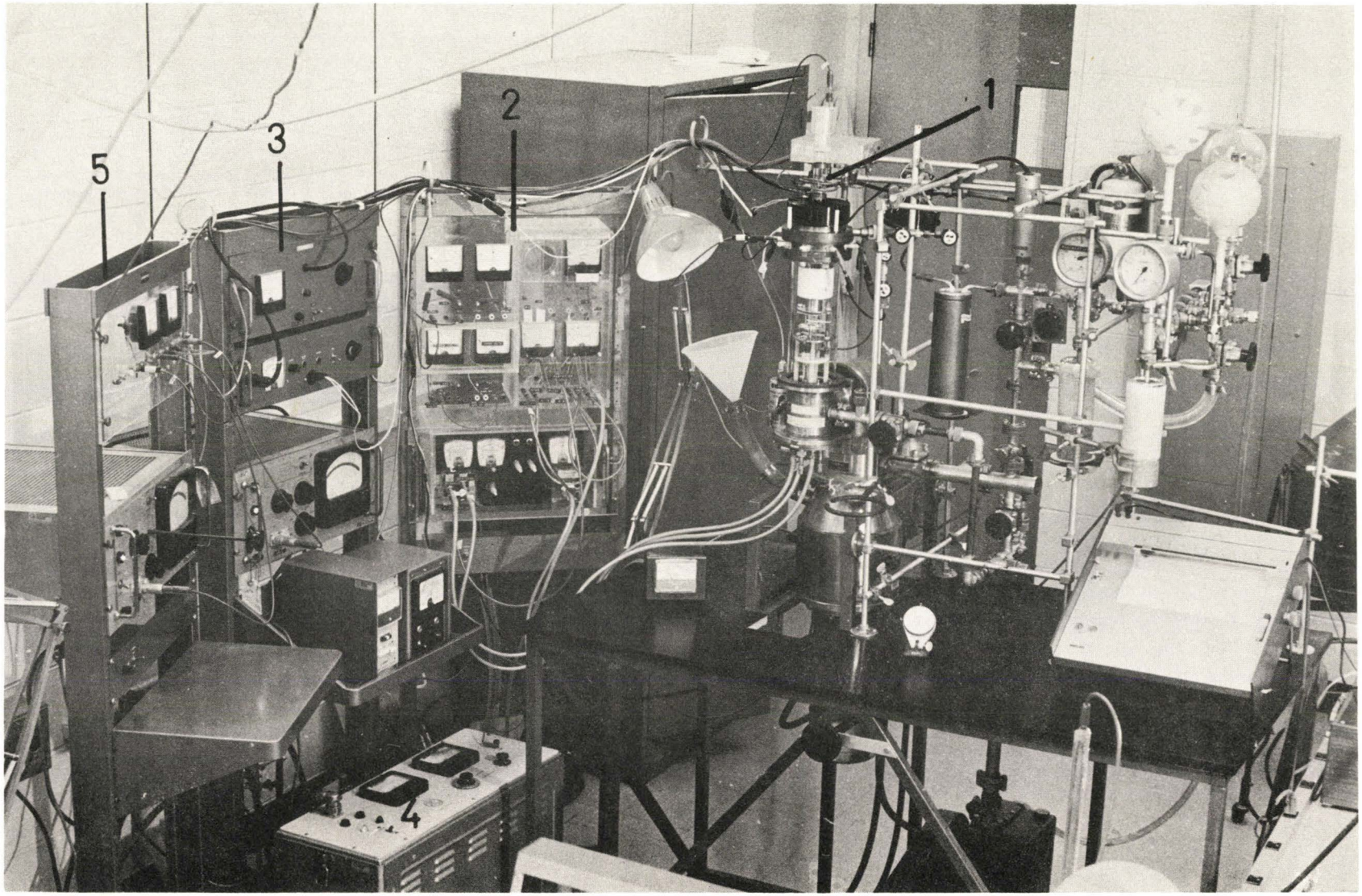

Fig. 6.1 The ion-accelerator system: 1, ion source; 2, current and voltage measuring devices; 3, ion source controls; 4, target high-tension power supply; 5, focussing controls.

extraction canal. Fig. (6.2) shows the combination of the oscillator and the magnetic coil around the ion source.

Below the ion source there is a series of focussing electrodes with 14 mm holes which are used to shape the ion beam. A variable positive focussing potential is supplied to the focussing electrodes in accordance with whether a small or large beam is desired. Though the exact arrangement of the focussing electrodes is somewhat arbitrary, one normally strives to have a sequence of potentials zero-positive-zero as proposed by Pierce [188].

A Faraday cup floating at -850 volts with respect to the target is used in order to prevent secondary electrons, which would give false current readings, from leaving the target. Each ion striking the target may produce several secondary electrons. If these electrons escape from the target the current readings will be higher because an electron leaving the target is electrically indistinguishable from a positive ion striking the target.

The target arrangement usually used for bombardment experiments is shown in Fig. (6.3). This arrangement can be modified to accommodate other experimental requirements, such as those explained in section (5.3) in connection with preparing thin films by sputtering. In addition, some experiments were carried out using a high-temperature target holder [118] which permits bombardments at temperatures as high as 600^{0}C. The use of non-conducting targets presented no problem, since charge build-up could be eliminated by using defocussed beams which produced secondary electrons from the metallic target support [65]. The target is connected to the negative terminal of a high tension power supply; the particular

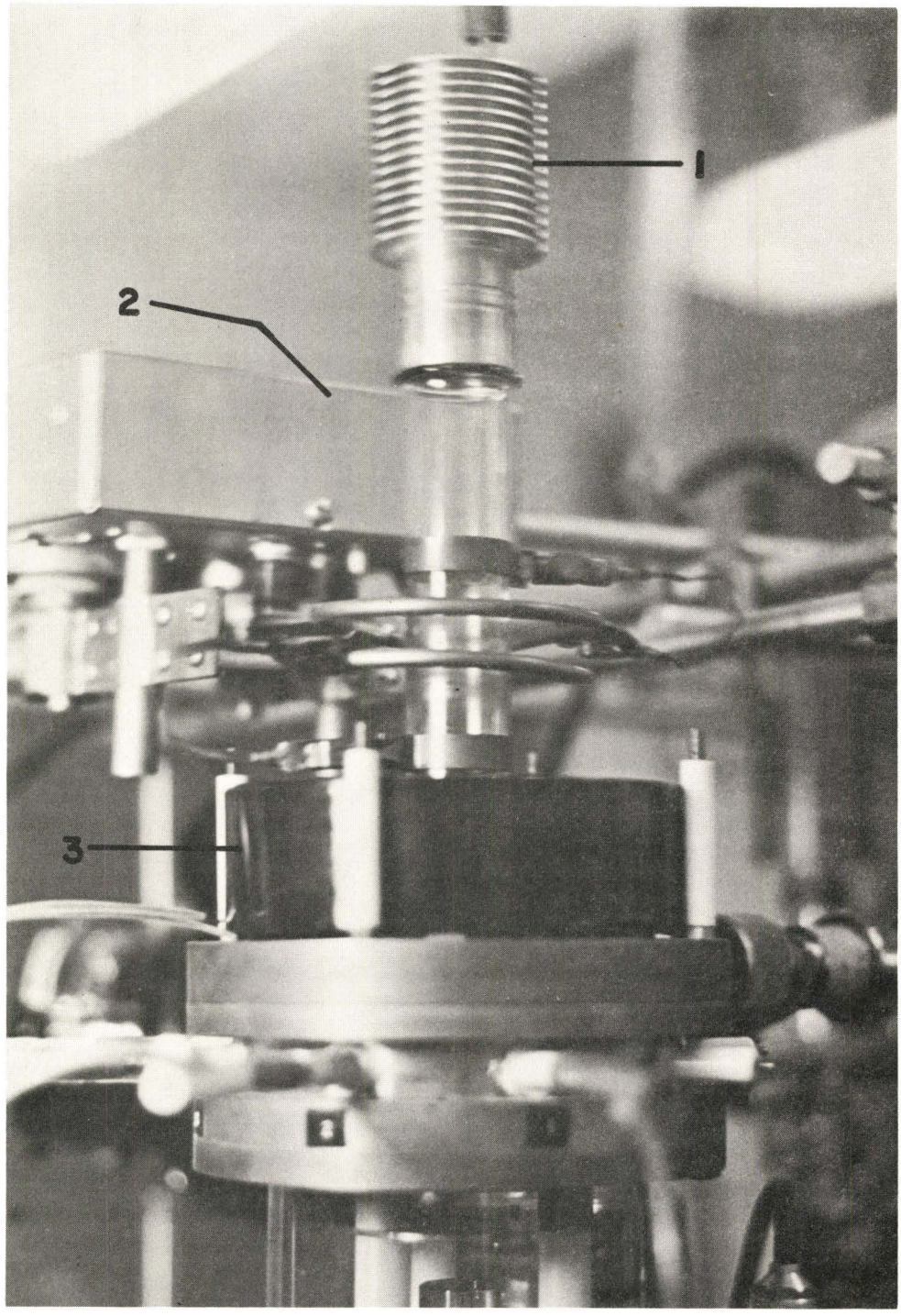

Fig. 6.2 The oscillator and magnetic coil: 1, the anode of the ion source; 2, rf oscillator; 3, magnetic coil.

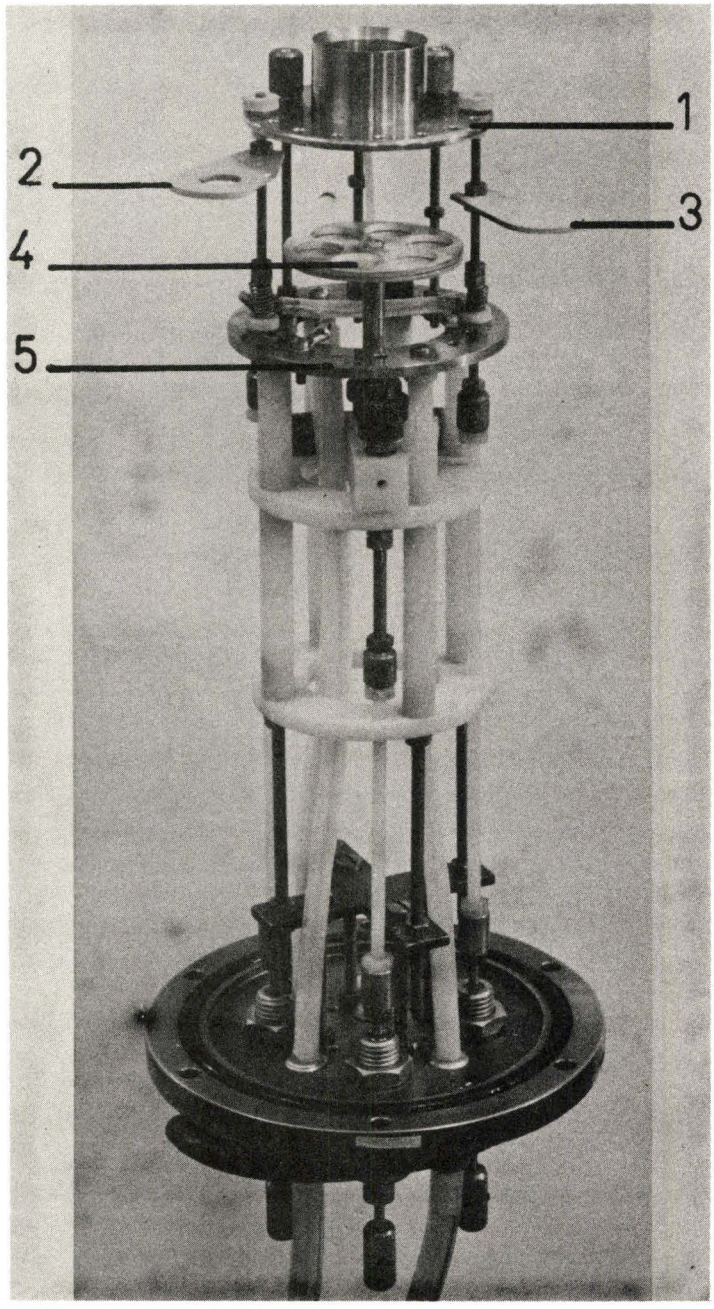

Fig. 6.3 The target holder: 1, upper part of Faraday cage; 2, shutter; 3, fluorescent screen; 4, vertically rotating target support with positions for six specimens; 5, lower part of Faraday cage.

model used, produced by SAMES (Grenoble), has an internal capacitance of <100 pF and also has a maximum current of 760 μA. It therefore presents a minimal health hazard.

An important component of the accelerator system is the vacuum pump. For this purpose, a 4" oil diffusion pump has been chosen, the alternative of ion pumping being eliminated since such pumps are unsatisfactory for inert gases. In order for the accelerator to operate properly, the pressure in the accelerating column should be below 1×10^{-5} torr, corresponding to a mean free path of ~750 cms. If the pressure is higher, the beam will not be properly focussed and will also be contaminated because of scattering from the gas molecules. In principle, one also encounters an x-ray problem. High-energy ions might strike the walls of the accelerating column, producing secondary electrons. These electrons might in turn be accelerated back toward the extraction canal, where they would strike and produce x-rays. A certain health hazard would thus arise.

6.3 Experimental and results

6.3.1 Effect of dose and dose rate on the crystallization process

A first series of bombardment experiments was carried out at a constant energy of 20 KeV, using Kr-ions, and with dose rates (i.e. currents) ranging from 1 to 20 $\mu A/cm^2$. The specimens were supported on 200-mesh copper or gold grids set in the small pockets of the target holder, and microscopic examinations were made after each bombardment. For a current of 5 $\mu A/cm^2$, the first observable crystallized

regions were seen at doses of ≈3 x 10^{15} ions/cm^2 in the form of small regions having diameters of 250-700 Å (Fig. (6.4a)). With increasing dose the crystallized regions increased in number and size until they began impinging (Fig. (6.4b)). The impingement finally went to completion at a dose of ≈9 x 10^{15} ions/cm^2, thus giving rise to complete crystallization with a crystallite size of 800-1000 Å (Fig. (6.4c)). Electron diffraction showed that the crystallites had a similar structure as in the other experiments, i.e. they were dominantly "cubic". The behaviour for other dose rates differed mainly in that, as seen in Fig. (6.5), the dose necessary for the onset of the crystallization was either higher (< 5 μA/cm^2) or lower (>5 μA/cm^2).

6.3.2 The effect of ion beam heating

The observation that the threshold crystallization dose depended on the current suggests that beam heating might have contributed to the bombardment-induced crystallization. Thus, according to the calculations given in appendix (C), if there is good contact between a 1000 Å thick ZrO_2 film (with thermal conductivity 0.01 cal/sec. cm. °C) and the grid, and also between the grid and the target holder, one would expect a ΔT of roughly 12°C due to a 5 μA/cm^2 current of 20 KeV ions. But if contact were incomplete ΔT could be much larger, perhaps enough to cause thermal crystallization. The following experiments have been undertaken, therefore, to demonstrate the effect of ion-beam heating.

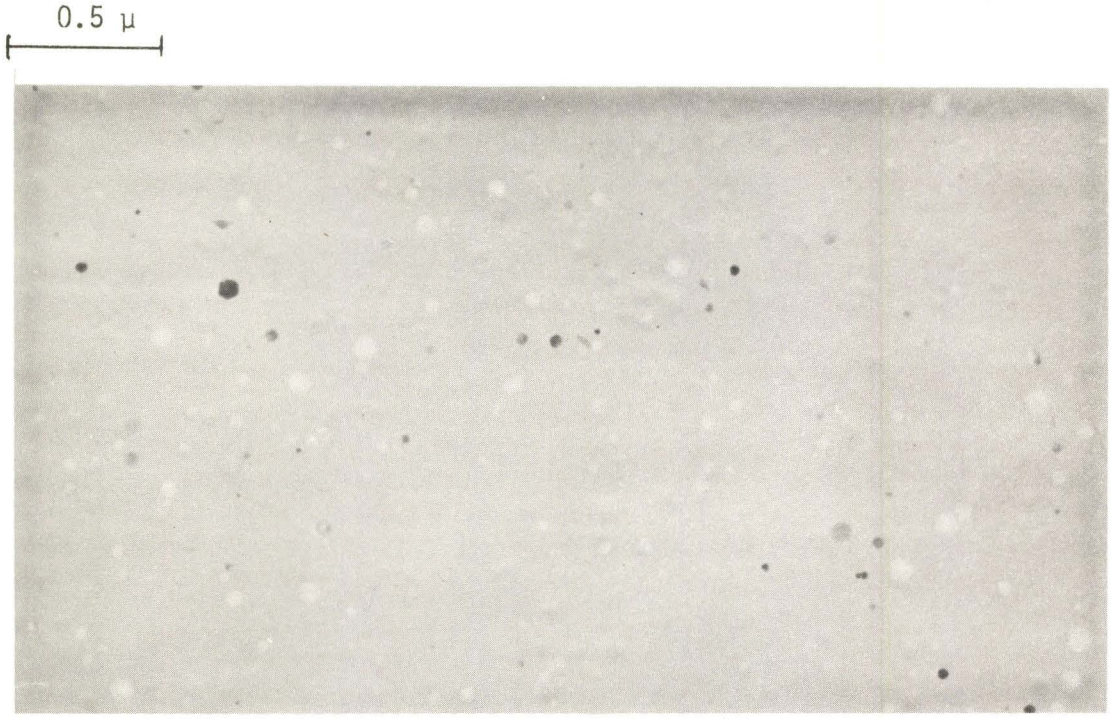

(a)

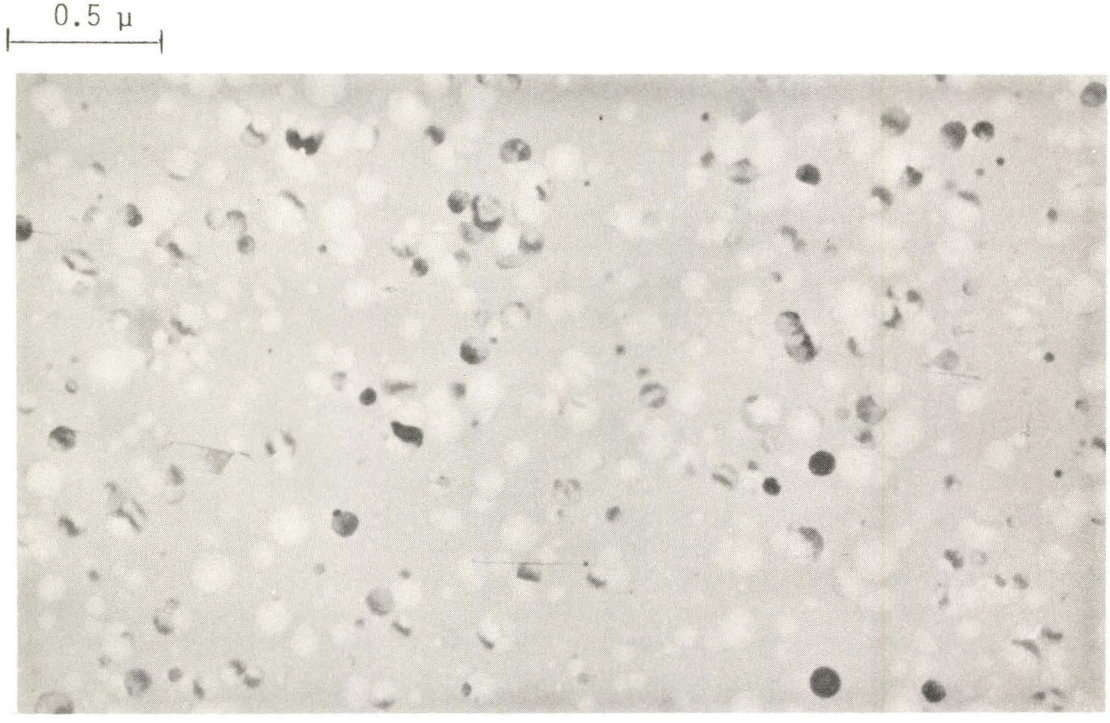

(b)

Fig. 6.4

0.5 μ

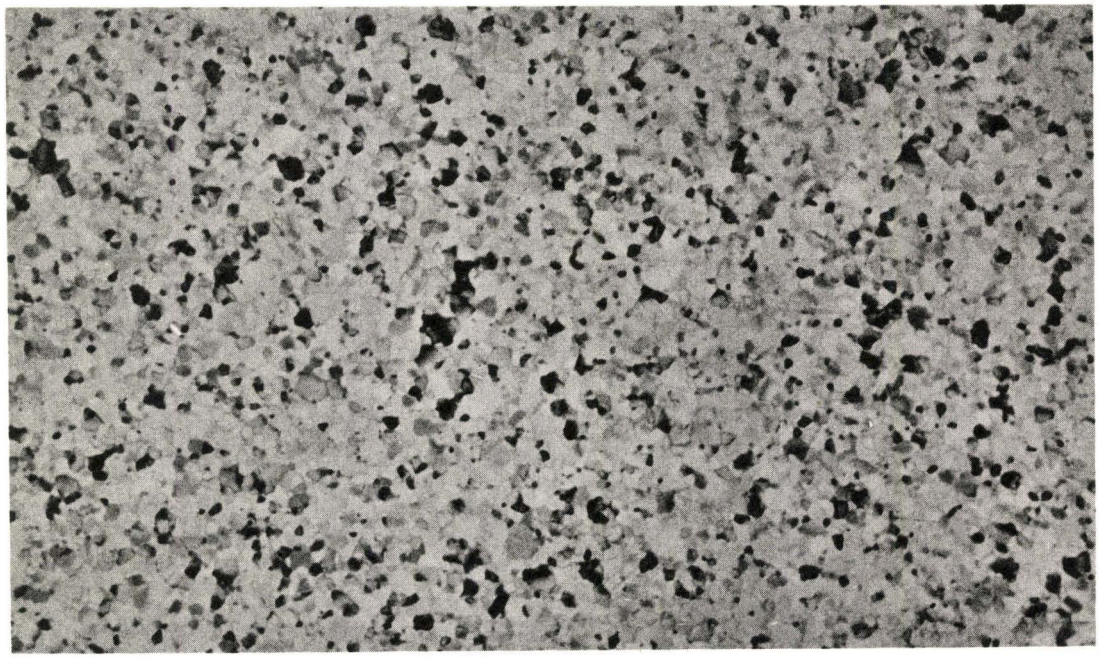

(c)

Fig. 6.4 (a) Crystallized regions produced by bombarding amorphous ZrO_2 with 3 x 10^{15} ions/cm^2 of 20 KeV Kr-ions at a current of 5 μA/cm^2. (b) As before but 6 x 10^{15} ions/cm^2. (c) As before but 9 x 10^{15} ions/cm^2.

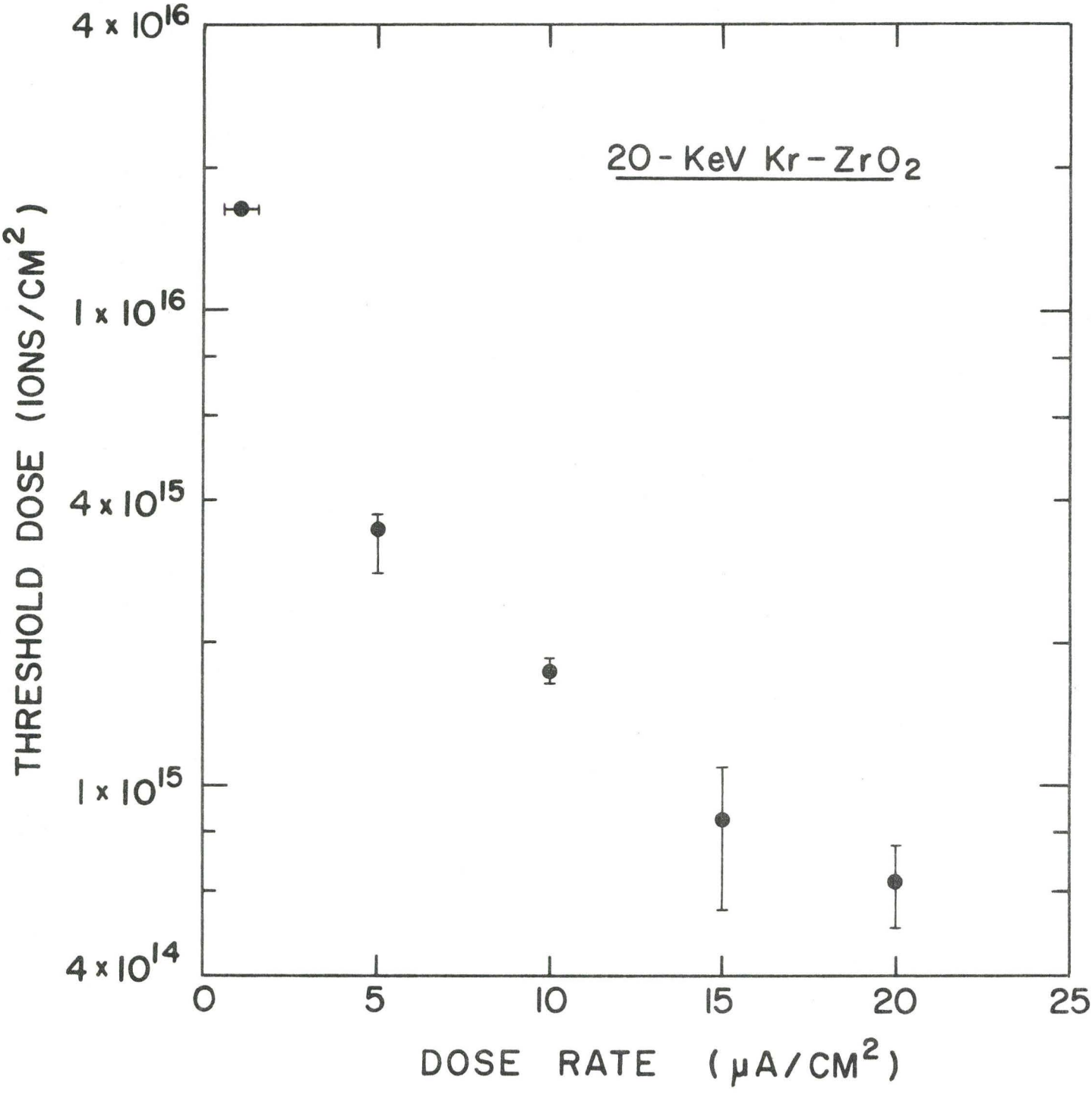

Fig. 6.5 Threshold dose for crystallization vs. dose rate (i.e. current) for bombardment of amorphous ZrO_2 with 20 KeV-Kr.

(a) Specimens supported by KCl. In an attempt to better define the effect of beam heating, bombardments were carried out in which the amorphous ZrO_2 was still attached to its ≈2 mm thick KCl substrate. The ΔT for 10 $\mu A/cm^2$ of 20-KeV ions is now predicted to be negligible, so it is particularly significant that similar results were obtained as in Fig. (6.4).

(b) Specimens shadowed by a grid. Another attempt to demonstrate what role, if any, is played by beam heating was made by bombarding amorphous ZrO_2 supported on a 200-mesh grid and at the same time with a 400 mesh grid lying loosely on top. If beam heating is important, both the covered and exposed parts should crystallize, whereas if bombardment induced crystallization is a dominantly impact effect, the shadow of the 400-mesh grid should be evident. It was found that, below 20 $\mu A/cm^2$, the covered parts were in fact void of crystalline regions (Fig. 6.6), suggesting that the temperature was lower than ≈550°C. For 20 $\mu A/cm^2$, on the other hand, the results indicated that beam heating sometimes assisted (Fig. 6.7). Films bombarded at 20 $\mu A/cm^2$ would thus appear to be subject to a temperature rise of roughly 525°C above ambient, hence those bombarded at, for example, 7 $\mu A/cm^2$ would have a temperature rise of only ≈160°C above ambient.

(c) Specimens heated during bombardment. A final attempt to illustrate the effect of heating was made by bombarding amorphous ZrO_2 films, supported on electron microscope grids, with 1 $\mu A/cm^2$ beam of 10 KeV-Kr while the target was held at 200°C. This was accomplished using the high-temperature target holder described in ref. [118]. No crystalline

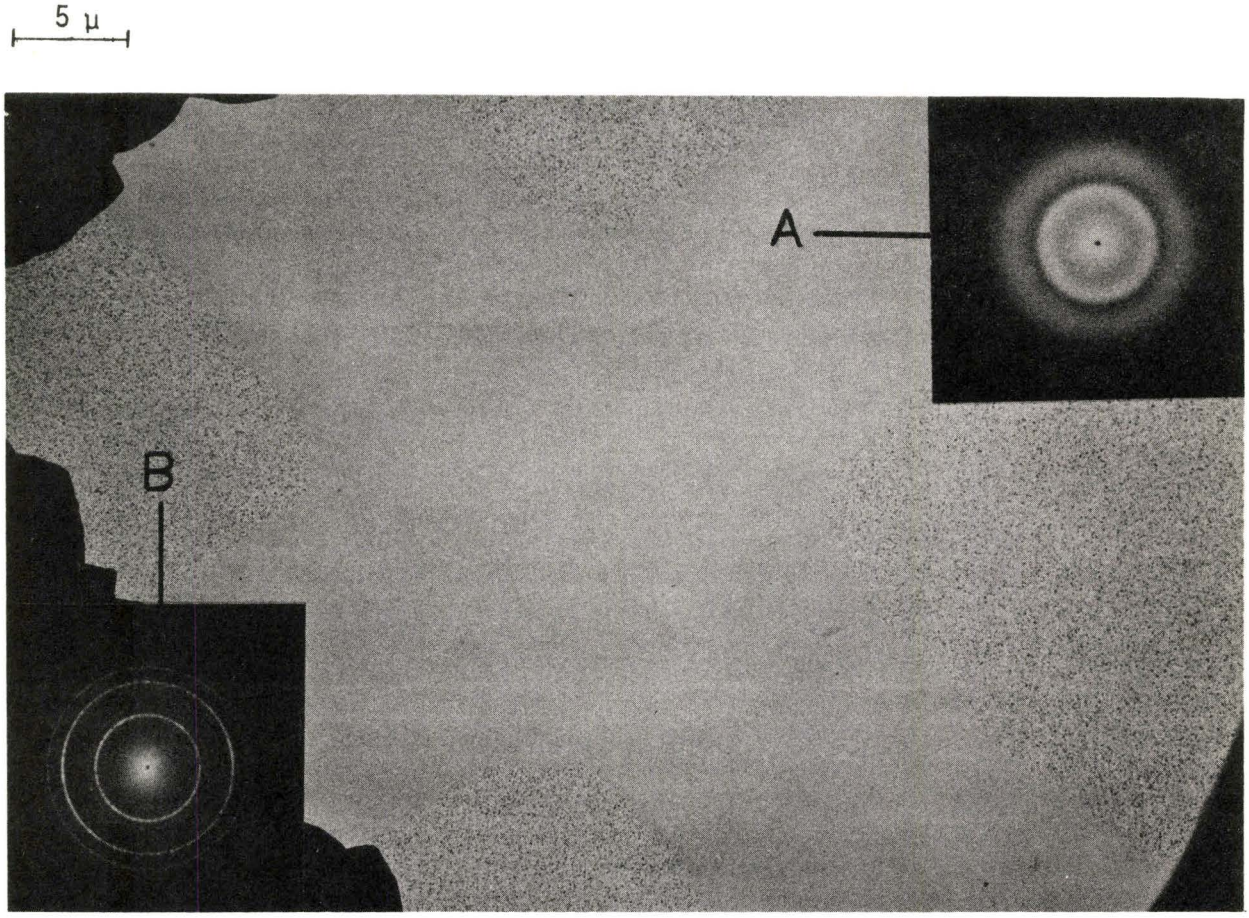

Fig. 6.6 Amorphous ZrO_2 supported on a 200-mesh grid and then bombarded with 9×10^{15} ions/cm^2 of 20 KeV-Kr through a 400-mesh grid. The current was 5 μA/cm^2. The shadowed region has remained amorphous, suggesting that ion-beam heating has not been significant for the particular current.

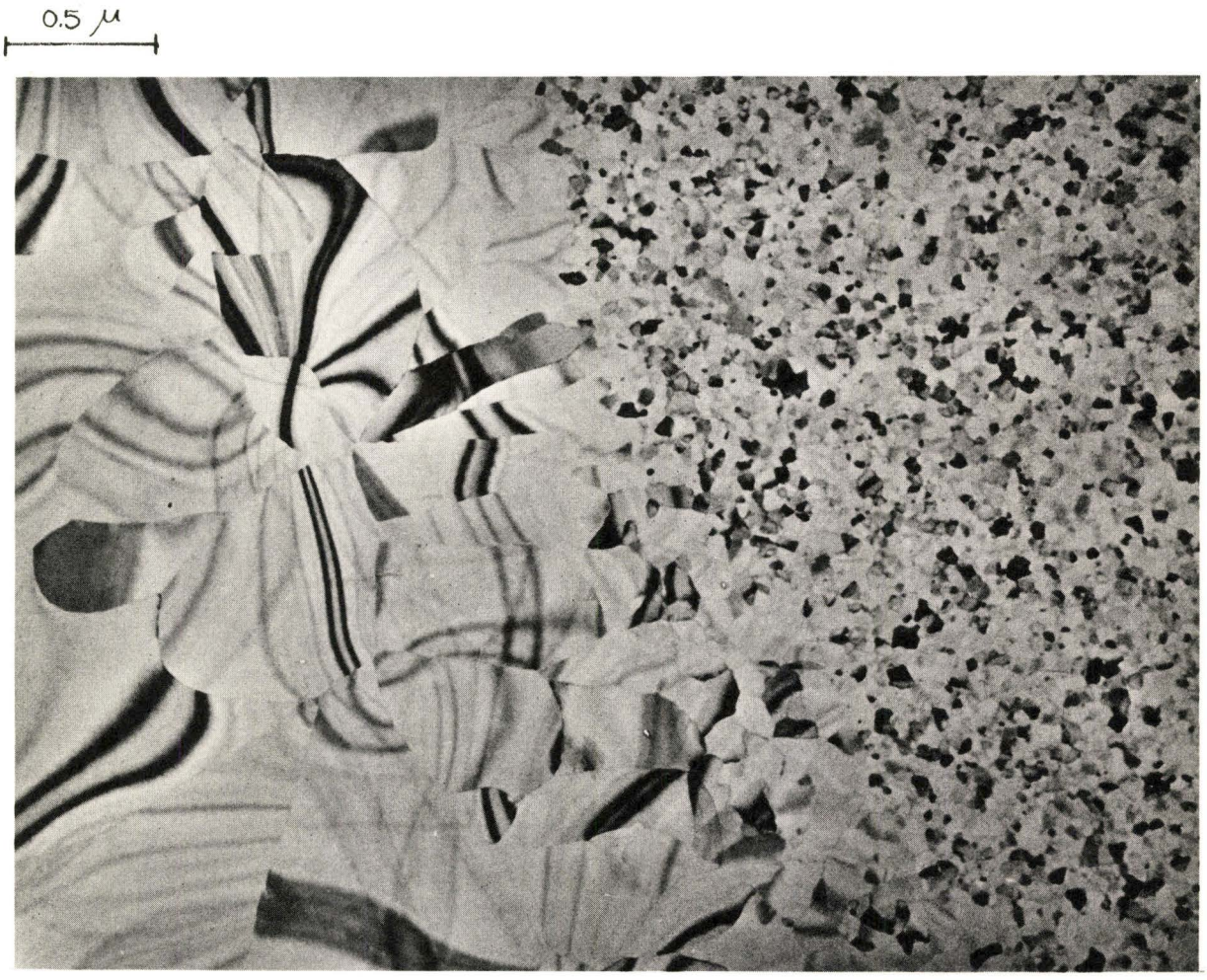

Fig. 6.7 Detailed view of interface between shadowed (left) and exposed (right) portions of an amorphous ZrO_2 film. The specimen was bombarded with 6×10^{14} ions/cm^2 of 20-KeV Kr at a current of 20 μA/cm^2. Note the occurrence of ordinary thermal crystallization, similar to Fig. (5.6), in the shadowed portion.

regions were observed for a dose of 1.9×10^{15} ions/cm^2, while crystalline regions appeared (as seen in Fig. 6.8) at dose of 5.6×10^{15} ions/cm^2. The results are in good agreement with those obtained with the same doses and a beam current of 5 μA/cm^2 but without heating the target holder (compare Fig. (6.4b) and Fig.(6.8)). We may remind the reader that crystallized regions appeared after 6 hr isothermal heating at 400^{0}C (Cf. Fig. 5.8) while a dose of 5.6×10^{15} ions/cm^2 is below the threshold dose, shown in Fig. 6.5, for a dose rate (i.e. current) of 1 μA/cm^2. One concludes, therefore, that the effect of heating during bombardment (either by ion-beam heating or deliberate heating of the target) is to assist the crystallization. The assistance could be either in nucleation plus growth together or in growth alone.

6.3.3 Annealing of bombarded specimens

These experiments were carried out to elucidate the problem posed in the preceding section, namely that thermal heating plays a role but the precise role is unclear. Let us suppose that small crystallized regions, unresolved by the electron microscope, exist in specimens bombarded with doses lower than the threshold doses shown in Fig. (6.5). Accordingly, specimens whether supported on grids (hence moderately low ΔT) or on their substrates (hence small ΔT) were bombarded to 4.5×10^{15} ions/cm^2 using 20 KeV Kr-ions and an ion beam current of 1 μA/cm^2. After bombardment, the specimens were heated at 75^{0}C for 5 mins and then examined with the Philips electron microscope (operated at 100 KeV). As seen in Fig. (6.9a) crystalline regions appeared with diameters ranging

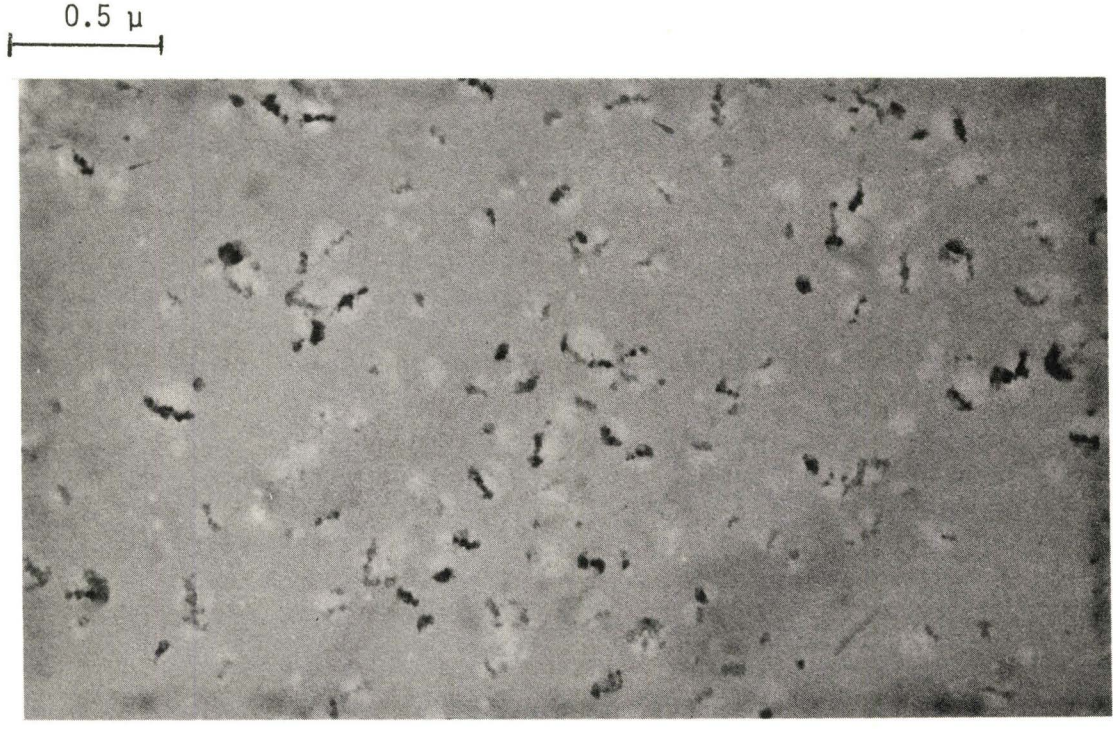

Fig. 6.8 Crystallized regions produced by bombarding amorphous ZrO_2 with 5.6×10^{15} ions/cm^2 of 10 KeV Kr-ions at a current of 1 μA/cm^2 while the target temperature was at 200^{0}C. (Compare with Fig. (6.4b).)

between 100 - 400 Å, thus less than those observed with other experiments. The corresponding dark field images of Fig. (6.9 a) are shown in Figs. (6.9b) to (6.9e). It was found that after taking eight dark field images in the same region, the crystalline regions slightly increased in size due to electron-beam heating (Fig. 6.9f).

In conclusion, the experimental evidence supports the view that amorphous ZrO_2 can be rendered crystalline by ion bombardment. This phenomenon is basically an impact effect as far as nucleation is concerned and any heating during or after bombardment serves mainly to assist the growth of the bombardment-induced crystalline regions.

6.3.4 Crystal size as a function of ion energy

A final series of experiments was performed to determine the size of the crystallized regions as a function of ion energy for a constant dose of 1×10^{16} ions/cm^2 and a constant current of 15 μA/cm^2. After each bombardment an area containing crystallized regions was photographed in bright and dark field, and estimates of the most probable size of the crystallized regions were obtained as summarized in Fig. (6.10). There was no evidence for a minimum cut off energy for the transformation as was observed with Ge [132]. More important to the present work, however, was the observation that the crystal size was only a slowly varying function of the ion energy. This is a further indication that ion impact plays a basic role in the crystallization, for had thermal effects dominated the crystal size should have been an exponential function of

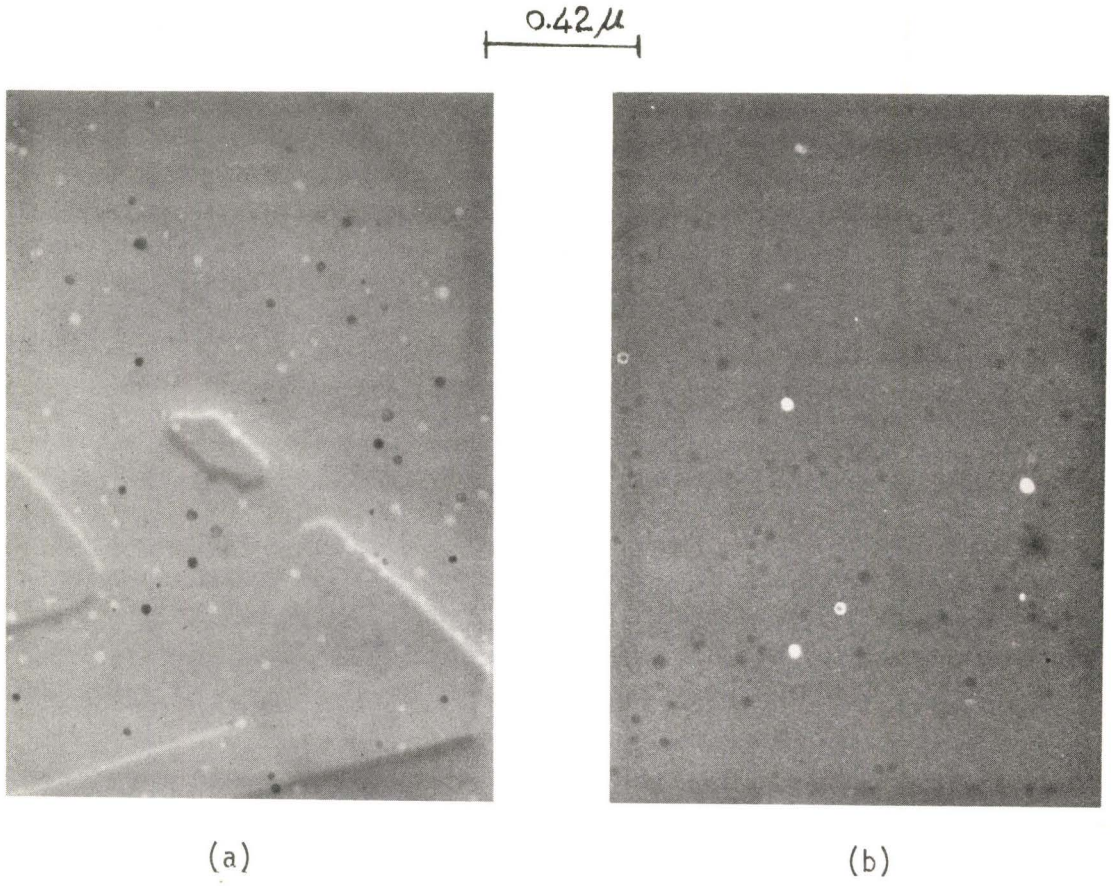
0.42 μ
(a)
(b)
(c)
(d)

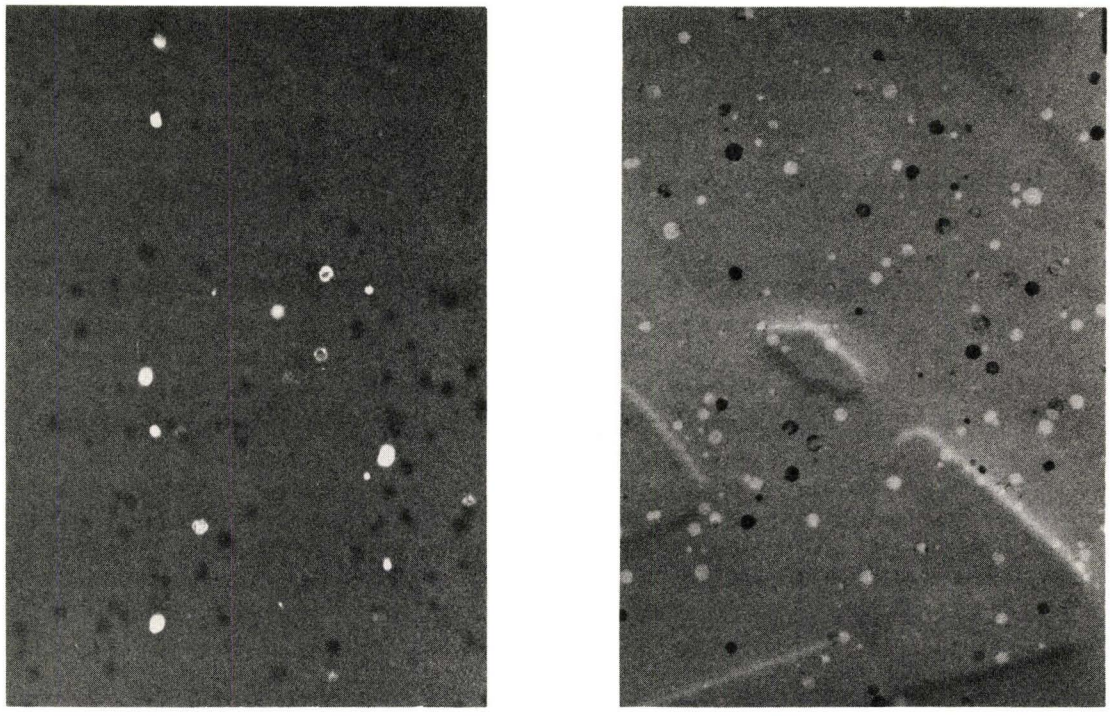

(e)

(f)

Fig. 6.9 Crystallized regions produced by bombarding amorphous ZrO_2 with 4.5×10^{15} ions/cm^2 of 20-KeV Kr-ions at a current of 1 μA / cm^2 and then heating in air at 75°C for 5 mins. (a) Bright-field image; (b) to (e) dark-field images for the same area as image (a); and (f) another bright-field image in the same area after taking 8 dark-field images. Note the slight increase in the crystallite size between Figs. (a) and (f) due to electron-beam heating.

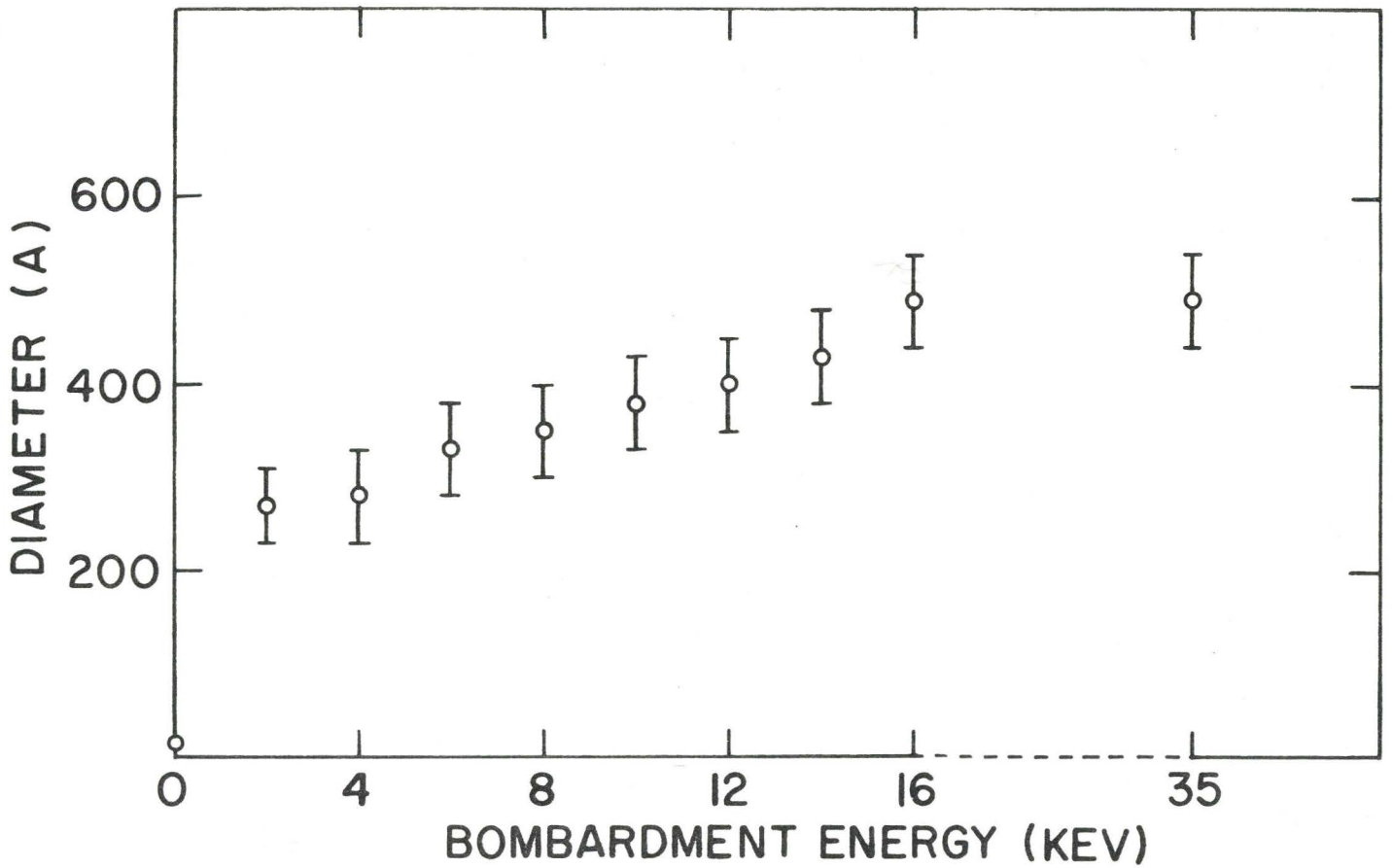

Fig. 6.10 Diameter of crystallized regions versus bombardment energy for bombardment-induced crystallization of amorphous ZrO_2. The dose was constant at 1×10^{16} Kr-ions/cm^2, the current being 15 μA/cm^2. The increase of the crystallite size with bombardment energy is expected to be exponential if thermal effects dominate.

the ion energy. This follows from Eq. (5.2):

$$\left(\frac{D_c^0 t}{\lambda}\right) \exp\left(\frac{-\Delta H_c}{RT}\right) \approx \text{crystal size}$$

when T would be given, for any thermal effects associated with ion impact, by

$$T = T_{ambient} + (\text{constant})\ (\text{energy})$$

6.4 Discussion

6.4.1 The bombardment-induced crystallization of amorphous ZrO_2

It has been shown that amorphous ZrO_2 transforms to a crystalline state due to ion impact, a phenomenon which has to our knowledge been previously described only for Ge [132,134] and SiO_2 [130], as described in sec. (4.4). This result can in principle be explained either by displacement cascades, thermal spikes, or radiation-enhanced diffusion, and we will first show that, by considering the behaviour of ZrO_2 in isolation from that of other substances, it is difficult to choose between these mechanisms.

As we have discussed in sec. (4.6.2), the displacement cascade mechanism presupposes that the displaced atoms created by an incident ion tend to rearrange themselves into a new structure without the occurrence of activated jumps. To estimate whether this mechanism could play a role in the crystallization of amorphous ZrO_2, we would simply state that a 500 Å diameter crystallized region formed by bombardment with 3×10^{15} ions/cm^2 of 20 KeV-Kr will contain roughly 2×10^7

displacements. Since such crystallized regions contain a comparable number of atoms roughly 6×10^6, one concludes that displacement effects occur on a sufficient scale to make them relevant to this work. We would, nevertheless, question this model. Our results show that the bombardment-induced crystallization of amorphous ZrO_2 is dose rate dependent, suggesting that ion-beam heating, while not the sole cause of the crystallization, at least assists.

According to the thermal-spike model, which was concluded to be the least objectionable with respect to other models discussed in sec. (4.6), one presupposes that the high local temperature near an ion impact induces the necessary activated jumps, essentially as in ordinary heating experiments. A rough estimate of its effectiveness in crystallizing amorphous ZrO_2 can be made as follows. To a first approximation, crystallization will be significant if the distance moved by the amorphous-crystalline interface, $D_c t/\lambda$ [75], is significantly greater than λ, where D_c is the diffusion coefficient relevant to the crystallization of the amorphous phase and λ is the mean atomic spacing (~2.5 Å), i.e. if

$$\frac{D_c t}{\lambda} = \left(\frac{D_c^0 t}{\lambda}\right) \exp\left(\frac{-\Delta H_c}{RT}\right) \gg \lambda \qquad (6.1)$$

The different terms of Eq. (6.1) will be discussed in the next section and for present purposes it is sufficient to note that D_c^0 can be taken as $3 \times 10^{-1 \pm 1}$; t, the duration of thermal spike, can be taken as 7×10^{-12} sec; ΔH_c, the activation enthalpy of the crystallization, can be taken as 54 ± 3 Kcal/mole, as determined in sec. (5.5.2); and T can be taken as the melting point of ZrO_2. Substituting into relation (6.1) we

conclude that $D_c t/\lambda$ is only 1 Å, and thus less than λ (with an average value of 2.5 Å). This at the first sight suggests that thermal spikes may play no role. The predicted value of $D_c t/\lambda$ is, however, so close to what is required that the uncertainities in D_c^0, t, and ΔH_c render a firm decision unjustified.

Finally, there are the mechanisms based on radiation-enhanced diffusion. Diffusion enhanced by excess point defects is commonly invoked to explain order-disorder changes in irradiated alloys [189] and was more recently proposed to explain the formation of second-phase precipitates in ion-implanted aluminum [190]. That the mechanism is geometrically possible in the present context follows for the same reason that was given in connection with the displacement-cascade mechanism. Thus, the number of displacements to which a typical crystallized region is subject, is similar to the number of atoms; therefore, even if the point defects survived for only a few atomic jumps they would significantly rearrange the structure. Likewise, that the mechanism is kinetically possible can also be shown. The ΔH for point-defect motion in amorphous ZrO_2 is not known, and, in fact, it is not clear that the concept of a point defect has any relevance to amorphous solids in view of the large amount of free volume [191]. It is sufficient, however, to consider point defects (vacancies) in cubic ZrO_2, for which ΔH is 31.2 kcal/mole and D_0 is 0.018 cm^2/sec [192], and assume that crystal growth occurs only due to impacts in pre-existing crystallites; any role of point-defect motion in the amorphous ZrO_2 would be additional to the assumed effect (Fig. 6.11). Then there are two alternatives depending on the assumed

source of heat:

(a) For thermal-spike heating and with t taken as 1.2×10^{-11} sec (Cf. sec. 6.4.2), corresponding to the lower ΔH, relation (6.1) gives $D_c t/\lambda$ equal to 4 Å.

(b) For ion-beam heating equivalent to that of a 7 $\mu A/cm^2$ beam, thence a temperature rise of roughly 160°C above ambient (cf. sec. 6.3), and with t taken as 60 sec, relation (6.1) gives $D_c t/\lambda$ equal to 17 Å. In either case $D_c t/\lambda$ is just sufficient to bring about crystallization.

In conclusion, considering the behaviour of ZrO_2 alone, a final decision as to the mechanism leading to bombardment-induced crystallization is not possible. Displacement cascades, thermal spikes, as well as radiation-enhanced diffusion (with either thermal-spike or ion-beam heating) can be each easily rationalized.

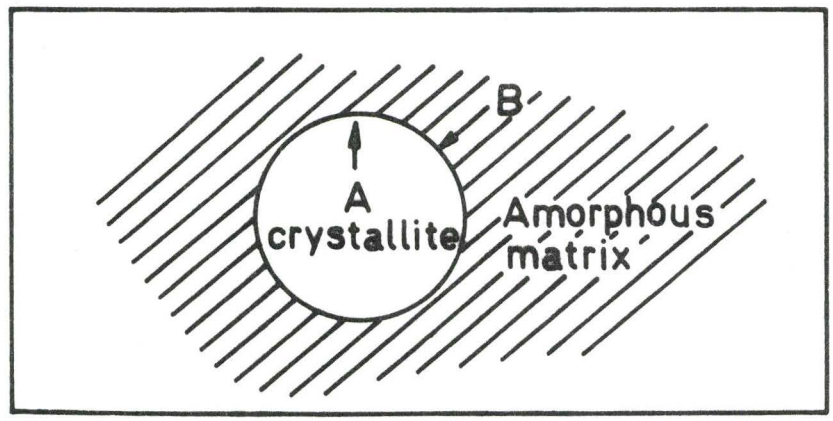

Fig. 6.11 Radiation-enhanced diffusion can lead to crystal growth both by motion within the crystallite (jumps of type A) and motion in the amorphous matrix (jumps of type B). Only type A jumps can be assessed quantitatively.

6.4.2 A self-consistent model for bombardment-induced structural changes

It is clear that the bombardment-induced crystallization of amorphous ZrO_2 can in principle be accounted for whether one assumes thermal or displacement effects to be the more important. We would propose that this ambiguity can be removed by considering the behaviour of a variety of solids on heavy ion impact, rather than amorphous ZrO_2 alone. In particular, one group of materials includes those which, as described in Ch. 4, either retain their crystallinity to quite high doses (e.g. BeO, Cr_2O_3, MgO, NiO, ThO_2, UO_2 and ZrO_2) or else are converted from an amorphous to crystalline state (namely ZrO_2). Here there is not much to be gained, since both thermal and displacement effects could as usual be invoked. A second group of materials, however, includes those which, when bombarded in a crystalline state, are amorphized (Cf. sec. 4.2) (e.g. Al_2O_3, GaAs, Ge, Si, SiO_2 and $ZrSiO_4$). This is a basically different type of behaviour, though is readily explained if thermal and displacement effects are assumed to play opposing roles.

Thus, suppose that the impact of heavy ions on both crystalline and amorphous substances leads in general to an initial disordering (or retention of disorder, as the case may be) due either to lattice strains, to displacement cascades, to the quenching in of small liquid-like regions, or to any other reason. The disordering would presumably take the form of small, approximately spherical, amorphous regions such as those found with Ge, Si and possibly GaAs [e.g. 104,106,114]. Suppose further that the disorder immediately tends to anneal once the high local temperature in the impact site falls below the melting point. Then, to a first approximation, the disorder will be eliminated only if the following

is true:

$$\frac{D_c t}{\lambda} = \left(\frac{D_c^0 t}{\lambda}\right) \exp\left(\frac{-\Delta H_c}{RT}\right) > \lambda \ . \qquad (6.1)$$

We will now consider each term in turn.*

(a) $D_c^0 \cdot D_c^0$ will be assigned an idealized range of values, $3 \times 10^{-1\pm1}$ cm^2/sec, as in previous work [75]. A possible justification of this for the particular case of disorder annealing lies in the fact that a fairly satisfactory Arrhenius relation can be constructed for Al_2O_3 using $D_c^0 = 0.3$, a D inferred from the observed crystallization temperature, plus a third D inferred, as suggested by Secrist and Mackenzie [147], from the viscosity of the liquid at the melting temperature. The relevant relation here is [147A]

$$D = \frac{RT}{6\lambda N_0 \eta} \ ,$$

where λ is the atomic spacing, N_0 is Avogadro's number, and η is the viscosity. η has the value 4.6 poises for Al_2O_3 at its melting temperature [147B], whence

$$D_{melting} = 3.4 \times 10^{-7} \ cm^2/sec \ .$$

(b) t. The time, t, can be estimated by evaluating $\int D_c dt$ for a $t^{-3/2}$ cooling law [8] and thence deducing an effective time, t_{eff}. Thus we have

$$\int_{t_1}^{t_2} D_c dt = D_c^0 \int_{t_1}^{t_2} \exp\left(\frac{-\Delta H_c}{R(T_\infty + At^{-3/2})}\right) dt,$$

*The origin of Eq. (6.1) is as follows. Turnbull and Cohen [83] argue that the velocity of growth of a planar-interface is: $v = (D/\lambda)(1-\exp(-\Delta G/RT))$. Assuming a high degree of undercooling this equation reduces to $v = D/\lambda$. The correction due to the large interfacial free-energy of the crystalline regions is introduced later (p. 146), and only qualitatively. However, possible size effects involving the probability of nucleation are at no time considered.

where t_1 is the time when T is equal to T_m, the melting temperature, t_2 is a subsequent time when T is slightly higher than T_∞, the macroscopic target temperature, and A is given by

$$A = 2(E/c\rho\kappa^{3/2})\ (8.59 \times 10^{-19})$$

Here E is the ion energy in keV, c is the heat capacity in cal/^{0}C-g, ρ is the density in g/cm^2, κ is the thermal diffusivity in cm^2/sec, and the initial factor of two assumes that the spike is near the surface. By substituting

$$T_\infty + At^{-3/2} = u^{-1};\quad T_\infty + At_1^{-3/2} = T_m;\quad T_\infty + At_2^{-3/2} \simeq 2T_\infty$$

and integrating by parts, one can generate an asymptotic series for $\int D_c dt$. The leading and by far the most important term of the series is, as can be readily checked by differentiation with respect to T_m,

$$\int D_c dt = (2D_c^0 RA^{2/3} T_m^{1/3}/3\Delta H_c)(1-T_\infty/T_m)^{-5/3}\exp(-\Delta H_c/RT_m) \qquad (6.2)$$

$$\equiv D_c^0\ t_{eff}\ \exp(-\Delta H_c/RT_m)$$

Further evaluation depends strongly on what is assumed for κ. In particular, for an ion energy of 20 keV, for A, T_m, and ΔH_c (54 kcal/mole, sec. 5.5.2) as for ZrO_2, and for κ = 0.001 cm^2/sec [8], one obtains $t_{eff} = 7 \times 10^{-12}$ sec. (Eq. (6.2) differs from Eq. (22.6) of Seitz and Koehler [8] mainly because the latter authors took t_1 as zero and t_2 as infinity. We note in this connection that taking t_2 as infinity is not acceptable for the model given here since it leads to an infinite value for t_{eff}.)

(c) $\Delta H_c \cdot \Delta H_c$, the activation enthalpy for crystallization of the disordered phase, can be estimated either from gas-release data [75] or from thermal-heating experiments such as those of sec. (5.4.2) or of Fleischer et al. [193]. Thus, the crystallization of a disordered phase should be complete when the distance moved by the disorder-crystal interface as given by Eq. (6.1) is comparable to x_c, the distance scale of the crystallization process. Hence, for $x_c \approx 200$ Å as for the bombardments of Fig. 6.10 an idealized D_0 of $3 \times 10^{-1\pm1}$ cm^2/sec, and t equal to 3 min one obtains

$$\Delta H_c \approx (69 \pm 5)\ T_c\ , \qquad (6.3a)$$

where T_c is the observed crystallization temperature.

(d) T. Finally, for T in Eq. (6.1) we substitute the melting point T_m since this is the temperature which appears in Eq. (6.2) This result is qualitatively reasonable, since T_m is the highest temperature at which crystallization <u>can</u> occur and therefore the temperature near which most <u>will</u> occur as a thermal spike cools.

Altogether then, the condition for bombardment-induced disorder being eliminated subsequent to an ion impact, namely Eq. (6.1), can be rewritten as

$$T_c/T_m < 0.23 \pm 0.07\ .$$

It is seen in table (6.1) that, for some 20 different substances, there are two distinct categories. The one, for which T_c/T_m lies below 0.27, contains those substances which either retain their crystallinity when bombarded to moderate doses or else (as with amorphous ZrO_2) undergo

Table (6.1)

The ratio (crystallization temperature)/(melting temperature)

Substance	T_c (^0C)	Time scale corresponding to T_c (min)	T_c/T_m ($^0K/^0K$)
(a) Substances showing good radiation stability			
ThO_2	400-450[199]	3	0.19-0.20
UO_2	(like ThO_2?)	...	≈0.22-0.23
MgO	325[75]	1	<0.20*
CaO	≈350[200]	5	≈0.22
NiO	285[75]	1	0.25
SnO_2	225[69]	6	0.19-0.27†
Cr_2O_3	445[75]	1	0.27
ZrO_2	530**	5	0.27
(b) Substances which readily amorphize			
TiO_2	480[75]	1	0.35
$ZrSiO_4$	760[113]	1	0.38
Fe_2O_3	535[75]	1	<0.43*
WO_3	475[46]	1	0.43
Al_2O_3	730[75]	1	0.43
GaP	≈500[201]	10	≈0.44
Ta_2O_5	740[60]	1	0.47
Nb_2O_5	585[60]	1	0.49
SiC	1200[204]	2	0.49
GaAs	≈500[201]	10	0.51
SiO_2	675[58]	5	0.55-0.57†*
Si	720[75]	1	0.59
Ge	470[75]	1	0.61

*Upper limit since T_m is known only as a lower limit.

**Present work (Cf. Ch.5)

†Calculated using the value 1597-2327^{0}C for T_m [69]

†*Calculated using the value 1400-1450^{0}C for T_m [202]

bombardment-induced crystallization. The other, for which T_c/T_m lies above 0.35, includes substances which are readily amorphized by ion impact. This includes Ge and SiO_2, for, as argued in sec. (4.4), the evidence for bombardment-induced crystallization with these substances concerns partial crystallization and the dominant effect of ion impact is to create disorder.

Diamond and U_3O_8 have been excluded from consideration in table (6.1) and may possibly be exceptions. Unfortunately, with neither is it obvious what to take as T_m, while with U_3O_8 estimates of T_c range from 200 to 800°C [74,194].

6.4.3 Comments on the model

Quantitatively, the picture presented above is not quite as straightforward as has been implied in that the value of T_c/T_m which is predicted to be the upper limit for annealing being significant (0.23 ± 0.07) is somewhat lower than that observed. One way around this difficulty is to modify the mechanism to take excess vacancies into account. Thus, the crystallization of disordered regions could in principle be aided by collisionally formed excess vacancies, and might therefore be governed by a lower ΔH than that inferred from gas-release or thermal-heating experiments. In support of excess vacancies playing a role, Mazey et al. [106] and Reid [118] have found that a plot of log (threshold dose) versus 1/T for inert-gas bombardment of Si has a slope of 0.3 eV and thus a similar value to that for vacancy motion in Si. This result may, however, be quite fortuitous and there is unfortunately little other evidence relevant to excess vacancies.

A further possibility is that, since disordered regions are very small (≤ 70 Å in diameter [104,106]), there may be a large interfacial free-energy contribution to their crystallization parameters:

$$\Delta H_c(\text{small radius}) = \Delta H_c\ (\text{macroscopic}) - 2\sigma V/r,$$

where σ is the relevant interfacial free energy and V is the molar volume. Though it is not obvious how to estimate this correction from first principles, a possible alternative is to make use of the fact that with Ge and Si isolated disordered regions anneal at about 200°C below the macroscopic T_c. This implies that $2\sigma V/r$ has a value such that Eq. (6.3a) should be replaced by

$$\Delta H_c \approx (69 \pm 5)\ (T_c - 200)\ . \qquad (6.3b)$$

The result would be to better justify the observed values of T_c/T_m.

6.4.4 Predictions

By way of concluding this chapter, we would like to discuss a number of substances for which predictions can be made. These include cases where either T_c is unknown or else where the ion-impact behaviour is unknown.

The following substances, which are all stable to ion impact [135], are predicted to have values for T_c as shown in brackets: CaF_2(<220°C), LiF (<50°C), NaCl (<40°C), UC (<420°C). The following substances, which have apparently not yet been studied by ion bombardment, have known values of T_c as shown in brackets and are predicted on this basis to retain their

crystallinity to either high or (with MgF_2) moderately high doses: BeO (300°C in 30 min [157]), Co-Au (160°C in 18 min [196]), Cu-Ag (100°C in 18 min [196]), MgF_2 (300°C in 30 min [197]), and ZnO (75-100°C in 2 min [198]). On the other hand, the following substances, which have again not been studied by ion bombardment, have known values of T_c as shown in the brackets and are predicted to <u>amorphize</u> at low doses: TeO_2 (400°C in 180 min [177]), MoO_3 (~400°C in 5 min [105]), V_2O_5 (~400°C in 5 min [203]), Bi_2O_3 (250°C in 60 min [177]), and olivine (570°C in 1 min [193]). It will be our attempt in the next chapter (Ch. 7) to verify some of these predictions.

Finally, it is worth pointing out that, on the basis of the present arguments, one would expect that bombardment of amorphous films of any of the materials which show good radiation stability (previously summarized in table (4.1)) would lead to crystallization. Conversely, amorphous films of materials that readily amorphized under ion impact (also previously summarized in table (4.2)) should resist impact-induced changes except possibly: (a) for minor extents of crystallization such as were found with Ge [132,134] and SiO_2 [130]; (b) for the appearance of metastable phases either due to the high temperature of the bombardment, or to a change in chemical composition (e.g. oxides losing oxygen) during bombardment. It will be our attempt in chapter 8 to explore some of these predictions.

CHAPTER 7

BOMBARDMENT-INDUCED PHASE TRANSFORMATIONS IN OTHER OXIDES: TeO_2, MoO_3, V_2O_5 and Bi_2O_3

7.1 Introduction

The main object of this chapter is to verify some of the predictions anticipated by the model for bombardment-induced structural changes discussed in the previous chapter (sec. 6.4.4). Attention will be given mainly to those predictions concerning possible amorphization on bombardment. Here TeO_2, MoO_3, V_2O_5 and Bi_2O_3, which have apparently never been studied by ion bombardment, would be particularly significant tests of the model since any disordering would occur in spite of the low values of T_c (the crystallization temperature), thence in spite of the effects of the ambient temperature and of beam heating. Using gas-release measurements and reflection electron diffraction, it will be shown that these oxides behave as predicted, i.e. they amorphize at low doses. These results further support the significance of the ratio T_c/T_m (the ratio (crystallization temperature)/(melting temperature)) as a criterion for predicting structural evolutions induced by bombardment. Other criteria for structural alterations on irradiation will be discussed at the end of this Chapter.

7.2 Materials

All experiments with TeO_2, MoO_3, V_2O_5 and Bi_2O_3 were performed on sintered pellets 1cm in diameter by 0.5 cm thick. They were prepared by cold pressing powders (suppliers are given in table (7.1)) in a circular

die without using any binder. The pellets were then placed in Pt crucibles and sintered for 12 hrs in air at 700°C for Bi_2O_3 and 600°C for the other oxides. The specimens had thus been annealed in air at a temperature higher than any to be experienced during subsequent experiments. Some physical properties for the four oxides used in this study are given in table (7.1), along with theoretical range data for 10 and 40 KeV-Kr^{85} ion bombardment.

7.3 Experimental

7.3.1 Ion bombardment

All bombardments were made in the accelerator described in sec. (6.2). Radioactive Kr^{85} was injected into the specimens at energies between 10 and 40 KeV, using doses between 6.2×10^{12} and 2.3×10^{16} ions/cm^2, and with dose rates (i.e. currents) ranging between 1 and 10 μA/cm^2. The doses will be given both in μAmin/cm^2 and in terms of ions/cm^2, the relation $1\mu Amin/cm^2 = 3.74 \times 10^{14}$ ions/cm^2 being used. Charge buildup was minimized by using beam areas larger than the sample, so that secondary electrons were produced on the metal target support [65].

For low-dose bombardments (i.e. those between 6.2×10^{12} to 1.3×10^{13} ions/cm^2), 4 samples were placed on the target holder, 3 of them were bombarded to approximate low doses, while the 4th was given an accurate dose which was higher than desired. The values of the low doses were then determined by measuring the radioactivity of the specimens, and comparing each low-dose specimen with the high-dose one. Using this technique, 6 to 9 specimens were bombarded for each dose and a dose accuracy of $\pm 10\%$ was usually achieved.

Table (7.1)

Some physical properties and range values for TeO_2, MoO_3, V_2O_5 and Bi_2O_3

	TeO_2	MoO_3	V_2O_5	Bi_2O_3
Physical properties				
crystal system	tetragonal	orthorhombic	orthorhombic	monoclinic
melting point (T_m)^{0}C	732	795	690	860
density (gm/cm^3)	6.04	4.69	3.357	8.55
molecular weight	159.6	143.9	181.9	466.0
mean molecular weight ($\bar{M}$)	53.2	36.0	26.0	93.2
Range values*(in $\mathring{A}$)				
$\bar{R}_{pj}$, 10 KeV, Kr	65	60	68	57
R_m, 10 KeV, Kr	54	50	57	48
$\bar{R}_{pj}$, 40 KeV, Kr	172	163	187	-
R_m, 40 KeV, Kr	145	140	157	-
Supplier	a	b	a	a

*For 20 KeV-Kr V_2O_5, $\bar{R}_{pj}$ = 112 $\mathring{A}$ and R_m = 95 $\mathring{A}$.

a Alfa Inorganics, Beverly, Mass., U.S.A. (ultra-pure powder).

b Analar, The British Drug Houses Ltd., Poole, England (commercially-pure powder).

7.3.2 Gas release measurements

Gas release measurements were carried out in two different ways:

(a) Some bombarded specimens were heated using the arrangement shown in Fig. 7.1 [75], where a stream of He or O_2 flowing at constant rate is passed over the sample and through a β-counting chamber while the sample is heated linearly at 25°C/min. The counter and the thermocouple were connected to a two-channel recorder so that the rate of gas release ($\frac{dF}{dt}$, where F is the fractional gas release) and the temperature of the specimen were recorded simultaneously. This differential gas-release system has been calibrated using pure metals (Sn and Al) bombarded at high doses where release peaks are expected to appear at the melting temperatures. The calibration showed that the apparent temperatures, as recorded in the $\frac{dF}{dt}$ vs. T curves are too high by 85 ± 3°C, and all the figures to follow were drawn taking this into account. The temperature difference is not a random error but due rather to a time lag for the gas to reach the counting chamber and a further hold-up within the counting chamber (which depends on the chamber volume) [75].

(b) Other bombarded specimens were step-heated, i.e. alternately heated isochronally in air with hold times of 5 min and then cooled to room temperature for counting. The heatings were spaced at intervals of 75 to 100°C, so that each heating could be treated without regard to those preceding it (cf. sec. 4.5 of [41]).

The β-counter used for radioactivity measurements consisted of a Philips GM probe PW4351 and a Philips PW4237 scalar with high voltage supply PW4290. The GM probe had a halogen gas as quenching agent and a mica end-window with a thickness of 3.5-4.0 mg/cm^2; it was thus ideally

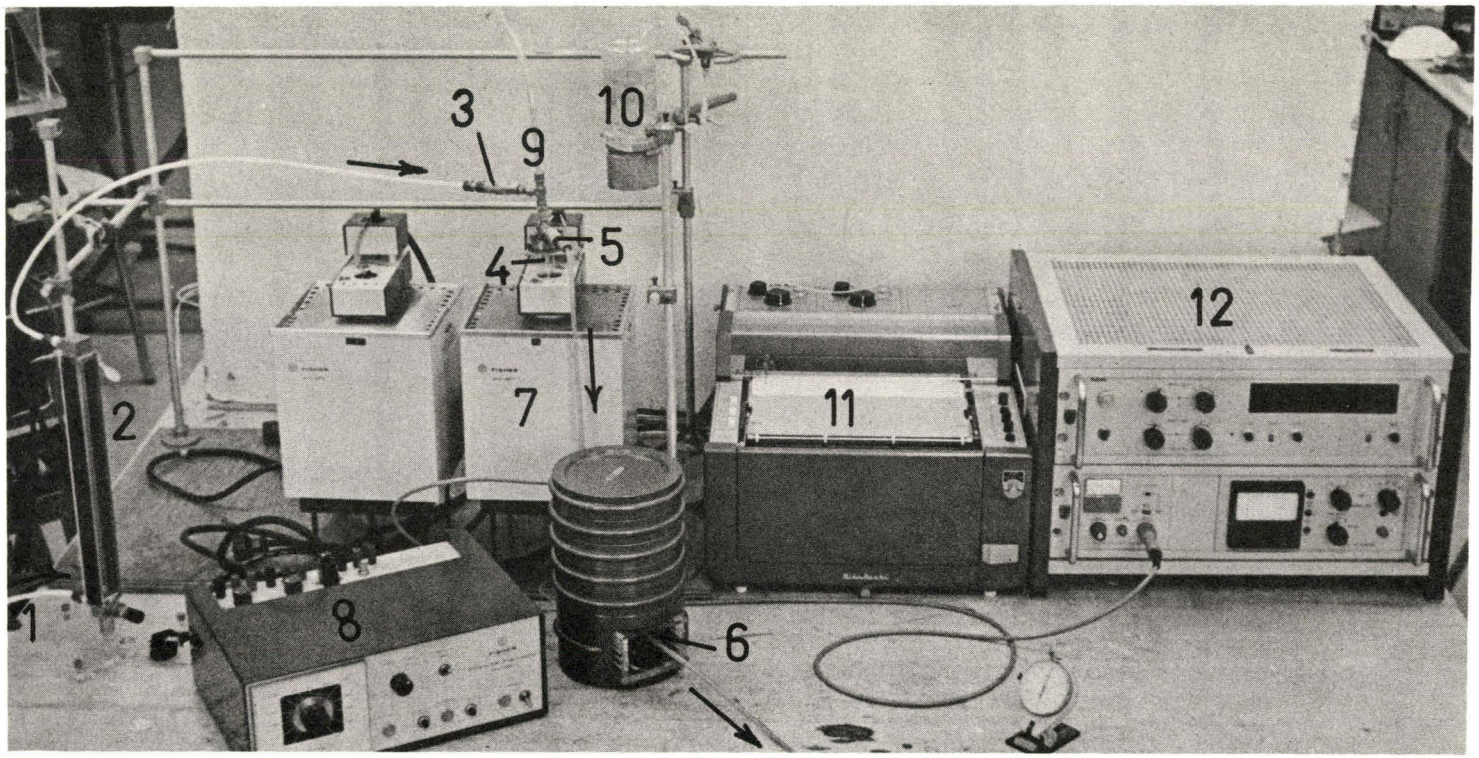

Fig. 7.1 Experimental arrangement used for differential gas-release measurements: 1, gas inlet; 2, flowmeter; 3, gas connection to the furnace insert; 4, quartz furnace insert tube; 5, gas outlet from the furnace insert; 6, counting chamber; 7, furnace; 8, temperature programmer to obtain the required rate of heating (25°C/min); 9, thermocouple; 10, thermocouple cold junction; 11, two-channel recorder; 12, GM counting system.

suited for the 675 KeV betas emitted by Kr^{85}.

7.3.3 Electron microscopy

The specimen surfaces of the sintered pellets were examined before and after ion bombardment and following various annealing treatments with the reflection electron diffraction unit of a Philips EM-300 electron microscope. Because the materials are non-conductors the charges produced on the samples by the electron beam were neutralized by a low-voltage electron gun. All patterns obtained by reflection were made using 60 to 80 kV electrons. It was found that the use of low electron energies (thus less electron penetration) for specimens bombarded with high-energy ions (thus thick altered layers) gives the best resolution for the structure of the transformed bombarded layer.

7.4 Analysis

The methods generally used for analyzing gas-release curves have been described in Ch. 3. For the analysis, the range of the bombarding ions and the shape of the range profile have to be known. Since experimental depth-distribution data are not available for the oxides used in this study, the range parameters were calculated using two different approaches as follows:

(a) $\bar{R}_{pj}$ was taken from a graph of $\bar{R}_{pj}$ versus mean atomic weight ($\bar{M}$) with fixed points for Al_2O_3, Nb_2O_5, WO_3 and Ta_2O_5 as derived by Schiøtt [205] using the LSS treatment outlined in sec. (2.3.2).

(b) $\bar{R}_{pj}$ was also calculated from the range equation for binary materials, A_xB_y, (Eq. 2.31) i.e.

$$R_{A_xB_y} = \frac{R_A R_B M_{A_xB_y}}{xM_A R_B + yM_B R_A}$$

where M is the molecular weight and R is any range (mean, median, etc) in $\mu g/cm^2$. In this case, the range values for the components A and B are interpolated from a graph of $\bar{R}_{pj}$ vs. $\bar{M}$ with fixed points for e.g. C, Al, Si, Ge and Au as derived by Johnson and Gibbons[24] based on the LSS treatment. The ranges are shown in table (7.1) for 10 and 40 KeV Kr bombarded TeO_2, MoO_3 , V_2O_5, and Bi_2O_3, and for 20 keV Kr bombarded V_2O_5. They have been expressed as $\bar{R}_{pj}$ and as R_m (the median range); the latter was taken as $(\bar{R}_{pj})/1.19$ as for an ideal "xe^{-x}" distribution.

Values of activation enthalpies (ΔH) derived from gas-release curves are subject to a number of errors. These include [65,74]: (a) there is a major error of about 10-20 Kcal/mole due to the choice of an idealized range of values for k_o ($\sim 10^{15\pm1}$ sec^{-1}) or D_o ($\sim 3 \times 10^{-1\pm1}$ cm^2/sec) since values as low as 10^9 sec^{-1} for k_o or 10^{-10} cm^2/sec for D_o have been used in the literature; (b) there is a minor error (of ~2 Kcal/mole) in ΔH due to a factor of two uncertainity in the ion ranges; (c) there is a similar minor error as in (b) arising from the assumption about the shape of the distribution curves; and (d) there is another possible error of 1-2 Kcal/mole from heating each specimen to successively higher temperatures (in the case of isochronal annealing).

For evaluating the possible contribution of release by vaporization, as discussed in sec. (3.5), and thereby determing a "minimum vapourization

temperature" for the material used, it is necessary to know the vapour species of the material, and the relation between its pressure(P_{mm}) and the absolute temperature (T), i.e. log P_{mm} vs. $\frac{1}{T}$. The vapour species are not known for any of the oxides used in this study, except for MoO_3. In addition, the log P_{mm} vs. $\frac{1}{T}$ relationships are only applicable for particular ranges of temperature. Any evaluation is, therefore, rather inaccurate. On the other hand, the change in the release curves with varying dose can be taken as providing good evidence against vaporization especially in the temperature range of stage IB, which is of particular interest to this study. Thus, if vaporization were the dominant release process at low temperatures ($\leq T_{IB}$) then the release attributed to stage IB would not diminish with decreasing dose as would be expected. In effect, release due to vaporization would be dose independent.

7.5 Results

7.5.1 Gas-release measurements

The results of the gas-release measurements obtained for the oxides used in this study, bombarded at different doses and a constant energy of 10 KeV for TeO_2, MoO_3, and Bi_2O_3 and 20 KeV for V_2O_5, are shown in Figs. (7.2) to(7.8). The main feature of the release curves is the clear resolution of two stages (or two peaks in dF/dt vs. T curves): a low-temperature release dominating at high doses, and a high-temperature one favoured by intermediate and low-dose bombardments. Table (7.2) summarizes the analysis of the gas-release data.

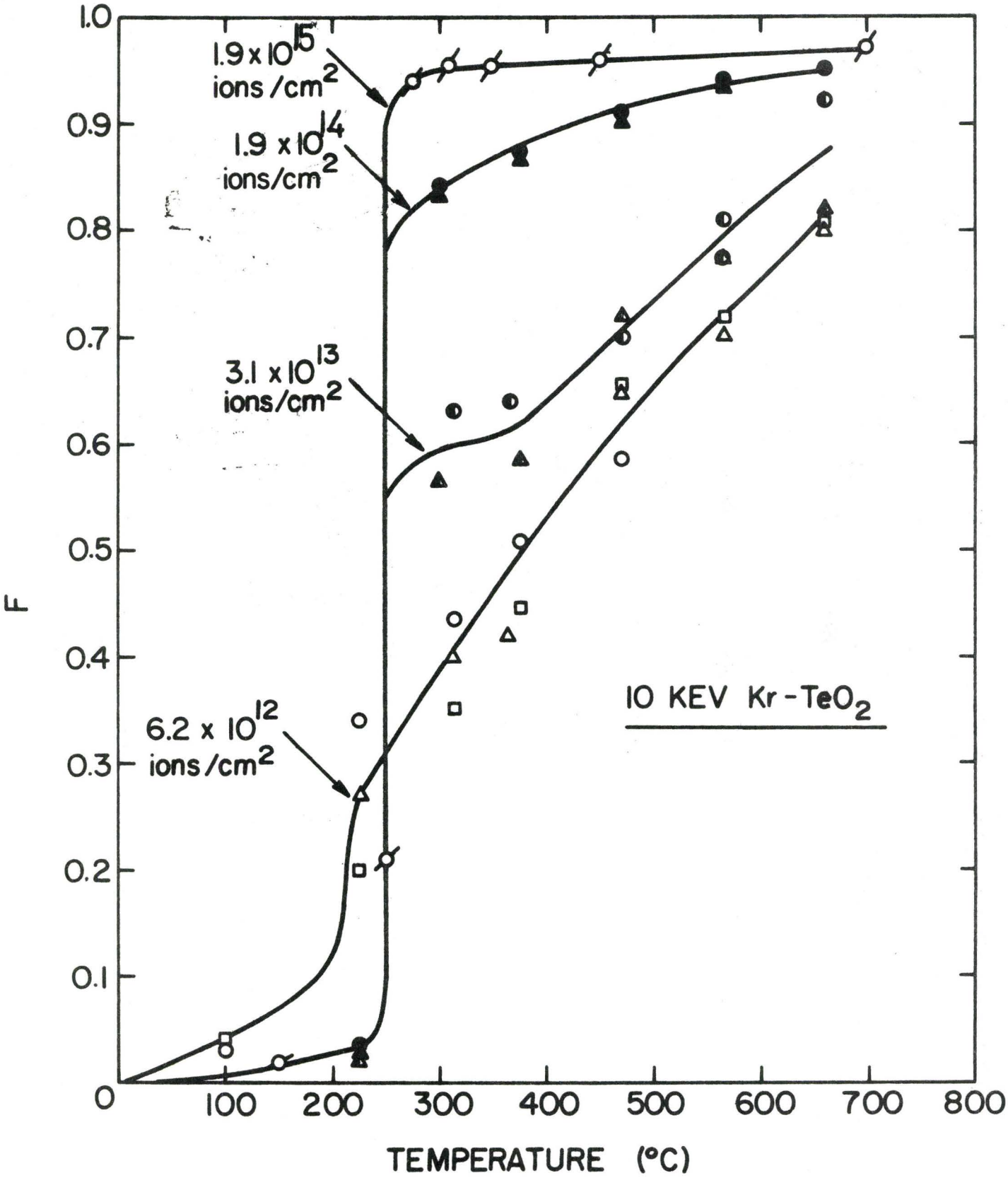

Fig. 7.2 F vs. T curves for TeO_2 specimens bombarded at four different doses with a bombardment energy of 10 KeV

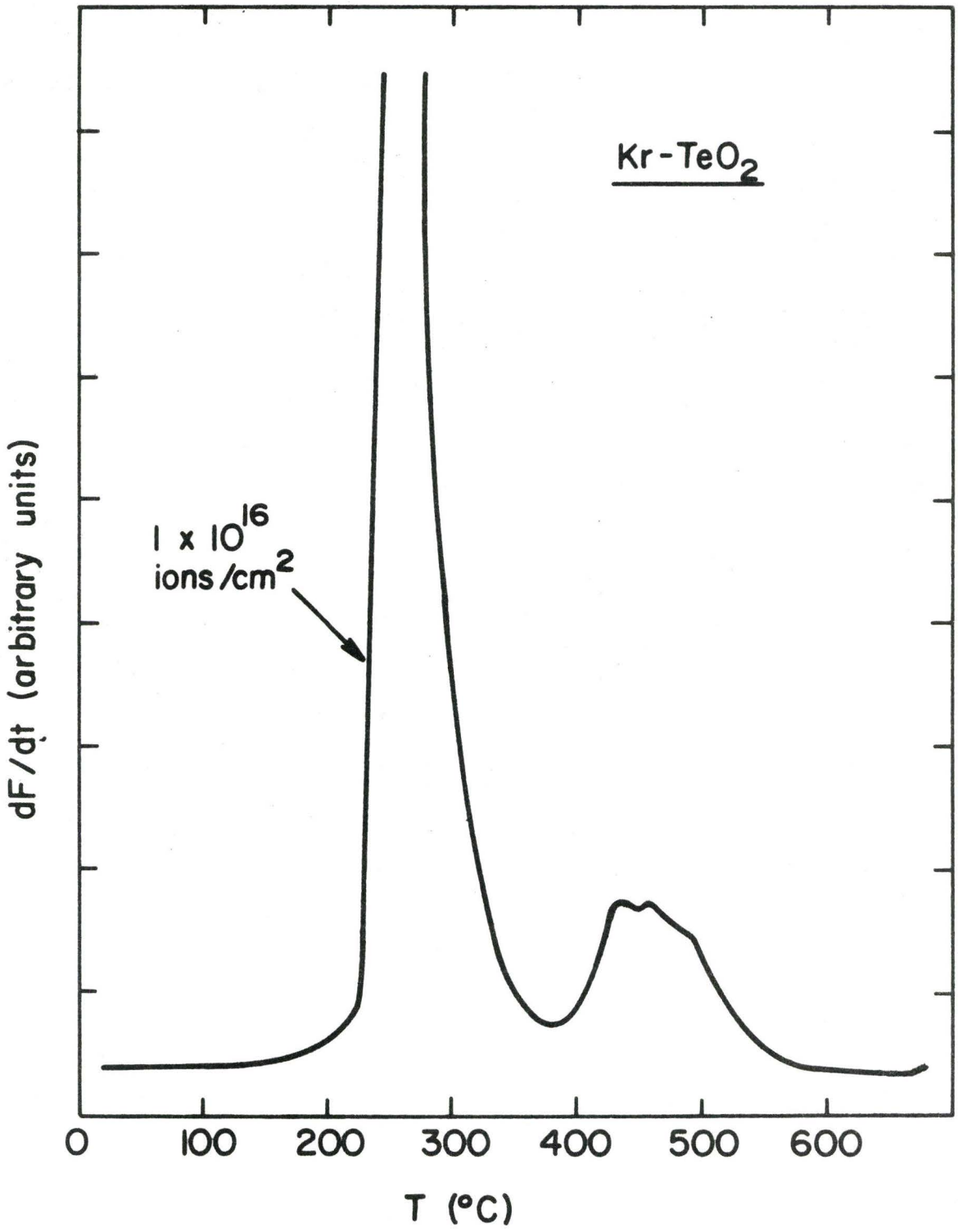

Fig. 7.3 Typical dF/dt vs. T curve for high-dose bombarded 10 KeV Kr-TeO_2. The small peak appearing at 400°C may be due to stage IIB, but this cannot be confirmed with the available information. The flow gas was He.

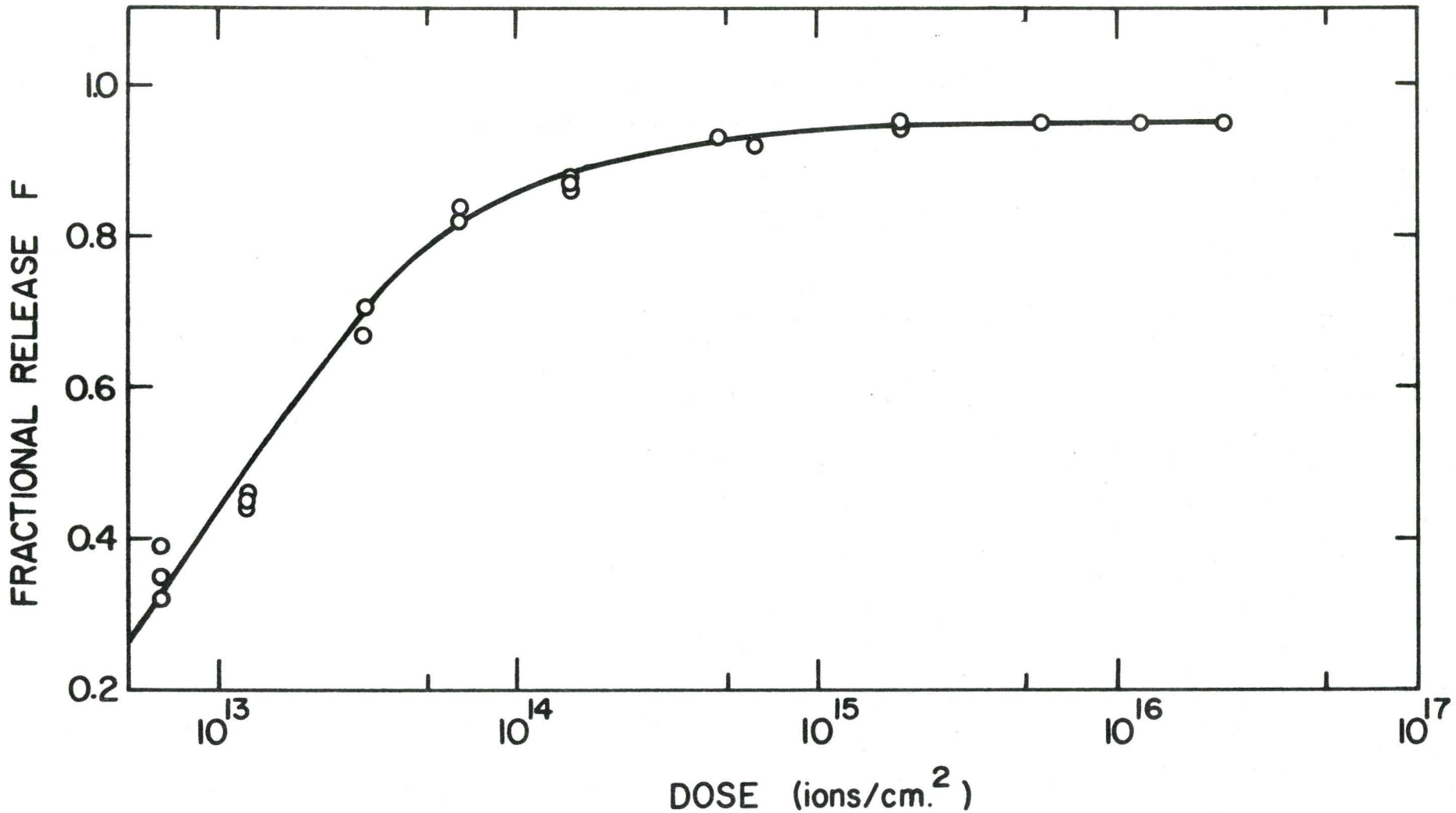

Fig. 7.4 Fraction F of Kr-85 released from TeO_2 bombarded at different doses and then annealed at 350°C for 5 min.

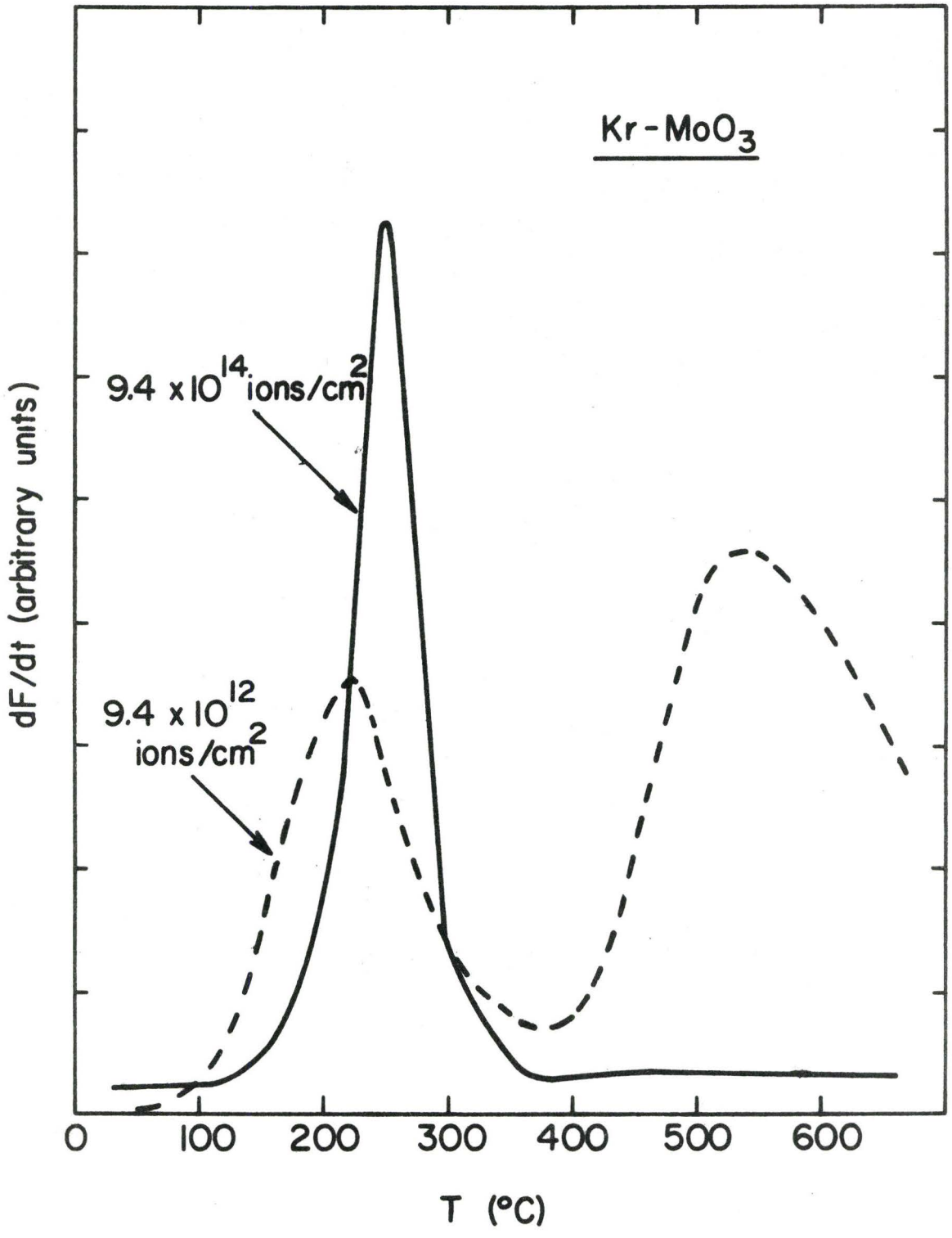

Fig. 7.5 Typical dF/dt vs. T curves for MoO_3 specimens which have been bombardment labeled with 10 KeV Kr-85. The flow gas was O_2.

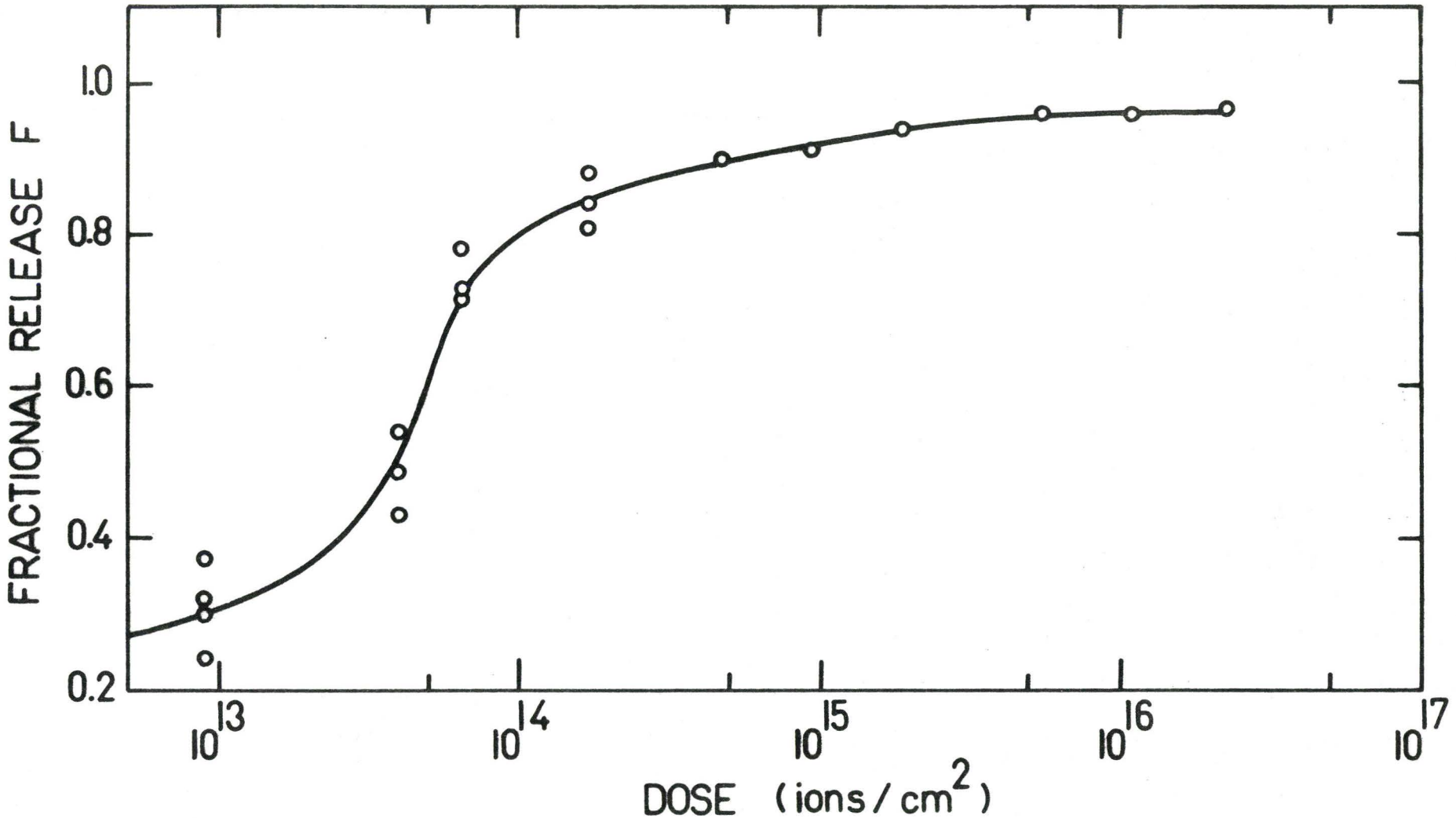

Fig. 7.6 Fraction F of Kr-85 released from MoO_3 bombarded at different doses and then annealed at 350°C for 5 min.

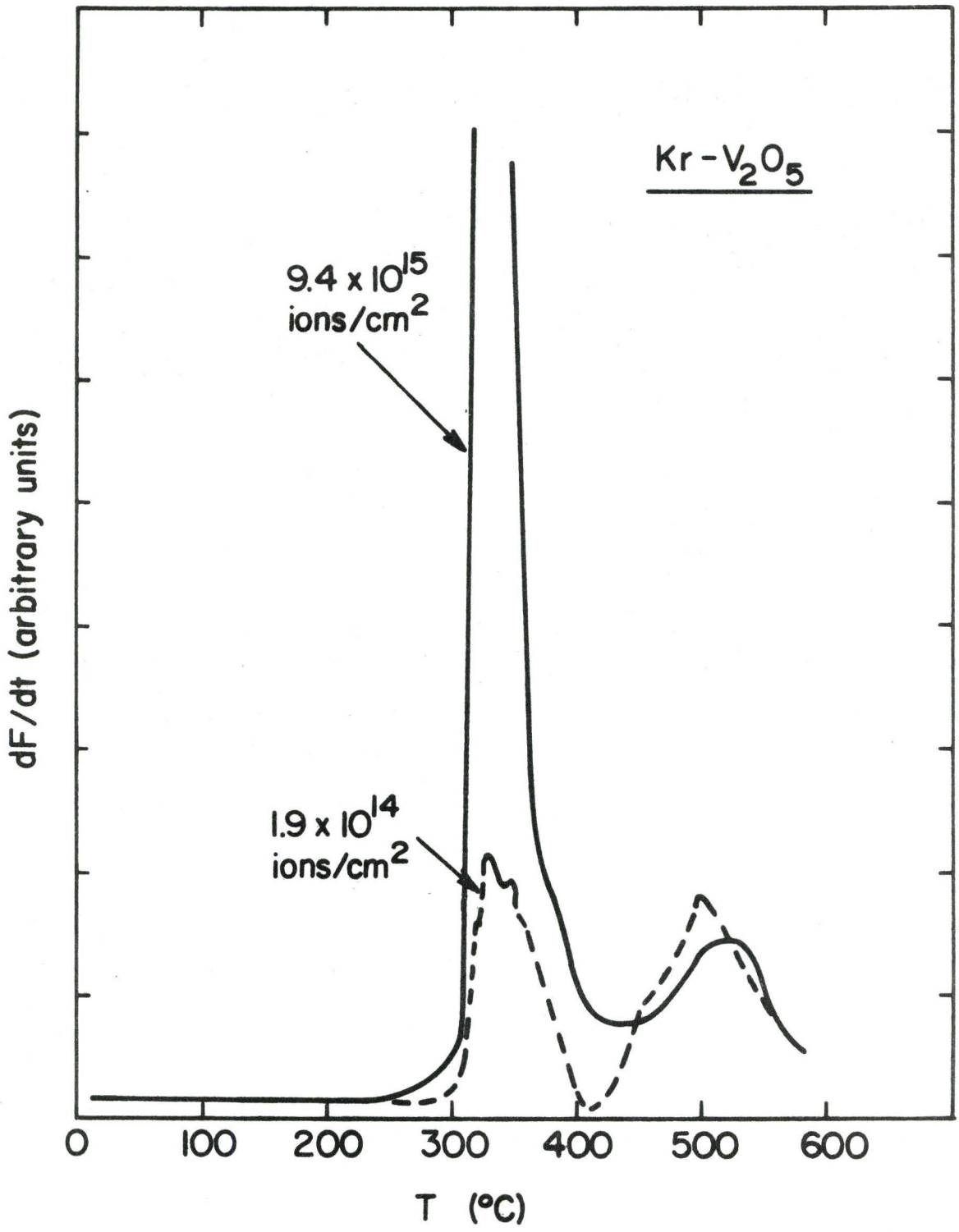

Fig. 7.7 Typical dF/dt vs. T curves for V_2O_5 specimens which have been bombardment labeled with 10 KeV Kr-85. The flow gas was He.

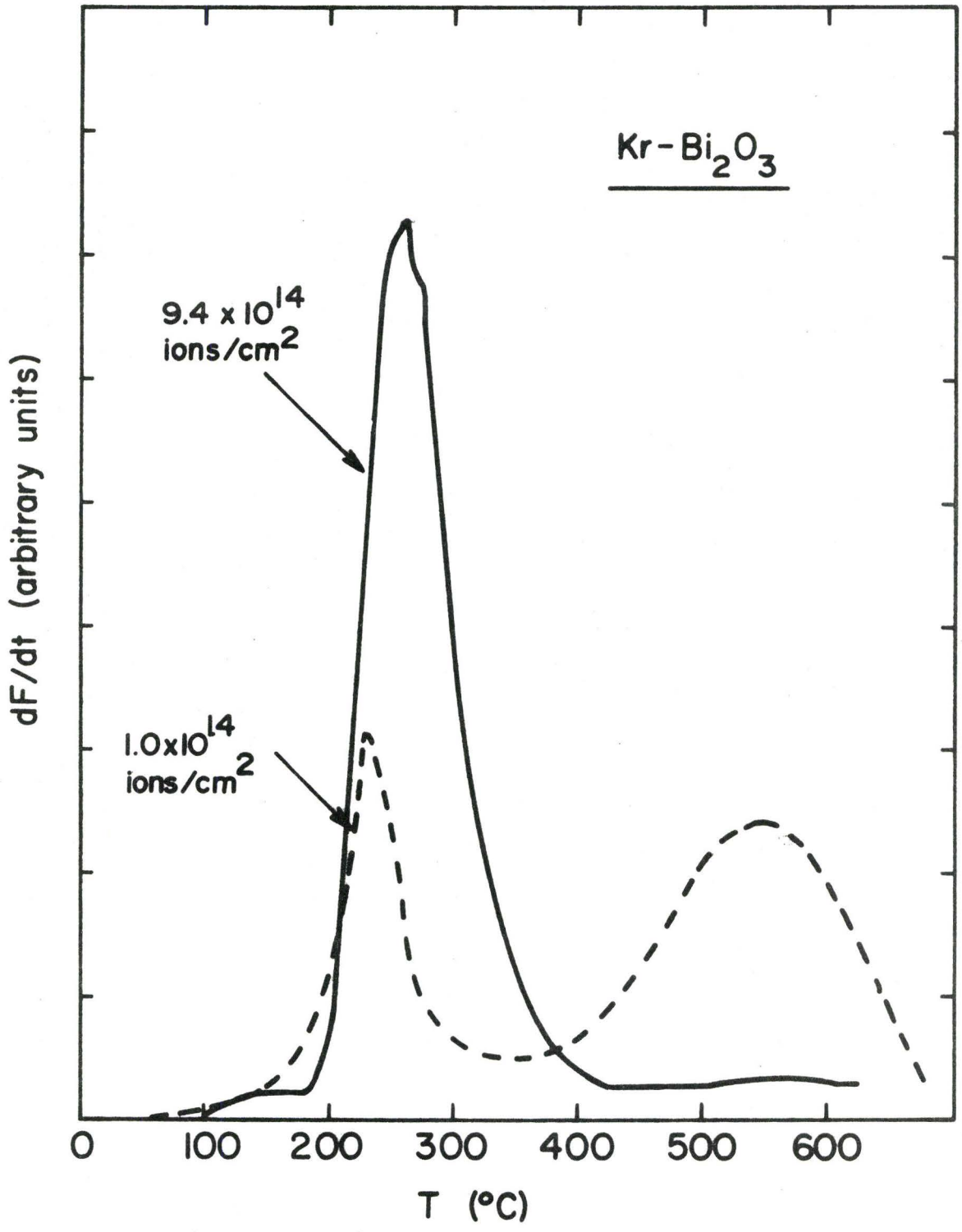

Fig. 7.8 Typical dF/dt vs. T curves for Bi_2O_3 specimens which have been bombardment labeled with 10 KeV Kr-85. The flow gas was O_2.

Table (7.2)

Analysis of gas-release data*

	TeO_2**	MoO_3	V_2O_5	Bi_2O_3
Number of spectra obtained	10	12	9	14
Low-temperature release				
T_{max} (^0C)†	260(±10)	250(±25)	330(±10)	260(±20)
$\Delta T_{1/2}$ †	30(±8)	50(±10)	34(±10)	70(±10)
observed ($\Delta T_{1/2}/T_{max}$) ($^0K/^0K$)	0.056	0.095	0.056	0.131
calculated ($\Delta T_{1/2}/T_{max}$) ($^0K/^0K$):				
(a) assuming single-jump motion	0.062	0.063	0.057	0.062
(b) assuming single-jump + sequential motion	0.110	0.106	0.123	0.104
(c) assuming "xe^{-x}" type distribution	0.206	0.163	0.149	0.164
calculated activation enthalpy (kcal/mole)††	40	36	46	-
High-temperature release				
T_{max}(^0C)†	-	510(±20)	460(±15)	545(±25)
$\Delta T_{1/2}$ †	-	120(±20)	76(±5)	130 (±20)
observed ($\Delta T_{1/2}/T_{max}$) ($^0K/^0K$)	-	0.153	0.104	0.158
calculated ($\Delta T_{1/2}/T_{max}$) ($^0K/^0K$)				
assuming "xe^{-x}" type distribution	-	0.164	0.150	0.146
calculated activation enthalpy (kcal/mole)	-	43	–	45
activation enthalpy from Eq. (3.16)	-	34±4	–	36±5

*(1) TeO_2, MoO_3 and Bi_2O_3 were bombarded with 10 keV, V_2O_5 with 20 keV-Kr.

(2) All temperatures recorded here are within ±5^{0}C.

**TeO_2 results in the form of dF vs. T are available only for high-dose bombardments.

†Values between brackets are due to the scattering in the results of different specimens.

††Assuming pure single-jump motion for TeO_2 and V_2O_5, and a process started with single-jump motion and and completed with sequential motion for MoO_3.

In analyzing the data the peak widths ($\Delta T_{1/2}/T_{max}$) (as defined in secs. (3.4.1) and (3.4.3)) have been used to help identify the stages. Thus, the low-temperature peaks have temperature widths (cf. table (7.2)) suggesting either pure single-jump motion (TeO_2 and V_2O_5), or a process started with single-jump motion and completed with sequential motion (MoO_3); only Bi_2O_3 is difficult to interpret. Also,the fractional gas release within this stage has been found to decrease with decreasing dose as shown, e.g., for TeO_2 (Fig. (7.4)) and MoO_3 (Fig. 7.6)). The low temperature peaks have, therefore, been identified as stage IB release, i.e. as being due to the annealing of bombardment-induced structural changes, with the identification only tentative in the case of Bi_2O_3.

Similarly, the widths of the high-temperature stages are found, at least with MoO_3 and Bi_2O_3, comparable to those calculated assuming diffusion of an "xe^{-x}" type distribution (cf. table 7.2). We conclude, therefore, that the high-temperature stage is probably stage IIA, i.e. related to volume diffusion of the implanted krypton.

7.5.2 Reflection electron diffraction

The reflection electron diffraction patterns of the bombarded surface layers confirmed the change to an amorphous phase in the high-dose bombardments for all the oxides used in this study (including Bi_2O_3). The results are shown in Figs. (7.9) to (7.12). As seen in these figures, the patterns of the as-prepared pellets have been replaced by diffuse halos after bombardment with doses as high as 1×10^{16} Kr-ions/cm^2

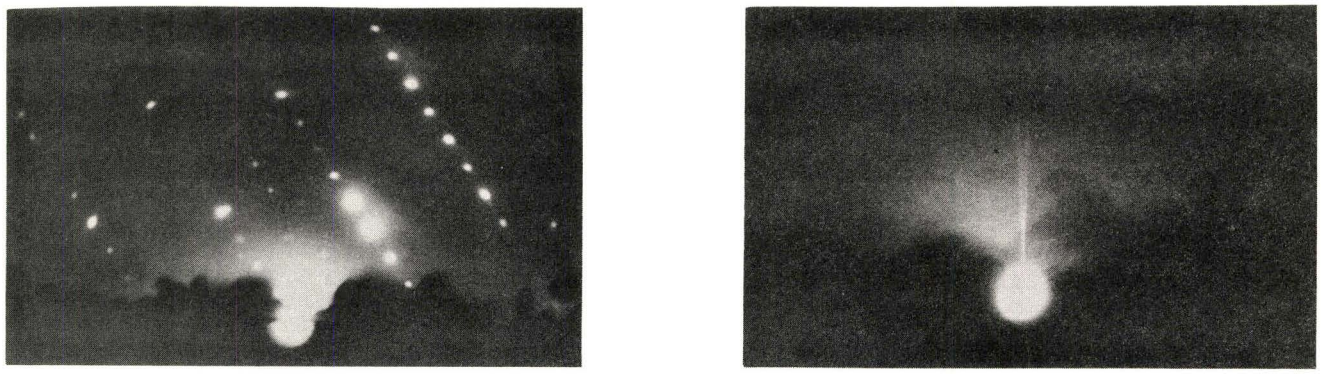

(a) Fig. 7.9 (b)

(a) Fig. 7.10 (b)

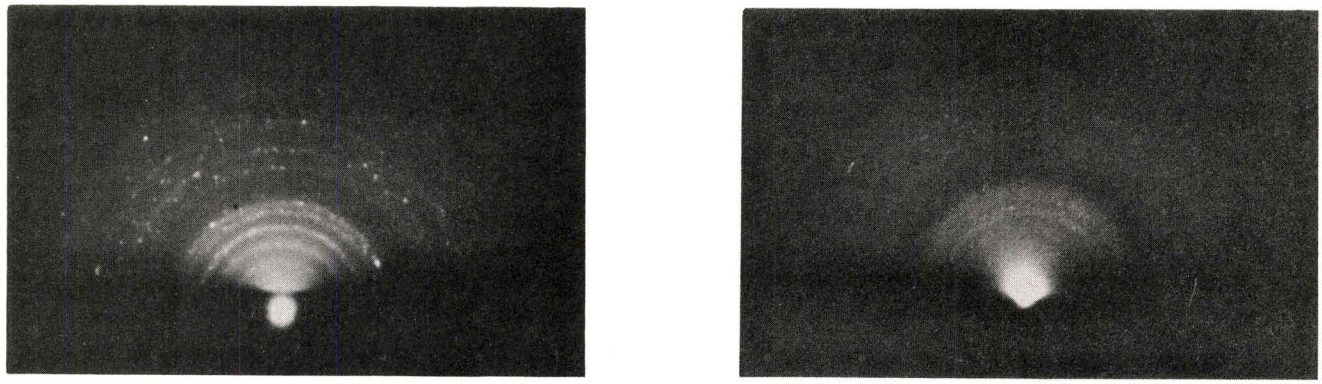

(a) Fig. 7.11 (b)

Fig. 7.9 Reflection electron diffraction patterns of sintered TeO_2 a) before bombardment and b) after bombardment with 9 x 10^{15} ions/cm^2 of 20-KeV Kr. Crystalline patterns were restored after heating to 350°C for 5 min.

Fig. 7.10 Reflection electron diffraction patterns of sintered MoO_3 a) before bombardment and b) after bombardment with 1.6 x 10^{16} ions/cm^2 of 40-KeV Kr. Crystalline patterns were restored after heating to 300°C for 5 min.

Fig. 7.11 Reflection electron diffraction patterns of sintered V_2O_5 a) before bombardment and b) after bombardment with 9 x 10^{15} ions/cm^2 of 40-KeV Kr. Crystalline patterns were restored after heating to 350°C for 5 min.

(a)

(b)

(c)

(d)

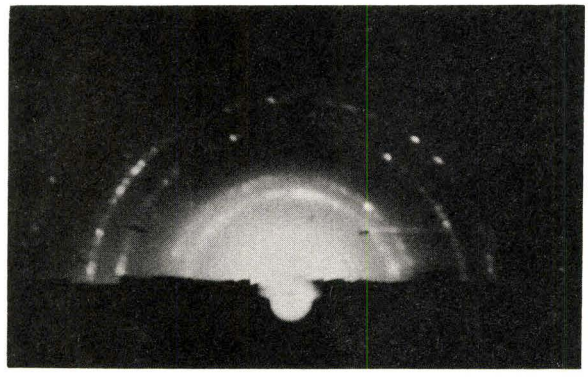

(e)

Fig. 7.12 Reflection electron diffraction patterns of sintered Bi_2O_3 a) before bombardment, b) after bombardment to a high dose (10^{16} ions/cm^2), c) like (b) but heated for 5 min at 285^{0}C, d) like (b) but heated for 5 min at 380^{0}C, e) like (b) but heated for 5 min at 660^{0}C. Crystalline patterns, apparently similar to (a), were restored after heating to 780 C for 5 min.

at 40 KeV*. Crystalline patterns apparently similar to the original patterns (except for Bi_2O_3) were completely restored at temperatures (given with the diffraction figures) comparable to those deduced from the low-temperature gas-release peaks (stage IB). For Bi_2O_3, however, the amorphous form first crystallized to a polycrystalline cubic form as shown in Fig. (7.12) and table (7.3) at temperatures between 250 and 700°C, the original single-crystal pattern being restored only at 780°C. Amorphous Bi_2O_3, like ZrO_2, TiO_2, and Al_2O_3, thus crystallized to a crystal structure different from that normally found. This result is worth investigating in detail in future work, as it may lead to the discovery of new structures.

With MoO_3 and V_2O_5, the diffraction patterns for specimens bombarded at doses $\geq 1 \times 10^{16}$ ions/cm^2 revealed a quite unexpected result: the amorphous halos were gradually replaced by a ring pattern corresponding to a phase apparently different from the starting materials. Because of the importance of such a result, which has never been observed before, this type of structural evolution will be described and discussed separately in Ch. 8.

7.6 Discussion

7.6.1 The low-temperature release and the annealing of bombardment-induced amorphousness

The present results have shown that TeO_2, MoO_3, V_2O_5, and Bi_2O_3 behave as predicted by the thermal-spike model presented in Ch. (6). Thus, they easily amorphize under ion-impact at doses $< 1 \times 10^{14}$ ions/cm^2,

*Specimens bombarded at lower energies show the same result but with much diffraction contribution from the underlying crystalline matrix. Also specimens bombarded at intermediate and low doses show the same effect.

Table (7.3)

Diffraction analysis of Bi_2O_3 bombarded with 1×10^{16} ions/cm^2, 40 KeV Kr and heated at 660°C for 5 min*

ring diameter D(mms) Fig.(7.12e)	d values (Å)	hkl
13.5	2.45	111
15.5	2.13	200
22.0	1.50	220
26.0	1.27	311
27.0	1.22	222
....	....	400
34.5	0.96	331
36.0	0.92	420

*The d spacings are calculated from the relation $2\lambda L/Dd$ as described in appendix A, sec. (A.1), with $\lambda L = 1.65$ and for reflection electron diffraction patterns taken at 80 KeV. The Miller indices have been identified by comparing the ratio of the ring diameters to the ratios of $(h^2 + k^2 + l^2)$ for low index reflections in cubic crystals (Ref. [206], p. 109]. This indicates that the structure is F.C.C. with a lattice parameter calculated from the relation $a = d(\sqrt{h^2+k^2+e^2})^{1/2}$ Å to be 4.27 Å.

Cubic Bi_2O_3 has been reported by a number of investigators. The results are summarized in Ref. [207], table (1), with different lattice parameters ranging between 5.25 to 10.93 Å and different crystal symmetry (B.C.C. or F.C.C. (CaF_2) or pseudocubic form), most of which does not agree with the present results. This could be attributed to one of the following: a new form of Bi_2O_3, formation of a hypostoichiometric oxide, or an impurity effect.

which are comparable to the doses required to disorder such materials as Si, Ge, and GaAs as given in table (4.2). Moreover, as shown in table (7.4), they have a ratio of T_c/T_m which lies between 0.47-0.63 and is thus greater than 0.3, the critical ratio suggested by the model of Chapter 6. One is thus not surprised at the pronounced tendency towards disordering.

As shown in table (7.4), the crystallization temperatures for bombardment-induced amorphousness (T_c) obtained here are somewhat lower than those obtained for amorphous thin films prepared by different techniques such as anodic oxidation (MoO_3 and V_2O_5 [203]) or reactive sputtering (TeO_2 and Bi_2O_3 [177] or V_2O_5 [206]). Similar disagreement in T_c has been noticed with other amorphous oxides prepared by different methods as we have previously pointed out in sec. (5.5.2) (table (5.2)). Again, we have no definite explanation for this discrepancy though we would point out that it could be attributed to the following:

1. Different methods of preparation could result in different degrees of disordering, since the latter depends mainly on the rate of formation, as mentioned in sec. (5.5.2) (e.g., the fact that the higher is the rate of formation the smaller is the grain size obtained is well known [209]). This could suggest a higher crystallization temperature for higher degrees of disordering; only future work can, however, give a final answer.

2. Using the same method of preparation, the crystallization temperatures could depend on the substrate. For example, the crystallization temperature for amorphous SnO_2 thin films prepared by reactive

Table (7.4)

Crystallization of bombardment-induced amorphousness in TeO_2, MoO_3, V_2O_5, and Bi_2O_3

Material	T_c (^0C)	T_c/T_m ($^0K/^0K$)	T_c for amorphous thin films, ^0C
TeO_2	260(±10)	0.53	400^{0}C in 180 min [177]
MoO_3	250(±25)	0.43	400^{0}C in 5 min [203]
V_2O_5	330(±10)	0.63	400^{0}C in 5 min [203], >150^{0}C in 24 hrs [208]
Bi_2O_3	260(±20)	0.47	250^{0}C in 60 min [177]

*T_m as given in table (7.1)

sputtering [69] has been found to be 550°C for unsupported films, 300°C for films supported on KCl, and 225°C for films supported on SnO_2 single crystals.

3. It will be shown in the next chapter (Ch. 8) that MoO_3 and V_2O_5 may form lower oxides if amorphized by bombardment due to a preferential loss of O_2. Thus, different methods of preparation could result in amorphous materials with different chemical compositions and thereby different behaviour during crystallization.

Another feature of the results is that the low-temperature release peaks, which are attributed to stage IB-release or the annealing of bombarded-induced amorphousness, are usually shifted to lower temperatures (of the order of 25-50°C and probably more for lower doses) for low-dose bombardments ($< 5 \times 10^{13}$ ions/cm^2). As we have mentioned in sec. (4.2), at low and intermediate doses the disorder is expected to be in the form of isolated amorphous regions rather than a continuous layer. Because of their small size (< 100 Å [e.g. 104]) and accordingly high surface free energy, they anneal at lower temperatures than those of continuous layers. A similar effect has been found with the ion bombardment of Si and Ge [120] where isolated disordered regions anneal at about 200°C below the macroscopic crystallization temperature.

7.6.2 High-temperature release

MoO_3 and Bi_2O_3 have shown at intermediate and low doses a gas-release component which can be attributed to stage IIA or normal volume diffusion and which might be expected to correlate with volume self-diffusion of the less mobile species. Unfortunately, however,

there is virtually nothing in the literatue from which one could determine the identity of the slower moving ion or from which one could deduce the values of its self-diffusion temperature and activation enthalpy. It is interesting, however, to note that Nováková and Jirů [210] have obtained a value of 41 kcal/mole for O_2 exchange in MoO_3 which is comparable to our result of 43 kcal/mole. This could be just a coincidence, and certainly more work is needed before insisting on there being a correlation.

As we have seen in sec. (3.4.1), the activation enthalpy for stage IIA release can also be correlated with the melting point ($T_m{}^0K$), for a great variety of materials, through the relation (Fig. 3.5):

$$\Delta H_{IIA} = (1.4 \pm 0.2)\ 10^{-3}.\ T_m \qquad eV$$

or

$$\Delta H_{IIA} = (32 \pm 4)\ T_m \qquad cal/mole$$

As shown in table (7.2) the values calculated in the present work are higher than those estimated using the above relation, This suggests that the relation is not as useful as once thought [135], a conclusion which follows also from a closer examination of Fig. 3.5.

7.6.3 Criteria for the structural stability of oxides and other non-metallic materials on irradiation

So far the ratio T_c/T_m has been shown to be a useful criterion for predicting the structural alterations of a large number of oxides and other non-metallic substances. In this section, we discuss other criteria which have been proposed during previous studies on radiation-induced structural transformations (see summary in Ch. 4).

An anisotropy criterion has been proposed by a number of investigators [e.g.74,97] as we have mentioned in sec. (4.5.1). Thus, it was generally stated that anisotropic substances tend to disorder on irradiation whereas cubic ones tend to remain crystalline. We should, first of all, note that this statement could be understood as implying that all cubic materials are isotropic, i.e. their elastic properties are the same in all directions. In fact, cubic materials are not necessarily isotropic; most F.C.C. metals, for instance, have their maximum value of Young's modulus along the [111] direction and the minimum along [100] (Cf. e.g. Ref. [165], Table XXIV)). Values of Young's modulus for oxides and other non-metallic substances are not known in detail, and the available data are therefore not sufficient to permit a direct quantitative test of the anisotropy criterion. However, we might still test the validity of the anisotropy criterion by examining the structures of materials having known responses to radiation. These, according to previous investigators, may be subdivided into two groups: cubic and non-cubic (anisotropic). As shown in table (7.5), of 21 cubic materials which are listed, 12 are known to be stable to high-dose bombardments, 8 are completely destroyed (amorphized), and 1 shows a tendency toward disordering in high-dose bombardments. On the other hand, 14 oxides are listed in table (7.6) in order of increasing departure from the cubic structure. This departure is taken in terms of the ratio of the largest lattice parameter to the smallest parameter in the structure in question. As shown in this table, although most non-cubic materials are unstable on irradiation, a simple correlation between the tendency

Table (7.5)

Radiation Sensitivity to Structural Transformations in Cubic Materials

Material	Structure	Sensitivity to radiation*
NaCl	NaCl	S
KCl	"	S
CaO	"	S
LiF	"	S
KI	"	S
KBr	"	S
MgO	"	PS
NiO	"	S
UC	"	S
BaF_2	CaF_2	S
UO_2	"	S
ThO_2	"	S
ZrO_2	"	S**
diamond	diamond	Am
Si	"	Am
Ge	"	Am
GaAs	zinc-blend	Am
GaSb	"	Am
GaP	"	Am
InSb	"	Am
CdTe	"	Am

*S ≡ Stable, Am ≡ amorphized, PS ≡ partially stable

**the cubic form of ZrO_2 is reported stable for fission fragment doses of 2×10^{16} fissions/cm^3 [97].

Table (7.6)

Radiation sensitivity to structural transformations in non-cubic-oxides

Material	Crystal system	Lattice parameters (Å)				Departure from the cubic structure*	Sensitivity to radiation**
		a_o	b_o	c_o	Ref.		
ZrO_2	Monoclinic	5.15	5.20	5.32	ASTM 13-307	1.03	cubic
SiO_2	Hexagonal	4.91	–	5.41	ASTM 5-0490	1.10	Am
TeO_2	Tetragonal	4.79	7.61	–	ASTM 11-694	1.59	Am
Ta_2O_5	Orthorhombic	6.18	3.66	3.88	ASTM 8-255	1.69	Am
TiO_2	Tetragonal	4.92	2.89	–	Ref. [211]	1.71	Am
WO_3	Monoclinic	7.29	7.52	3.83	ASTM 5-0363	1.96	Am
Bi_2O_3	Pseudoorth.	5.85	8.17	13.83	ASTM 14-699	2.36	Am
Al_2O_3	Hexagonal	4.76	—	12.99	ASTM 10-173	2.71	Am
Cr_2O_3	Hexagonal	4.95	—	13.54	Ref. [211]	2.74	P.Am
Fe_2O_3	Hexagonal	5.04	—	13.72	Ref. [211]	2.74	Am
V_2O_5	Orthorhombic	11.51	3.56	4.37	ASTM 9-387	3.19	Am
MoO_3	Orthorhombic	3.96	13.85	3.70	ASTM 5-0508	3.50	Am
U_3O_8	Orthorhombic	11.22	16.56	3.27	Ref. [211]	4.92	Am
Nb_2O_5	Monoclinic	20.24	3.82	20.24	Ref. [211]	5.85	Am

*Taken as the ratio of the largest lattice parameter to the smallest parameter in the structure in question. However, it has been pointed out to the writer since preparing this thesis that comparison of axial lengths is not a true criterion of anisotropy. Rather, the loss of cubic symmetry should have been considered.

**Am ≡ Amorphized, P.Am ≡ Partially amorphized.

towards disorder and the departure from the cubic structure does not exist. In fact, the two cases where a non-cubic oxide is stable or partly so occur randomly. The argument of relating structural stability of materials on irradiation with cubic or departure from cubic structures is obviously not completely satisfactory.

Alternatively, one might assess the anisotropy on the basis of bond directionality. For example, as seen in table (7.5), cubic materials with diamond or zinc blende structures (both of which have directional covalent bonds) are readily disordered on irradiation, whereas cubic materials with NaCl or CaF_2 structures (with non-directional ionic bonds) show good radiation stability.* In fact, it has been pointed out [212] that materials exhibiting a high degree of homopolar bonding and a low coordination number (as in diamond cubic, zinc blende, and also the wurtzite structures) form relatively stable amorphous solids, whereas it is extremely difficult to make amorphous solids from materials which do not contain a fairly high proportion of covalent bonding. This bond criterion had also been noted in early investigations dealing with radiation stability of materials. Goldschmidt [Cf. 88] had reported that little or no ionic bonding was found in minerals distorted by natural radioactivity. Crawford and Wittels [213] have also pointed out the importance of bond type on the extent and nature of radiation sensitivity. They studied the effect of fast-neutron irradiation on a number of minerals where there were indications that wide differences existed in the stability of the different cation-oxygen bonds. Thus, according

*It should be noted, however, that a crystal is not necessarily ionic because it has the NaCl structure. TiO, e.g., has an NaCl structure and yet is metallic!

to these authors, in order of decreasing stability under irradiation one would place (1) beryllium-oxygen, (2) aluminum-oxygen, (3) zirconium-oxygen, and (4) silicon-oxygen, which is also claimed to be the order of decreasing ionicity of binding. We note, however, that Crawford and Wittels [213] did not show how they calculate the amount of ionic character in these oxides, and that according to our calculations (Cf. table 7.7) their order is incorrect. We would also dispute the relative order of Al_2O_3 and ZrO_2 as far as radiation stability is concerned.

In order to put the correlation between irradiation stability and bond type on a more quantitative basis one could make use of Pauling's approximate equation [214],

$$\text{Amount of ionic character} = 1 - \exp(-\tfrac{1}{4}(x_A - x_B))$$

where x_A and x_B are the electronegativities of atoms A and B respectively. This relation is shown in Fig. (7.13).

The amount of ionic character for 35 substances of known radiation behaviour (Cf. table (4.1) and (4.2)) is given in table (7.7). The electronegativities of the elements are taken from Gordy and Thomas [215]. They give selected values which depend on the valency of the element. The materials in table (7.7) have been arranged in order of increasing ionicity. Significantly, 18 substances which amorphize readily have an amount of ionic character ≤ 55, 10 substances which are stable have values ≥ 67, and 5 substances with varying behaviour have values of ionic character ranging between 60 and 63. Considering the <u>calculated</u> values for the percentage of ionic character, given in table (7.7), the

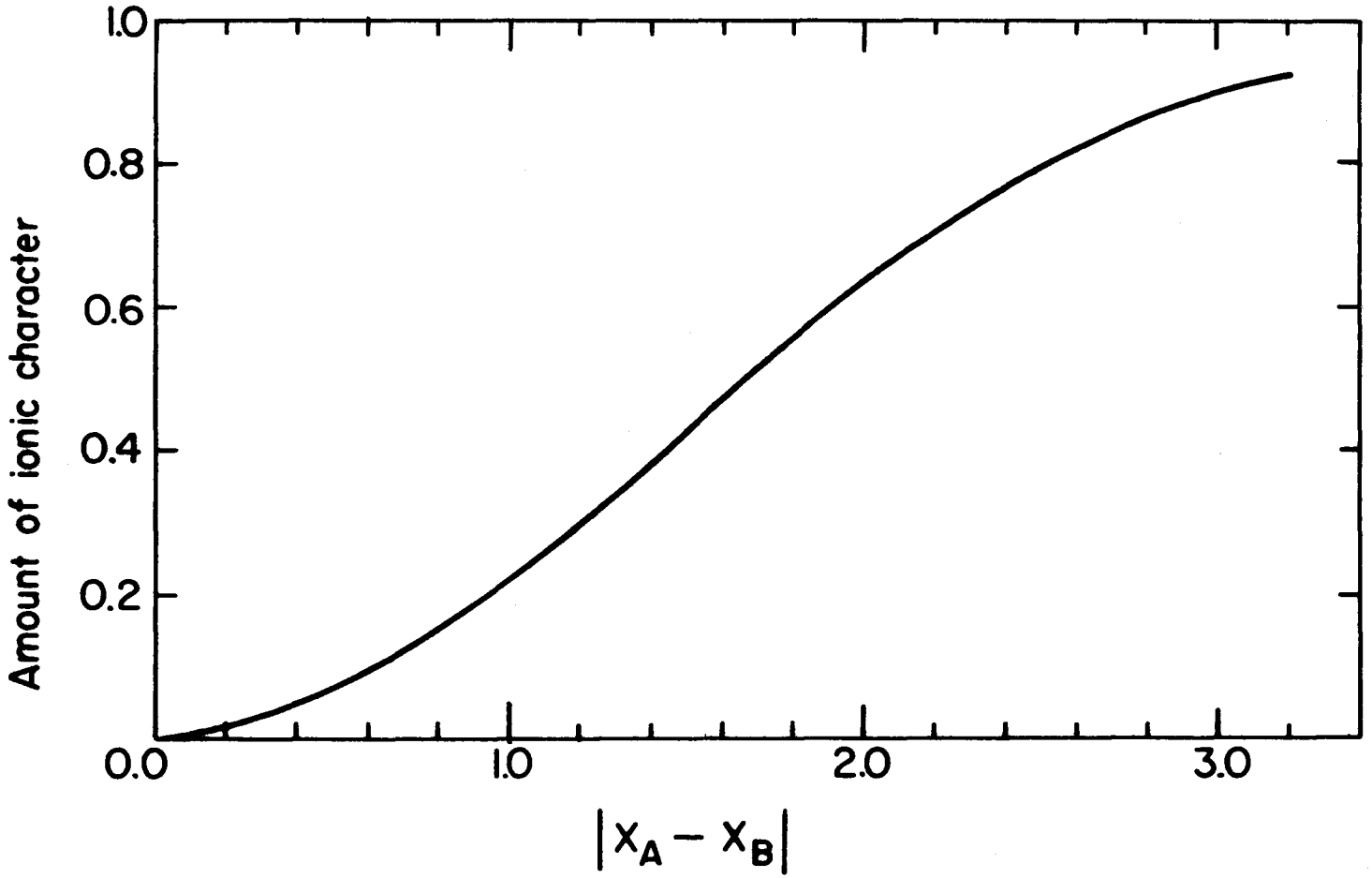

Fig. 7.13 Curve relating the amount of ionic character of a bond to the electronegativity difference of the two atoms A and B as calculated from Pauling's equation [214].

Table (7.7)

Amount of ionic character in various materials

Material AB	X_A*	X_B*	X_A-X_B	%age** ionic character	Material AB	X_A*	X_B*	X_A-X_B	%age** ionic character
Ge	1.8	1.8	0	0	Nb_2O_5	1.7	3.5	1.8	55
Si	1.8	1.8	0	0	MoO_2 (Mo^{IV})	1.6	3.5	1.9	60
GaAs	1.5	2.0	0.5	7	TiO_2	1.6	3.5	1.9	60
GaP	1.5	2.1	0.6	9	Cr_2O_3(Cr^{III})	1.6	3.5	1.9	60
CdTe	1.5	2.1	0.6	9	Al_2O_3	1.5	3.5	2.0	63
InSb	1.5	2.1	0.6	9	ZrO_2	1.5	3.5	2.0	63
GaSb	1.5	2.1	0.6	9	V_2O_3 (V^{III})	1.4	3.5	2.1	67
SiC	1.8	2.5	0.7	12	ThO_2(Th^{IV})	1.4	3.5	2.1	67
TeO_2	2.1	3.5	1.4	39	UO_2(U^{IV})	1.4	3.5	2.1	67
MoO_3(Mo^{VI})	2.1	3.5	1.4	39	NaCl	0.9	3.0	2.1	67(75)*+
WO_3(W^{VI})	2.0	3.5	1.5	43	KBr	0.8	2.8	2.0	63(75)*+
V_2O_5 (V^{V})	1.9	3.5	1.6	47	KI	0.8	2.6	1.8	52(75)*+
U_3O_8(U^{VI})	1.9	3.5	1.6	47	KCl	0.8	3.0	2.2	70(82)*
SiO_2	1.8	3.5	1.7	52	MgO	1.2	3.5	2.3	74
Bi_2O_3	1.8	3.5	1.7	52	CaO	1.0	3.5	2.5	80
Fe_2O_3(Fe^{III})	1.8	3.5	1.7	52	LiF	0.95	3.9	2.95	89
NiO	1.8	3.5	1.7	52	BaF_2	0.9	4.0	3.1	89
Ta_2O_5	1.7	3.5	1.8	55					

*Values are from Gordy and Thomas [215]

**As derived from Fig. (7.13)

*+Values between brackets are experimentally determined (cf. Pauling [214])

bond type criterion can be taken as a reliable guide for the stability of the materials under irradiation with the following two exceptions:

(1) Bi_2O_3, SiO_2, Fe_2O_3 and NiO have the same amount of ionic character (52%) yet they have completely different response to radiation. Thus, Bi_2O_3, Fe_2O_3 and SiO_2 completely amorphize whereas NiO does not show any significant structural change at all.

(2) MgO has a high amount of calculated ionic character (74%) compared with those of alkali halides, yet the oxide showed indications of structural damage at doses $\leq 2 \times 10^{16}$ ions/cm^2 [74]. At such doses, the alkali halides and even ThO_2 and UO_2 (the latter with lower amounts of ionic character) have proven the absence of any significant structural damages.

Another criterion, which has been pointed out by Berman et al. [97] and Matzke and Whitton [74], is the following: materials expected to be more susceptible to structural alterations under irradiation are those which exist in different modifications which result from for example, polymorphism, polytypism, thermal instability (e.g. chemical decomposition at high temperatures), or high defect concentration (e.g. shear structures). Thus, e.g., SiO_2, Al_2O_3, TiO_2, Bi_2O_3, Fe_2O_3 and U_3O_8 all exist in two or more polymorphic forms and all show a high tendency toward disordering. Also, V_2O_5, MoO_3, and WO_3 are known to form a number of lower oxides (with different structures) as they lose oxygen. It has been shown in this chapter that V_2O_5 and MoO_3 are readily amorphized by ion impact,while Nghi has shown it for WO_3 [46]; and, it will be shown in the next chapter that at least V_2O_5 and MoO_3 undergo a transformation to their lower oxides

with high-dose ion bombardment, probably due to preferential oxygen loss.

Nevertheless, this criterion is best described as only a rough guide, for there are many easily disordered materials which have only one form (Ge, Si, III-V compounds).

In conclusion, two criteria thus appear to be reasonably successful in predicting the structural stability of materials on irradiation. These are the thermal-spike model presented in Ch. 6, which centers on the value of the ratio T_c/T_m; and the bond-type criterion given in this chapter, which concerned the amount of ionic character. The two criteria are perhaps different descriptions of the same underlying properties, although it did not appear feasible to pursue the subject further.

CHAPTER 8

ON THE INCREASE IN THE ELECTRICAL CONDUCTIVITY OF MoO_3 AND V_2O_5 BY ION BOMBARDMENT (STRUCTURAL CHANGES IN VERY HIGH DOSE BOMBARDMENTS)*

8.1 Introduction

As we have seen in the previous chapter, the experiments with MoO_3 and V_2O_5 were in the first instance intended simply for studying their possible amorphization by ion impact. However, it soon became apparent that there was an unexpected additional feature: the amorphous halos were gradually replaced by a ring pattern at doses >1 x 10^{16} ions/cm^2. This chapter is, therefore, intended to describe this new phenomenon, which turns out to be a gradual crystallization to lower oxides, due evidently to a preferential oxygen loss. These lower oxides, MoO_2 and V_2O_3, are known from other work to be either metallic or nearly so, with the result that the structural evolution can be followed by measuring the electrical conductivity in parallel with electron-diffraction examinations. In effect, a marked increase (factor of roughly 10^7) in electrical conductivity is observed.

Electrical conductivity measurement is a commonly used method for investigating radiation effects in oxides. An increased conductivity was, for example, noted for neutron bombardment of Al_2O_3, TiO_2, and ZrO_2 [92,217], during proton bombardment of Al_2O_3 and MgO [218], after proton

*For the most part, this chapter is based on a paper by the author and Dr. R. Kelly [216].

bombardment of discontinuous films of Ta_2O_5 containing islands of metallic Ta [219], for Ne-bombarded ZrO_2 [217], and for what was effectively the formation of an Si-O-Al cermet by Al bombardment of SiO [220]. These examples (as well as others referred to by Ref. [92]) have mainly involved conductivity increases which were either transient or small. Only in the two cases where bombardment with heavy ions was used was there an effect similar to what we have observed with MoO_3 and V_2O_5, the conductivity increasing by a factor of 5000 with ZrO_2 [217] and by a factor of 10^8 with Si-O-Al [220].

8.2 Experimental

8.2.1 General Procedure

The specimens used in this study were prepared in the form of circular pellets as described in sec. (7.2). They were subjected to bombardment by a 10 $\mu A/cm^2$ beam of Kr or O_2 ions at energies varying between 2.5 and 40 keV. The depth of oxide which would be altered under these conditions depends on the mechanism of damaging, with possible values of 0-30 Å for true surface effects [221], 0-300 Å for effects correlating with the damage mean range [22], and 0-3000 Å or even more for effects involving diffusion [72]. Any property changes caused by ion impact would thus be confined to thin surface layers.

Following the bombardments, the specimens were first examined for electrical conductivity and then for structural changes. The conductivity increase was followed by measuring the sheet resistance by a four-point probe dc method as will be described in the next subsection; the structural changes were sought by reflection electron diffraction

as outlined in sec. (7.3.3).

8.2.2 Measurement of sheet resistance

As can be seen from Fig. (8.1a), the resistance of a rectangularly shaped section of film (or thin layer) measured in a direction parallel to the film surface is given by

$$R = \frac{\rho}{w} \frac{\ell}{b} . \qquad (8.1a)$$

If $\ell = b$, this then becomes

$$R = \frac{\rho}{w} = R_s \qquad (8.1b)$$

so that the resistance R_s of a square film is independent of the size of the square; i.e. it depends only on the resistivity and thickness. The quantity R_s is called the "sheet resistance" of the film and is expressed in "ohms per square". If the thickness is known, the resistivity is readily obtained from

$$\rho = w R_s . \qquad (8.1c)$$

Measurements of sheet resistance were made after bombardment, in air at room temperature, by a linear four-point probe D.C. method. The basic model for this method is indicated in Fig. (8.1b). Four sharp probes are placed on a flat surface of the material to be measured, current is passed through the two outer electrodes, and the floating potential is measured across the inner pair. The experimental circuit used for the measurements is illustrated in Fig. (8.1c). A Fell probe of the type used with Ge was chosen, the weight per point being 20 gms, the points being 0.1 cm apart, and the tip radius being 1×10^{-2} cm.

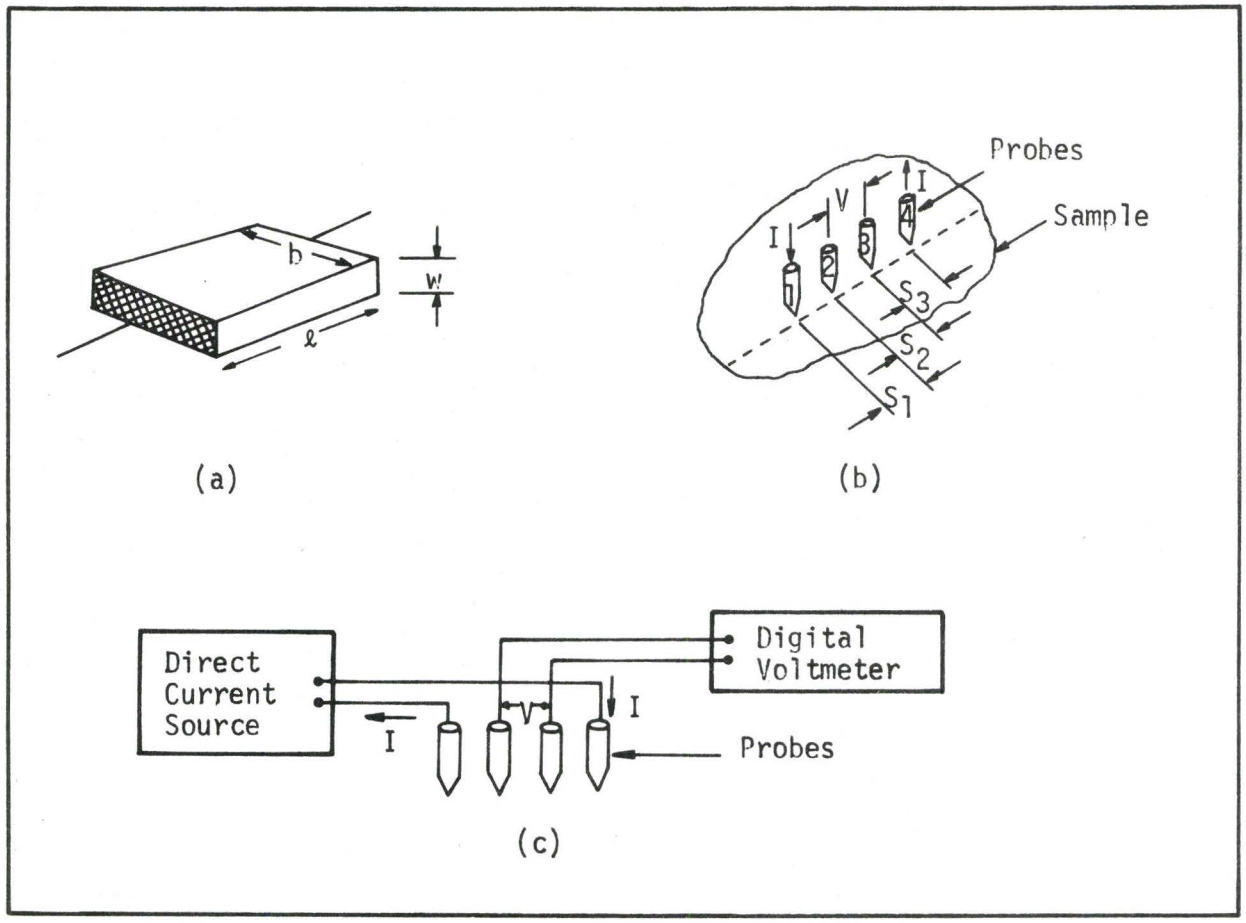

Fig. 8.1 Measurement of sheet resistance, (a) definition of sheet resistance, (b) in-line four-point probe, (c) circuit used for resistivity measurements.

The current source used was a Keithly model 225 with a full scale range of 10^{-7} to 10^{-1} ampere and 0.02% resolution. Its accuracy is claimed to be within 0.005% of full range for no-load-to-full-load on the 10^{-1} to 10^{-6} ampere ranges. During measurements various D.C. currents ranging from 0.5×10^{-6} to 10^{-3} ampere were applied in order to confirm ohmic behaviour. The Keithly model 160 digital multimeter was used as a D.C. voltmeter. It has a range of ±1 microvolt per digit to 1000 volts full scale in seven decade ranges and with 0.1% accuracy of reading (i.e. ± 1 digit) on all ranges.

Due to the uncertainty in the thickness, w, of the conducting layer the results have with one exception been expressed in terms of sheet conductivity ($ohm^{-1}.\square$), using the expression appropriate for a thin layer with a non-conducting bottom surface [222]:

$$\sigma_s = \sigma w = (I/\pi V)\ell n2 \qquad (8.2a)$$

The exception was unbombarded V_2O_5, which turned out to be slightly conductive so that the relation appropriate for a semi-infinite medium was required:

$$\sigma = I/2\pi sV \, . \qquad (8.2b)$$

Here s is the spacing of the points. The correction for the finite width and thickness of the specimens can be inferred from Figs. (6) and (11) of Valdes' work [222] to be unimportant; the correction for the non-zero initial conductivity of V_2O_5 was made by substracting $(I/V)_o$, i.e. the initial value of (I/V), from the bombarded values. (The validity of the latter correction rests with the assumption that the probes penetrate right through the altered surface layer. If they do not,

the correction is far more complicated [223]).

8.3 Results

8.3.1 MoO_3

Fig. (8.2) illustrates the variation of electrical conductivity for MoO_3 bombarded with 40 KeV Kr as a function of dose. The curve can be regarded as consisting of three more or less distinct regions:

(a) Region I: σ_s gradually increases from an undetectable (and apparently non-ohmic) initial value well below 1×10^{-7} $ohm^{-1}.\square$ to about 0.1×10^{-4} $ohm^{-1}.\square$ at a dose of $\sim 1 \times 10^{16}$ ions/cm^2. The corresponding diffraction patterns of specimens bombarded in this region indicated the gradual transformation to an amorphous state (Fig.(8.3a) and (8.3b)). Such a change has been previously discussed for MoO_3 in sec. (7.5).

(b) Region II: σ_s grows rapidly from 0.1×10^{-4} to 5×10^{-4} $ohm^{-1}.\square$ at a dose of $\sim 2 \times 10^{17}$ ions/cm^2. The electron diffraction examinations, after bombardments within this region, revealed the gradual replacement of the amorphous halos by a ring pattern corresponding to a phase different from the starting material (Fig. (8.3c)). This could be regarded, if desired, as a further example of bombardment-induced crystallization, a phenomena previously confirmed in detail with ZrO_2 (Cf. Ch.6).

(c) Region III: By the beginning of this region, σ_s apparently ceases to increase further while the formation of the new crystalline phase is complete. The diffraction pattern was in close agreement with that expected for MoO_2 (Fig. 8.3d) and table (8.1). No other crystalline

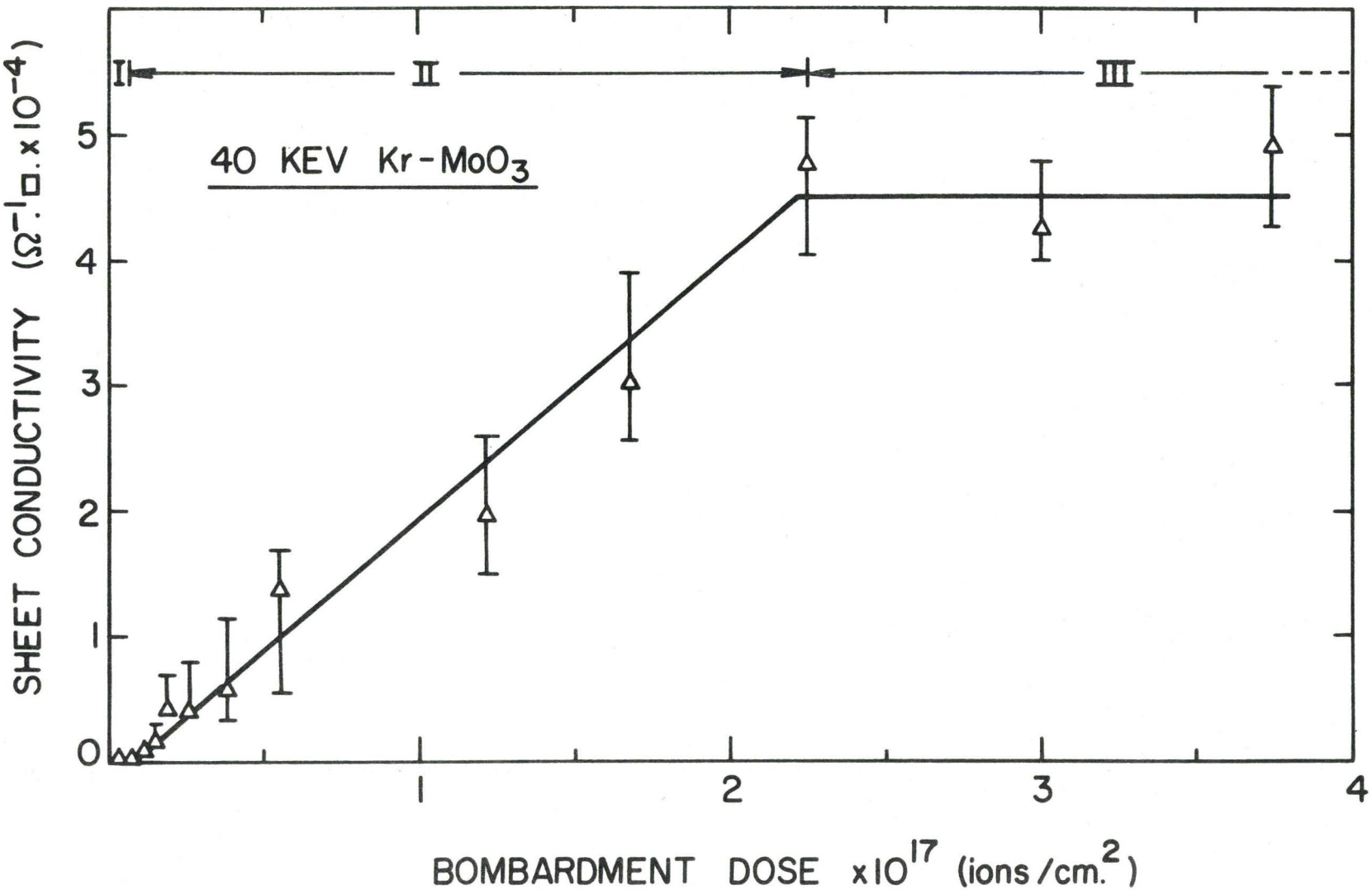

Fig. 8.2 Sheet conductivity vs. bombardment dose for MoO_3 specimens bombarded with 40 KeV-Kr.

(a)

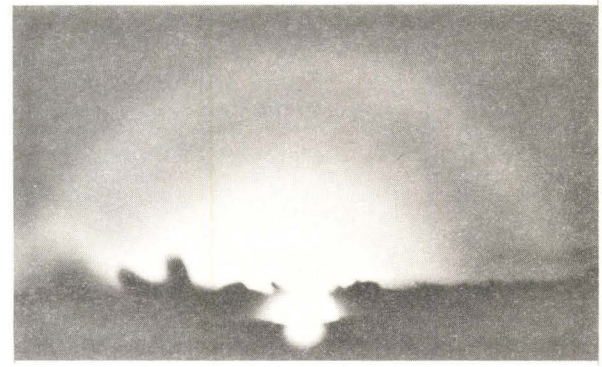

(b)

(c)

(d)

Fig. 8.3 Reflection electron diffraction patterns of MoO_3: (a) before bombardment, (b) after bombardment with 1.9×10^{16} ions/cm^2, (c) after bombardment with 1.3×10^{17} ions/cm^2, and (d) after bombardment with 4×10^{17} ions/cm^2. Note that Fig. 8.3(a) & (b) are similar though not identical to Fig. 7.10(a) and (b).

Table (8.1)

Diffraction analysis of MoO_3 following bombardment with 3.7×10^{17} ions/cm^2 of 40 keV-Kr

d values in Å, as calculated from Fig. (8.3C)*	MoO_2 ASTM - 5 - 0452 dÅ	I/I_o
....	4.78	20
3.45	3.41	100
....	2.804	30
2.42	2.433	50
	2.420	85
	2.405	40
	2.397	50
2.18	2.176	30
	2.171	10
	2.147	30
1.92	1.833	35
1.69	1.718	55
	1.704	80
	1.692	50

*See appendix (A), sec. (A.3)

phase could be identified, either as an intermediary or as a minor constituent, on the basis of the seven oxides from MoO_2 to MoO_3 [224], (See table A. 2). It is conceivable that further changes might have occurred at still higher doses, though this is regarded as unlikely in view of the apparent saturation in the conductivity vs. dose curve for doses above 2×10^{17} ions/cm^2. It is also possible that the new crystalline phase was a heretofore unknown form which had a diffraction pattern similar to MoO_2, for the seven oxides known are certainly not all that exist. (The latter statement is made by analogy with vanadium, where the list of oxides tends to grow annually).

Taking the thickness of the conducting layer for the saturated condition in region III as being either 300 Å (as for an effect correlating with the damage mean range) or 3000 Å (as for an effect involving diffusion), one finds that the bulk resistivity of the layer is about 10^{-2} or 10^{-1} ohm.cm, as compared with the value $>>10^7$ ohm.cm for the starting material. The effect of ion impact on the conductivity of MoO_3 is thus extreme, occuring to an extent similar to that realized in Al-bombarded SiO [220].

Additional experiments were carried out with lower Kr energies and with 40 keV-O_2 at a uniform dose of 4×10^{17} ions/cm^2. The resulting sheet conductivities, as summarized in table (8.2), suggest that bombardment-enhanced conductivity with MoO_3 occurs to an extent which: (a) increases with ion energy, and (b) is more significant for ion beams which are "neutral" (i.e. Kr) rather than "oxidizing" (i.e. oxygen). Table (8.2) also includes estimates of the mean projected ion ranges and of the

Table (8.2)

Sheet conductivity for MoO_3 and V_2O_5 following bombardment with ~3 x 10^{17} ions/cm^{2*}

Target	Energy (KeV) and ion	Sheet conductivity (ohm-1 □)	Mean projected ion range(A)**	Damage mean range(A)†
MoO_3	2.5-KeV Kr	0.74 x 10^{-5}	15[a]	13
	10.0-KeV Kr	10 x 10^{-5}	60[b]	50
	20.0-KeV Kr	25 x 10^{-5}	99[b]	83
	40.0-KeV Kr	48 x 10^{-5}	163[b]	136
	40.0-KeV O	8 x 10^{-5}	652[c]	453
V_2O_5	40.0-KeV Kr	11 x 10^{-4}	187[b]	156

* 3 x 10^{17} ions/cm^2 for V_2O_5 and 3.7 x 10^{17} ions/cm^2 for MoO_3.

** (a) Taken as 1/4 of the value for 10 KeV-Kr
(b) Taken as calculated for table (7.1)
(c) Taken by analogy with Kr-SiO_2 and O-SiO_2 [24] as four times the value for 40 KeV-Kr

† As calculated from the WSS [22] (Cf. sec. 2.4).

damage mean ranges [22]. These values would correspond roughly to the depth of the bombardment-enhanced conductivity in the event that the enhancement were a normal damage effect.

MoO_2 was apparently the final crystallization product also in specimens bombarded with 40 keV oxygen.

8.3.2 V_2O_5

Similar results were obtained for V_2O_5. The as-prepared pellets were found, in agreement with previous work on V_2O_5 [225,226], to conduct at room temperature, with bulk resistivities of about 10^4 ohm.cm. In fact, the previously observed values, obtained using single crystals rather than sinters, were 10^2 to 10^3 ohm.cm. The difference probably lies in grain-boundary effects. Bombardment with 40 keV Kr gave rise to a marked conductivity increase which was similar in both magnitude and in response to dose to that found with MoO_3. The results could be represented either in terms of the sheet conductivity, σ_s (Fig. 8.4), or in terms of the ratio $(I/V)/(I/V)_o$, where $(I/V)_o$ is the initial value of I/V (Fig. 8.5). In the former case the relevant formulae was,following the comments of Sec. 8.2.2,

$$\sigma_s = \frac{\ell n 2}{\pi} \left(\frac{I}{V} - \left(\frac{I}{V}\right)_o\right)$$

Taking the thickness of the conducting layer at saturation as being again either 300 or 3000 Å, one finds that the bulk resistivity of the layer is about 3×10^{-3} or 3×10^{-2} ohm.cm, as compared with 10^4 ohm.cm for the starting material.

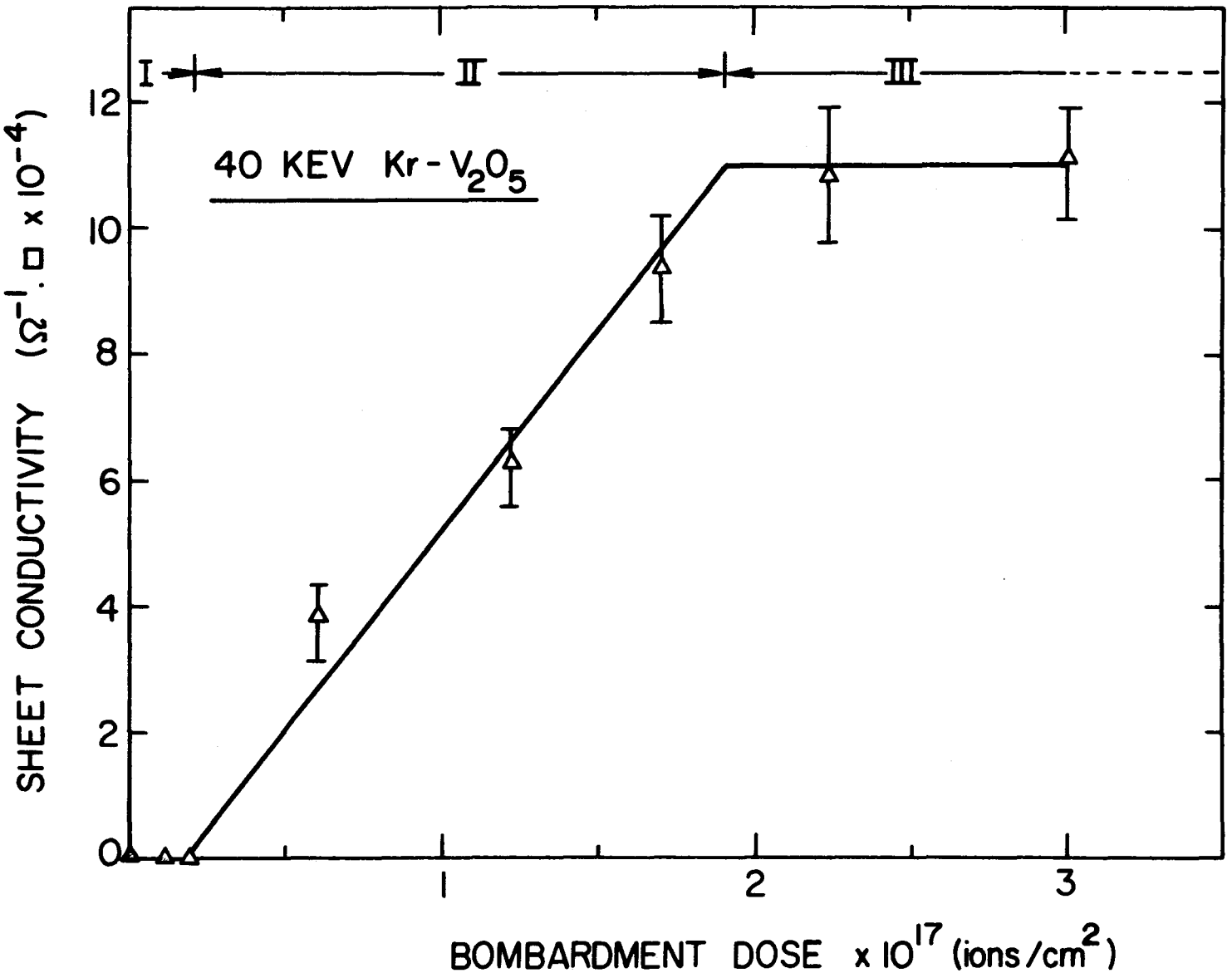

Fig. 8.4 Sheet conductivity vs. bombardment dose for V_2O_5 specimens bombarded with 40 KeV-Kr.

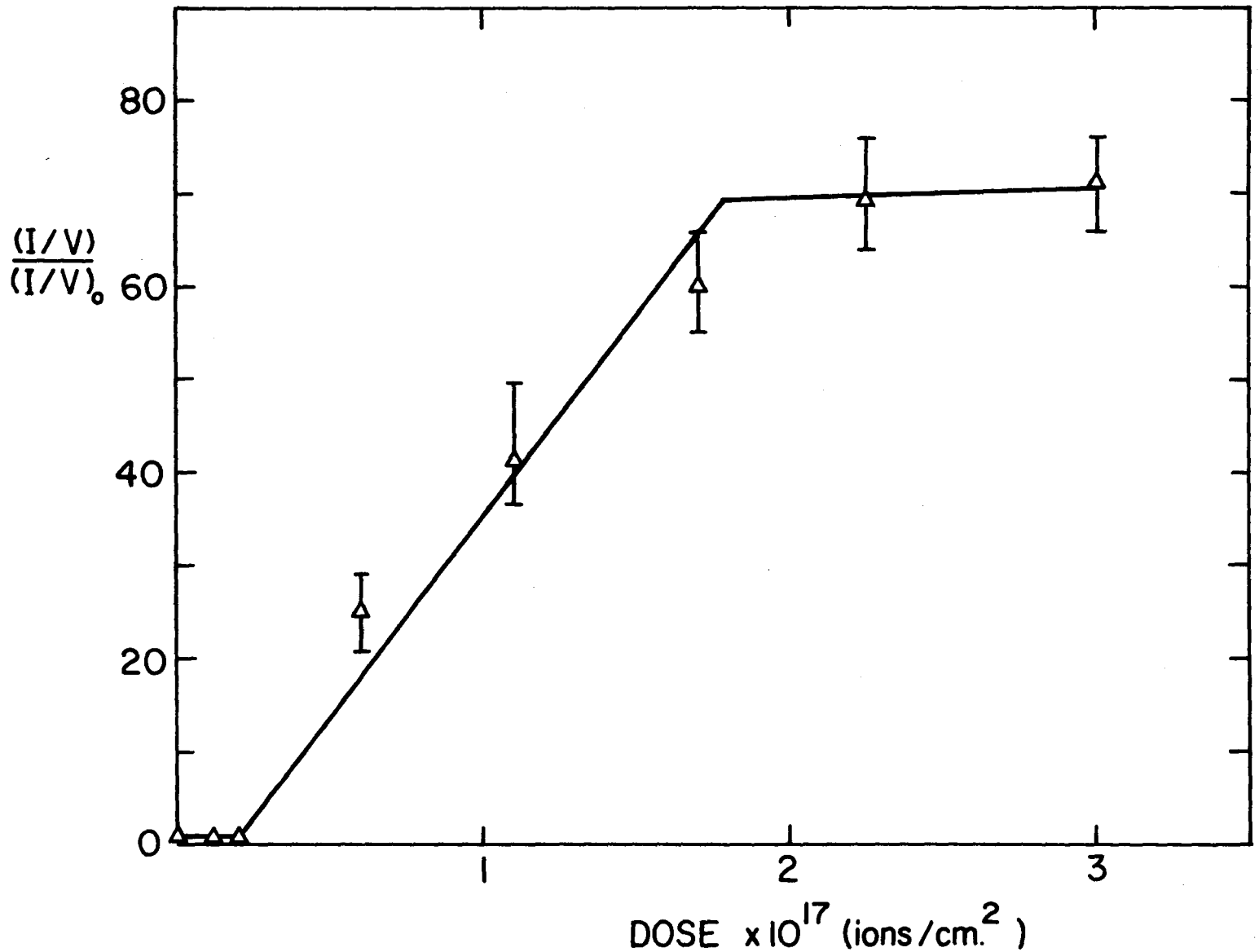

Fig. 8.5 Conductivity measurements of V_2O_5 represented in terms of the ratio $(I/V)/(I/V)_0$, where $(I/V)_0$ is the initial value of (I/V).

(a)

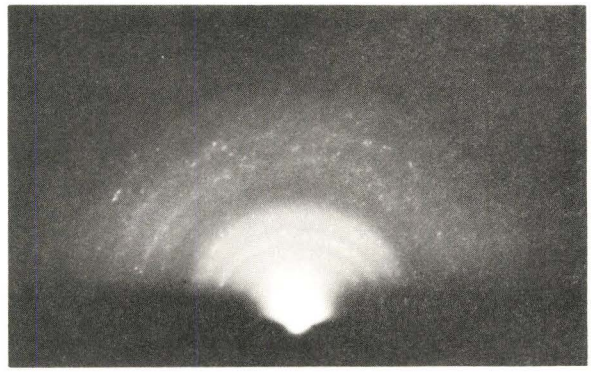

(b)

(c)

Fig. 8.6 Reflection electron diffraction patterns of V_2O_5: (a) before bombardment, (b) after bombardment with 9×10^{15} ions/cm^2, 40 keV Kr, and (c) after 3×10^{17} ions/cm^2, 40 keV Kr. Note that Fig. 8.6(a) and (b) are the same as Fig. 7.11(a) and (b).

Table (8.3)

Diffraction analysis of V_2O_5 following bombardment with 3×10^{17} ions/cm^2 of 40 keV-Kr

d values in Å, as calculated from Fig. (8.6.c)*	V_2O_3 ASTM I - 1293 dÅ	I/I_o
3.81	3.65	60
2.72	2.70	80
2.56	2.47	60
....	2.32	2
2.20	2.18	20
....	2.03	2
1.82	1.83	25
1.70	1.69	100

*See appendix (A), sec. (A.3)

As shown in Fig. (8.6), the diffraction patterns of bombarded V_2O_5 indicate a gradual transformation from a crystalline to amorphous state (as described in sec. 7.5.) , and then to a new polycrystalline structure. The final crystallization product is apparently V_2O_3 (table 8.3), which has a corundum structure at room temperature. This identification was made taking into account the eight known oxides from V_2O_3 to VO_2 as well as V_2O_5, for all of which diffraction data were available. Information on the oxides from VO_2 to V_2O_5 is much less complete and these were not considered. The possibility therefore exists here, as with MoO_3, that the new crystalline phase was not V_2O_3 but rather another oxide (known or unknown) which had a diffraction pattern similar to V_2O_3. (Cf. Appendix (A) sec.(A.3)).

8.3.3 Stability of conductivity changes

Further experiments were carried out to determine if the conductivity increases with MoO_3 and V_2O_5 were, like those found by Griffiths with Al_2O_3 and MgO [218], of a transient nature. The results for specimens stored in air at room temperature are shown in Fig.(8.7) from which we see that the times for one-half conductivity loss are ~6 hours for MoO_3 and ~12 hours for V_2O_5.

The conductivity increases are thus of an intermediate degree of transiency. The loss of conductivity is undoubtedly due to re-oxidation of the MoO_2 or V_2O_3 and, as such, could be prevented by depositing a surface film such as SiO_2.

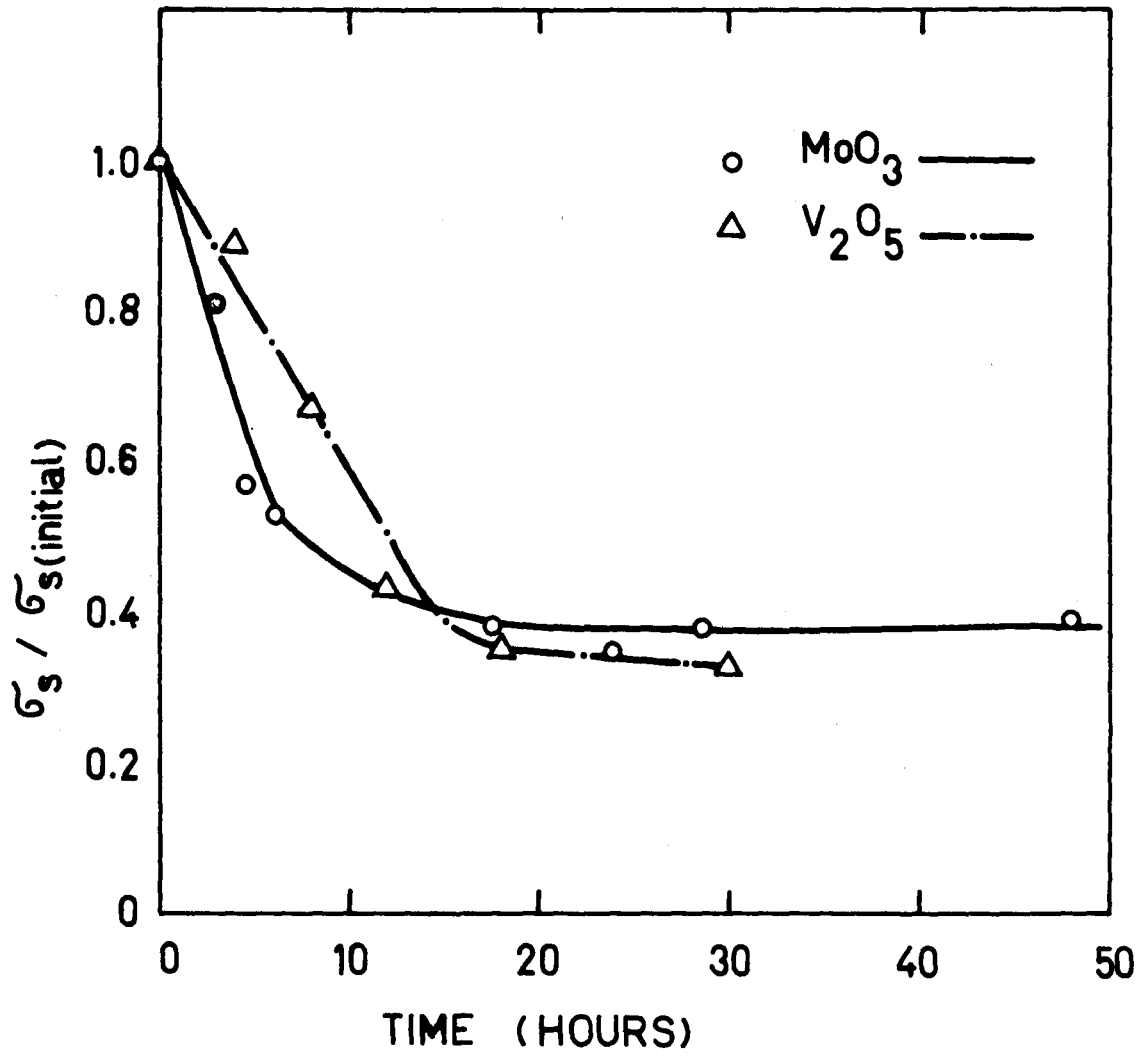

Fig. 8.7 The decrease in the conductivity for MoO_3 and V_2O_5 specimens bombarded with 3.7×10^{17} ions/cm^2 of 40 KeV-Kr and stored in air at room temperature.

8.4 Discussion

The main results of the present chapter involve a demonstration that ion impact on MoO_3 and V_2O_5 causes a marked conductivity increase and, at the same time, a conversion of the surface layers first to an amorphous state and then to crystalline MoO_2 and V_2O_3. Evidence for the appearance of lower oxides during bombardment has been previously noted for Fe_2O_3 and CuO in work by Wehner et al. [227], while the closely analogous phenomenon of preferential sputtering from binary alloys was described by Gillam [228]. This section is, therefore, intended to discuss the results in terms of three effects: whether the conductivity changes are related to the appearance of the lower oxides, the mechanism for the formation of the lower oxides, and the reason for the lower oxides being crystalline. In addition, the practical implications of the effect will be briefly discussed.

8.4.1 Relation between conductivity and oxide type

MoO_3 and V_2O_5 are representatives of a group of oxides in which the random oxygen vacancies which ordinarily lead to non-stoichiometry can be effectively removed from the system by clustering, such that various intermediate phases ("shear structures") having properties different from those of the parent compound are generated [229]. There are seven known examples in the series MoO_2 to MoO_3 [224], including MoO_3 (a semi-conductor with very high resistivity at room temperature [230]), $Mo_{17}O_{47}$ (which has the lowest resistivity in the series [224]), and MoO_2 (a material whose conduction type is still unsettled [231] though which

has a relatively low resistivity [232]), The series V_2O_3 to V_2O_5 is even more complex, there being 12 known phases (App. (A), table A.3) of which the following are metallic at room temperature: V_2O_3, V_4O_7, V_5O_9, V_6O_{11}, V_7O_{13} [233]. Of the remainder, four have yet to have their conductivity type determined: V_8O_{15}, V_6O_{13}, V_4O_9, V_3O_7.

The properties of those Mo and V oxides which are important in the present context, as well as certain experimental results, are summarized in Table (8.4). Considering both the compositions and the resistivities, there is seen to be an obvious correlation between the conductivity changes and the structural changes.

8.4.2 Mechanism for formation of lower oxides

The problem of why lower oxides should appear during ion bombardment of MoO_3 and V_2O_5, i.e. of why oxygen should be preferentially lost, can be settled only in part with the information available. The crucial detail is, in our opinion, the thickness of the altered surface layer. Direct measurements of this thickness are, unfortunately, still unavailable, though a rough estimate can still be made based on the fact that the conductivity increases are complete at about 2×10^{17} ions/cm^2.*

Let us assume that saturation (as in Fig. 8.2) occurs when the sputtered thickness becomes comparable to the altered thickness. Taking the sputtering coefficients, S, for 40 keV Kr impact on MoO_2 or V_2O_3 as

---

*One might at first sight think that the diffraction patterns also serve to estimate the thickness. Thus the patterns of the MoO_2 or V_2O_3 formed with 40 keV Kr normally showed no traces of the underlying MoO_3 or V_2O_5 for an electron energy of 60 KV, from which we conclude that the total altered layer is > 50 Å thick. We thus obtain only a lower limit to the thickness, and the actual altered thickness could, in principle, be much thicker.

Table (8.4)

Bulk resistivities for Mo and V oxides

Oxide	Bulk resistivity from present work (ohm.cm)	Bulk resistivity from previous work (ohm.cm)
a. Mo-oxides:		
unbombarded MoO_3	$>>10^7$	$>10^8$[230]
bombarded MoO_3 (i.e. MoO_2)	0.01 to 0.1	....
$Mo_{17}O_{47}$*	....	<0.05[224]
MoO_2	....	~0.5[232]
b. V-oxides:		
unbombarded V_2O_5	10^4	10^4; 300[225,226]
bombarded V_2O_5 (i.e. V_2O_3)	0.003 to 0.03	
V_4O_7, V_5O_9, V_6O_{11}, V_7O_{13}*	....	10^{-1} to 10^{-3}[233]
V_2O_3*	....	10^{-2} to 10^{-3}[234,235]

*These oxides have the significance of showing the lowest resistivities in each of the series considered.

being similar to the extrapolated values for TiO_2 or Al_2O_3, i.e. about 4 atoms/ions [236], the altered thickness follows as

$$x = BtS/N \approx 1000 \text{ Å}.$$

Here Bt is the bombardment dose and N the atomic density. The altered thickness is thus atomically large.

The point is that such a thickness is not possible if the preferential oxygen loss is due solely to a surface effect such as normal sputtering [221] or bombardment-enhanced vaporization [36]; rather, a long-range effect, i.e. one which either correlates with the damage mean range or involves diffusion, is indicated (perhaps in conjunction with a surface effect). Significantly, Gillam [228] reached a similar conclusion for his binary alloys, namely that the altered layer had a thickness which was established by the diffusion of point defects.

There will be no further speculation on the details of the mechanism for oxygen loss except to point out an important property of both MoO_3 and V_2O_5. Oxygen appears to be exceedingly mobile in these oxides, as shown by the fact that specimens having effective radii of 10,000 to 30,000 Å exchange all their oxygen, with the exchange step at the surface (rather than diffusion in the bulk) being rate controlling (e.g. [210]). This removes a possible objection to mechanisms involving diffusion, though in no way proves them necessary.

8.4.3 Crystallization of MoO_2 and V_2O_3

The transition, during the bombardment of MoO_3 and V_2O_5, from an amorphous state to a state consisting of crystalline MoO_2 and V_2O_3 was not expected.

Amorphous-crystalline transitions induced by bombardment have been confirmed previously with ZrO_2 (Ch. 6), SiO_2 [130], and Ge [132,134], being extensive only in the first case. However, with MoO_3 and V_2O_5 the transformation was accompanied by a change in the chemical composition and the mechanism of the crystallization should be different from those discussed for ZrO_2, SiO_2, and Ge. We would suggest that with MoO_3 and V_2O_5 there is a possible analogy with systems such as FeO/Fe_2O_3 and UO_2/U_3O_8, where only the higher oxide has a stable amorphous state (tables (4.1))*. Thus, as more and more oxygen is driven from MoO_3 and V_2O_5, crystallization sets in spontaneously. (This result agrees, incidentally, with the discussion on bond character in sec. 7.6.3 . Higher valence states tend to have higher electronegativities, thence (when interpreted in terms of the difference $X_{cation}-X_{oxygen}$) greater extents of covalency).

A possible objection to this argument might lie in why V_2O_3 crystallizes spontaneously, whereas the isostructural substances Al_2O_3, Cr_2O_3, and Fe_2O_3 do not. The point here is probably that the structure is irrelevant; it appears from sec. 7.6.3 to be the bond character alone which is important.

---

*FeO has not been studied explicitly, but the closely related compounds CaO, MgO, and NiO also resisted amorphization [74].

8.4.4 Implications

The effects described here may have important implications. (a) They show that there may be a severe limitation on the use of certain oxides in a radiation environment, particularly if the oxides are being used in their traditional role as high-voltage insulators. (b) They show that, if one desires either to prepare thin films by sputtering oxide cathodes or else to clean an already prepared film by ion impact, it is important to know whether the oxide is subject to preferential oxygen loss. (c) They suggest an approach for developing new solid-state devices: for example, conductive patterns could be traced out on insulating or semi-conducting oxides simply by bombarding them through a mask.

CHAPTER 9

SUMMARY AND SUGGESTIONS FOR FURTHER RESEARCH

9.1 Summary

1. ZrO_2 can be readily prepared as a thin, amorphous film by ion-beam sputtering of anodized Zr and collection of the deposit on unheated KCl.
2. The amorphous-crystalline transition of ZrO_2 occurs at 520 ± 10°C in 5 min for macroscopically heated specimens. The crystallization products initially give a diffraction pattern comparable to that of cubic ZrO_2, though with weak lines attributable to monoclinic ZrO_2 also present.
3. The crystallization process involves a large increase in the apparent particle size from ≥10 Å to 300-500 Å, and is governed by an activation enthalpy in the vicinity of 50 kcal/mole (present data) or possibly somewhat lower (data of Livage)
4. It has been demonstrated, for the first time, that crystalline regions are also formed during high-dose bombardment of amorphous ZrO_2 with 2-35 KeV krypton ions. It was possible to show that this crystallization was a dominantly impact effect, for low ion currents (< 20 $\mu A/cm^2$), as far as nucleation is concerned, and any heating during or after bombardment served mainly to assist the growth of the bombardment-induced nuclei.

5. Considering the behaviour of ZrO_2 alone, a final decision as to the mechanism leading to bombardment-induced crystallization is not possible. Displacement cascades, thermal spikes, as well as radiation-enhanced diffusion (with either thermal spike or ion-beam heating) can be each easily rationalized.
6. Combining our understanding of ion-impact crystallization of amorphous ZrO_2 with the results concerning the behaviour of 20 other solids, a thermal-spike model is presented which predicts the behaviour of these materials under ion impact.
7. According to this model, the criterion for the preservation of disorder (amorphousness) following ion impact is that $D_c t/\lambda$ be much less than λ, where D_c is the diffusion coefficient for crystallization, t is the effective duration of a thermal spike measured for temperatures below the melting point ($\approx 7 \times 10^{-12}$ sec), and λ is the mean atomic spacing. This in turn implies a further relation, namely that the ratio T_c/T_m = (crystallization temperature)/(melting temperature) be greater than 0.23 ± 0.07. Significantly, twelve substances which amorphize readily have $T_c/T_m > 0.35$, while eight substances which are stable (including ZrO_2 which shows the sequence amorphous → crystalline) have $T_c/T_m \leq 0.27$.
8. It is argued that possible refinements to the thermal-spike model would include taking excess vacancies into account and allowing for surface free-energy effects.

9. It has been suggested if the thermal-spike model is really valid, then it should be possible to make certain predictions. Specifically, TeO_2, MoO_3, V_2O_5, and Bi_2O_3 have values of T_c and T_m which are such as to imply that they will amorphize under ion impact, such amorphization occurring in spite of T_c being rather low.

10. Using gas-release measurements and reflection electron diffraction, it has been shown that TeO_2, MoO_3, V_2O_5 and Bi_2O_3 behave as predicted. Thus, they amorphize under ion impact at relatively low doses ($< 1 \times 10^{14}$ ions/cm^2). Moreover, the values of T_c are found in all cases to be even lower than expected, so the test of the model is particularly stringent.

11. Other criteria for the stability of materials on irradiation have been discussed. Thus, using the results of 38 oxides and non-metallic substances it has been shown that an anisotropy criterion based on whether the crystal structure is cubic or non-cubic, is not satisfactory.

12. Alternatively, a bond-type criterion based on estimating the amount of ionic character has been shown to be a useful guide for predicting the stability of materials on irradiation. Significantly, 18 substances which amorphize readily have an amount of ionic character ≤ 0.55, 10 substances which are stable have values ≥ 0.67, and 5 substances with varying behaviour have values of ionic character ranging between 0.60 and 0.63.

13. Two criteria thus appear to be reasonably successful in predicting radiation-stability. These are the thermal-spike model , which centers on the value of the ratio T_c/T_m, and the bond-type model.

The latter concerns the amount of ionic bond character. The two criteria are perhaps different descriptions of the same underlying properties, though it did not appear feasible to pursue the subject further.

14. Materials that have a number of structural modifications are expected to be more susceptible to structural alterations under irradiation. This is, however, only a very rough guide for predicting the stability on irradiation.

15. Somewhat unexpectedly, reflection electron diffraction indicates a major structural evolution induced by high-dose bombardment of MoO_3 and V_2O_5. Thus, the initially crystalline MoO_3 and V_2O_5 first amorphized ($\geq 4 \times 10^{13}$ ions/cm^2), but subsequently crystallized ($> 1 \times 10^{16}$ ions/cm^2) to lower oxides. The appearance of these lower oxides, MoO_2 and V_2O_3, is an indication of preferential oxygen loss.

16. The formation of the lower oxides was accompanied by a marked resistivity decrease. With MoO_3 it amounted to a decrease of $>>10^8$ in the bulk resistivity (from $>>10^7$ Ωcm to 10^{-1} Ωcm), while with V_2O_5 it amounted to a decrease of 10^6 (from 10^4 Ωcm to 10^{-2} Ωcm).

17. MoO_2 and V_2O_3 are known from other work to be either metallic or nearly so, with bulk resistivities of roughly 0.5 Ωcm (MoO_2) and 0.01 Ω cm (V_2O_3); their presence is thus fully sufficient to explain the results.

18. The reason for the preferential loss of O_2 from MoO_3 and V_2O_5 is only partially understood. The fact that the altered layers have

thicknesses of roughly 1000 Å shows convincingly, however, that neither sputtering nor bombardment enhanced vaporization is by itself the cause of the loss. Rather a long-range effect, i.e. one which involves diffusion, is indicated perhaps in conjunction with a surface effect.

19. It is pointed out that a necessary, though not sufficient, condition for a diffusion effect being involved in the preferential oxygen loss is that oxygen be mobile. A significant detail is therefore that MoO_3 and V_2O_5 (along with WO_3) are nearly unique amongst oxides in showing rapid and complete exchange with isotopically-labeled oxygen.

9.2 Suggestions for further research

There are several additional areas of investigation which this study has suggested.

(1) Experimental studies of bombardment-induced conductivity increases in oxides have great practical implications as outlined in sec. (8.4.4). A research program should be developed to study this phenomenon, in the following respects:

(a) Investigating the phenomenon in other oxides besides V_2O_5 and MoO_3. Of particular interest are those oxides which have a large number of intermediate and non-stoichiometric phases such as WO_3, TiO_2, Ta_2O_5, and Nb_2O_5.

(b) Analyzing the altered layers on the bombarded oxides by backscattering and channeling effects. These techniques will give valuable information on the composition and the depth of the altered layer.

(c) Studying the electrical properties of the altered layers with a view to the possibility of developing solid-state devices. Possible devices include thin film resistors (an obvious application), rectifying diodes (perhaps possible with V_2O_5 since V_2O_5 is naturally an n-type semiconductor), and switches (perhaps possible in those cases such as VO_2 where a metal-semiconductor transition occurs just above room temperature).

(d) Further experimental studies should provide the necessary information required for complete understanding of the problem of the preferential loss of oxygen from oxides on bombardment. A quantitative model could be then developed.

(2) Future research on bombardment-induced crystallization of amorphous ZrO_2 or other oxides could involve:

(a) Further investigations on the temperature dependence of radiation-enhanced crystallization. For this purpose, it would be helpful to have a proper cooling stage for the ion accelerator so that low-temperature bombardments could be undertaken.

(b) Studying the effect of the mass of the bombarding ions on the crystallization. Light ions (e.g. H^+ or He^+ ions) would be particularly interesting since they simulate the effect of neutron irradiation though under controlled bombardment conditions.

(c) It would be possible, then, to reach a final decision on a more quantitative basis about the mechanism of the crystallization process.

(3) It would be interesting to verify more predictions from those anticipated from the thermal-spike model given in Ch. 6. This could involve:

(a) Testing the radiation stability of crystalline BeO, MgF_2, ZnO, Co-Au, and Cu-Ag alloys, which have been predicted to be stable under ion impact.

(b) Bombarding amorphous films of materials that show good radiation stability such as UO_2, ThO_2, and other substances as given in table (4.1). They should undergo bombardment-induced crystallization similar to that found with amorphous ZrO_2.

(c) Determining the crystallization temperatures for amorphous CaF_2, LiF, NaCl, and UC and comparing them with the predicted values.

(d) The model suggests that if highly disordered (amorphous) regions induced by irradiation undergo self annealing during bombardment then a metastable crystalline phase may possibly arise. Thus monoclinic ZrO_2 is well known to be transformed to the cubic form under normal bombarding conditions, but an amorphous state might possibly arise in a low-temperature bombardment. Also, α-Al_2O_3 transforms to the amorphous form under normal conditions but might yield the γ-(cubic) form at higher temperatures. This prediction is particularly worth investigating in future work, because it could provide a more complete understanding of the phenomenon of bombardment-induced structural changes.

(4) The above experiments, which are all basically concerned with the thermal-spike model of chapter 6, have an importance beyond the limited topic of bombardment-induced transformations. This is because direct evidence for thermal spikes playing a role in radiation damage is very limited.

(5) Other areas of research could involve:

(a) Studying the effect of the method of preparation on the structure of amorphous materials. This could explain, for example, the difference in the crystallization behaviour of an amorphous substance prepared by different methods.

(b) Studying the crystallographic modifications which arise during crystallization. In some cases, such as TeO_2, the results are apparently trivial, but in others, such as Bi_2O_3, we have shown in chapter 7 that metastable forms arise. Nb_2O_5 might be the most fruitful of all as it has at least seven subtley different crystal variants and possibly many others.

(c) Studying the crystallographic modifications which arise during oxygen loss as with V_2O_5 and MoO_3. The main problem here is that the oxides tend to remain amorphous until a low oxide is reached, but if crystallinity could be restored, as by heating in vacuum, it might prove feasible to synthesize entire series of shear phases.

APPENDIX (A)

ANALYSIS OF ELECTRON DIFFRACTION DATA

A.1 General

Throughout this dissertation, the structures of the materials used, before and after irradiation, were determined by electron diffraction. The observations were made with the normal transmission electron diffraction aspect of the "Siemens Elmiskop I" operated at 100 KeV, for the ZrO_2 thin films, and with the reflection electron diffraction attachment of the Philips EM-300 operated at 60 and 80 KeV for the sintered pellets of TeO_2, MoO_3, V_2O_5, and Bi_2O_3. In either case, the interplanar spacings, d in $\mathring{A}$, were calculated according to the equation:

$$d = \frac{\lambda L}{R} , \qquad (A.1)$$

where λ is the electron wave length, in $\mathring{A}$; L is the camera length, or the distance from the specimen to the screen or plate, in cms; and R is the polycrystalline ring radius, i.e. the distance from the central spot of the pattern, in cms. The factors affecting the accuracy in determining the d spacings using Eq. (A.1) are discussed in detail by Hirsch et al. [Ref. 206 , sec. 5.7].

In practice, the values of λ and L are not measured separately but are determined as a product λL (constant for a given experimental arrangement) by diffracting from a polycrystalline calibration specimen whose lattice spacings are known accurately from x-ray measurements.

An Au pattern has been used in our case, and the product λL, known as the camera constant in units of $\mathring{A}$.cms, has been determined for the cases given in table (A.1).

Table (A.1)
The camera constants

Experimental* arrangement	electron energy(KeV)	wave length($\mathring{A}$)	camera const. λL ($\mathring{A}$ cm)
TED with Siemens (I) EM	100	0.037	1.99
RED with Philips EM-300	80	0.042	1.65
RED " " "	60	0.049	1.90

*TED ≡ Transmission Electron Diffraction
RED ≡ Reflection Electron Diffraction

When the camera constant is determined, for the given experimental arrangement, attempts can be made to identify an unknown structure by using Eq. (A.1) to generate a set of d values. These values are then compared with those reported in the standard ASTM cards for the oxides which are expected.

When using x-ray data in connection with electron diffraction patterns, it must be remembered that the structure factor F is different for x-rays and electrons. Thus, lines appearing in the x-ray pattern may not appear in the electron diffraction pattern and vice versa, and intensities are different.

A.2 On the structure of the crystallization product of amorphous ZrO_2

The analysis of electron diffraction patterns of the crystallization products of amorphous ZrO_2 (table 5.1) shows that the structure is nominally

cubic except for a few weak rings in the diffraction pattern. Such extra rings were also obtained for ZrO_2 prepared by anodic oxidation [154], by thermal heating of Zr in O_2 at 300°C [158a], and by vacuum evaporation [162]. In an attempt to reveal the origin of these extra rings, a special technique was used to obtain the diffraction pattern in which the beam current was reduced to almost zero, all intermediate apertures were removed, and then the intermediate lens control and condenser II fine control were adjusted to obtain well focussed photographs. Using this technique, a diffraction pattern similar to that obtained from dominantly monoclinic thin films (Fig. (A.1c)) was found superimposed on the nominally cubic diffraction pattern as shown in Fig. (A.1b). The original diffraction pattern (i.e. Fig.(A.1a)) of the same area is restored when the diffraction conditions returned to normal, i.e. when using an intermediate aperture of 50μ diameter. In effect, the pattern

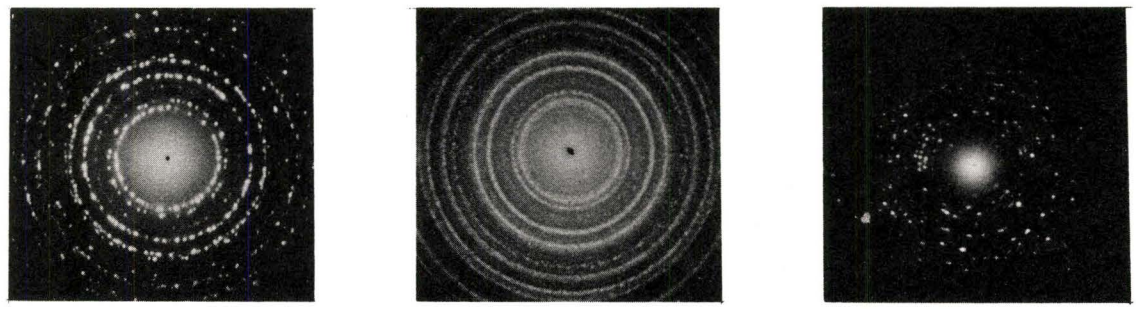

(a) (b) (c)

Fig. (A.1) Nominally cubic ZrO_2, (b) nominally cubic ZrO_2 with weakly superimposed monoclinic rings, and (c) monoclinic ZrO_2.

in Fig. (A1.b) is not due to any heating effect. It was concluded, therefore, that the extra rings in diffraction patterns similar to Fig. (A1.a) were part of the set corresponding to the monoclinic structure but which had been too weak to be characterized by the usual diffraction technique. We have no explanation, however, as to why these particular extra rings appeared in the cubic patterns.

A.3 Available diffraction data for Mo and V-oxides

The available diffraction data for Mo and V-oxides are given in tables (A.2) and (A.3). The d-values estimated from the diffraction patterns of high-dose bombarded MoO_3 and V_2O_5 (given in table (8.1) and and (8.3) respectively), calculated as described in sec. (A.1), have been compared with these available data to determine the crystal structure.

Table (A.2)

Available Diffraction Data for Mo-Oxides

MoO_3 ASTM 5 - 0508		η-MoO_3* ASTM-9 - 209		Mo_9O_{26} ASTM 12 - 753	
dÅ	I/I_o	dÅ	I/I_o	dÅ	I/I_o
6.93	34	6.04	10	7.21	40
3.81	82	3.92	100	6.15	20
3.463	61	3.60	60	4.029	40
3.260	100	3.39	30	3.763	15
3.006	13	3.34	10	3.610	15
2.702	19	2.811	10	3.576	100
2.655	35	2.717	30	3.515	20
2.607	6	2.669	30	3.366	100
2.527	12			3.361	15
2.332	12			3.285	20
...	...			...	...

*high temperature form

Table (A.2) cont'd...

Mo_9O_{26}(At 750°C) ASTM 5 - 0441 dÅ	I/I_o
8.4	10
7.5	15
7.0	20
5.75	35
4.37	60
4.18	20
4.11	10
4.02	90
3.90	70
3.79	55
...	...

Mo_8O_{23}(At 700°C) ASTM 5 - 0339 dÅ	I/I_o
8.1	10
6.13	30
4.47	60
4.22	20
4.05	100
3.96	60
3.47	70
3.42	90
3.32	10
3.26	25
...	...

Mo $O_{2.80}$ ASTM 12 - 517 dÅ	I/I_o
11.5	40
10.25	40
7.260	40
6.375	15
5.741	20
5.407	40
5.139	15
4.267	15
3.938	100
3.831	60
...	...

$Mo_{17}O_{47}$ ASTM 13 - 345 dA	I/I_o
14.57	60
10.83	40
9.82	40
9.48	40
8.91	40
7.260	40
5.597	35
4.462	35
4.219	60
4.051	40
...	...

Mo_4O_{11} ASTM 13 - 142 dA	I/I_o
9.63	40
6.67	40
6.054	40
5.640	20
4.706	45
4.219	55
4.044	20
3.928	100
3.675	20
3.601	95
...	...

*Mo_4O_{11} ASTM 5 - 0337 dA	I/I_o
12.3	30
5.19	10
4.53	25
4.24	45
4.00	100
3.95	65
3.75	95
3.48	85
3.33	10
3.26	20
...	...

*high temperature form

Table (A.2) cont'd...

MoO_2 ASTM 5 - 0452 dÅ	I/I_o
4.78	20
3.41	100
2.804	30
2.433	50
2.420	85
2.405	40
2.397	50
2.176	30
2.171	10
2.147	30
...	...

Table (A.3)

Available Diffraction Data for V - Oxides

V_2O_5 ASTM 9 - 387 dÅ	I/I_o
5.76	40
4.38	100
4.09	35
3.48	7
3.40	90
2.88	65
2.76	35
2.687	15
2.610	40
2.492	7
...	...

V_3O_5 ASTM 9 - 148 dÅ	I/I_o
4.64	50
4.15	30
3.29	100
3.24	30
2.86	100
2.63	100
2.51	50
2.458	10
2.417	50
2.316	10
...	...

VO_2 ASTM 9 - 142 dÅ	I/I_o
3.31	30
3.20	100
2.68	30
2.43	40
2.422	60
2.418	30
2.139	50
2.131	50
2.048	10
2.022	30
...	...

Table (A.3) cont'd...

V_8O_{15} ASTM 10 - 349	
dÅ	I/I_o
4.44	20
3.66	40
3.28	100
3.10	80
2.98	60
2.57	20
2.56	20
2.493	40
2.439	40
2.425	50
...	...

V_7O_{13} ASTM 10 - 196	
dÅ	I/I_o
5.15	5
4.65	20
4.04	5
3.74	70
3.30	80
3.25	40
3.09	80
2.97	100
2.72	5
2.71	5
...	...

V_6O_{11} ASTM 11 - 4	
dÅ	I/I_o
5.06	5
4.87	10
3.84	80
3.32	100
3.19	20
3.06	100
2.93	100
2.79	10
2.62	40
2.58	10
...	...

V_5O_9 ASTM 10 - 55	
dÅ	I/I_o
7.74	5
5.10	20
3.97	80
3.36	5
3.32	100
3.28	5
3.17	5
3.08	10
3.04	80
2.90	5
...	...

V_4O_7 ASTM 11 - 3	
dÅ	I/I_o
6.06	5
5.16	20
4.10	50
3.70	10
3.33	100
3.28	20
3.06	20
2.98	70
2.86	20
2.78	70
...	...

V_2O_3 ASTM 1 - 1293	
dÅ	I/I_o
3.65	60
2.70	80
2.47	60
2.32	2
2.18	20
2.03	2
1.83	25
1.69	100
1.61	2
1.57	3
...	...

Table (A.3) cont'd...

VO		$VO_{0.2}$	
ASTM 10 - 313		ASTM 10 - 321	
dÅ	I/I_o	dÅ	I/I_o
2.38	30	2.26	100
2.06	80	2.08	80
1.45	100	1.77	30
1.24	60	1.48	50
1.19	60	1.35	60
1.03	50	1.24	100
0.944	50		
0.920	70		

* * *

APPENDIX B

ANALYSIS OF ISOTHERMAL ANNEALING CURVES FOR THE CRYSTALLIZATION OF AMORPHOUS ZrO_2

Livage et al. [159] have published data showing the percentage crystallization of amorphous ZrO_2 as a function of time, deduced from DTA, at temperatures 290 , 300, 315 and 347^{0}C, but they did not analyze their results. In this appendix the activation enthalpy for crystallization is calculated from their data using a standard rate kinetics analysis.

Damask and Dienes [237] have reviewed the various methods of analyzing annealing curves, and the method used here is described as the "method of cross cut". If the thermal crystallization occurs by a single activated process with constant activation enthalpy ΔH, then the rate of increase of crystallization can be expressed as:

$$\frac{dn}{dt} = K_o e^{-\Delta H/kT} \qquad (B.1)$$

where n = fractional crystallization

T = absolute temperature, ^{0}K

K_o = a constant (assuming 1st order)

Since n = 0 at time t = 0, eq. (B.1) integrates to

$$n = K_o t e^{-\Delta H/kT}$$

By drawing horizontal lines, as indicated on Fig. (B.1), it is clear that

$$K_o t_{1e}^{-\Delta H/kT_1} = K_o t_{2e}^{-\Delta H/kT_2}$$

or

$$\ell n \frac{t_2}{t_1} = \frac{\Delta H}{k} \left(\frac{1}{T_2} - \frac{1}{T_1}\right) \qquad (B.2)$$

Thus, by drawing horizontal lines through the published data of Livage et al. [159] as shown in Fig. (B.1), the required activation enthalpy may be determined as given in table (B.1).

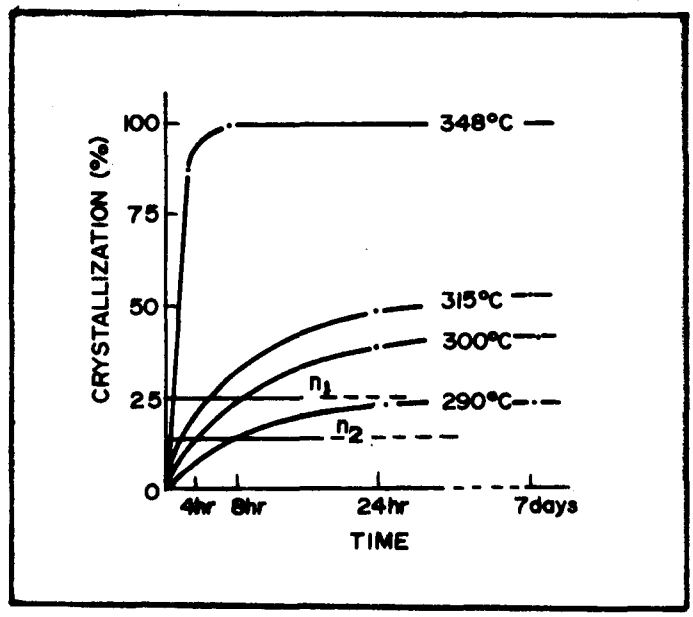

Fig. B.1 Crystallization kinetics of amorphous ZrO_2 deduced from DTA (After Livage et al. [159])

Table (B.1)

n	t_1(hrs)	t_2(hrs)	T_1(^{0}K)	T_2(^{0}K)	ΔH(kcal/mole)
1	1	4	621	588	30.9
1	5	8	588	573	23.7
2	0.5	2	621	588	30.9
2	2	4	588	573	72.0

The scatter is rather extreme, but it is nevertheless clear that one is dealing with a ΔH of roughly 30 to 50 kcal/mole.

APPENDIX (C)

ESTIMATION OF THE TEMPERATURE RISE OF ZrO_2 THIN FILMS DUE TO ION-BEAM HEATING

C.1 Film supported on a grid

We assume a 1000 Å thick ZrO_2 film (with thermal conductivity, κ, 0.01 cal/sec.cm°C) in good contact with a 200 mesh Cu grid and bombarded with 20-KeV ions at a current of 5 $\mu A/cm^2$. The amount of heat, q, produced from such a beam during 60 sec. is 1.43 cal/cm^2. The temperature rise $\Delta T(^\circ C)$, in this case, can be estimated from the relation

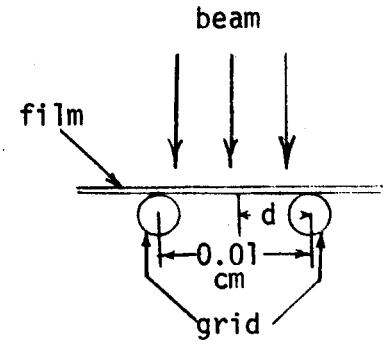

(film supported on a grid)

$$\Delta T = \frac{q.d}{\kappa.a.t}$$

to be 12°C. Note that a, the area, is to be taken as $10^{-5} \times 10^{-2}$ cm^2.

C.2 Film supported on KCl

We assume the same bombardment conditions as in (C.1) but with the film supported on a 2 mm thick KCl substrate. The temperature rise in this case, using the relation in (C.1) is $<<1^\circ C$, which means that it is negligible.

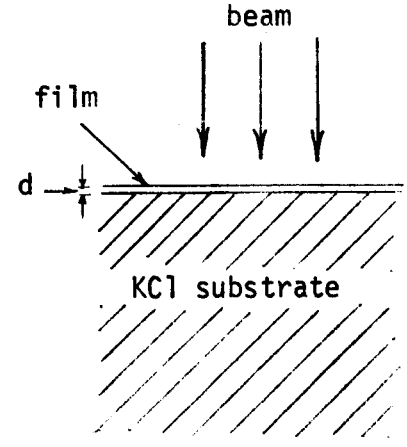

(film supported on KCl)

C.3 Free film

In this case, the temperature rise can be obtained from the relation

$$\Delta T = \frac{q}{n.c.}$$

where n is the specimen weight in gms, c is the heat capacity, 0.16 cal/^{o}C gm, and q is the amount of heat. Assuming a current of 1 $\mu A/cm^2$ for 1/2 min, q works out to 0.143 cal/cm^2 and ΔT will therefore be 2×10^4 ^{o}C. This is extremely high, and could easily evaporate the film.

REFERENCES

1. G. Carter and J. S. Colligon, "Ion bombardment of solids", (Heinemann, London), (1968).
2. R. S. Nelson, "The observation of atomic collisions in crystalline solids", (North-Holland, Amsterdam), (1968).
3. M. W. Thompson, "Defects and radiation damage in metals", (Cambridge Univ. Press, Cambridge), (1969).
4. J. W. Mayer, L. Eriksson, and J. A. Davies, "Ion implantation in semiconductors", (Academic Press, New York), (1970).
5. R. S. Nelson, D. J. Mazey, and J. A. Hudson, J. Nucl. Mat., 37 (1970) 1.
6. D. G. Walker, J. Nucl. Mat., 37 (1970) 48.
7. G. H. Kinchin and R. S. Pease, Rept. Prog. Phys., 18 (1955) 1.
8. F. Seitz and J. S. Koehler, Sol. State Phys., 2 (1956) 307.
9. G. H. Dienes and G. H. Vineyard, "Radiation effects in solids", (Interscience, New York), (1957).
10. D. S. Billington and J. M. Crawford, "Radiation damage in solids", (Princton Univ. Press, Princton), (1961).
11. L. T. Chadderton, "Radiation damage in crystals", (Methuen, London), (1965).
12. M. Kaminsky,"Atomic and ionic impact phenomena on metal surfaces", (Springer-Verlag, Berlin), (1965).
13. B. T. Kelly, "Irradiation damage to solids", (Pergamon Press, New York), (1966).

14. F. Seitz, Disc. Faraday Soc., 5, (1949) 271.

15. J. Lindhard, M. Scharff, and H. E. Schiøtt, Mat. Fys. Medd. Dan. Vid. Selsk, 33 (1963) No. 14.

16. J. Lindhard, V. Nielsen, and M. Scharff, Mat. Fys. Medd. Dan. Vid. Selsk, 36 (1968) No. 10.

17. P. Sigmund, Appl. Phys. Letters, 14 (1969) 114.

18. P. Sigmund, Rad. Effects, 1 (1969) 15.

19. J. R. Beeler, GEC Rept. TM-63-10-13, (1963).

20. P. Sigmund, G. P. Scheidler, and G. Roth, Proc. Conf. on "Solid state research with accelerators", Ed. A. N. Goland, (1967) p. 374.

21. P. Sigmund and J. B. Sanders, Proc. Int. Conf. on "Applications of ion beams to semiconductor technology", Ed. P. Glotin, (Editions Ophrys) (1967) p. 215.

22. K. B. Winterbon, P. Sigmund, and J. B. Sanders, Mat. Fys. Medd. Dan. Vid. Selsk., 37 (1970) No. 14.

23. J. Lindhard, V. Nielsen, M. Scharff, and P. V. Thomsen, Mat. Fys. Medd. Dan. Vid. Selsk., 33 (1963) No. 10.

24. W. S. Johnson and J. F. Gibbons, "Projected range statistics in semiconductors", (Stanford University, U.S.A.), (1970).

25. B. Domeij, F. Brown, J. A. Davies, and M. McCargo, Cand. J. Phys., 42 (1964) 1624.

26. P. Jespersgård and J. A. Davies, Cand. J. Phys., 45 (1967) 2983.

27. H. E. Schiøtt, Cand. J. Phys., 46 (1968) 449.

28. J. L. Whitton and Hj. Matzke, Cand. J. Phys., 44 (1966) 2905.

29. J. B. Sanders, Cand. J. Phys., 46 (1968) 455.

30. L. E. Thomas, T. Schober, and R. W. Balluffi, Rad. Effects, 1 (1969), 257, 269 and 279.

31. L. C. Feldman and J. W. Rodgers, J. Appl. Phys., 41 (1970) 3776.

32. D.I.R. Norris, Phil. Mag., 19 (1969) 653.

33. H. J. Stein, F. L. Vook, and J. A. Borders, Appl. Phys. Letters, 16 (1970) 106.

34. M. W. Thompson and R. S. Nelson, Phil. Mag., 7 (1962) 2015.

35. M. W. Thompson, Phil. Mag., 18 (1968) 377.

36. R. S. Nelson, Phil. Mag., 11 (1965) 291.

37. J. A. Brinkman, J. Appl. Phys., 25 (1954) 961.

38. J. A. Brinkman, Amer. J. Phys., 24 (1956) 246.

39. A. Seeger, In "Radiation damage in solids", (Int. Atomic Energy Agency, Vienna), 1 (1962) 101.

40. A. Seeger, Phys. Letters, 8 (1964) 296.

41. R. Kelly and Hj. Matzke, J. Nucl. Mat., 20 (1966) 171.

42. R. Kelly and Č. Jech, J. Nucl. Mat., 30 (1969) 269.

43. Hj. Matzke, Proc. 5th Jugoslav Summer School on the "Physics of ionized gases", (Herceg-Novi), (1970).

44. R. Kelly and L. Q. Nghi, Rad. Effects, 6 (1970) 247.

45. J.P.S. Pringle, private communication, (1969).

46. L. Q. Nghi, Ph.D. thesis, McMaster University, (1971).

47. R. Kelly, Can. J. Chem., 39 (1961) 2411.

48. Hj. Matzke and Č. Jech, J. Phy. Chem. Solids, 31, (1970) 753 .

49. Hj. Matzke, Solid State Comm., 7 (1969) 549.

50. A. Auskern, J. Amer. Ceram. Soc., 47 (1964) 390.

51. Č. Jech and R. Kelly, Proc. Brit. Ceram. Soc., 9 (1967) 259.

52. G. Carter and L. Leck, Proc. Roy. Soc. A261 (1961) 303.

53. E. V. Kornelsen, Can. J. Phys., 42 (1964) 364; and E. V. Kornelsen and M. K. Sinha, Can. J. Phys., 46 (1968) 613.

54. J. A. Davies and P. Jespergard, Can. J. Phys., 44 (1966) 1631.

55. Hj. Matzke, J. Mat. Sci., 2 (1967) 444.

56. R. Kelly and Hj. Matzke, to be published.

57. R. Kelly and Č. Jech, Proc. Brit. Ceram. Soc., 9 (1967) 243.

58. Hj. Matzke, Phys. Stat. Sol., 18 (1966) 285.

59. Hj. Matzke, Rad. Effects, 3 (1970) 93.

60. R. Kelly, Unpublished work on Ta_2O_5 and Nb_2O_5.

61. Hj. Matzke, Can. J. Phys., 46 (1968) 621.

62. R. Kelly, Č. Jech, and Hj. Matzke, Phys. Stat. Sol., 25 (1968) 641.

63. Hj. Matzke, Z. Naturforschg., 22a (1967) 507.

64. Hj. Matzke, G. Rickers, and G. Sørensen, Z. Naturforschg., 24a (1969) 820.

65. R. Kelly and Hj. Matzke, J. Nucl. Mat., 17 (1965) 179; and Hj. Matzke, unpublished work.

66. Hj. Matzke, Nucl. Appl., 2 (1966) 131.

67. Hj. Matzke, J. Nucl. Mat., 21 (1967) 190.

68. Hj. Matzke, J. Nucl. Mat., 30 (1969) 110; and Hj. Matzke and F. Springer, Rad. Effects, 2 (1969) 11.

69. E. Giani, M.Sc. thesis, McMaster University, (1971).

70. Hj. Matzke, G. Rickers and G. Sørensen, Acta Met., to be published.

71. R. Kelly and F. Brown, Acta Met., 13 (1965) 169.

72. R. Kelly and E. Ruedl, Phys. Stat. Sol., 13 (1966) 55; and E. Ruedl and R. Kelly, J. Nucl. Mat., 20 (1966) 269.

73. C. W. Tucker and F. J. Norton, J. Nucl. Mat., 2 (1960) 329.

74. Hj. Matzke and J. L. Whitton, Can. J. Phys., 44 (1966) 995.

75. Č. Jech and R. Kelly, J. Phys. Chem. Solids, 30 (1969) 465.

76. Č. Jech, Phys. Stat. Sol., 21 (1967) 481.

77. Hj. Matzke, Rad. Effects, 3 (1970) 93. (same as Ref. 59).

78. O. Meyer and J. W. Mayer, J. Appl. Phys., 41 (1970) 4166.

79. S. T. Picraux, N.G.E. Johansson, and J. W. Mayer, in "Semiconductor silicon", (The electrochemical Society, New York), (1969), p. 422.

80. J. M. Fairfield and B. L. Crowder, Trans. Met. Soc., AIME, 245 (1969) 469.

81. K. E. Manchester, J. Electrochem. Soc., 115 (1968) 656.

82. N.G.E. Johansson, D. Sigurd, and K. Björkquist, Rad. Effects, 6 (1970) 257.

83. D. Turnbull and M. H. Cohen, in "Modern aspects of the vitreous state", (Butterworths,London), (1960).

84. W. C. Broegger, Salmonsens Store Illustrerede Konversationslexicon, 1 (1893) 742; Abstract in Z. Krist., 25 (1896) 427.

85. J. Joly, Phil. Mag., 13 (1907) 381; J. Joly and E. Rutherford, Phil. Mag., 25 (1917) 644.

86. A. Hamberg. Geol. För Stochn. Föch., 36 (1914) 31.

87. K. Chudoba and M. Stackelberg, Z. Krist., 95 (1936) 230; 97 (1937) 252.

88. A. Pabst, Am. Mineralogist, 3 (1952) 137.

89. O. Mügge, Zentrallblatt f. Min. u. Geol.,(1922) 721, 753.

90. E. P. Wigner, J. Appl. Phys., 17 (1946) 857.

91. V. V. Penkovskii, "Effects of radiation on metals",(Elsevier, Amsterdam) (1964).

92. J. F. Kircher and R. E. Bowman, "Effects of radiation on materials and components", (Reinhold, New York), (1964).

93. A. C. Damask, in "Studies in radiation effects", Ed. G. J. Dienes, (Gordon and Breach, New York) (1967), Vol. 2.

94. D. Lesueur, C. R. Acad. Sci., 266 (1968) 1038.

95. J. Bloch, J. Nucl. Mat., 2 (1962) 203.

96. W. Primak, Phys. Rev., 110 (1958) 1240.

97. R. W. Berman, M. L. Bleiberg, and W. Yeniscavich, J. Nucl. Mat., 2, (1960) 129.

98. A. Guinier, M. Lambert, and R. Comes, in "Interaction of radiation with solids," Ed. A. Bishay (Plenum Press, New York) (1967) p. 319.

99. U. Gonser and B. Okkerse, J. Phys. Chem. Solids, 7 (1958) 55.

100. F. E. Fugita and U. Gonser, J. Phys. Soc. Japan, 13 (1958) 1068.

101. R. L. Jacobson and G. K. Wehner, J. Appl. Phys., 36 (1965) 2674.

102. U. F. Gianola, J. Appl. Phys., 28 (1957) 868.

103. T. Itoh, T. Inada and K. Kanekawa, Appl. Phys. Letters, 12 (1968) 244.

104. J. R. Parsons, Phil. Mag., 12 (1965) 1159.

105. L. N. Large and R. W. Bicknell, J. Mat. Sci., 2 (1967) 589.

106. D. J. Mazey, R. S. Nelson, and R. S. Barnes, Phil. Mag., 17 (1968) 1145.

107. J. R. Parsons and C. W. Hoelke, in "Radiation effects in semiconductors" (Ed. F. L. Vook) (Plenum, New York) (1968), p. 339.

108. D. J. Mazey and R. S. Nelson, Rad. Effects, 1 (1969) 229.

109. F. H. Eisen, B. Welch, J. E. Westmoreland, and J. W. Mayer, Proc. Conf. Atomic Collision Phenomena in Solids,(North-Holland, Amsterdam), (1970).

110. R. S. Nelson and D. J. Mazey, J. Mat. Sci., 2 (1967) 211.

111. R. S. Nelson and D. J. Mazey, Can. J. Phys., 46 (1968) 689.

112. T. C. McGill, S. L. Kurtin, and G. A. Shifrin, J. Appl. Phys., 41 (1970) 246.

113. Č. Jech and R. Kelly, J. Phys. Chem. Solids, 31 (1970) 41.

114. M. Bertolli, in "Radiation effects in semiconductors" (Ed. F.L. Vook) (Plenum, New York),(1968) p. 311.

115. O. Hauser and M. Schenk, Phys. Stat. Sol., 6 (1964) 83.

116. P. W. Levy and O. F. Kammerer, Phys. Rev., 100 (1955) 1787.

117. M. D. Matthews, AERE (Harwell, England) Rept.- 6802 (1971).

118. I. Reid, M.Sc. Thesis, McMaster Univ., (1971).

119. J. A. Davies, J. Denhartog, L. Eriksson, and J. W. Mayer, Cand. J. Phys., 45 (1967) 4053.

120. J. W. Mayer, L. Eriksson, S. T. Picraux, and J. A. Davies, Cand. J. Phys., 46 (1968) 663.

121. B. L. Crowder, R. S. Title, M. H. Brodsky, and G. D. Pettit, Appl. Phys. Letters, 16 (1970) 205.

122. G. E. Klein, Oak Ridge (U.S.A.), Rept. ORNL-1852 (1955).

123. M. C. Wittels and F. A. Sherrill, J. Appl. Phys., 27 (1956) 643.

124. M. C. Wittels and F. A. Sherrill, J. Appl. Phys., 28 (1957) 606.

125. J. H. Crawford and M. C. Wittels, Proc. 2nd Int. Conf. on the peaceful use of atomic energy (Geneva) P1679, United Nations (1958).

126. M. C. Wittels, J. O. Steigler, and F. A. Sherrill, React. Sci. and Tech., 16 (1962) 237.

127. M. C. Wittels, J. O. Steigler, and F. A. Sherrill,React. Sci. and Tech., 17 (1963) 435.

128. J. Adam and B. Cox, React.Sci. and Tech., 11 (1959) 31; Phys. Rev. Letters, 3 (1959) 543;and React. Sci. and Tech., 17 (1963) 436.

129. O. Hauser and M. Schenk, in "Interaction of radiation with solids", Ed. A. Bishay (Plenum Press, New York), (1967) p. 429.

130. S. Weissmann and K. Nakajima, J. Appl. Phys., 34 (1963) 3152.

131. M. C. Wittels and F. A. Sherrill, Phys. Rev., 93 (1954) 1117.

132. J. R. Parsons and R. W. Balluffi, J. Phys. Chem. Solids, 25 (1964) 263.

133. J. E. Westmoreland and P. Sigmund, Rad. Effects, 6 (1970) 187.

134. C. M. Cox, Jr., Ph.D. Thesis, University of Virginia (1967).

135. Hj. Matzke, Proc. Int. Conf. "Applications of ion beams to semiconductor technology", Grenoble (1967) p. 369.

136. Hj. Matzke, same as Ref. (43) but p. 354.

137. G. R. Piercy, J. Phys. Chem. Solids, 23 (1962) 463.

138. M. J. Buerger, in "Phase transformation in solids", Ed. by R. Smoluckowski (John-Wiley, New York), (1951) p. 183.

139. M. Balarin and M. Schenk, Phys. Stat. Sol., 17 (1966) 91.

140. O. Hauser and H. Schenk, Phys. Stat. Sol., 18 (1966) 547.

141. S. Unger and M. Schenk, Phys. Stat. Sol. (a) 4 (1971) 693.

142. M. E. Fine, "Phase transformations in condensed solids" (The Macmillan Co., New York), (1964).

143. J. Burke, "The kinetics of phase transformations in metals", (Pergamon Press, New York), (1965).

144. H. M. Naguib and R. Kelly, J. Nucl. Mat., 35 (1970) 293.

145. L. I. Maissel and R. Glang, "Handbook of thin-film technology" (McGraw-Hill, New York) (1970).

146. "Non-crystalline solids", Ed. by V. D. Fréchette (John Wiley & Sons, Inc., New York), (1960).

147. D. R. Secrist and J. D. Mackenzie, Amer. Ceram. Soc., 48 (1965) 487.

147a. A. V. Grosse, Science, 145 (1964) 50.

147b. G. Urbain and R. Rossin, C.R. Acad. Sci., 255 (1962) 3161.

148. S. Mader, in "Recrystallization, grain growth, and textures" (ASM, Metal Park, Ohio) (1966) p. 523.

149. S. Mader, in "The use of thin films in physical investigations", Ed. by J. C. Anderson (Academic Press, New York), (1966) p. 433.

150. A. Guinier,"X-ray diffraction", Translated by P. Lorrain, (W.H. Freeman & Co., London), (1963).

151. H. Richter, J. Vac. Sci. and Tech., 6 (1969) 855.

152. H. Richter and G. Breitling, Z. Naturforsch., 13a (1958) 988.

153. C.N.J. Wagner, J. Vac. Sci. and Tech., 6 (1969) 650.

154. P.H.G. Draper and J. Harvey, Acta. Met., 11 (1963) 873.

155. D. L. Douglass and J. Van. Landuyt, Acta. Met., 13 (1965) 1069.

156. R. A. Ploc, Chalk River (Canada), Report AECL-2794 (1967).

157. A.I.Sviridova, Optics Spectroscopy, 13 (1962) 236.

158. Č. Jech, G. M. Zhabrova, S. Z. Roginskii and M. D. Shibanová, Radiokhimiya, 4 (1962) 355.

158[a]. I. I. Korobkov and D. V. Ignatov, Dokl. Akad. Naouk., S.S.S.R., No. 3 (1958) 257.

159. J. Livage, K. Doi, and C. Mazieres, J. Am. Ceram. Soc., 51 (1968) 349.

160. K. S. Mazdiyasni, C. T. Lynch, and J. S. Smith, J. Amer. Ceram. Soc., 48 (1965) 372, and ibid, 49 (1966) 286.

161. R. C. Garvie, J. Phys. Chem., 69 (1965) 1238.

162. I. A. El-Shanshoury, V. A. Rudenko, and I. A. Ibrahim, J. Am. Ceram. Soc., 53 (1970) 264.

163. W. J. McG. Tegart, "The electrolytic and chemical polishing of metals", (Pergamon Press, London), (1959) p. 102.

164. R. D. Misch, Acta Met., 5 (1957) 179.

165. C. S. Barret and T. B. Massalski, "Structure of metals", (McGraw-Hill, New York) (1966).

166. B. G. Bagley and D. Turnbull, J. Appl. Phys., 39 (1968) 5681.

167. B. G. Bagley, H. S. Chen, and D. Turnbull, Mat. Res. Bull., 3 (1968) 159.

168. J. E. Bailey, Proc. Roy. Soc. (London), A279 (1964) 395.

169. H. Rawson, "Inorganic glass-forming systems" (Academic Press, New York) (1967).

170. G. Hass, Optik, 1 (1946) 134.

171. G. Hass, Vacuum, 2 (1952) 331.

172. M. Shiojiri, J. Phys. Soc. Japan, 21 (1966) 335.

173. J. Kakinoki, K. Katada, T. Hanawa, and T. Ino, Acta Cryst., 13 (1960) 171.

174. W. H. Zachariasen, J. Amer. Chem. Soc., 54 (1932) 3841.

175. M. Denoux and J. J. Trillat, Compt. Rend. Acad. Sci. Paris, 258 (1964) 4683.

176. Yu. M. Polezhaev, Russ. J. Phys. Chem., 41 (1967) 1590.

177. M. L. Lieberman and R. C. Medrud, J. Electrochem. Soc., 116 (1969) 242.

178. M. L. Lieberman, J. Appl. Phys., 40 (1969), 2659.

179. P. T. Sarjeant and R. Roy, Mat. Res. Bull., 3 (1968), 265.

180. W. H. Rhodes and R. E. Carter, J. Am. Ceram. Soc., 49 (1966) 244.

181. S. K. Bhattacharyya, G. Srinivasan, and N. D. Ganguly, J. Indian Chem. Soc., 41 (1964) 233.

182. A. Natarajan, G. V. Chandrashekhar, C.N.R. Rao., Chem. Eng. Data, 13 (1968) 235.

183. A. L. Dragoo and J. J. Diamond, J. Am. Ceram. Soc., 50 (1967) 568.

184. G. Hass and A. P. Bradford, J. Opt. Soc. Amer., 44 (1954) 810.

185. R. Kelly and H. M. Naguib, in "Atomic collision phenomena in solids", Eds. D. W. Palmer et al. (North-Holland, Amsterdam) (1970) p. 172.

186. C. J. Beevers and R. S. Nelson, Phil. Mag., 8 (1963) 1189.

187. V. M. Fetz and H. Oechsner, Zeit. Angew. Phys., 12 (1960) 250.

188. J. R. Pierce, "Theory and design of electron beams" (Van Nostrand New York) (1954) p. 98.

189. G. J. Dienes, in "Interaction of radiation with solids", Ed. A. Bishay (Plenum Press, New York), (1967) p. 445.

190. P. A. Thackery and R. S. Nelson, Phil. Mag., 19 (1969) 169.

191. M. H. Cohen and D. Turnbull, J. Chem. Phys., 31 (1959) 1164.

192. L. A. Simpson and R. E. Carter, J. Amer. Ceram. Soc., 49 (1966) 139.

193. R. L. Fleischer, P. B. Price, and R. M. Walker, General Electric (U.S.A.) Report 64-RL-3831 M (1964).

194. R. M. Berman, Bettis (U.S.A.) Report WAPD-TM-350 (1962).

195. I. S. Kerr, Acta Cryst., 9 (1956) 879.

196. S. Mader, A. S. Nowick, and H. Widmer, Acta Met., 15 (1967) 203.

197. W. D. Kingery, J. M. Woulbroun, and R. L. Coble in "Advances in glass technology", Part 2 (Plenum Press, New York) (1963) p. 24.

198. R. W. Mickelsen and W. D. Kingery, J. Appl. Phys., 37 (1966) 3541.

199. V. Balek, J. Mat. Sci., 4 (1969) 919.

200. Hj. Matzke, unpublished work on CaO.

201. G. Carter, W. A. Grant, J. D. Haskell, and G. A. Stephens, Rad. Effects, 6 (1970) 277.

202. J. D. Mackenzie, J. Am. Ceram. Soc., 43 (1960) 615.

203. M. Arora and R. Kelly, unpublished data on MoO_3 and V_2O_5.

204. R. R. Hart, H. L. Dunlop, and O. J. March, Rad. Effects, 9 (1971) 261.

205. H. E. Schiøtt, private communication.

206. P. B. Hirsch, A. Howie, R. B. Nicholson, D. W. Pashley, and M. J. Whelan, "Electron microscopy of thin crystals" (Butterworths, London), (1969).

207. E. M. Levin and R. S. Roth, J. Res. Nat. Bur. Std., 68A (1964) 189.

208. T. N. Kennedy, R. Hakim, and J. D. Mackenzie, Mat. Res. Bul., 2 (1967) 193.

209. A. S. Nowick and S. Mader, IBM J. Res. Dev., 9 (1965) 358.

210. J. Novakova and P. Jirů, Collection Czechoslov. Chem. Comm., 29 (1964) 114.

211. R.W.G. Wyckoff, "Crystal structures", (Interscience Publ., New York), Vol. 1-3, (1965).

212. T. C. MacAvoy, in "An atomistic approach to the nature and properties of materials", Ed. by J. A. Pask (John Wiley, New York (1967), Ch. 6.

213. J. H. Crawford, Jr. and M. C. Wittels, Proc. Int. Conf. on Peaceful Uses of Atomic energy, (United Nations) Vol. 7 (1956) p. 654.

214. L. Pauling, "Nature of the Chemical Bond", (4th edn.) (Cornell Univ. Press), (1967).

215. W. Gordy and W. J. Orville Thomas, J. Chem. Phys., 34 (1956) 439.

216. H. M. Naguib and R. Kelly, to be submitted to J. Phys. Chem. Solids.

217. P. J. Harrop, N.J.M. Wilkins, and J. N. Wanklyn, Proc. Brit. Ceram. Soc., 9 (1967) 279.

218. L. B. Griffiths, Nature, 188 (1960) 43.

219. W. R. Hardy, Ph.D. Thesis, McMaster University (1971).

220. L. E. Collins, P. A. O'Connell, J. G. Perkins, F. R. Pontet, and P. T. Stroud, Nucl. Instr. and Methods, 92 (1971) 455.

221. P. Sigmund, Phys. Rev., 184 (1969) 383.

222. L. B. Valdes, Proc. IRE, 42 (1954) 420.

223. A. H. Tong and A. Dupnock, J. Electrochem. Soc., 118 (1971) 390.

224. L. Kihlborg, Acta Chem. Scand., 13 (1959) 954.

225. J. Haemers, C. R. Acad. Sci. Paris, 259 (1964) 3740.

226. I. B. Patrina and V. A. Ioffe, Soviet Phys-Solid State, 6 (1965) 2581.

227. G. K. Wehner, C. E. Kenknight and D. Rosenberg, Planet.Space Sci., 11 (1963) 1257.

228. E. Gillam, J. Phys. Chem. Solids, 11 (1959) 55.

229. N. N. Greenwood, "Ionic crystals, lattice defects, and non-stoichiometry", (Butterworths, London), (1968).

230. V. J. Rudolph, Sonderdruck, 8 (1963) 86.

231. D. Adler, Solid State Physics, 21 (1968) 1.

232. R. C. Vickery and J. C. Hipp, J. Appl. Phys., 37 (1966) 2926.

233. H. Okinaka, K. Nagasawa, K. Kosuge, Y. Bando, S. Kachi, and T. Takada, J. Phys. Soc. Japan, 28 (1970) 798; ibid, 28 (1970) 803; and ibid, 29 (1970) 245.

234. F. J. Morin, Phys. Rev. Letters, 3 (1959) 34.

235. J. Feinleib and W. Paul, Phys. Rev., 155 (1967) 841.

236. R. Kelly, Can. J. Phys., 46 (1968) 473.

237. A. C. Damask and G. J. Dienes, "Point defects in metals", (Gordon and Breach, New York) (1963).